

# QUANTUM CONTROL OF SINGLE MOLECULAR IONS

A novel route to precision measurements on single  
molecules using quantum technologies

**Inauguraldissertation**

zur

Erlangung der Würde eines Doktors der Philosophie  
vorgelegt der  
Philosophisch-Naturwissenschaftlichen Fakultät  
der Universität Basel

von

**Mudit Sinhal**

2021

Originaldokument gespeichert auf dem Dokumentenserver der Universität Basel  
edoc.unibas.ch

Genehmigt von der Philosophisch-Naturwissenschaftlichen Fakultät auf Antrag von

Prof. Dr. Stefan Willitsch, Prof. Dr. Philipp Treutlein und Prof. Dr. Jeroen Koelemeij

Basel, 21.09.2021

Prof. Dr. Marcel Mayor  
Dekan der Philosophisch - Naturwissenschaftlichen Fakultät

To my wife and my parents  
Thank you for your love and support

# ABSTRACT

Trapped atoms and ions are among the best-controlled quantum systems which find widespread applications in quantum sciences. For molecules, a similar degree of control is currently lacking owing to their complex energy-level structure. Quantum-logic protocols in which atomic ions serve as probes for molecular ions are a promising route for achieving this level of control, especially for homonuclear species that decouple from blackbody radiation.

In this thesis, we report experimental progress in the quantum state control of single trapped  $\text{N}_2^+$  molecules.  $\text{N}_2^+$  is a homonuclear diatomic molecule with no permanent dipole moment. Thus all rotational-vibrational (rovibrational) transitions are rendered dipole-forbidden in its electronic ground state. Therefore,  $\text{N}_2^+$  is an ideal test bed for precision spectroscopic studies, for tests of fundamental physics, for the realization of mid-IR frequency standards and clocks, and for implementation of molecular qubits for quantum information and computation applications.

Here, a single  $\text{N}_2^+$  ion is produced selectively in the ground rovibronic state and trapped in a radiofrequency ion trap together with one  $\text{Ca}^+$  ion. In a first step, the  $\text{Ca}^+$  ion is used to cool the  $\text{N}_2^+$  to the ground state of the trapping potential. A quantum-nondemolition protocol is then implemented on the  $\text{Ca}^+ - \text{N}_2^+$  two-ion string in order to detect the rotational state of the  $\text{N}_2^+$  ion. The protocol maps the internal state of the  $\text{N}_2^+$  ion onto the external motion which is then detected by the  $\text{Ca}^+$  ion. The employed state-detection scheme is non-invasive and does not destroy the molecule or the molecular state. The spin-rovibronic state of the molecule is detected with fidelities exceeding 99%. Furthermore, as an application of the state-detection scheme, the transition frequency and the vibronic Einstein-A coefficient of an electric-dipole transition of the molecular ion is measured.

In an effort to develop a complete and conscientious understanding of the mechanism exploited in the rovibronic-state detection of the molecule, this thesis theoretically investi-

gates electric-dipole transitions between molecular states best described by different Hund's coupling cases. The Hamiltonians for specific states are presented and subtle effects due to the molecular-hyperfine structure and mixing of rotational states are discussed.

This thesis also discusses our setup of a system of narrow linewidth lasers for coherent manipulations of the atomic and the molecular ions. For the  $\text{Ca}^+$  ion, a cavity stabilized, 729 nm, ECDL is first stabilized to a high finesse cavity for linewidth narrowing and improved short term stability. In order to detect and compensate the long term drifts of the cavity, the 729 nm laser frequency is then compared to an UTC-referenced ultrastable laser at 1572 nm via an optical frequency comb. A stability of  $\sim 1 \times 10^{-13}$  is demonstrated in 1 s. For experiments on the  $\text{N}_2^+$  ion, a mid-IR quantum-cascade laser at 4574 nm is stabilized to the optical frequency comb. A sum-frequency generation process, with the cavity stabilized 729 nm laser, is employed in order to bridge the gap between the mid-IR laser and the near-IR comb. A tight lock with a signal-to-noise ratio of  $\sim 30$  dB is demonstrated. The experimental and theoretical developments in this thesis lay the foundations for new approaches to precision spectroscopy and coherent control experiments on molecules.

# ACKNOWLEDGMENTS

*“If I have seen further it is only by standing on the shoulders of giants.”*

- Sir Issac Newton

I am grateful to a number of friends, family members and colleagues for their help, advice, encouragement and support during the pursuit of my doctoral studies.

First, I would like to thank Prof. Dr. Stefan Willitsch for giving me the opportunity to join the molecular Quantum Technologies (QuTe) project. His mentorship and encouragement, specially during long phases of failed experiments and unsuccessful results, really helped me in keeping up my motivation. I would like to thank Prof. Dr. Philipp Treutlein for periodically reviewing my research and advising me on the next possible steps. I would also like to thank Dr. Jeroen Koelemeij for assessing this thesis as a co-examiner.

It would like to express my greatest appreciation towards Dr. Ziv Meir. It would not be far fetched to assume that the research accomplished during my doctoral studies would not have been possible without his extraordinary brilliance. His research dexterity, methodology and tenaciousness have left me with valuable scientific skills. I would like to thank Dr. Kaveh Najafian and Dr. Alexander Dörfler for helping me settle in Basel and their companionship and discussions on both professional and personal matters. I would like to thank Mikolaj Roguski and Aleksandr Shlykov for providing a stimulating and lively work environment. I would also like to thank Dr. Tomislav Damjanovic, Ludger Ploenes and Patrick Straňák for their help on many experimental and theoretical matters, and Dr. Ardita Kilaj, Dr. Claudio von Planta, Dr. Thomas Kierspel, Moritz Weegen, Pietro Vahramian, Lei Xu, Amit Mishra and Dr. Yanning Yin for fruitful discussions and interactions specially outside of the university. I am indebted to everyone in the group for their contribution to my development as a scientist. The functioning of the research group would not be possible without the

expertise of the staff members. Thank you Philipp Knöpfel and Grischa Martin for all the help and incredible mechanical constructions of our experimental parts. Thank you Georg Holderied Salvisberg and Dr. Anantoly Johnson for help with electronics and lasers, both for work and hobby, and for pet-sitting my beloved cat Bella during my vacations. I would also like to thank our staff members Maya Greuter, Mariella Schneiter and Markus Ast for the smooth operations of the group.

I would like to extend my gratitude to Prof. Dr. Jonathan Home and Prof. Dr. Kenneth R. Brown who introduced me to the world of ion trap physics by providing me with internship opportunities. I am immensely grateful.

Thank you Pranshul Awasthi, my beloved wife. Without your selfless support, dedication, and patience, this thesis would not have been possible. I owe you a lot. I thank my mother Sangeeta Agarwal, and my father Manoj Kumar Agarwal - who taught me everything of value and provided me with a loving and caring environment, and an education surpassing their means. I would like to thank my brother Piyush Sinhal for all our countless fights. I am blessed to have you and wish you all the best in your present and future endeavors - live long and prosper. My uncle Sanjay Agarwal, my aunt Puspa Agarwal and my cousins Dipali and Aditya Agarwal, thank you. One of the major reasons that lead me to pursue academics is the love and encouragement I received from my grandparents, especially my grandfather Lalit Kumar Agarwal who taught me the importance of education. I cannot thank them enough. I would also like to thank my in laws Shantanu, Suman and Aditi Awasthi for their encouragement especially during difficult times.

Finally, I would like to thank my friends Dr. Koushik Chatterjee, Prashant Kartikeya and Anurag Reddy for standing by me through thick and thin. I would like to thank Shaheen Perveen and Dr. Harsh Beria. You guys have been a pillar of support. My school friends Abhisek Samanthy, Nikhil Pratap and Ashutosh Agrawala and all my college friends thank you for all the happy, crazy and joyful memories I carry.

# Table of Contents

	Page
<b>1 Introduction</b> . . . . .	1
<b>2 Molecular systems and the <math>N_2^+</math> ion</b> . . . . .	7
2.1 Molecular systems . . . . .	7
2.1.1 Space-fixed and molecule-fixed reference frames . . . . .	7
2.1.2 Hund's coupling cases . . . . .	8
2.1.3 Symmetries in diatomic molecules: Inversions and Permutations . . . . .	12
2.2 The $N_2^+$ molecular ion . . . . .	19
2.2.1 The $X^2\Sigma_g^+$ electronic state . . . . .	19
2.2.2 The $A^2\Pi_u$ electronic state . . . . .	20
2.2.3 The $B^2\Sigma_u^+$ electronic state . . . . .	21
2.3 Energy levels of the $N_2^+$ ion . . . . .	22
2.3.1 The $X^2\Sigma_g^+(v = 0)$ state . . . . .	23
2.3.2 The $A^2\Pi_u(v = 2)$ state . . . . .	27
<b>3 Hyperfine effects in the ac-Stark effect in the <math>N_2^+</math> ion</b> . . . . .	35
3.1 Dispersive light-matter interaction . . . . .	36
3.1.1 Optical-dipole force . . . . .	37
3.1.2 Scattering rate . . . . .	37
3.2 Transition-dipole matrix elements . . . . .	39
3.2.1 Hund's case (b) to Hund's case (b) transitions without fine- structure coupling . . . . .	39
3.2.2 Hund's case (b) to Hund's case (b) transitions including fine- structure coupling . . . . .	45

3.2.3	Hund's case (b) to Hund's case (a) transitions including fine-structure coupling . . . . .	51
3.2.4	Hund's case (b) to Hund's case (a) transitions including fine-structure and hyperfine-structure coupling . . . . .	57
3.2.5	Hund's case (b) to Hund's case (a) transitions including mixing of states . . . . .	63
3.3	ac-Stark effect in $N_2^+$ . . . . .	65
3.3.1	Effects due to the hyperfine structure . . . . .	69
3.3.2	Off-resonant photon-scattering rates . . . . .	72
<b>4</b>	<b>Spectrally Pure, SI-referenced lasers for high-precision spectroscopy . .</b>	<b>74</b>
4.1	The 729 nm and the OFC laser systems . . . . .	77
4.1.1	The PDH stabilization setup . . . . .	77
4.1.2	The OFC stabilization setup . . . . .	79
4.1.3	Beam Delivery setup . . . . .	84
4.2	The 4574 nm laser system . . . . .	84
4.2.1	The Characterization Setup . . . . .	86
4.2.2	Stabilization Setup . . . . .	103
4.2.3	Beam Delivery Setup . . . . .	106
<b>5</b>	<b>Quantum control of a single trapped <math>N_2^+</math> ion . . . . .</b>	<b>120</b>
5.1	The Experimental setup . . . . .	122
5.2	Preparation of $N_2^+$ in the rovibronic ground state . . . . .	124
5.3	Cooling of external motion of the $N_2^+$ ion . . . . .	126
5.3.1	Sympathetic Doppler cooling of $Ca^+$ and $N_2^+$ ions . . . . .	127
5.3.2	Sympathetic sideband cooling of the $Ca^+-N_2^+$ two-ion string . . . . .	129
5.4	Quantum-nondemolition state detection of $N_2^+$ . . . . .	131
5.4.1	Suppression of motional excitation due to the $Ca^+$ ion . . . . .	141
5.4.2	Estimation of the state-detection fidelities . . . . .	142
5.5	Force spectroscopy . . . . .	145
5.5.1	Determination of the fitting function for Rabi sideband oscillations . .	148
5.6	Coherent manipulation of the $N_2^+$ ion . . . . .	154

5.7 Implications and summary . . . . .	156
<b>6 Conclusion and outlook . . . . .</b>	<b>159</b>
<b>Appendices</b>	
<b>A Ac-Stark effect in Ca<sup>+</sup> atomic ions . . . . .</b>	<b>162</b>
A.1 Valence contributions . . . . .	162
A.2 Core contributions . . . . .	165

# List of Figures

1.1	The International System of Units (SI) . . . . .	4
2.1	Hund's coupling cases (a) . . . . .	10
2.2	Hund's coupling cases (b) . . . . .	11
2.3	Energy level structure of the $X^2\Sigma_g^+$ state of $N_2^+$ molecular ion . . . . .	20
2.4	Energy level structure of the $A^2\Pi_u$ state of $N_2^+$ molecular ion . . . . .	21
2.5	Hyperfine structure of the $B^2\Sigma_u^+$ state of $N_2^+$ molecular ion. . . . .	22
3.1	Hund's case (b) to Hund's case (b) transitions excluding fine-structure coupling . . . . .	44
3.2	Hund's case (b) to Hund's case (b) transitions . . . . .	50
3.3	Hund's case (b) to Hund's case (a) transitions . . . . .	55
3.4	ac-Stark shift experienced by a $N_2^+$ ion in the ground state . . . . .	67
3.5	The $R_{11}(1/2)$ transition in $N_2^+$ $I = 0$ . . . . .	68
3.6	Hyperfine structure effects in the $R_{11}(1/2)$ transition in $N_2^+$ . . . . .	69
3.7	The $R_{11}(1/2)$ transition in $I = 2$ $N_2^+$ . . . . .	70
3.8	Comparison of the $R_{11}(1/2)$ transition in $N_2^+$ between the $I = 0$ and $I = 2$ molecules . . . . .	71

3.9	Comparison between ac-Stark shift and photon scattering for a ground state $N_2^+$ ion due to an off-resonant laser . . . . .	73
4.1	Relevant energy levels of the $Ca^+$ and $N_2^+$ ions for precision spectroscopy . .	75
4.2	Stabilization setup for the 729 nm and the OFC laser systems . . . . .	76
4.3	Allan deviations of the 729 nm laser . . . . .	83
4.4	Stabilization setup for the 4574 nm QCL . . . . .	87
4.5	Measurements for determining the QCL tuning coefficient . . . . .	89
4.6	Measurements of the discriminator slope and laser frequency noise for FNPSD determination . . . . .	90
4.7	Measured noises of the QCL . . . . .	91
4.8	QCL linewidth and modulation bandwidth measurements . . . . .	93
4.9	QCL modulation bandwidth measurements . . . . .	94
4.10	Comparisons of linewidths and locking performance of different QCLs . . .	98
4.11	Effects of optical feedback into the QCL . . . . .	99
4.12	Schematic of setup for current noise measurements . . . . .	101
4.13	Comparisons of current noise of different drivers . . . . .	102
4.14	Beat note of the QCL with the OFC . . . . .	105
4.15	QCL-Ion Alignment . . . . .	108
4.16	QCL Beam Characterization . . . . .	108
4.17	Simulated alignment of the QCL on the ion . . . . .	109
4.18	QCL-Ion Alignment . . . . .	109
4.19	Ac-Stark shift measurements . . . . .	111

4.20 Bloch sphere representation of the Ramsey ac-Stark shift measurement technique . . . . .	113
4.21 Ramsey ac-Stark shift measurement . . . . .	115
4.22 Measurements of the $\text{Ca}^+$ ion coherence . . . . .	116
4.23 Measurement of small ac-Stark shifts . . . . .	117
4.24 Automatized alignment of the QCL on the ion . . . . .	119
5.1 Schematic of the experimental setup . . . . .	122
5.2 REMPI schemes for the ionization of $\text{N}_2$ . . . . .	125
5.3 Relevant energy levels of the $\text{Ca}^+$ and $\text{N}_2^+$ ions . . . . .	128
5.4 Sympathetic Doppler cooling of $\text{N}_2^+$ . . . . .	129
5.5 Sympathetic sideband cooling of $\text{Ca}^+-\text{N}_2^+$ two-ion string . . . . .	130
5.6 Schematic for the state detection of $\text{N}_2^+$ . . . . .	133
5.7 Ac-Stark shift generated on $\text{N}_2^+$ by the one-dimensional optical lattice . . . . .	137
5.8 Quantum non-demolition state detection of $\text{N}_2^+$ . . . . .	139
5.9 Motional excitation due to $\text{Ca}^+$ . . . . .	141
5.10 Likelihood Estimate . . . . .	144
5.11 Non-destructive force spectroscopy on a single $\text{N}_2^+$ molecule . . . . .	146
5.12 Ac-Stark shift calibration . . . . .	153
5.13 Simplified energy-level scheme of $\text{N}_2^+$ to illustrate the effect of vibrational excitation on the ODF . . . . .	155

# List of Tables

2.1	Quantum numbers describing different angular momenta for molecules . . . .	9
2.2	Molecular constants for the $X^2\Sigma_g^+(v = 0)$ band in $N_2^+$ . . . . .	26
2.3	Mixing coefficients and state energies for the $X^2\Sigma_g^+(v = 0)$ rotational states .	27
2.4	Molecular constants for the $A^2\Pi_u(v = 2)$ band in $N_2^+$ . . . . .	33
2.5	Mixing coefficients and state energies for the $A^2\Pi_u(v = 2)$ rotational states .	33
3.1	Comparison between Hönl-London factors . . . . .	64
4.1	Different QCLs investigated in this thesis . . . . .	97
4.2	Summary of current noise measurements for three different QCL drivers . . .	103
A.1	Different parameters for $Ca^+$ ion. . . . .	164

# Chapter One

## Introduction

The two convoluted subjects of time and light govern countless aspects of lives of almost all living organisms on our planet. Early humans, hundreds of centuries before the establishment of civilisations, entrusted their day to the periodic rising and setting of the sun. Periodic behaviour of the weather that seemed to be related to the movement of the sun, formed the basis of migration of life on earth. Units of days, months and years naturally followed as humans started settling into civilisations. They formed the basis on which crops were sown and cultivated and livestock were farmed. As civilisations progressed nature's clocks started proving insufficient since the measured unit scales proved too large for many practical purposes. Natural oscillators were soon supplemented by man-made time-keeping devices. Around 3500 BC, the Egyptians divided the day into shorter sections by observing the shadow cast by various man-made objects due to the sun's position [1, 2]. This later led to the development of sundials. Clepsydrae and hour glasses relying on controlled flow of water were invented around 1500 BC [2]. These were the first time measurement devices which did not rely on light from celestial objects. Around the fourteenth century, mechanical clocks driven by flowing water started to appear as well. Although these allowed for finer divisions of a day, they were often difficult to manufacture, control and steer, were only locally available and depending on the flow of water, lost or gained time easily.

The discovery that the period of oscillation of a suspended pendulum was independent of

the pendulum's mass by Galileo Galilei in the 17th century [3], led to significant advances in time-keeping. Pendulum clocks improved significantly from their first design by Christiaan Huygens [4, 5] in the mid 17th century, where they had an error of less than a minute in a day, to the early 20th century where they could achieve accuracies better than hundredth of a second in a day [6]. The 19th century marked the invention of techniques for synchronizing the then available clocks [7, 8]. The advent of Quartz oscillators in the early 20th century further pushed the field. Quartz clocks soon proved their superiority with respect to pendulum clocks [9]. Time periods as small as 20 ns (corresponding to oscillation frequencies of 50 MHz) could be measured with a fractional precision exceeding  $10^{-10}$ . Modern and improved versions of quartz oscillators still form the basis for many modern time keeping devices [10].

In the early 1930s it became clear that further improvements in time keeping for scientific tasks would require new developments. It had been realized that atoms and molecules have characteristic resonances. Unperturbed transitions in matter were universal (every atom/molecule of the same kind has the same transition frequency) and unlike the previous time-keeping devices, atoms and molecules did not wear out. In the 1930s and 40s, Isidor Rabi and his colleagues at Columbia University developed basic concepts for atomic and molecular oscillators based on his experimental techniques of atomic beam magnetic resonances [11, 12]. The business of time keeping again started relying on light and electromagnetic fields in general. In 1949, the National Bureau of Standards (NBS) built the first molecular clock based on ammonia (which operated at 23.8 GHz) [13, 14]. Although it operated at a much higher frequency, its stability was comparable to the then existing quartz standards. In 1955, the National Physical Laboratory (NPL) in England built the world's first practical Cesium atomic frequency standard with superior performance [15]. By the 1960s, Cs frequency standards were developed at several national metrological institutes around the world. By international agreement, in 1967, the second was defined as the duration of 9,192,631,770 periods of the radiation corresponding to the transition between two hyperfine levels  $|F = 4, m_F = 0\rangle \leftrightarrow |F = 3, m_F = 0\rangle$  in the ground  $^2S_{1/2}$  state of the  $^{133}\text{Cs}$

atom [16, 17].

The 1960s also marked the arrival of lasers [18–20]. Although, initially believed to be “a solution looking for a problem”, the emergence of lasers opened up many new possibilities in various scientific fields including frequency metrology. By the late 1960s, lasers stabilized to atomic and molecular resonances became reliable tools for spectroscopic investigations [21, 22]. Frequency measurement techniques, such as harmonic generation [23, 24] and heterodyne mixing [25] were also developed in order to measure the very high frequencies at which lasers operate. Long (but often cumbersome) frequency synthesis chains were constructed to link the optical frequencies of lasers to the microwave output of Cs frequency standards [26]. These developments also allowed for comparison of different Cs standards and transition frequencies could now be measured precisely with fractional frequency instabilities as small as  $5 \times 10^{-13}$  in many Cs clocks [27]. The invention of optical reference cavities and frequency stabilization techniques [28] allowed for the narrowing of the linewidth of lasers for high-precision interrogations. The 1990s and 2000s marked the invention of the optical frequency comb [29, 30] due to remarkable research by John Hall and Theodor Hänsch (which led to them being awarded the Nobel prize in 2005 [31, 32]). Optical frequency combs provided convenient ways of measuring optical frequencies in the radiofrequency domains. They also allowed for absolute frequency stabilization of lasers which could then in-turn be used to accurately measure transitions in atoms and molecules.

Today, frequency metrology forms the basis for the most accurate measurements on earth. Because of this, on the 20th May 2019 - the world metrology day, the International System of Units (SI) was revised [33]. The definitions of the all base units except mole depended on the definition of a second. Fig. 1.1 shows old and the new definitions of the seven base units.

In addition to time keeping, frequency metrology has applications in several fields like precision spectroscopy [34, 35], tests of fundamental physics [36, 37], astronomy [38], gravitational wave detections [39, 40], satellite communication [41], GPS [42, 43] and geodesy [44, 45]

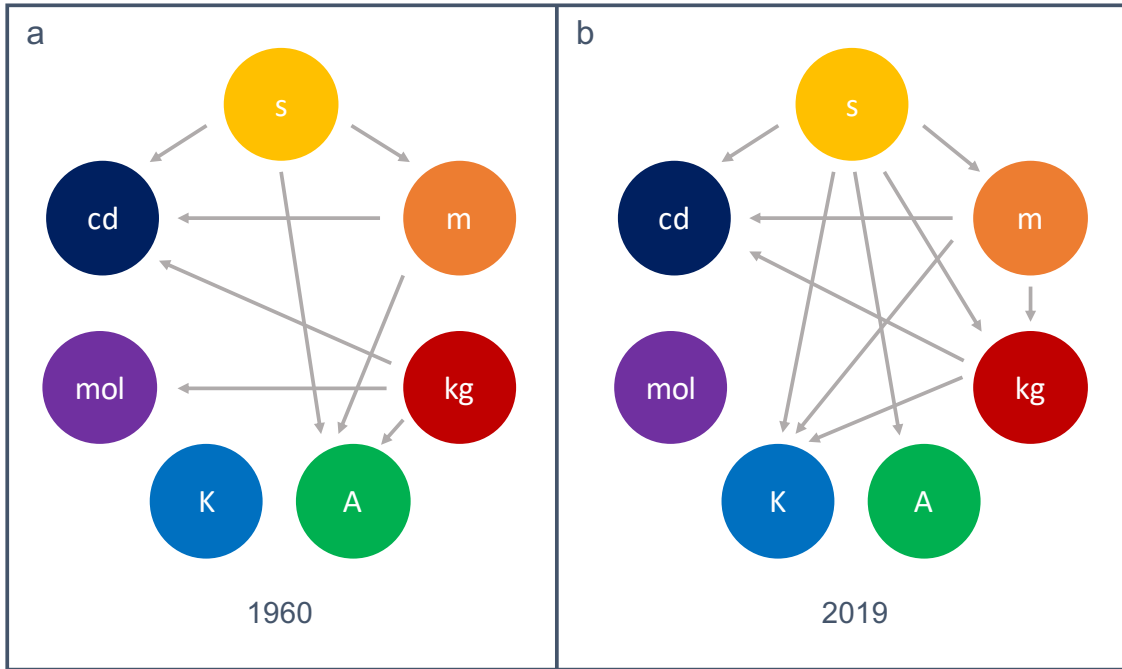


**Figure 1.1 The International System of Units (SI).** (a) The seven base units of the SI system set in the 1960s. Only definitions of the meter (m), the ampere (A) and the Candela (cd) were dependent on the definition of the second (s) (grey arrows). Definitions of the mole (mol) and the independent Kelvin (K) are also shown. (b) After the redefinition of the SI in 2019, all base units except the mol now depend on the definition of s.

to name a few. Commercially available Hydrogen masers have reached uncertainties of  $\sim 1 \times 10^{-13}$  while modern laboratory Cs fountain clocks have been demonstrated to have relative uncertainties of  $\sim 2 \times 10^{-16}$  [46]. The  $^2S_{1/2}(F=0) \leftrightarrow ^2F_{7/2}(F=3)$  octupole transition at a transition frequency of 642 THz (467 nm) in the  $^{171}\text{Yb}^+$  ion has been measured to a relative frequency uncertainty of  $1.1 \times 10^{-18}$  and an accuracy of  $3 \times 10^{-18}$  [34] while the hyperfine induced  $^1S_0 \leftrightarrow ^3P_0$  clock transition in  $^{27}\text{Al}^+$  ion at 1123 THz (267 nm) has been measured with accuracies of  $9.4 \times 10^{-19}$  (although with a lower frequency uncertainty of  $1.2 \times 10^{-15}$ ) [35]. The  $^1S_0 \leftrightarrow ^3P_0$  transition at 429.5 THz (698 nm) in neutral  $^{87}\text{Sr}$  optical lattice clock has been measured to an accuracy of  $1.3 \times 10^{-18}$  with a frequency uncertainty of  $1.1 \times 10^{-18}$  [47] and the  $^1S_0 \leftrightarrow ^3P_0$  transition in neutral Yb optical lattice clock has been measured to an accuracy of  $1.4 \times 10^{-18}$  and a frequency instability of  $3.2 \times 10^{-19}$  [44].

It can be noted from the discussions in the previous paragraph that while the field of atomic and atomic ion spectroscopy has leaped forwards in the past two decades, similar advancements for molecules and molecular ions have been lacking. The best measurements currently reported for molecular ions are on the  $\text{HD}^+$  ion [48] demonstrating uncertainties of  $2.9 \times 10^{-12}$ . This can largely be attributed to the complex energy level structure of molecules. While on one hand these transitions offer many additional possibilities for novel experiments with molecules [49–52], they hinder cooling and non-destructive detection of most molecules directly using techniques developed for experiments on the atomic counterparts.

In an effort to develop novel theoretical and experimental tools for the study of molecules, this thesis deals with precision investigations of the  $^{28}\text{N}_2^+$  molecular ion.  $\text{N}_2^+$  is a homonuclear diatomic molecule featuring electric-dipole-forbidden transitions within the rovibrational manifolds of its electronic states. It is an ideal candidate for high-resolution and high-precision spectroscopy [53,54], tests of possible time variations of the proton-to-electron mass ratio [55], development of molecular qubits and new frequency standards [53, 54, 56] and studies of state-to-state chemistry [57–60] and state and energy controlled reactions on the single particle level.

Chapter 2 serves as a general introduction to molecular systems and discusses the electronic states of the  $\text{N}_2^+$  molecule. Hamiltonians for specific vibronic states are presented. Mixing of rotational states due to various terms of the Hamiltonians are also explored and transition frequencies and mixing coefficients for specific states are calculated. On the basis of these discussions, in chapter 3, a consistent theory of electric-dipole-allowed transitions in the  $\text{N}_2^+$  molecular ion is developed. Effects due to hyperfine structure and mixing of rotational states on the ac-Stark shift experienced by the  $\text{N}_2^+$  because of off-resonant light are also discussed. Chapter 5 presents a key advancement in the quantum control of molecules. The ac-Stark effect is exploited for the non-demolition rovibronic state detection of  $\text{N}_2^+$ . As an application of the state detection method, measurement of a dipole-allowed rovibronic transition of the molecular ion is also presented. Based on the state-detection technique,

prospects for precision spectroscopy on dipole forbidden transitions in  $N_2^+$  in the near future are discussed. The development of a system of linewidth-narrowed and absolutely-referenced lasers for such precision investigations is presented in chapter 4. Although the  $N_2^+$  ion has been focused on here, the techniques presented are general and can be extended to a variety of diatomic and polyatomic molecules.

# Chapter Two

## Molecular systems and the $\text{N}_2^+$ ion

As stated in the introductory chapter, a key advancement presented in this thesis is the non-demolition rovibronic-state detection of  $\text{N}_2^+$ . The employed state-detection scheme relied on optical-dipole forces generated due to dispersive interactions between light and the  $\text{N}_2^+$  molecule. Before investigating the details of such off-resonant phenomena, it is necessary to set the stage and examine key concepts necessary for such studies. This chapter begins with a discussion of general molecular systems. Various limiting cases of angular momenta coupling in molecules and the associated symmetries are discussed rigorously and in a consistent manner. Following the general discussions, the  $\text{N}_2^+$  molecule is introduced. Different electronic states of the  $\text{N}_2^+$  ion are explored and the energy levels of specific vibronic states are evaluated from the energy Hamiltonians. Subtle effects such as the mixing of states due to various terms of the Hamiltonians are also presented. The vibronic states discussed here are employed in the following chapters for the state-detection of  $\text{N}_2^+$ .

### 2.1 Molecular systems

#### 2.1.1 Space-fixed and molecule-fixed reference frames

Two reference frames become important for examining light-molecule interactions [61]. Properties of light are described easily in a space-fixed reference frame while molecular angular

momenta and their couplings can best be realized in a simple manner in a molecule-fixed frame of reference. A transformation between these frames is essential in exploring interactions between light and molecule. The coordinates of a point  $i$  in the molecule-fixed axis system  $(x_i, y_i, z_i)$  are related to its coordinates in the space-fixed axis system,  $(X_i, Y_i, Z_i)$ , by the Euler angles  $(\phi, \theta, \chi)$ . The transformation can be given by [62],

$$\begin{bmatrix} x_i \\ y_i \\ z_i \end{bmatrix} = \begin{bmatrix} \cos \phi \cos \theta \cos \chi - \sin \phi \sin \chi & \sin \phi \cos \theta \cos \chi + \cos \phi \sin \chi & -\sin \theta \cos \chi \\ -\sin \phi \cos \chi - \cos \phi \cos \theta \sin \chi & \cos \phi \cos \chi - \sin \phi \cos \theta \sin \chi & \sin \theta \sin \chi \\ \cos \phi \sin \theta & \sin \phi \sin \theta & \cos \theta \end{bmatrix} \begin{bmatrix} X_i \\ Y_i \\ Z_i \end{bmatrix}. \quad (2.1)$$

For linear molecules, it is customary to align the molecule-fixed  $z$  axis with the internuclear axis. The molecule-fixed  $z$  axis points in the direction of a vector starting from the first nucleus and connecting the other nuclei of the molecule. The orientation of a linear molecule can then be described completely by the Euler angles  $(\phi, \theta)$ . The third angle ( $\chi$ ) quantifies a rotation about the  $z$  axis, and is not well-defined for diatomic molecules due to the absence of off-axis nuclei [61, 62]. The angle ( $\chi$ ) can thus be arbitrarily chosen.

### 2.1.2 Hund's coupling cases

Molecules exhibit a variety of angular momenta. A description of the relevant angular momenta for diatomic molecules is given in table 2.1. The hierarchy of coupling of angular momenta are defined by Hund's coupling cases. Hund's coupling cases determine terms in molecular Hamiltonians that dominate over other terms. Smaller non-dominant terms can be treated as perturbations leading to simpler solutions of the Hamiltonians. In addition, the Hund's coupling cases help in determining the ordering of the energy levels of molecules.

Several Hund's coupling cases exist. A complete description of different Hund's cases can be found in [61, 63, 64]. Here, two important and often encountered limiting cases, the

Symbol	Molecule-fixed projection	Space-fixed projection	Quantum Number
$n$	–	–	Electronic
$v$	–	–	Vibrational
$R$	–	–	Nuclear-rotation
$N$	–	–	Rotation-orbital
$L$	$\Lambda$	–	Electronic-orbital
$S$	$\Sigma$	$M_S$	Electronic-spin
$I$	$I_Z$	$M_I$	Nuclear-spin
$J$	$\Omega$	$M_J$	Total angular momenta excluding nuclear spin
$F$	–	$M_F$	Total angular momenta including nuclear spin

**Table 2.1** Quantum numbers describing different angular momenta for molecules.

Hund’s coupling cases (a) and (b) are presented.

### 2.1.2.1 Hund’s coupling case (a)

A schematic representation of the Hund’s case (a) rovibronic states for a diatomic molecule is given in fig. 2.1a. The coupling scheme follows:

$$\vec{\Omega} = \vec{\Lambda} + \vec{\Sigma}, \quad (2.2a)$$

$$\vec{J} = \vec{R} + \vec{\Omega}. \quad (2.2b)$$

**Hyperfine coupling in Hund’s case (a) molecules** Two cases for the coupling of the nuclear spin  $I$  can arise as shown in 2.1b and c [65, 66]. In the case (a <sub>$\alpha$</sub> ) (fig. 2.1b), the magnetic interaction of the nuclear moment with the electronic orbital and spin moments is sufficiently strong and the nuclear spin is quantized along the molecule-fixed internuclear axis. Since the strengths of the hyperfine couplings are typically many orders weaker as compared to the electronic moments, this case is not expected to arise often. In the case

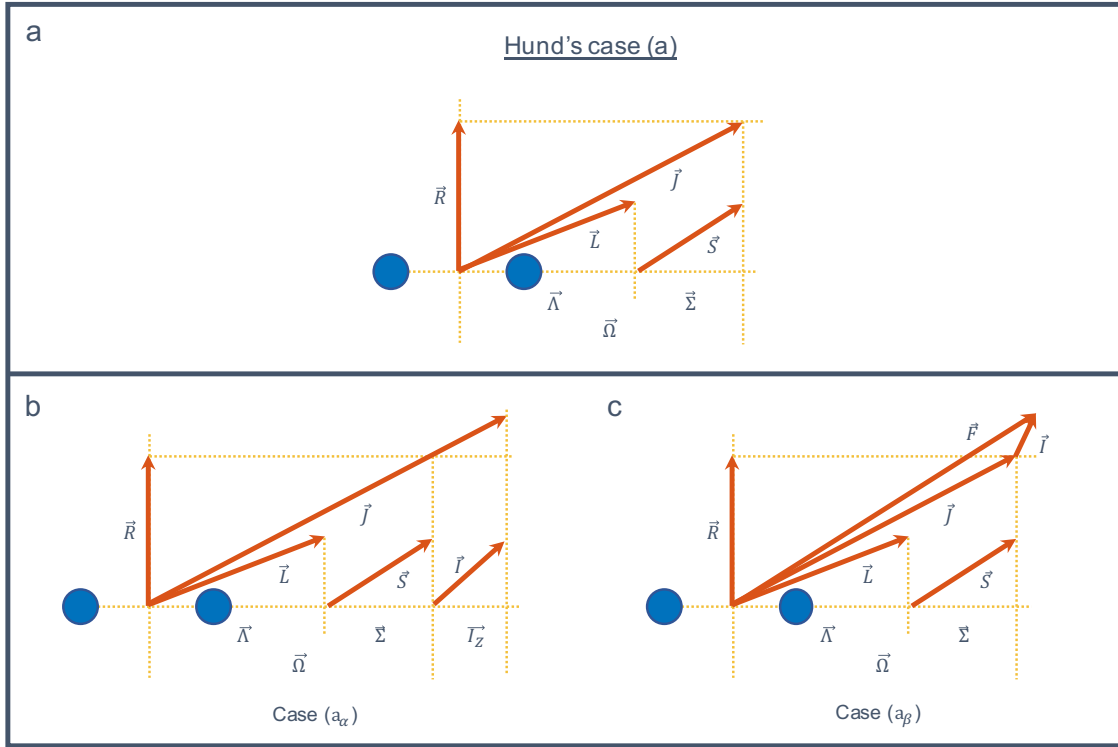


**Figure 2.1** Hund's coupling cases (a).

( $a_\beta$ ), the nuclear spin is quantized along the space-fixed coordinate frame (hence the subscript  $\beta$ ) as shown in fig. 2.1c.

The Hund's case ( $a_\beta$ ) is the most commonly occurring hyperfine-coupling case. For this case,

$$\vec{F} = \vec{J} + \vec{I}. \quad (2.3)$$

The first excited electronic  $A^2\Pi_u$  band of  $N_2^+$  are best described by Hund's coupling case ( $a_\beta$ ). The good quantum numbers for this coupling case are  $n, v, \Lambda, S, \Sigma, \Omega, J, I, F$  and  $M_F$ . Thus, a good basis representing states aptly described by Hund's coupling case ( $a_\beta$ ) can be given as  $|n, \Lambda; v; S, \Sigma; \Omega, J, I, F, M_F\rangle$ . If the hyperfine couplings are ignored, the basis simplifies to the Hund's coupling case (a) basis given by,  $|n, \Lambda; v; S, \Sigma; \Omega, J, M_J\rangle$ .

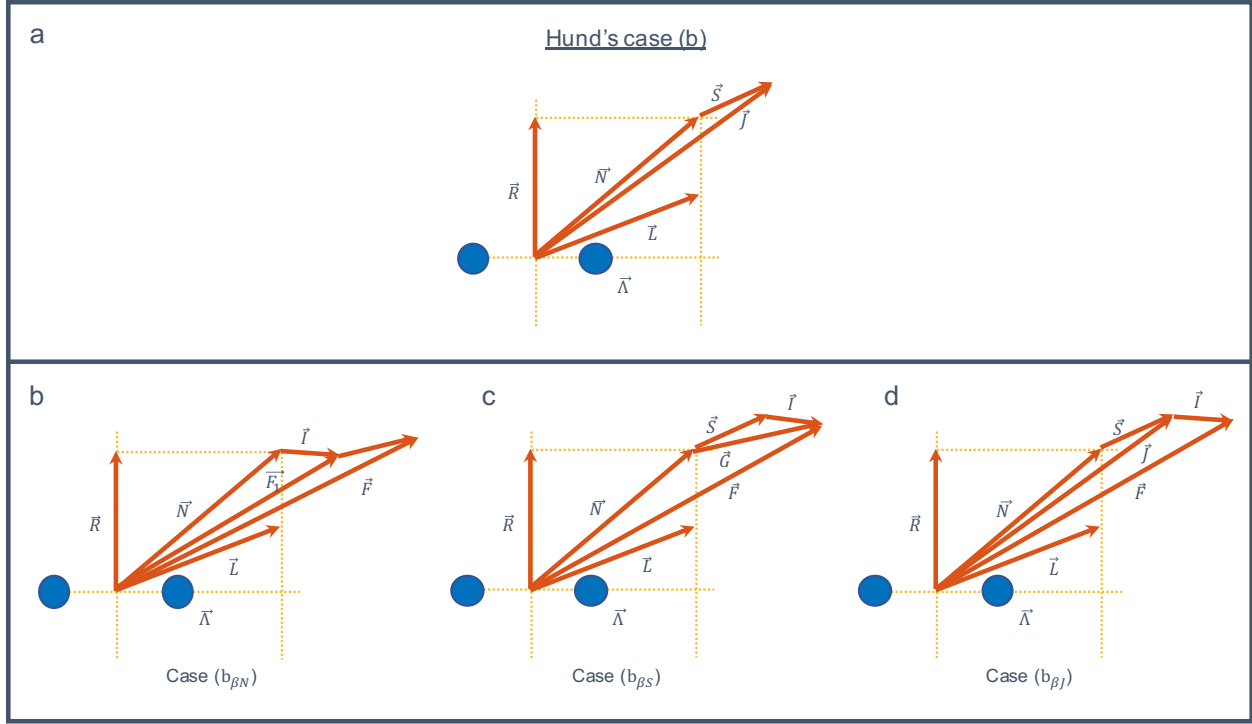


Figure 2.2 Hund's coupling cases (b).

### 2.1.2.2 Hund's coupling case (b)

A schematic representation of the Hund's case (b) rovibronic states for a diatomic molecule is given in fig. 2.2a. Here the coupling scheme follows:

$$\vec{N} = \vec{\Lambda} + \vec{R}, \quad (2.4a)$$

$$\vec{J} = \vec{N} + \vec{S}. \quad (2.4b)$$

**Hyperfine coupling in Hund's case (b) molecules** Three cases for the coupling of the nuclear spin  $I$  can arise as shown in 2.2b, c and d [65, 66]. In the case  $(b_{\beta N})$  (fig. 2.1b),  $\vec{I}$  first couples to  $\vec{N}$ . The resultant moment  $\vec{F}_1$  then couples to  $\vec{S}$ . In the case  $(b_{\beta S})$  (fig. 2.1c),  $\vec{I}$  first couples to  $\vec{S}$ . The resultant moment  $\vec{G}$  then couples to  $\vec{N}$ . Since the strengths of the hyperfine couplings are typically many orders weaker as compared to the electronic and orbital moments, both of these cases are not expected to arise often.

The Hund's case  $(b_{\beta J})$  is the most commonly occurring hyperfine-coupling case (fig.

2.2d). For this case,

$$\vec{F} = \vec{J} + \vec{I}. \quad (2.5)$$

The rotational states of the ground  $X^2\Sigma_g^+$  and second excited  $B^2\Sigma_u^+$  electronic states of  $N_2^+$  are best described by Hund's coupling case ( $b_{\beta J}$ ). The good quantum numbers for this coupling case are  $n, v, \Lambda, N, S, J, I, F$  and  $M_F$ . Thus, a good basis representing states described by Hund's coupling case ( $b_{\beta J}$ ) can be given as  $|n, \Lambda; v; N, \Lambda, S, J, I, F, M_F\rangle$ . As before, if the hyperfine couplings are ignored, the basis simplifies to the Hund's coupling case (b) basis given by,  $|n, \Lambda; v; N, \Lambda, S, J, M_J\rangle$ .

It is always possible to express the quantum numbers and basis states of one coupling scheme in terms of the quantum numbers and basis states of other schemes via Clebsch-Gordon coefficients. Such transformations become important specially when dealing with transitions between states described by different coupling schemes, as will be seen later.

### 2.1.3 Symmetries in diatomic molecules: Inversions and Permutations

An understanding of symmetries of molecular wavefunctions is important because transitions between rotational levels are limited by selection rules based on the the total state symmetry. In order to study the symmetry of the wavefunctions, proper distinction between *space-fixed* symmetry operators and *molecule-fixed* symmetry operators must be made. The parities of rotational states are defined only by the space-fixed inversion operator,  $E^*$ . Additionally, for homonuclear molecules, the behavior of the identical nuclei under the effect of space-fixed permutation operator,  $P_{12}$ , must also be considered.

The effect of space-fixed  $E^*$  and  $P_{12}$  symmetry operators on molecular wavefunctions can be related to the molecular-fixed geometric symmetry operations, i.e., rotation, reflection, inversion and improper rotation (also known as rotation-reflection). The effect of  $E^*$  and  $P_{12}$  can thus be studied from a group theory approach by identifying the symmetry point groups

of molecules, relating  $E^*$  and  $P_{12}$  to the point group operators and studying the effect of these operator on the molecular wavefunctions [67]. For diatomic molecules, the effect of the operators  $E^*$  and  $P_{12}$  can directly be evaluated on the rovibronic wavefunctions. A detailed description can be found in [61]. Here, relevant results applicable for homonuclear diatomic molecules are presented.

### 2.1.3.1 Inversion symmetry of rotational levels

The space-fixed inversion operator,  $E^*$ , is defined as an operator which transforms a function,  $f(X_i, Y_i, Z_i)$ , into the function,  $f(-X_i, -Y_i, -Z_i)$  [61, 67], i.e,

$$E^* f(X_i, Y_i, Z_i) = f(-X_i, -Y_i, -Z_i). \quad (2.6)$$

From the above equation, it is clear that  $(E^*)^2 = I$ , where  $I$  is the space-fixed identity operator. Additionally, the operator  $E^*$  commutes with the molecular Hamiltonian [61, 63]. Thus the total rovibronic wavefunction,  $\psi(X_i, Y_i, Z_i)$ , is an eigenstate of the operation  $E^*$  with the eigenvalues  $\pm$  as,

$$E^* \psi(X_i, Y_i, Z_i) = \pm \psi(X_i, Y_i, Z_i), \quad (2.7)$$

where  $i$  is over all particles (including electrons, protons and neutrons) of the diatomic molecule.

Ro-vibronic states transforming according to the + sign are said to be positive parity states. States which transform according to the – sign are said to be negative parity states.

**Inversion symmetry of Hund’s case (a) rotational states** The good quantum numbers and the basis states for rovibronic states best described by Hund’s coupling case (a) have been described above in section 2.1.2. Hyperfine structure contribute to small effects in the energy levels and do not have any consequence on the parities of the rovibronic states. The effect of  $E^*$  on Hund’s case (a) states can be obtained by considering the product rep-

resentation of the basis state (excluding hyperfine structure) and evaluating the effect of  $E^*$  on individual parts [61], i.e,

$$E^* |n, \Lambda; v; S, \Sigma; J, \Omega, M_J\rangle = E^* |n, \Lambda\rangle \cdot E^* |v\rangle \cdot E^* |S, \Sigma\rangle \cdot E^* |J, \Omega, M_J\rangle. \quad (2.8)$$

The behaviour of the individual parts of the above equation has been described in section (6.9) of [61]. These are,

$$E^* |n, \Lambda^s\rangle = (-1)^{(\Lambda+s)} |n - \Lambda^s\rangle, \quad (2.9a)$$

$$E^* |v\rangle = (+1) |v\rangle, \quad (2.9b)$$

$$E^* |S, \Sigma\rangle = (-1)^{(S-\Sigma)} |S, -\Sigma\rangle, \quad (2.9c)$$

$$E^* |J, \Omega, M_J\rangle = (-1)^{(J-\Omega)} |J, -\Omega, M_J\rangle, \quad (2.9d)$$

where the superscript,  $s$ , in (2.9a) distinguishes  $\Sigma^-$  states and  $\Sigma^+$ .  $s$  is odd for  $\Sigma^-$  states and even for  $\Sigma^+$  (and higher  $\Lambda$ ) states. The superscripts (+) and (-) of the  $\Sigma^+$  and  $\Sigma^-$  states define the reflection symmetry of these states along an arbitrary plane containing the internuclear axis. Since  $\Lambda > 0$  states always appear in pairs of symmetric and anti-symmetric states with respect to reflection in such a plane, the labels  $\pm$  are omitted for  $\Lambda > 0$  states.

The equation (2.9c) can also be written as,

$$E^* |S, \Sigma\rangle = (-1)^{(\Sigma-S+2(S-\Sigma))} |S, -\Sigma\rangle = (-1)^{(\Sigma-S)} |S, -\Sigma\rangle. \quad (2.10)$$

The complete behavior of Hund's case (a) states can thus be given by,

$$E^* |n, \Lambda^s; v; S, \Sigma; J, \Omega, M_J\rangle = (-1)^{(\Lambda+s+\Sigma-S+J-\Omega)} |n, -\Lambda^s; v; S, -\Sigma; J, -\Omega, M_J\rangle. \quad (2.11)$$

We note that  $\Omega = \Lambda + \Sigma$  for diatomic molecules. The equation thus simplifies as,

$$\begin{aligned} E^* |n, \Lambda^s; v; S, \Sigma; J, \Omega, M_J\rangle &= (-1)^{(s-S+J)} |n, -\Lambda^s; v; S, -\Sigma; J, -\Omega, M_J\rangle \\ &= (-1)^{(p)} |n, -\Lambda^s; v; S, -\Sigma; J, -\Omega, M_J\rangle, \end{aligned} \quad (2.12)$$

where,

$$p = J - S + s. \quad (2.13)$$

**Inversion symmetry of Hund's case (b) rotational states** The inversion symmetry for states best described by Hund's coupling case (b) can be given as [61],

$$E^* |n, \Lambda^s; v; N, \Lambda, S, J, M_J\rangle = (-1)^{(N+s)} |n, -\Lambda^s; v; N, -\Lambda, S, J, M_J\rangle. \quad (2.14)$$

**Comments on space-fixed inversion symmetries** From (2.12) and (2.14), it can be seen that the basis functions of Hund's case (a) and Hund's case (b) states (except for the case when  $\Lambda = 0$  in states described by Hund's coupling case (b) - see (2.14)) are not eigenfunction states of the space-fixed inversion operator. Conversely, it can be stated that neither of the states have a definite parity. However, it can be noted from (2.12) and (2.14) that a superposition of the degenerate basis functions do carry a definite parity. For example parity states for the Hund's case (a) basis can be given as,

$$|n, \Lambda^s; J, M; +\rangle = \frac{1}{\sqrt{2}} \{ |n, \Lambda^s; S, \Sigma; J, \Omega, M\rangle + (-1)^{(p)} |n, -\Lambda^s; S, -\Sigma; J, -\Omega, M\rangle \}, \quad (2.15a)$$

$$|n, \Lambda^s; J, M; -\rangle = \frac{1}{\sqrt{2}} \{ |n, \Lambda^s; S, \Sigma; J, \Omega, M\rangle - (-1)^{(p)} |n, -\Lambda^s; S, -\Sigma; J, -\Omega, M\rangle \}. \quad (2.15b)$$

If a perturbation lifts the two-fold degeneracy without destroying the parity, the two functions above are the eigenfunctions of the molecular system.

From (2.14) it can be seen that for the special case of  $\Sigma^\pm$  states with ( $\Lambda = 0$ ), the basis state is an eigenfunction of the symmetry operator,

$$E^* |n, 0^s; v; N, 0, S, J, M_J\rangle = (-1)^{(N+s)} |n, 0^s; v; N, 0, S, J, M_J\rangle. \quad (2.16)$$

Thus, the  $\Sigma^\pm$  states have a definite parity given by (2.16).

It can also be seen from (2.15a) and (2.15b) that the factor  $p = J - S + s$  causes the phase factor  $(-1)^{(p)}$  to alternate as  $J$  increases. For example, for a given  $J$ , if the lower energy state of the almost degenerate levels has a  $(-)$  parity and the upper energy state has a  $(+)$  parity, the parities swap for the next  $J$ . Some texts [61, 63, 64, 68] hence refer to an alternative  $e/f$  parity labelling scheme. For integral values of  $J$ , levels with parity  $(-1)^J$  and  $(-1)^{J+1}$  are labelled as  $e$  and  $f$  parity states respectively. For half-integral values of  $J$ , levels with parities  $(-1)^{J-1/2}$  and  $(-1)^{J+1/2}$  are labelled as  $e$  and  $f$  parity states respectively.

**Comments on molecule-fixed inversion symmetries** A note can also be made on the *molecule-fixed* parity operator  $i$ . This transforms any molecule-fixed function as,

$$if(x_i, y_i, z_i) = \pm f(-x_i, -y_i, -z_i). \quad (2.17)$$

For the case of homonuclear diatomic molecules which possess a center of symmetry, states which are symmetric with respect to  $i$  (+ sign in the above equation) are referred to as *gerade*( $g$ ). States which are anti-symmetric with respect to  $i$  (− sign in the above equation) are referred to as *ungerade*( $u$ ). The *molecule-fixed* symmetry operator  $i$  does not define the total parity of the states.

### 2.1.3.2 Permutation symmetry of rotation levels

The space-fixed permutation operator,  $P_{12}$ , can be defined for homonuclear diatomic molecules with identical nuclei. The operator prescribes the behavior of total wavefunction including the nuclear spin (unlike the operator  $E^*$  which acts only the rovibronic wavefunction) under an interchange of the identical nuclei,

$$P_{12} \psi_{tot} = +\psi_{tot} \text{ (for bosons),} \quad (2.18a)$$

$$P_{12} \psi_{tot} = -\psi_{tot} \text{ (for fermions).} \quad (2.18b)$$

(2.18a) corresponds to a *symmetric* behavior (sometimes labelled as  $s$  symmetry) under exchange of identical nuclei with integral nuclear spins. Such particles are known as bosons. (2.18b) corresponds to an *anti-symmetric* behavior (sometimes labelled as  $a$  symmetry) under exchange of identical nuclei with half-integral nuclear spins. Such particles are known as fermions.

For identical nuclei 1 and 2 at positions  $(X_1, Y_1, Z_1)$  and  $(X_2, Y_2, Z_2)$  in the space-fixed coordinate system, the operator  $P_{12}$  transforms the positions as,

$$\begin{aligned} P_{12}(X_1, Y_1, Z_1; X_2, Y_2, Z_2) \\ = (X_2, Y_2, Z_2; X_1, Y_1, Z_1) = (-X_1, -Y_1, -Z_1; -X_2, -Y_2, -Z_2), \end{aligned} \quad (2.19)$$

where the last equality holds because the origin of the space-fixed coordinate system is at the center-of-mass of the two identical nuclei. Thus, for the nuclei,  $P_{12}$  has the same effect as  $E^*$ . The difference arises from the fact that  $P_{12}$  has no effect on the position of electrons. For an electron  $i$  at a space-fixed position given by  $(X_i, Y_i, Z_i)$ , the operator gives,

$$P_{12}(X_i, Y_i, Z_i) = (X_i, Y_i, Z_i). \quad (2.20)$$

**Permutation symmetry of Hund's case (a) rotational states** Similar to (2.9), the permutation relations for Hund's case (a) basis states can be given by,

$$P_{12} |n, \Lambda_t^s\rangle = (-1)^{(s)} (-1)^{(t+\Lambda)} |n - \Lambda_t^s\rangle, \quad (2.21a)$$

$$P_{12} |v\rangle = (+1) |v\rangle, \quad (2.21b)$$

$$P_{12} |S, \Sigma\rangle = (-1)^{(S-\Sigma)} |S, -\Sigma\rangle, \quad (2.21c)$$

$$P_{12} |J, \Omega, M_J\rangle = (-1)^{(J-\Omega)} |J, -\Omega, M_J\rangle, \quad (2.21d)$$

where the subscript  $t$  in the equation above distinguishes the  $g$  states from the  $u$  states.  $t$  is even for  $g$  states and odd for  $u$  states.

From the above equations, the total symmetry can be given as,

$$P_{12} |n, \Lambda_t^s; v; S, \Sigma; J, \Omega, M_J\rangle = (-1)^{(p+t)} |n, -\Lambda_t^s; v; S, -\Sigma; J, -\Omega, M_J\rangle, \quad (2.22)$$

where as before in (2.12)  $p = J - S + s$ .

**Permutation symmetry of Hund's case (b) rotational states** The corresponding transformation under the space-fixed permutation operator for Hund's case (b) states can be given as,

$$P_{12} |n, \Lambda_t^s; v; N, \Lambda, S, J, M_J\rangle = (-1)^{(N+s+t)} |n, -\Lambda_t^s; v; N, -\Lambda, S, J, M_J\rangle. \quad (2.23)$$

**Comments on space-fixed permutation symmetries** From (2.22) and (2.23), it can be seen that the basis functions of Hund's case (a) and Hund's case (b) states are not

eigenfunctions of the space-fixed permutation operator. Like 2.15, a definite symmetry ( $s$  or  $a$ ) state can be constructed by considering a superposition of the basis states.

For Hund's case (a) states, it can be easily seen that (2.15) states are eigenstates of the  $P_{12}$  operator,

$$\begin{aligned}
P_{12} [|n, \Lambda_t^s; J, M; \pm\rangle] &= P_{12} \left[ \frac{1}{\sqrt{2}} \{ |n, \Lambda_t^s; S, \Sigma; J, \Omega, M\rangle \pm (-1)^{(p)} |n, -\Lambda_t^s; S, -\Sigma; J, -\Omega, M\rangle \} \right] \\
&= \frac{1}{\sqrt{2}} \{ P_{12} |n, \Lambda_t^s; S, \Sigma; J, \Omega, M\rangle \pm (-1)^{(p)} P_{12} |n, -\Lambda_t^s; S, -\Sigma; J, -\Omega, M\rangle \} \\
&= \frac{1}{\sqrt{2}} \{ (-1)^{(p+t)} |n, -\Lambda_t^s; S, -\Sigma; J, -\Omega, M\rangle \\
&\qquad\qquad\qquad \pm (-1)^{(2p+t)} |n, \Lambda_t^s; S, \Sigma; J, \Omega, M\rangle \} \\
&= \pm (-1)^{(t)} \left[ \frac{1}{\sqrt{2}} \{ |n, \Lambda_t^s; S, \Sigma; J, \Omega, M\rangle \right. \\
&\qquad\qquad\qquad \left. \pm (-1)^{(p)} |n, -\Lambda_t^s; S, -\Sigma; J, -\Omega, M\rangle \} \right].
\end{aligned} \tag{2.24}$$

Thus for  $g$  states, positive parity (+) states are symmetric ( $s$ ) and negative parity (−) states are anti-symmetric ( $a$ ). For  $u$  states, positive parity (+) states are anti-symmetric ( $a$ ) and negative parity (−) states are anti-symmetric ( $s$ ).

From (2.23) it can be seen that for the special case of  $\Sigma_{g/u}^{\pm}$  states with ( $\Lambda = 0$ ), the basis state is an eigenfunction of the symmetry operator,

$$P_{12} |n, 0_t^s; v; N, 0, S, JM_J\rangle = (-1)^{(N+s+t)} |n, 0_t^s; v; N, 0, S, JM_J\rangle. \tag{2.25}$$

**Nuclear Spin statistics** Since nuclear spin is usually weakly coupled to other angular momenta, they can be treated as perturbations and be described by a separate wavefunction  $|\psi_{ns}\rangle$ . Their effect with respect to the nuclear-spin wavefunction, the operator  $P_{12}$  can be defined as,

$$P_{12} |\psi_{ns}\rangle = \pm |\psi_{ns}\rangle = (-1)^{(I_T - I_1 - I_2)} |I_1, I_2, I_T\rangle, \tag{2.26}$$

where  $\vec{I}_T = \vec{I}_1 + \vec{I}_2$ . Nuclear spin states with the higher statistical weight are called *ortho* states while those with lower statistical weights are called *para* states [61].

The requirements set by the space-fixed permutation operator (2.18) restrict the nuclear spin states that can combine with rotational states (2.24) and (2.25) [61] (i.e., not all nuclear-spins couple with all rotational states in-order to satisfy the permutation symmetry of identical nuclei for homonuclear diatomic molecules). This effect is discussed in detail for the  $X^2\Sigma_g^+$ ,  $A^2\Pi_u$  and  $B^2\Sigma_u^+$  states of  $^{14}\text{N}_2^+$  in the section below.

## 2.2 The $\text{N}_2^+$ molecular ion

Since  $\text{N}_2^+$  is a homonuclear diatomic molecule and shows the  $P_{12}$  permutation symmetry, not all nuclear-spin states couple to each rotational state as is evident from discussions above (2.1.3.2). Each atom of  $\text{N}_2^+$  has a nuclear-spin  $I_1 = I_2 = 1$ , making  $\text{N}_2^+$  a bosonic system. The total spin,  $I$ , of  $\text{N}_2^+$  can be given by  $\vec{I} = \vec{I}_1 + \vec{I}_2$ . Thus the possible values of nuclear spins are  $I = 0, 1$  and  $2$ . Of these, the  $I = 0$  and  $2$  nuclear-spin states are symmetric with respect to  $P_{12}$  ( $\text{N}_2^+$  with these nuclear-spin states are called *ortho*- $\text{N}_2^+$ ) and the  $I = 1$  nuclear-spin state is anti-symmetric ( $\text{N}_2^+$  with these nuclear-spin states are called *para*- $\text{N}_2^+$ ) [61],

$$P_{12} |\psi_{ns}(I = 0, 2)\rangle = + |\psi_{ns}(I = 0, 2)\rangle, \quad (2.27a)$$

$$P_{12} |\psi_{ns}(I = 1)\rangle = - |\psi_{ns}(I = 1)\rangle. \quad (2.27b)$$

The coupling of nuclear spin to the fine-structure states is also discussed below.

### 2.2.1 The $X^2\Sigma_g^+$ electronic state

Fig. 2.3a. shows the Hund's case (b) ro-vibrational structure of the  $X^2\Sigma_g^+$  electronic ground state of  $\text{N}_2^+$ . Since the electronic-spin is  $1/2$ , the fine-structure (spin-orbit) states,  $J$ , can have values between  $N - 1/2$  ( $F_2$  states) and  $N + 1/2$  ( $F_1$  states), where  $N$  refers to the rotational quantum number. The parity under space-fixed inversion operator are labelled by the symbols  $+$  and  $-$  (evaluated according to (2.16)). The alternate parity labels  $e$  and  $f$  are also shown.

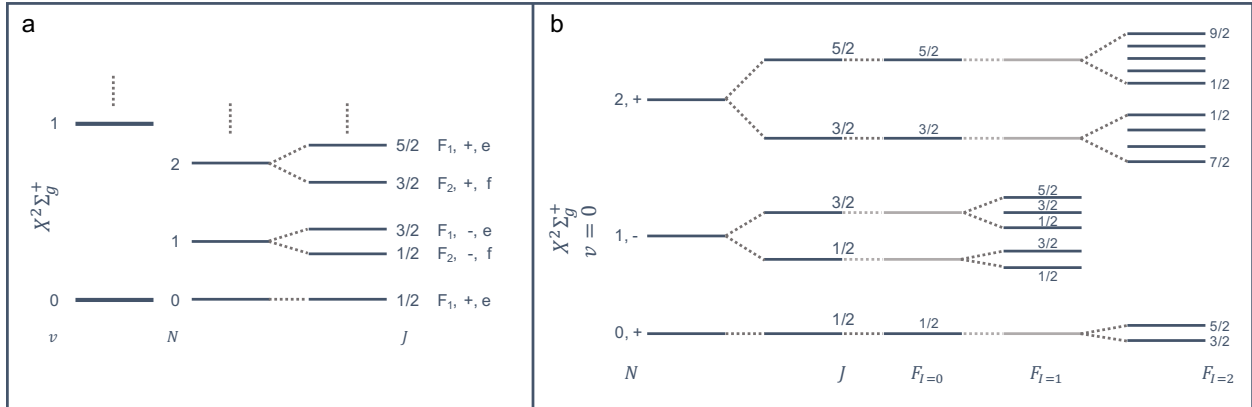


**Figure 2.3 Energy level structure of the  $X^2\Sigma_g^+$  state of  $N_2^+$  molecular ion.** (a)  $X^2\Sigma_g^+$  state of  $N_2^+$  molecular ion.  $v$  is the vibrational,  $N$  the rotational and  $J$  the fine-structure (spin-orbit) quantum number. Parities of each states under the  $E^*$  operator are labelled by the labels  $\pm$  or by the labels  $e/f$ . (b) Hyperfine structure,  $F$ , of the  $X^2\Sigma_g^+$  state of  $N_2^+$  molecular ion in the ground vibrational state ( $v = 0$ ). Not all rotational states couple to all possible nuclear spins ( $I = 0, 1$  and  $2$ ). Levels grayed out do not exist due to nuclear-spin statistics. Not shown are the Zeeman splitting of the hyperfine states under a magnetic field.

The hyperfine coupling is limited by nuclear-spin statistics. States with positive parity  $+$  ( $N = \text{even}$ ) couple only with  $I = 0$  and  $2$  total nuclear spins, such that the total wave-function is symmetric. States with negative parity  $-$  ( $N = \text{odd}$ ) couple only with  $I = 1$  total nuclear spin, such that the total wave-function is symmetric again. This is shown in fig. 2.3b.

## 2.2.2 The $A^2\Pi_u$ electronic state

Fig. 2.4a. shows the parity-defined Hund's case (a) ro-vibrational structure of the  $A^2\Pi_u$  first electronic excited state of  $N_2^+$ . These are not simple Hund's case (a) basis states, but linear combinations of them which have well defined parities (2.15). Since transitions will occur between states of well defined parities, it is advantageous to look at linear combinations of pure Hund's case (a) basis states.

Since  $\Lambda = \pm 1$  and  $\Sigma = \pm 1/2$ ,  $\Omega = \pm 1/2$  and  $\pm 3/2$  ( $F_2$  and  $F_1$  states respectively). The fine-structure (spin-orbit) states,  $J$ , with the respective parities are shown. The parity,

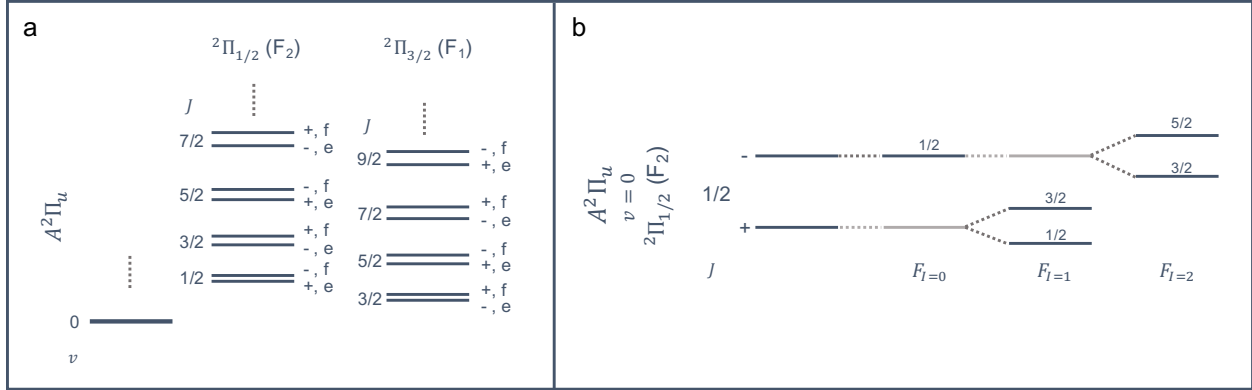


**Figure 2.4 Energy level structure of the  $A^2\Pi_u$  state of  $N_2^+$  molecular ion.**

(a)  $A^2\Pi_u$  state of  $N_2^+$  molecular ion.  $v$  is the vibrational quantum number. For  $\Pi$  states, the projection of the electronic-orbital quantum number on the molecular-axis  $|\Lambda|=1$ . Due to spin-orbit interaction, for the electronic spin  $S = 1/2$ , the states are split in  $|\Omega|=1/2$  and  $3/2$  manifolds.  $J$  the fine-structure (spin-orbit) quantum number. Parities of each states under the  $E^*$  operator are labelled by the labels  $\pm$  or by the labels  $e/f$ . (b) Hyperfine coupling of the  $A^2\Pi_u$ ,  $v = 0$ ,  $|\Omega|=1/2$  rotational state of  $N_2^+$  molecular ion. Not all rotational states couple to all possible nuclear spins ( $I = 0, 1$  and  $2$ ). Levels grayed out do not exist due to nuclear-spin statistics. Not shown are the Zeeman splitting of the hyperfine states under a magnetic field.

as before, under space-fixed inversion operator are labelled by the symbols  $+$  and  $-$ . The alternate parity labels  $e$  and  $f$  are also shown.

The hyperfine coupling is limited by nuclear-spin statistics. Since the  $A^2\Pi_u$  state has an *ungerade* symmetry, states with positive parity  $+$  have anti-symmetric rotational wavefunctions (as  $t$  is odd in (2.24)) and couple only with  $I = 1$  total nuclear spin such that the total wave-function is symmetric. States with negative parity  $-$  have symmetric rotational wavefunctions and couple only with  $I = 0$  and  $2$  total nuclear spins, such that the total wave-function is symmetric again. An example of this is shown in Fig. 2.4b.

### 2.2.3 The $B^2\Sigma_u^+$ electronic state

The rotational structure of the second electronic excited Hund's case (b)  $B^2\Sigma_u^+$  state of  $N_2^+$  is the same as that of the  $X^2\Sigma_g^+$  (see Fig. 2.3a.).

Since the  $B^2\Sigma_u^+$  has an *ungerade* symmetry under the molecule-fixed operator  $i$ , the

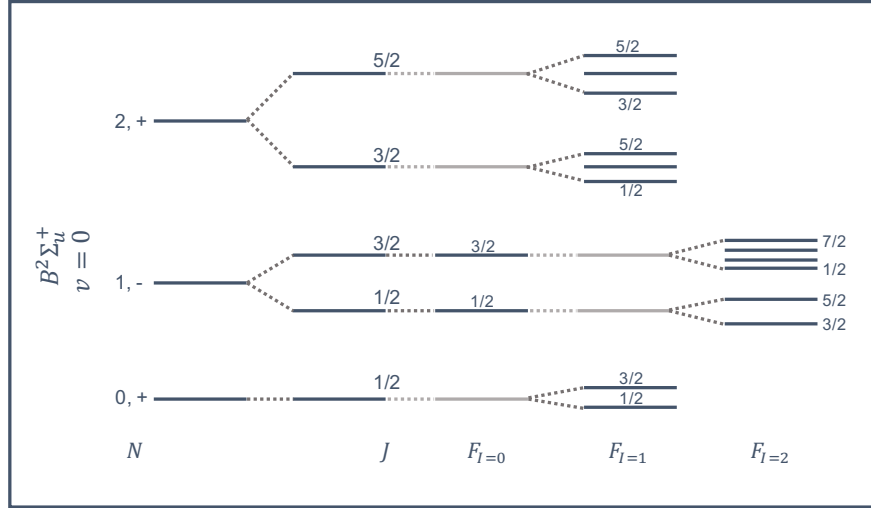


**Figure 2.5** Hyperfine structure,  $F$ , of the  $B^2\Sigma_u^+$  state of  $N_2^+$  molecular ion in the ground vibrational state ( $v = 0$ ). Not all rotational states couple to all possible nuclear spins ( $I = 0, 1$  and  $2$ ). Levels grayed out do not exist due to nuclear-spin statistics. Not shown are the Zeeman splitting of the hyperfine states under a magnetic field.

positive parity  $+$  ( $N = \text{even}$ ) states have anti-symmetric rotational wavefunctions and couple only with  $I = 1$  total nuclear spin, such that the total wave-function is symmetric. States with negative parity  $-$  ( $N = \text{odd}$ ) have symmetric rotational wavefunctions and couple only with  $I = 0$  and  $2$  total nuclear spins, such that the total wave-function is symmetric again. This is shown in Fig. 2.5.

## 2.3 Energy levels of the $N_2^+$ ion

A proper examination of the energy levels of the Hund's case (a)  $A^2\Pi_u$  state and the Hund's case (b)  $X^2\Sigma_g^+$  state of  $N_2^+$  is essential in order to understand interactions induced by light between these states. The energy levels of the states can be obtained by explicitly writing out the effective Hamiltonian,  $\hat{H}_{\text{eff}}$ , and diagonalizing it in order to obtain the eigenenergies and eigenvectors of the Hamiltonian. In order to evaluate the origin and the consequences of off-diagonal terms appearing in the complete  $\hat{H}_{\text{eff}}$  matrix, each contribution to the Hamiltonian is presented separately and investigated. Off-diagonal terms in the Hamiltonian result in a

mixing of the state being examined with other states.

The effective Hamiltonian,  $\hat{H}_{\text{eff}}$ , for molecules in general can be given as [69, 70],

$$\hat{H}_{\text{eff}} = \hat{H}_{T_v} + \hat{H}_{\text{so}} + \hat{H}_{\text{rot}} + \hat{H}_{\text{cd}} + \hat{H}_{\text{sr}} + \hat{H}_{\Lambda\text{D}} + \hat{H}_{\text{cd-}\Lambda\text{D}} + \hat{H}_{\text{hfs}} + \hat{H}_{\text{cd-hfs}}, \quad (2.28)$$

where  $\hat{H}_{T_v}$  represents the vibronic term-value (or the band origin),  $\hat{H}_{\text{so}}$  - the spin-orbit coupling,  $\hat{H}_{\text{rot}}$  - the rotational kinetic energy,  $\hat{H}_{\text{cd}}$  - the centrifugal-distortion corrections to rotation,  $\hat{H}_{\text{sr}}$  - the electron spin-rotation interaction,  $\hat{H}_{\Lambda\text{D}}$  - the  $\Lambda$  doubling,  $\hat{H}_{\text{cd-}\Lambda\text{D}}$  - the centrifugal distortion corrections to  $\Lambda$  doubling,  $\hat{H}_{\text{hfs}}$  - the hyperfine (magnetic and electric) interactions and  $\hat{H}_{\text{cd-hfs}}$  - the centrifugal distortion corrections to the hyperfine interaction. The explicit operators for each Hamiltonian terms can be found in literature [71]. Depending on the level of theory being considered, higher order terms (e.g. terms corresponding to the Zeeman interactions with external magnetic fields) may be included in order to explain a certain rotational spectrum. However, such terms are beyond the scope of this thesis. [53] investigates the effect of such terms for the ground  $X^2\Sigma_g^+$  state of  $\text{N}_2^+$ . Here, we focus on the  $v = 0$  and  $v = 2$  vibrational states of the  $X^2\Sigma_g^+$  and  $A^2\Pi_u$  electronic states of  $\text{N}_2^+$  respectively. Although the Hamiltonians presented here is independent of the vibrational states chosen, the molecular constants used for the evaluation of the Hamiltonians depend on the vibrational state. For different vibrational states, the corresponding constants should be substituted.

### 2.3.1 The $X^2\Sigma_g^+(v = 0)$ state

The rotational states of the ground  $X^2\Sigma_g^+(v = 0)$  vibronic state in  $\text{N}_2^+$  belong either to the  $J = N + 1/2$  ( $F_1$ ) or to the  $J = N - 1/2$  ( $F_2$ ) spin-rotation component. The Hamiltonian can be expressed in the Hund's case ( $b_{\beta_J}$ ) basis as a matrix with the elements,

$$\hat{H}_{\text{eff}} = \begin{bmatrix} \hat{H}_{11} & \hat{H}_{12} \\ \hat{H}_{21} & \hat{H}_{22} \end{bmatrix} = \begin{bmatrix} \langle F_1' | \hat{H}_{\text{eff}} | F_1 \rangle & \langle F_1' | \hat{H}_{\text{eff}} | F_2 \rangle \\ \langle F_2' | \hat{H}_{\text{eff}} | F_1 \rangle & \langle F_2' | \hat{H}_{\text{eff}} | F_2 \rangle \end{bmatrix} \quad (2.29)$$

where

$$|F_1'\rangle = |N', \Lambda' = 0, S' = 1/2, J' = N' + S', I', F', M_F'\rangle \quad (2.30)$$

and

$$|F_2'\rangle = |N', \Lambda' = 0, S' = 1/2, J' = N' - S', I', F', M_F'\rangle \quad (2.31)$$

represent the parity conserved basis states for the  $X^2\Sigma_g^+$  state. As will be seen below, the effective Hamiltonian mixes rotational states between the  $F_1$  and  $F_2$  manifolds. Thus, this choice of the  $2 \times 2$  truncated Hamiltonian makes it mathematically effortless to calculate the state energies and mixing coefficients<sup>1</sup>

**The spin-orbit Hamiltonian** The spin-orbit Hamiltonian for the Hund's case (b) is often small [61]. For the case of  $X^2\Sigma_g^+$  states in  $N_2^+$  with  $\Lambda = 0$ , the spin-orbit coupling is zero. The contribution to the Hamiltonian for the  $X^2\Sigma_g^+$  states is thus set to zero.

**The rotational Hamiltonian** In the Hund's case ( $b_{\beta_J}$ )-basis, the matrix elements of the rotational Hamiltonian are diagonal and can be given in terms of the rotational constant,  $B_v$ , as [72],

$$\hat{H}_{\text{rot}} = \delta_{N'N} \delta_{S'S} \delta_{J'J} \delta_{I'I} \delta_{F'F} \delta_{M_F'M_F} \begin{bmatrix} B_v N(N+1) & 0 \\ 0 & B_v N(N+1) \end{bmatrix}. \quad (2.32)$$

**The centrifugal-distortion Hamiltonian** The rotational motion of the nuclei of the molecule causes centrifugal distortion. In the Hund's case ( $b_{\beta_J}$ )-basis, the centrifugal distortion Hamiltonian is also diagonal and can be expressed in terms of the centrifugal distortion

---

<sup>1</sup>In order to consider mixing of terms between different vibrational and electronic states of the molecule, the  $2 \times 2$  matrix in 2.29 must be expanded. However, such terms are often small and they are neglected in this thesis.

constant,  $D_v$ , as [72],

$$\hat{H}_{\text{cd}} = \delta_{N'N} \delta_{S'S} \delta_{J'J} \delta_{I'I} \delta_{F'F} \delta_{M'_F M_F} \begin{bmatrix} -D_v [N(N+1)]^2 & 0 \\ 0 & -D_v [N(N+1)]^2 \end{bmatrix}. \quad (2.33)$$

**The spin-rotation Hamiltonian** The spin-rotation Hamiltonian can be expressed in terms of the spin-rotation constant,  $\gamma_v$ , as [73],

$$\hat{H}_{\text{sr}} = \delta_{N'N} \delta_{S'S} \delta_{J'J} \delta_{I'I} \delta_{F'F} \delta_{M'_F M_F} \begin{bmatrix} +1/2\gamma_v N & 0 \\ 0 & -1/2\gamma_v (N+1) \end{bmatrix}. \quad (2.34)$$

As with the previous Hamiltonians, the spin-rotation Hamiltonian is also diagonal in the  $F_1$  and  $F_2$  basis.

**The hyperfine Hamiltonian** The hyperfine-structure Hamiltonian exhibits several contributions and can be written as [74, 75],

$$\hat{H}_{\text{hfs}} = \hat{H}_{b_F} + \hat{H}_t + \hat{H}_{eqQ} + \hat{H}_{c_I}, \quad (2.35)$$

where  $\hat{H}_{b_F}$  describes the Fermi-contact interaction,  $\hat{H}_t$  is the dipolar hyperfine interaction,  $\hat{H}_{eqQ}$  is the quadrupolar hyperfine interaction and  $\hat{H}_{c_I}$  is the magnetic nuclear spin-rotation interaction. The dominant Fermi contact Hamiltonian is considered here. The remaining hyperfine contributions can be found in [56, 74, 75].

The Fermi-contact Hamiltonian can be expressed as,

$$\hat{H}_{b_F} = \begin{bmatrix} \langle F_1' | \hat{H}_{b_F} | F_1 \rangle & \langle F_1' | \hat{H}_{b_F} | F_2 \rangle \\ \langle F_2' | \hat{H}_{b_F} | F_1 \rangle & \langle F_2' | \hat{H}_{b_F} | F_2 \rangle \end{bmatrix}, \quad (2.36)$$

where, the individual matrix elements between two states can be written as [74],

$$\begin{aligned} \langle N', S', J', I', F', M'_F | \hat{H}_{b_F} | N, S, J, I, F, M_F \rangle &= b_{F,v} \delta_{N'N} \delta_{S'S} \delta_{I'I} \delta_{F'F} \delta_{M'_F M_F} \\ &(-1)^{F+I+J'+J+N+S+1} \sqrt{I(I+1)(2I+1)} \sqrt{(S(S+1))(2S+1)} \\ &\sqrt{(2J'+1)(2J+1)} \begin{Bmatrix} I & J' & F \\ J & I & 1 \end{Bmatrix} \begin{Bmatrix} S & J' & N \\ J & S & 1 \end{Bmatrix}. \end{aligned} \quad (2.37)$$

Constant	Value	Reference
$B_0$	1.9223897(53) cm <sup>-1</sup>	[76]
$D_0 \times 10^6$	5.9748(50) cm <sup>-1</sup>	[76]
$\gamma_0 \times 10^3$	9.1965(90) cm <sup>-1</sup>	[76]
$b_{F,0}$	102.4(1.1) MHz	[77]

**Table 2.2 Molecular constants for the  $X^2\Sigma_g^+(v=0)$  band in  $N_2^+$ .** Values in parenthesis represent  $1\sigma$ -uncertainties and apply to the last digits.

It can be noted that the Fermi-contact hyperfine Hamiltonian has off-diagonal terms which mix rotational states between the  $F_2$  and  $F_1$  manifolds. The Kronecker-delta terms in (2.37) dictate that states with different  $N$ ,  $S$ ,  $I$ ,  $F$  or  $M_F$  do not mix. In other words, rotational states belonging to the  $F_1$  manifold with  $J = N + S$  mix with rotational states in the  $F_2$  manifold with  $J = N - S$  while preserving the remaining quantum numbers. It can also be noted that for the case of  $I = 0$  molecules, the Fermi-contact Hamiltonian is zero and there is no mixing of states or change in energy levels of the rotational state.

Tab. 2.3 shows the mixing coefficients and the state energies for the  $N = 0$  and  $N = 2$  manifold for the  $X^2\Sigma_g^+(v=0)$  vibronic band in  $N_2^+$  calculated by diagonalizing the total effective Hamiltonian. The molecular constants used for the  $X^2\Sigma_g^+(v=0)$  band for  $N_2^+$  are listed in tab. 2.2. The contribution due to the vibronic Hamiltonian,  $\hat{H}_{T_v}$ , for this ground state vibronic band is zero<sup>2</sup>. It can be noted from tab. 2.3 that  $F_1$ ,  $N = 0$  states are pure states with no mixing. This is expected since there are no corresponding  $F_2$ ,  $N = 0$  states. Similar is the case for the  $N = 2$ ,  $F_1$ ,  $F = 9/2$  state. Since there is no corresponding  $F = 9/2$  state in the  $N = 2$ ,  $F_2$  manifold, the state is pure with no mixing.

---

<sup>2</sup>In the case when mixing between different vibrational and electronic states is considered, the vibronic Hamiltonian is non-zero. However, as stated before, higher order terms in the Hamiltonian which result in such mixing have been ignored in this thesis.

State		Mixing Coefficient		State Energy
		$F_1 = J + 1/2$	$F_2 = J - 1/2$	
$N = 0$	$F_1, J = 1/2, F = 3/2$	1	0	-153.6 MHz
	$F_1, J = 1/2, F = 5/2$	1	0	102.4 MHz
$N = 2$	$F_1, J = 5/2, F = 1/2$	0.99409	0.10859	345.92 GHz
	$F_1, J = 5/2, F = 3/2$	0.98478	0.17381	345.96 GHz
	$F_1, J = 5/2, F = 5/2$	0.98212	0.18823	346.02 GHz
	$F_1, J = 5/2, F = 7/2$	0.98783	0.15556	346.09 GHz
	$F_1, J = 5/2, F = 9/2$	1	0	346.16 GHz
	$F_2, J = 3/2, F = 1/2$	0.10859	-0.99409	345.45 GHz
	$F_2, J = 3/2, F = 3/2$	0.17381	-0.98478	345.41 GHz
	$F_2, J = 3/2, F = 5/2$	0.18823	-0.98212	345.35 GHz
$F_2, J = 3/2, F = 7/2$	0.15556	-0.98783	345.29 GHz	

**Table 2.3** Mixing coefficients and state energies for  $X^2\Sigma_g^+(v = 0)$  rotational states. The state energies are referenced to the  $X^2\Sigma_g^+, v = 0, N = 0, J = 1/2$  state in the  $I = 0$   $N_2^+$  molecule.

### 2.3.2 The $A^2\Pi_u(v = 2)$ state

Since a given rotational level of the  $^2\Pi$  state can belong to either  $|\Omega| = 3/2$  ( $F_1$ ) manifold or the  $|\Omega| = 1/2$  ( $F_2$ ) manifold, a simple understanding of the Hamiltonian can be achieved by expressing the basis states as  $|^2\Pi_\Omega^\pm, J, I, F, M_F\rangle$  [69, 78–80]. The superscripts,  $\pm$ , here refer to the total parity of the  $^2\Pi_\Omega$  state being considered. Since none of the Hamiltonians presented here mix the positive and the negative parity states, i.e., there are no off-diagonal matrix elements between the positive and the negative parity states, it becomes mathematically simpler to compute the Hamiltonian between the positive and the negative parity states

separately, i.e.,

$$\begin{aligned} \hat{H}_{\text{eff}}^{\pm} &= \begin{bmatrix} \hat{H}_{11}^{\pm} & \hat{H}_{12}^{\pm} \\ \hat{H}_{21}^{\pm} & \hat{H}_{22}^{\pm} \end{bmatrix} \\ &= \begin{bmatrix} \left\langle {}^2\Pi_{1/2}^{\pm}, J', I', F' \left| \hat{H}_{\text{eff}}^{\pm} \right| {}^2\Pi_{1/2}^{\pm}, J, I, F \right\rangle & \left\langle {}^2\Pi_{3/2}^{\pm}, J', I', F' \left| \hat{H}_{\text{eff}}^{\pm} \right| {}^2\Pi_{1/2}^{\pm}, J, I, F \right\rangle \\ \left\langle {}^2\Pi_{1/2}^{\pm}, J', I', F' \left| \hat{H}_{\text{eff}}^{\pm} \right| {}^2\Pi_{3/2}^{\pm}, J, I, F \right\rangle & \left\langle {}^2\Pi_{3/2}^{\pm}, J', I', F' \left| \hat{H}_{\text{eff}}^{\pm} \right| {}^2\Pi_{3/2}^{\pm}, J, I, F \right\rangle \end{bmatrix}. \end{aligned} \quad (2.38)$$

The above  $2 \times 2$  matrix is valid as long as the Hamiltonian  $\hat{H}_{\text{eff}}$  does not mix states of different  $J$  (or  $I$  or  $F$ ) while conserving parity, i.e.,  $J' = J$  (or  $I' = I$  or  $F' = F$  or  $M'_F = M_F$ ). In case a Hamiltonian mixes  $J$  (as is the case with the hyperfine Hamiltonian), the above  $2 \times 2$  matrix element matrix must be expanded to include non-zero expectation values of  $\hat{H}_{\text{eff}}$  between a  $J$  state and all possible  $J'$  states.

Sometimes the Hamiltonian is expressed in the  $e/f$  basis, i.e. in  $\left| {}^2\Pi_{\Omega}^{e/f}, J, I, F, M_F \right\rangle$  basis as is done in [76,81]. However as long as the parity definitions are kept consistent the Hamiltonians will be identical irrespective of the convention employed.<sup>3</sup>

**The spin-orbit Hamiltonian** The spin-orbit Hamiltonian in the  $\left| {}^2\Pi_{\Omega}^{\pm}, J, I, F, M_F \right\rangle$  basis is [78]

$$\hat{H}_{\text{so}}^{\pm} = \delta_{J'J} \delta_{I'I} \delta_{F'F} \delta_{M'_F M_F} \begin{bmatrix} -A_v/2 & 0 \\ 0 & A_v/2 \end{bmatrix}, \quad (2.39)$$

where  $A_v$  is the spin-orbit coupling constant for the vibrational band  $v$ . Since  $A_v$  has a negative value for  $\text{N}_2^+$  (see table ), the  ${}^2\Pi_{1/2}^{\pm}$  manifold is higher in energy than the  ${}^2\Pi_{3/2}^{\pm}$

---

<sup>3</sup>Some references [76,81,82] employ a different parity conventions compared to this thesis. Thus at first it may appear that the results discussed here does not match those in the references. However, using consistent parity definitions give the same results. Some references like [70, 83] seem to be inconsistent in definition of its parity between the  $X^2\Sigma_g^+$  states and the  $A^2\Pi_u$  states. Thus, extra precaution must be taken when writing out the Hamiltonians.

states. This ordering is referred to as *inverted*  $^2\Pi$  system. For molecules with positive  $A_v$ , the  $^2\Pi_{3/2}^\pm$  manifold is higher in energy. Such a system is known as *regular*.

The correction to the spin-orbit Hamiltonian due to centrifugal motion of the molecule can be given by the centrifugal-distortion parameter  $A_{D_v}$  as [81],

$$\hat{H}_{\text{cd-so}}^\pm = \delta_{J'J} \delta_{I'I} \delta_{F'F} \delta_{M'_F M_F} \begin{bmatrix} -A_{D_v} z / 2 & 0 \\ 0 & A_{D_v} (z - 2) / 2 \end{bmatrix}, \quad (2.40)$$

where  $z = (J' + 1/2)^2$ .

This spin-orbit Hamiltonian has no off-diagonal elements. Thus, there is no mixing between states. For the spin-rotation Hamiltonians, the positive and negative parity states have identical energies, i.e., the states remain degenerate in energies.

**The rotational Hamiltonian** The rotational Hamiltonian in our basis can be given as [78],

$$\hat{H}_{\text{rot}}^\pm = \delta_{J'J} \delta_{I'I} \delta_{F'F} \delta_{M'_F M_F} \begin{bmatrix} B_v z & B_v \sqrt{z - 1} \\ B_v \sqrt{z - 1} & B_v (z - 2) \end{bmatrix}, \quad (2.41)$$

where  $B_v$  is the rotational constant for the vibrational level ( $v$ ) under consideration and  $z = (J' + 1/2)^2$  as before. The rotational Hamiltonian thus mixes states with the same quantum number  $J$  differing in  $\Omega$ . There is no mixing between  $+$  and  $-$  parity states, i.e,  $\Omega = +1/2$  states mix only with the  $\Omega = +3/2$  states and  $\Omega = -1/2$  states mix only with  $\Omega = -3/2$  states. It can be seen from the off-diagonal terms that such a mixing is dependent on the quantum number  $J$  and is sometimes labelled as *inhomogeneous* mixing in the literature [61, 63]. The mixing between different  $\Omega$  states gets more pronounced as  $J$  increases. The off-diagonal terms of the rotational Hamiltonian causes the uncoupling of the electronic spin  $S$  from the molecule-fixed internuclear axis. As  $J$  increases, the  $S$ -uncoupling increases and it becomes more favorable for the electronic spin to couple to the molecular rotation. Thus for high  $J$ , a Hund's case (b) picture becomes more suitable for describing the molecular states.

**The centrifugal-distortion Hamiltonian** The rotational motion of the nuclei of the molecule causes centrifugal distortion. In terms of the centrifugal distortion constant  $D_v$ , the centrifugal distortion Hamiltonian can be given as [81],

$$\hat{H}_{\text{cd}}^{\pm} = \delta_{J'J} \delta_{I'I} \delta_{F'F} \delta_{M'_F M_F} \begin{bmatrix} -D_v[z^2 + z - 1] & -2D_v[z - 1]\sqrt{z - 1} \\ -2D_v[z - 1]\sqrt{z - 1} & -D_v[z^2 - 3z + 3] \end{bmatrix}. \quad (2.42)$$

Thus like the rotational Hamiltonian, the centrifugal distortion also mixes states with the same  $J$  but differing in  $\Omega$  while conserving parity. Since  $D_v$  is typically several orders of magnitude smaller when compared to  $B_v$ , inclusion of  $\hat{H}_{\text{cd}}$  does not affect the energy levels of the molecule substantially.

**The spin-rotation Hamiltonian** Since molecular constants in the A state is highly correlated, the spin-rotation constant  $\gamma_v$  is set to zero [76,78,81]. The remaining constants then effectively include the spin-rotation energy for the  $A^2\Pi_u$  state.

**The  $\Lambda$ -doubling Hamiltonian** The  $\Lambda$ -doubling Hamiltonian,  $\hat{H}_{\Lambda\text{D}}$ , can be given as [78],

$$\hat{H}_{\Lambda\text{D}}^+ = \delta_{J'J} \delta_{I'I} \delta_{F'F} \delta_{M'_F M_F} \begin{bmatrix} -(-1)^{(J'-1/2)}(J' + 1/2)(\frac{1}{2}p_v + q_v) & -(-1)^{(J'-1/2)}(J' + 1/2)\frac{\sqrt{z-1}}{2}q_v \\ -(-1)^{(J'-1/2)}(J' + 1/2)\frac{\sqrt{z-1}}{2}q_v & 0 \end{bmatrix}, \quad (2.43)$$

$$\hat{H}_{\Lambda\text{D}}^- = \delta_{J'J} \delta_{I'I} \delta_{F'F} \delta_{M'_F M_F} \begin{bmatrix} (-1)^{(J'-1/2)}(J' + 1/2)(\frac{1}{2}p_v + q_v) & (-1)^{(J'-1/2)}(J' + 1/2)\frac{\sqrt{z-1}}{2}q_v \\ (-1)^{(J'-1/2)}(J' + 1/2)\frac{\sqrt{z-1}}{2}q_v & 0 \end{bmatrix}, \quad (2.44)$$

where  $p_v$  and  $q_v$  are the  $\Lambda$ -doubling constants.

Unlike previous terms, the  $\Lambda$ -doubling Hamiltonian depends on the parity of the state and is different for + and - parity states. Thus the parity states which were degenerate, are split by the  $\Lambda$ -doubling Hamiltonian.

It can also be seen that the  ${}^2\Pi_{1/2}$  states have a larger splitting due to non-zero  $H_{11}$  terms of the Hamiltonian which depends on both  $p_v$  and  $q_v$ . The  ${}^2\Pi_{3/2}$  states split only due to mixing of different  $\Omega$  states for the same  $J$  and parity (as the  $H_{22}$  terms of the Hamiltonian are zero). The splitting is thus much smaller than the splittings of the  ${}^2\Pi_{1/2}$  states and are dependent only on the parameter  $q_v$ .

The  $\Lambda$ -doubling, in reality, occurs due to matrix elements between  $\Omega$  components of the  ${}^2\Pi$  and all  ${}^2\Sigma$  states [70, 84]. Non-zero matrix elements mix different  $\Lambda$  states giving rise to the so-called  $L$ -uncoupling (in addition to the  $S$ -uncoupling) where the  $L$  starts decoupling from the inter-molecular axis. This effect is treated as a perturbation and is effectively included in the parameters  $p_v$  and  $q_v$  [84].

**The centrifugal corrections to  $\Lambda$ -doubling Hamiltonian** The second-order centrifugal-distortion corrections to  $\Lambda$ -doubling can be given as [78],

$$\hat{H}_{\text{cd-}\Lambda\text{D}}^+ = \delta_{J'J} \delta_{I'I} \delta_{F'F} \delta_{M'_F M_F} \begin{bmatrix} -(-1)^{(J'-1/2)}(J'+1/2)^3 D_{p_v} & -(-1)^{(J'-1/2)}(J'+1/2)^3 \sqrt{z-1} D_{q_v} \\ -(-1)^{(J'-1/2)}(J'+1/2)^3 \sqrt{z-1} D_{q_v} & -(-1)^{(J'-1/2)}[z-1] D_{q_v} \end{bmatrix}, \quad (2.45)$$

$$\hat{H}_{\text{cd-}\Lambda\text{D}}^- = \delta_{J'J} \delta_{I'I} \delta_{F'F} \delta_{M'_F M_F} \begin{bmatrix} (-1)^{(J'-1/2)}(J'+1/2)^3 D_{p_v} & (-1)^{(J'-1/2)}(J'+1/2)^3 \sqrt{z-1} D_{q_v} \\ (-1)^{(J'-1/2)}(J'+1/2)^3 \sqrt{z-1} D_{q_v} & (-1)^{(J'-1/2)}[z-1] D_{q_v} \end{bmatrix}, \quad (2.46)$$

where  $D_{p_v}$  and  $D_{q_v}$  are second-order distortion-correction constant. These constants are often orders of magnitude smaller when compared to  $p_v$  and  $q_v$ .

**The hyperfine Hamiltonian** The magnetic hyperfine Hamiltonian is the dominant hyperfine term for the  $A^2\Pi_u$  state in  $\text{N}_2^+$  [78, 85]. The Hamiltonian can be given as [78],

$$\hat{H}_{\text{hfs}}^{\pm} = \delta_{I'I} \delta_{F'F} \delta_{M'_F M_F} G(J', J, I', F') \begin{bmatrix} \hat{H}_{\text{hfs11}}^{\pm} & \hat{H}_{\text{hfs12}}^{\pm} \\ \hat{H}_{\text{hfs21}}^{\pm} & \hat{H}_{\text{hfs22}}^{\pm} \end{bmatrix}, \quad (2.47)$$

where,

$$\begin{aligned} \hat{H}_{\text{hfs11}}^{\pm} &= (-1)^{(J-1/2)} \begin{pmatrix} J' & 1 & J \\ -1/2 & 0 & 1/2 \end{pmatrix} [a_v - (b_v + c_v)/2] \\ &\mp \frac{-1}{\sqrt{2}} \begin{pmatrix} J' & 1 & J \\ -1/2 & 1 & -1/2 \end{pmatrix} d_v, \end{aligned} \quad (2.48)$$

$$\hat{H}_{\text{hfs12}}^{\pm} = (-1)^{(J+1/2)} \begin{pmatrix} J' & 1 & J \\ -3/2 & 1 & 1/2 \end{pmatrix} \frac{b_v}{\sqrt{2}}, \quad (2.49)$$

$$\hat{H}_{\text{hfs21}}^{\pm} = \mathcal{H}_{\text{hfs12}}^{\pm}, \quad (2.50)$$

$$\hat{H}_{\text{hfs22}}^{\pm} = (-1)^{(J-1/2)} \begin{pmatrix} J' & 1 & J \\ -3/2 & 0 & 3/2 \end{pmatrix} [a_v + (b_v + c_v)/2], \quad (2.51)$$

and

$$\begin{aligned} G(J', J, I', F') &= [(2J' + 1)(2J + 1)I'(I' + 1)(2I' + 1)]^{0.5} \\ &(-1)^{(J'+I'+F')} \begin{Bmatrix} F' & J' & I' \\ 1 & I' & J \end{Bmatrix}, \end{aligned} \quad (2.52)$$

where  $a_v$ ,  $b_v$ ,  $c_v$  and  $d_v$  are the Frosch-Foley magnetic-hyperfine parameters.

Thus, the magnetic-hyperfine Hamiltonian mixes states of different  $\Omega$  and  $J$  while conserving the quantum numbers  $I$ ,  $F$  and the parity of the state. The mixing of the quantum number  $J$  is limited by the selection rules of the Wigner-3j symbols to  $\Delta J = J' - J = 0, \pm 1$ . The simple  $2 \times 2$  Hamiltonian must thus be expanded to a  $6 \times 6$  form (except for the lower states of the  $J = 3/2$  and  $1/2$  states for which a  $5 \times 5$  and  $3 \times 3$  matrices are sufficient respectively) in order to include mixing of different  $J$ .

Constant	Value	Reference	Constant	Value	Reference
$T_{20}$	12732.84033(13) $\text{cm}^{-1}$	[76]	$q_2 \times 10^4$	-3.3696(50) $\text{cm}^{-1}$	[76]
$B_2$	1.6973871(53) $\text{cm}^{-1}$	[76]	$a_2$	66(5) MHz	[85]
$D_2 \times 10^6$	5.9609(50) $\text{cm}^{-1}$	[76]	$b_2$	9 MHz	[85]
$A_2$	-74.63428(23) $\text{cm}^{-1}$	[76]	$c_2$	-35 MHz	[85]
$A_{D_2} \times 10^5$	-7.142(73) $\text{cm}^{-1}$	[76]	$d_2$	77 MHz	[85]
$p_2 \times 10^3$	5.118(14) $\text{cm}^{-1}$	[76]			

**Table 2.4 Molecular constants for the  $A^2\Pi_u(v=2)$  band in  $\text{N}_2^+$ .** Values in parentheses represent  $1\sigma$ -uncertainties.

State	Mixing Coefficient						State Energy
	$F_1, J-1$	$F_1, J$	$F_1, J+1$	$F_2, J-1$	$F_2, J$	$F_2, J+1$	
$F_1, J=3/2, F=1/2$	-	-0.999	8.3(-5)	0	-0.037	3.3(-6)	380.7008 THz
$F_1, J=3/2, F=3/2$	-	0.999	-1.5(-4)	-2.8(-6)	0.037	-6.2(-6)	380.7007 THz
$F_1, J=3/2, F=5/2$	-	0.999	-2.0(-4)	-3.5(-6)	0.037	-8.1(-6)	380.7007 THz
$F_1, J=3/2, F=7/2$	-	-0.999	2.0(-4)	0	-0.037	8.1(-6)	380.7006 THz

**Table 2.5 Mixing coefficients and state energies for the  $A^2\Pi_u(v=2)$  rotational states.** It can be noted that the state  $J=1/2$  does not exist for the  $F_1$  manifold. Values in parenthesis are powers of ten. The dominant mixing is between states with the same  $J$  quantum numbers. The state energies are defined with respect to the ground  $X^2\Sigma_g^+, v=0, J=1/2$  state of the  $I=0 \text{N}_2^+$  molecule.

It can also be noted from the hyperfine factor  $G(J', J, I', F')$  that the Wigner-6j symbol vanishes for the  $I'=0$  nuclear-spin isomer. Thus, there is no  $J$  mixing for the  $I=0$  nuclear-spin isomer [62]. This is expected since for the  $I=0$  nuclear-spin,  $F=J$  and the hyperfine terms do not mix  $F$ .

Tab. 2.5 shows the mixing coefficients and the state energies for the  $\left|{}^2\Pi_{3/2}^\pm, J=3/2, I=2, F, M_F\right\rangle$  manifold for the  $A^2\Pi_u(v=2)$  vibronic band in  $\text{N}_2^+$  calculated by diagonalizing the total effective Hamiltonian after adding the band origin. The molecular constants used for the  $A^2\Pi_u(v=2)$  band for  $\text{N}_2^+$  are listed in tab. 2.2. The contribution due

to the vibronic Hamiltonian,  $\hat{H}_{T_v}$ , for this vibronic state is given by,

$$\hat{H}_{T_v} = T_{20} \begin{bmatrix} 1 & 0 \\ 0 & 1 \end{bmatrix}, \quad (2.53)$$

where  $T_{20}$  is the vibronic origin given in tab. 2.4.

In summary, this chapter serves to introduce molecular systems and sets the stage by discussing the  $N_2^+$  molecule. Various angular-momenta-coupling cases have been examined, symmetry considerations in molecular systems have been discussed and electronic states of the  $N_2^+$  molecule relevant for the following chapters have been presented. Hamiltonians for the Hund's case (b)  $X^2\Sigma_g^+$  state and the Hund's case (a)  $A^2\Pi_u$  state of  $N_2^+$  have also been treated and effects like mixing of rovibrational states in the  $N_2^+$  molecule have been explored. State-energies and state-mixing coefficients have also been calculated for the  $N_2^+$  molecule, based on molecular constants taken from literature. The concepts discussed here are applied in the following chapter for investigating electric-dipole transitions in  $N_2^+$ .

# Chapter Three

## Hyperfine effects in the ac-Stark effect in the $\text{N}_2^+$ ion

Owing to the advances in the quantum control of the internal and external degrees of freedom, cold and ultracold atoms and molecules are now being employed for high-precision investigations. Experiments in well-controlled environments have paved the way for applications such as state- and energy-controlled ultracold chemistry [86–89], precision spectroscopic measurements [90,91], studies beyond the standard model of physics [92,93], determination of fundamental constants of the universe and their possible time variations [37,49,94,95], and quantum computation [96–98] and simulations [99,100]. Often, such experiments aim at probing matter-matter (e.g. study of collisions between atoms and molecules) and/or light-matter interactions. In comparison to atoms, the complex energy structure of molecules often hinder direct application of experimental techniques and lead to more involved theoretical investigations.

This chapter deals with the theoretical study of the interaction of molecules with light. Although various parts of the theory of electric-dipole-allowed transitions in molecules can be found in literature [61,63,64,101,102], a complete and consistent description of hyperfine-structure effects for transitions between states described by different Hund’s cases is hardly available. Thus, in this chapter transition parameters for electric-dipole-allowed transitions

in molecules, like the transition-dipole matrix elements and Hönl-London factors, are calculated from first principles. Subtle effects due to the hyperfine structure and mixing of rotational states in molecules are investigated in detail. The objective of this chapter is to develop a conscientious understanding of ac-Stark effects in molecule due to its interaction with far-detuned light. Such effects were exploited in our experiments (presented in section (5.4)) for the non-demolition state detection of the  $\text{N}_2^+$  molecular ion. Although, the  $\text{N}_2^+$  molecular ion is chosen as a prototypical example for the theoretical study presented here, many of the concepts and calculations are directly applicable to other molecules.

$\text{N}_2^+$  is a homonuclear diatomic molecule with no permanent-electric-dipole moment. Of the many possible electronic states, interactions between the ground ( $X^2\Sigma_g^+$ ), the first-excited ( $A^2\Pi_u$ ) and the second-excited ( $B^2\Sigma_u^+$ ) states due to light are discussed here. The  $X^2\Sigma_g^+ \leftrightarrow A^2\Pi_u$  band is often referred to as the Meinel band system [103] with transitions between them lying in the red and near-infrared spectral regions. Transitions in the first negative  $X^2\Sigma_g^+ \leftrightarrow B^2\Sigma_u^+$  band system [104] lie in the ultraviolet and visible spectrum.

### 3.1 Dispersive light-matter interaction

Energy levels of atoms and molecules experience a shift due to an ac-Stark potential which arises as a result of the interaction of their dipole moment with far-off-resonant radiation [105]. In the case of an in-homogeneous ac-Stark shift, the gradient of the shift can be used to exert a well-defined optical-dipole force (ODF). Such forces have been used to trap neutral atoms and molecules [106, 107], perform quantum-state-controlled chemical reactions [86, 108, 109], quantum simulations [110, 111] and quantum information processing [112, 113]. Recently, ODFs have also been employed in the detection of the internal states of trapped neutrals and ions [114–116].

Off-resonant photon scattering is often an unwanted effect due to the non-resonant radiation. It gives rise to effects like deconfining radiation pressure in trapping experiments and

state-loss in atoms and molecules. Thus, an understanding of the both optical dipole forces and scattering rate is important to make effective use of dispersive light-matter interaction in experiments.

### 3.1.1 Optical-dipole force

The ODF experienced by an atom or molecule due to far-off-resonant radiation can be given by [105],

$$F_{\text{ODF}}(\mathbf{r}) = -\nabla U_{\text{dip}}(\mathbf{r}), \quad (3.1)$$

where  $U_{\text{dip}}$  is the ac-Stark potential at position  $\mathbf{r}$  in space given by,

$$U_{\text{dip}}(\mathbf{r}) = -\frac{3\pi c^2}{2\omega_0^3} \left( \frac{\Gamma}{\omega_0 - \omega} + \frac{\Gamma}{\omega_0 + \omega} \right) I(\mathbf{r}). \quad (3.2)$$

Here,  $c$  is the speed of light in vacuum,  $\omega_0$  is the transition angular frequency of a dipole-allowed transition interacting with the far-off-resonant radiation of angular frequency  $\omega$ ,  $I(\mathbf{r})$  is the intensity of radiation at position  $\mathbf{r}$  in space given by,

$$I(\mathbf{r}) = 2\varepsilon_0 c |\tilde{E}(\mathbf{r})|^2, \quad (3.3)$$

where  $\tilde{E}(\mathbf{r})$  is the electric-field amplitude of the radiation at the position  $\mathbf{r}$ .  $\Gamma$  is the spontaneous-emission rate of the excited level defined as [105],

$$\Gamma = \frac{\omega_0^3}{3\pi\varepsilon_0\hbar c^3} |\langle e | \boldsymbol{\mu} | g \rangle|^2, \quad (3.4)$$

where  $\varepsilon_0$  is the vacuum permittivity, and the last term is the square of the absolute expectation value of the dipole-matrix element,  $\boldsymbol{\mu}$ , between the ground state  $|g\rangle$  and the excited state  $|e\rangle$  which are coupled by the off-resonant radiation.

### 3.1.2 Scattering rate

The photon-scattering rate due to far-off-resonant radiation can be given by [105],

$$\Gamma_{\text{sc}} = \frac{3\pi c^2}{2\hbar\omega_0^3} \left( \frac{\omega}{\omega_0} \right)^3 \left( \frac{\Gamma}{\omega_0 - \omega} + \frac{\Gamma}{\omega_0 + \omega} \right)^2 I(\mathbf{r}). \quad (3.5)$$

An interesting observation can be made specially when the off-resonant radiation is relatively closely detuned to the transition. In such cases the detuning,  $\Delta = |\omega_0 - \omega|$ , is small and counter-rotating terms consisting of  $\omega_0 + \omega$  as denominators in (3.2) and (3.5) can be neglected in the rotating-wave approximation. The expressions are simplified as [105],

$$U_{\text{dip}}(\mathbf{r}) = -\frac{3\pi c^2}{2\omega_0^3} \left(\frac{\Gamma}{\Delta}\right) I(\mathbf{r}), \quad (3.6a)$$

$$\Gamma_{\text{sc}} = \frac{3\pi c^2}{2\hbar\omega_0^3} \left(\frac{\Gamma}{\Delta}\right)^2 I(\mathbf{r}). \quad (3.6b)$$

Thus, both the optical-dipole potential (and consequently the ODF) and the scattering rate are directly proportional to the intensity of the radiation. A difference arises because while the dipole potential (and ODF) has a  $1/\Delta$  dependence, the scattering rate falls as  $1/\Delta^2$ . Thus, high intensities and big detunings lead to large ODFs with low scattering rates.

Discussions above make it clear that the transition-dipole matrix element,  $\boldsymbol{\mu}$ , is an important quantity which quantifies the interaction of matter with resonant and off-resonant light. The following sections of the chapter focus on calculating  $\boldsymbol{\mu}$  for molecules. Due to the large number of angular momenta involved, a discussion of the quantum numbers and their various coupling rules are presented. Symmetry properties of molecules, which restrict transitions between different molecular states, are put forward. The transition-dipole matrix elements are developed for different couplings of the angular momenta and in a consistent fashion with an emphasis on the  $X^2\Sigma_g^+$ ,  $A^2\Pi_u$  and  $B^2\Sigma_u^+$  states of  $\text{N}_2^+$ . The energy levels of the  $X^2\Sigma_g^+$  and  $A^2\Pi_u$  states of  $\text{N}_2^+$  are also computed from the involved Hamiltonians and subtle effects like mixing of rotational states due to hyperfine interactions are discussed. Finally, the ac-Stark shift and scattering rate in  $\text{N}_2^+$  due to off-resonant light and effects due to hyperfine interactions are explored.

## 3.2 Transition-dipole matrix elements

### 3.2.1 Hund's case (b) to Hund's case (b) transitions without fine-structure coupling

Although fine-structure coupling is often non-negligible in the case of molecules, a quantitative analysis is presented here as a basis for the development of more involved transition-dipole matrix elements.

An example of Hund's case (b) to Hund's case (b) transitions in molecules can be the  $B^2\Sigma_u^+ \leftrightarrow X^2\Sigma_g^+$  transitions in  $N_2^+$  in the absence of spin-orbit coupling. The basis state mentioned in (2.1.2) for Hund's coupling case (b), in absence of spin-orbit coupling, further simplifies as  $|n, \Lambda; v; N, \Lambda, M_N; S, M_S\rangle$ . The states are completely separable, i.e.,

$$|n, \Lambda; v; N, \Lambda, M_N; S, M_S\rangle = |n, \Lambda\rangle \otimes |v\rangle \otimes |N, \Lambda, M_N\rangle \otimes |S, M_S\rangle. \quad (3.7)$$

The transition dipole moment can then be calculated as,

$$\langle n', \Lambda'; v'; N', \Lambda', M'_N, S', M'_S | \boldsymbol{\mu}^{(s)} | n'', \Lambda''; v''; N'', \Lambda'', M''_N, S'', M''_S \rangle. \quad (3.8)$$

Here  $\boldsymbol{\mu}^{(s)}$  is the electric-dipole moment operator relative to the space-fixed-axis system. In general, for every Cartesian vector  $\mathbf{v}$ , a first-rank spherical tensor can be defined as [61, 117],

$$T_0^1[\mathbf{v}] = v_Z, \quad (3.9a)$$

$$T_{\pm 1}^1[\mathbf{v}] = \mp \frac{1}{\sqrt{2}}(v_X \pm iv_Y). \quad (3.9b)$$

Using the above, the  $p^{th}$  component of the transition-dipole matrix element in spherical-tensor notation can be expressed as,

$$\langle n', \Lambda'; v'; N', \Lambda', M'_N; S', M'_S | T_p^1[\boldsymbol{\mu}^{(s)}] | n'', \Lambda''; v''; N'', \Lambda'', M''_N; S'', M''_S \rangle. \quad (3.10)$$

The components of the dipole matrix element in spherical tensor notation in the original space-fixed coordinate system,  $T_p^1[\boldsymbol{\mu}^{(s)}]$ , can be expressed in terms of the respective components in the molecule-fixed coordinate system,  $T_q^1[\boldsymbol{\mu}^{(m)}]$ , by Wigner rotation matrices,  $\mathcal{D}_{pq}^{(1)}(\phi, \theta, \chi)$ , as [62],

$$T_p^1[\boldsymbol{\mu}^{(s)}] = \sum_{q=-1}^{+1} [\mathcal{D}_{pq}^{(1)}(\phi, \theta, \chi)]^* T_q^1[\boldsymbol{\mu}^{(m)}]. \quad (3.11)$$

The Euler angles  $(\phi, \theta, \chi)$  describe the relative orientation of the two frames of reference [61, 62]. Here the quantity  $[X]^*$  refers to the complex quantity of the matrix  $X$ .

Substituting (3.11), equation (3.10) can be expressed as,

$$\begin{aligned} & \langle n', \Lambda'; v'; N', \Lambda', M'_N; S', M'_S | T_p^1[\boldsymbol{\mu}^{(s)}] | n'', \Lambda''; v''; N'', \Lambda'', M''_N; S'', M''_S \rangle = \\ & \sum_{q=-1}^{+1} \langle n', \Lambda'; v'; N', \Lambda', M'_N; S', M'_S | [\mathcal{D}_{pq}^{(1)}(\phi, \theta, \chi)]^* T_q^1[\boldsymbol{\mu}^{(m)}] | n'', \Lambda''; v''; N'', \Lambda'', M''_N; S'', M''_S \rangle. \end{aligned} \quad (3.12)$$

The molecule-fixed electric-dipole-moment operator acts only on the vibronic part and the Wigner-D matrix acts only on the rotational part [61], using (3.7), (3.12) simplifies as,

$$\begin{aligned} & \langle n', \Lambda'; v'; N', \Lambda', M'_N; S', M'_S | T_p^1[\boldsymbol{\mu}^{(s)}] | n'', \Lambda''; v''; N'', \Lambda'', M''_N; S'', M''_S \rangle = \\ & \sum_{q=-1}^{+1} \langle n', \Lambda'; v' | T_q^1[\boldsymbol{\mu}^{(m)}] | n'', \Lambda''; v'' \rangle \langle N', \Lambda', M'_N | [\mathcal{D}_{pq}^{(1)}(\phi, \theta, \chi)]^* | N'', \Lambda'', M''_N \rangle \langle S', M'_S | S'', M''_S \rangle \\ & = \delta_{S'S''} \delta_{M'_S M''_S} \sum_{q=-1}^{+1} \langle n', \Lambda'; v' | T_q^1[\boldsymbol{\mu}^{(m)}] | n'', \Lambda''; v'' \rangle \langle N', \Lambda', M'_N | [\mathcal{D}_{pq}^{(1)}(\phi, \theta, \chi)]^* | N'', \Lambda'', M''_N \rangle, \end{aligned} \quad (3.13)$$

where we have used the relation,

$$\langle S', M'_S | S'', M''_S \rangle = \delta_{S'S''} \cdot \delta_{M'_S M''_S}, \quad (3.14)$$

and  $\delta$  is the Dirac-delta function.

The eigenfunctions of a vector operator  $\vec{V}$ , defined by its quantum number  $V$ , its molecule-fixed projection quantum number  $m$  and its space-fixed projection quantum number  $M$  are

related to the Wigner-D matrix as [62],

$$|V, m, M\rangle = \sqrt{\frac{2V+1}{8\pi^2}} [\mathcal{D}_{Mm}^{(V)}(\phi, \theta, \chi)]^*, \quad (3.15a)$$

$$\langle V, m, M| = \sqrt{\frac{2V+1}{8\pi^2}} [\mathcal{D}_{Mm}^{(V)}(\phi, \theta, \chi)]. \quad (3.15b)$$

The matrix element of a Wigner-D matrix,  $[\mathcal{D}_{pq}^{(1)}(\phi, \theta, \chi)]^*$  between the states mentioned above can thus be evaluated as,

$$\begin{aligned} \langle V', m', M' | [\mathcal{D}_{pq}^{(1)}(\phi, \theta, \chi)]^* | V'', m'', M'' \rangle &= \frac{\sqrt{2V'+1}\sqrt{2V''+1}}{8\pi^2} \int_0^{2\pi} \int_0^{2\pi} \int_0^\pi \\ &[\mathcal{D}_{M'm'}^{(V')}(\phi, \theta, \chi)] [\mathcal{D}_{pq}^{(1)}(\phi, \theta, \chi)]^* [\mathcal{D}_{M''m''}^{(V'')}(\phi, \theta, \chi)]^* \sin(\theta) d\theta d\phi d\chi \\ &= (-1)^{(M'-m')} \sqrt{2V'+1}\sqrt{2V''+1} \begin{pmatrix} V' & 1 & V'' \\ -M' & p & M'' \end{pmatrix} \begin{pmatrix} V' & 1 & V'' \\ -m' & q & m'' \end{pmatrix}, \end{aligned} \quad (3.16)$$

where we have used relations of the Wigner-D matrices [62],

$$\mathcal{D}_{Mm}^{(V)}(\phi, \theta, \chi) = (-1)^{(M-m)} [\mathcal{D}_{-M-m}^{(V)}(\phi, \theta, \chi)]^*, \quad (3.17a)$$

$$\begin{aligned} \iiint \mathcal{D}_{M_3 m_3}^{(V_3)}(\phi, \theta, \chi) \mathcal{D}_{M_2 m_2}^{(V_2)}(\phi, \theta, \chi) \mathcal{D}_{M_1 m_1}^{(V_1)}(\phi, \theta, \chi) \\ \sin(\theta) d\theta d\phi d\chi = 8\pi^2 \begin{pmatrix} V_1 & V_2 & V_3 \\ M_1 & M_2 & M_3 \end{pmatrix} \begin{pmatrix} V_1 & V_2 & V_3 \\ m_1 & m_2 & m_3 \end{pmatrix}. \end{aligned} \quad (3.17b)$$

Thus the rotational quantum number  $N$ , its projection quantum number on the space-fixed quantization axis  $M_N$  and its projection quantum number on the internuclear axis  $\Lambda$  can be expressed as [61, 62],

$$|N'', \Lambda'', M_N''\rangle = \sqrt{\frac{2N''+1}{8\pi^2}} [\mathcal{D}_{M_N'' \Lambda''}^{(N'')}(\phi, \theta, \chi)]^*, \quad (3.18a)$$

$$\langle N', \Lambda', M_N'| = \sqrt{\frac{2N'+1}{8\pi^2}} [\mathcal{D}_{M_N' \Lambda'}^{(N')}(\phi, \theta, \chi)]. \quad (3.18b)$$

Hence, the angular part (last term) of (3.13) can be expressed as,

$$\begin{aligned} & \langle N', \Lambda', M'_N | [\mathcal{D}_{pq}^{(1)}(\phi, \theta, \chi)]^* | N'', \Lambda'', M''_N \rangle \\ &= \sqrt{2N'+1} \sqrt{2N''+1} (-1)^{(M'_N - \Lambda')} \begin{pmatrix} N' & 1 & N'' \\ -M'_N & p & M''_N \end{pmatrix} \begin{pmatrix} N' & 1 & N'' \\ -\Lambda' & q & \Lambda'' \end{pmatrix}. \end{aligned} \quad (3.19)$$

Substituting (3.19) in (3.13),

$$\begin{aligned} & \langle n', \Lambda'; v'; N', \Lambda', M'_N; S', M'_S | T_p^1[\boldsymbol{\mu}^{(s)}] | n'', \Lambda''; v''; N'', \Lambda'', M''_N; S'', M''_S \rangle \\ &= (-1)^{(M'_N - \Lambda')} \delta_{S' S''} \delta_{M'_S M''_S} \sqrt{2N'+1} \sqrt{2N''+1} \begin{pmatrix} N' & 1 & N'' \\ -M'_N & p & M''_N \end{pmatrix} \\ & \quad \sum_{q=-1}^{+1} \begin{pmatrix} N' & 1 & N'' \\ -\Lambda' & q & \Lambda'' \end{pmatrix} \langle n', \Lambda'; v' | T_q^1[\boldsymbol{\mu}^{(m)}] | n'', \Lambda''; v'' \rangle. \end{aligned} \quad (3.20)$$

For non-zero evaluations, a Wigner-3j symbol  $\begin{pmatrix} J_1 & J_2 & J_3 \\ M_1 & M_2 & M_3 \end{pmatrix}$  must satisfy the following criteria [62],

$$M_i \in \{-J_i, -J_i + 1, \dots, +J_i\}, \quad (3.21a)$$

$$M_1 + M_2 + M_3 = 0, \quad (3.21b)$$

$$|J_1 - J_2| \leq J_3 \leq J_1 + J_2, \quad (3.21c)$$

$$(J_1 + J_2 + J_3) \text{ is an integer (and an even integer if } M_1 = M_2 = M_3 = 0). \quad (3.21d)$$

For the transitions occurring in the band  $B^2\Sigma_u^+ \leftrightarrow X^2\Sigma_g^+$  being discussed here,  $\Lambda' =$

$\Lambda'' = 0$ . Thus from (3.21b),  $q = 0$  in (3.20),

$$\begin{aligned}
& \langle n', \Lambda'; v'; N', \Lambda', M'_N; S', M'_S | T_p^1[\boldsymbol{\mu}^{(s)}] | n'', \Lambda''; v''; N'', \Lambda'', M''_N; S'', M''_S \rangle \\
&= (-1)^{(M'_N)} \delta_{S'S''} \delta_{M'_S M''_S} \sqrt{2N'+1} \sqrt{2N''+1} \begin{pmatrix} N' & 1 & N'' \\ -M'_N & p & M''_N \end{pmatrix} \\
&\quad \begin{pmatrix} N' & 1 & N'' \\ 0 & 0 & 0 \end{pmatrix} \langle n', \Lambda'; v' | T_0^1[\boldsymbol{\mu}^{(m)}] | n'', \Lambda''; v'' \rangle. \quad (3.22)
\end{aligned}$$

Such transitions have often been labelled as *parallel* transitions in literature [61].

Additional selection rules for the given transitions can be identified from properties of Wigner-3j symbols in (3.22). From (3.21c), we get the relation,  $\Delta N = 0, \pm 1$ . From (3.21d) and the second Wigner-3j symbol in (3.22),  $\Delta N = 0$  transitions are forbidden. Thus only  $\Delta N = \pm 1$  transitions are possible. This selection rule ensures that only  $+$   $\leftrightarrow$   $-$  parity transitions are allowed as is expected for dipole-allowed transitions. Additionally, from discussions on nuclear-spin statistics presented earlier, we can note that there is no change in the overall nuclear-spin. The electronic spin and its projection on the space-fixed axis are also conserved (given by the Dirac-delta products in (3.22)). For incident light polarized along the direction  $p$ , the selection rule for  $M_N$  can be identified as  $M'_N - M''_N = p$  from (3.21b).

Since the square of the transition-dipole matrix element is often encountered in equations describing light-matter interactions, from (3.22),

$$\begin{aligned}
& |\langle n', \Lambda'; v'; N', \Lambda', M'_N; S', M'_S | T_p^1[\boldsymbol{\mu}^{(s)}] | n'', \Lambda''; v''; N'', \Lambda'', M''_N; S'', M''_S \rangle|^2 \\
&= \delta_{S'S''}^2 \delta_{M'_S M''_S}^2 (2N'+1)(2N''+1) \begin{pmatrix} N' & 1 & N'' \\ -M'_N & p & M''_N \end{pmatrix}^2 \\
&\quad \begin{pmatrix} N' & 1 & N'' \\ 0 & 0 & 0 \end{pmatrix}^2 |\langle n', \Lambda'; v' | T_0^1[\boldsymbol{\mu}^{(m)}] | n'', \Lambda''; v'' \rangle|^2. \quad (3.23)
\end{aligned}$$

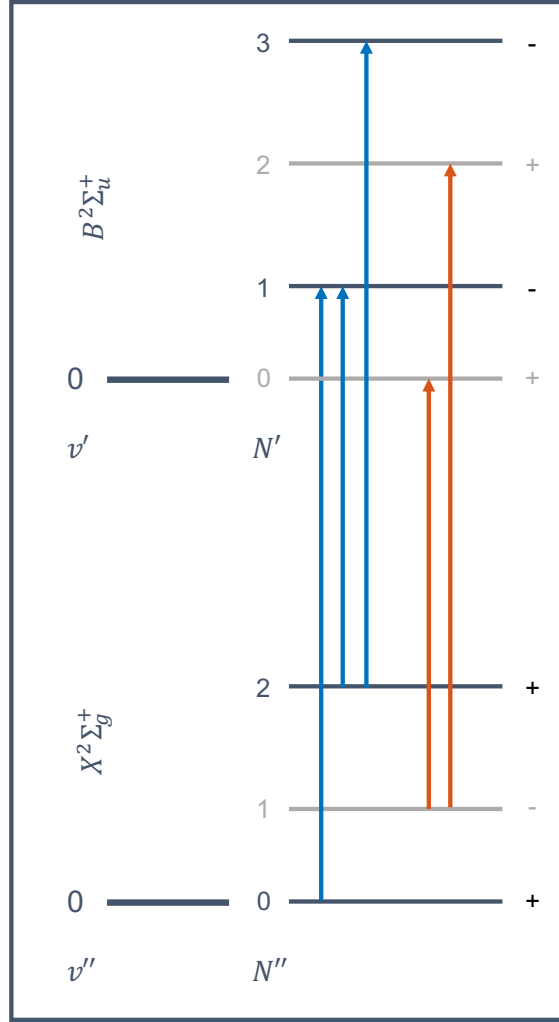


**Figure 3.1** Transition between the  $X^2\Sigma_g^+$  and  $B^2\Sigma_u^+$  electronic states of  $N_2^+$ . For *ortho*- $N_2^+$ , transitions (blue) from the ground ( $N'' = 0$ ) and the first excited ( $N'' = 2$ ) positive parity rotational states (black) are shown. In the case of *para*- $N_2^+$ , transitions (orange) from the ground ( $N'' = 1$ ) negative parity rotational state (grey) are also shown.

The rovibronic part in the equation above,  $|\langle n', \Lambda'; v' | T_0^1[\boldsymbol{\mu}^{(m)}] | n'', \Lambda''; v'' \rangle|^2$ , can be expressed as [118],

$$|\langle n', \Lambda'; v' | T_0^1[\boldsymbol{\mu}^{(m)}] | n'', \Lambda''; v'' \rangle|^2 = \frac{3\varepsilon_0 h c^3}{2\omega_0^3} A_{\text{vibronic}}, \quad (3.24)$$

where  $\varepsilon_0$  is the permittivity of free space,  $h$  is the Planck's constant,  $c$  is the speed of light in vacuum,  $\omega_0$  is the transition frequency and  $A_{\text{vibronic}}$  is the Einstein-A coefficient for the given vibronic band.

Equation (3.23), can be simplified as,

$$\begin{aligned}
& |\langle n', \Lambda'; v'; N', \Lambda', M'_N; S', M'_S | T_p^1[\boldsymbol{\mu}^{(s)}] | n'', \Lambda''; v''; N'', \Lambda'', M''_N; S'', M''_S \rangle|^2 \\
&= \frac{3\varepsilon_0 \hbar c^3}{2\omega_0^3} S A_{\text{vibronic}} \left[ \sqrt{(2N' + 1)} \begin{pmatrix} N' & 1 & N'' \\ -M'_N & p & M''_N \end{pmatrix} \right]^2,
\end{aligned} \tag{3.25}$$

where,

$$S = \delta_{S'S''}{}^2 \delta_{M'_S M''_S}{}^2 (2N'' + 1) \begin{pmatrix} N' & 1 & N'' \\ 0 & 0 & 0 \end{pmatrix}^2 \tag{3.26}$$

is called the Hönl-London factor for the transition.

The square of the transition-dipole moment thus depends on vibronic Einstein- $A$  coefficient, the rotational Hönl-London factors and a polarization dependent term (given by the square brackets in (3.25)). As will be seen in the proceeding sections all electric-dipole allowed rovibronic transitions can be decomposed into the same factors, the values of which will depend on the nature of the rovibronic states involved.

### 3.2.2 Hund's case (b) to Hund's case (b) transitions including fine-structure coupling

The spin-orbit (fine-structure) coupling couples the rotational quantum number,  $N$ , and the electronic-spin quantum number,  $S$ , giving rise to the total angular momentum (excluding nuclear spin),  $J$ . The coupling scheme follows,

$$\vec{N} + \vec{S} = \vec{J}. \tag{3.27}$$

The good quantum numbers and the proper basis states when including the spin-orbit coupling has been described in (2.1.2). We use the basis state  $|n, \Lambda; v; N, \Lambda, S, J, M_J\rangle$ . The transition dipole moment can then be calculated as,

$$\langle n', \Lambda'; v'; N', \Lambda', S', J', M'_J | \boldsymbol{\mu}^{(s)} | n'', \Lambda''; v''; N'', \Lambda'', S'', J'', M''_J \rangle, \tag{3.28}$$

Following (3.9), the  $p^{th}$  component of the transition-dipole matrix element in terms of spherical tensors can be expressed as,

$$\langle n', \Lambda'; v'; N', \Lambda', S', J', M'_J | T_p^1[\boldsymbol{\mu}^{(s)}] | n'', \Lambda''; v''; N'', \Lambda'', S'', J'', M''_J \rangle. \quad (3.29)$$

Using (3.11) and expressing the space-fixed dipole-moment operator in the molecule-fixed coordinate system,

$$\begin{aligned} & \langle n', \Lambda'; v'; N', \Lambda', S', J', M'_J | T_p^1[\boldsymbol{\mu}^{(s)}] | n'', \Lambda''; v''; N'', \Lambda'', S'', J'', M''_J \rangle \\ &= \sum_{q=-1}^{+1} \langle n', \Lambda'; v'; N', \Lambda', S', J', M'_J | [\mathcal{D}_{pq}^{(1)}(\phi, \theta, \chi)]^* T_q^1[\boldsymbol{\mu}^{(m)}] | n'', \Lambda''; v''; N'', \Lambda'', S'', J'', M''_J \rangle \\ &= \sum_{q=-1}^{+1} \langle n', \Lambda'; v' | T_q^1[\boldsymbol{\mu}^{(m)}] | n'', \Lambda''; v'' \rangle \langle N', \Lambda', S', J', M'_J | [\mathcal{D}_{pq}^{(1)}(\phi, \theta, \chi)]^* | N'', \Lambda'', S'', J'', M''_J \rangle, \end{aligned} \quad (3.30)$$

where the basis states have been separated into the vibronic and rotational components as,

$$|n, \Lambda; v; N, \Lambda, S, J, M_J\rangle = |n, \Lambda; v\rangle \otimes |N, \Lambda, S, J, M_J\rangle. \quad (3.31)$$

The last term of (3.30) can be simplified by the Wigner-Eckart theorem. It states that the matrix elements of spherical tensor operators between states of definite angular momentum can be expressed as a product of two parts - a reduced dipole-matrix element which is independent of the orientation of the angular-moment and a numeric factor called the Clebsch-Gordon coefficient [62], i.e.,

$$\begin{aligned} \langle \alpha', V', M' | T_p^{(k)}[x] | \alpha'', V'', M'' \rangle &= \langle V'', M'', k, p | V', M' \rangle \langle \alpha', V' || T^{(k)}[x] || \alpha'', V'' \rangle \\ &= (-1)^{(V'-M')} \begin{pmatrix} V' & k & V'' \\ -M' & p & M'' \end{pmatrix} \langle \alpha', V' || T^{(k)}[x] || \alpha'', V'' \rangle, \end{aligned} \quad (3.32)$$

where  $\alpha'(\alpha'')$  represents other angular momenta operators except the angular momentum operator  $V'(V'')$ ,  $M'(M'')$  is the projection of  $V'(V'')$  on the space-fixed quantization axis

and  $T_p^{(k)}[x]$  is the  $p^{th}$  component of the rank ( $k$ ) spherical tensor  $T[x]$ . The last term in the equation above is the reduced-matrix element. The dot in the spherical tensor operator  $T^{(k)}[x]$  represents the space-fixed index with respect to which the matrix element was reduced [62].

Following the Wigner-Eckart theorem, the matrix element of the Wigner-D matrix between the rotational states in (3.30) can be simplified as,

$$\begin{aligned} & \langle N', \Lambda', S', J', M'_J | [\mathcal{D}_{pq}^{(1)}(\phi, \theta, \chi)]^* | N'', \Lambda'', S'', J'', M''_J \rangle \\ &= (-1)^{(J'-M'_J)} \begin{pmatrix} J' & 1 & J'' \\ -M'_J & p & M''_J \end{pmatrix} \langle N', \Lambda', S', J' || [\mathcal{D}_{\dot{q}}^{(1)}(\phi, \theta, \chi)]^* || N'', \Lambda'', S'', J'' \rangle. \end{aligned} \quad (3.33)$$

The reduced matrix element of the above equation can be further simplified using the relation [62],

$$\begin{aligned} \langle \alpha', V'_1, V'_2, V' || T^{(k)} || \alpha'', V''_1, V''_2, V'' \rangle &= \delta_{V'_2, V''_2} (-1)^{(V'_1+V'_2+V''+k)} \\ & \sqrt{2V'+1} \sqrt{2V''+1} \begin{Bmatrix} V'_1 & V' & V'_2 \\ V'' & V''_1 & k \end{Bmatrix} \langle \alpha', V'_1 || T^{(k)} || \alpha'', V''_1 \rangle, \end{aligned} \quad (3.34)$$

where  $\alpha'$  ( $\alpha''$ ) represents other angular momenta except the quantum numbers  $V'_1$  ( $V''_1$ ),  $V'_2$  ( $V''_2$ ),  $V'$  ( $V''$ ). The respective vectors are coupled as  $\vec{V}' = \vec{V}'_1 + \vec{V}'_2$  and  $\vec{V}'' = \vec{V}''_1 + \vec{V}''_2$ . The tensor operator  $T^{(k)}$  acts only on the variables of the vector space pertaining to  $\vec{V}'_1$  and  $\vec{V}''_1$ . The double-row symbols in the curly braces are the Wigner-6j symbols [61, 62].

It can be noted that  $\vec{J} = \vec{N} + \vec{S}$  and that the Wigner-D matrix acts only on the rotational space containing  $\vec{N}$  [61]. Thus (3.33) can be simplified as,

$$\begin{aligned} & \langle N', \Lambda', S', J', M'_J | [\mathcal{D}_{pq}^{(1)}(\phi, \theta, \chi)]^* | N'', \Lambda'', S'', J'', M''_J \rangle \\ &= (-1)^{(J'-M'_J)} (-1)^{(N'+S'+J''+1)} \delta_{S', S''} \sqrt{2J'+1} \sqrt{2J''+1} \begin{pmatrix} J' & 1 & J'' \\ -M'_J & p & M''_J \end{pmatrix} \\ & \begin{Bmatrix} N' & J' & S' \\ J'' & N'' & 1 \end{Bmatrix} \langle N', \Lambda' || [\mathcal{D}_{\dot{q}}^{(1)}(\phi, \theta, \chi)]^* || N'', \Lambda'' \rangle. \end{aligned} \quad (3.35)$$

Following the Wigner-Eckart theorem and properties of Wigner-rotation matrices, the reduced matrix element in the above equation can further be simplified as [61],

$$\langle N', \Lambda' || [\mathcal{D}_{.q}^{(1)}(\phi, \theta, \chi)]^* || N'', \Lambda'' \rangle = (-1)^{(N' - \Lambda')} \sqrt{2N' + 1} \sqrt{2N'' + 1} \begin{pmatrix} N' & 1 & N'' \\ -\Lambda' & q & \Lambda'' \end{pmatrix}. \quad (3.36)$$

Equation (3.35) can be thus written as,

$$\begin{aligned} & \langle N', \Lambda', S', J', M'_J | [\mathcal{D}_{pq}^{(1)}(\phi, \theta, \chi)]^* | N'', \Lambda'', S'', J'', M''_J \rangle \\ &= (-1)^{(J' - M'_J)} (-1)^{(N' + S' + J'' + 1)} (-1)^{(N' - \Lambda')} \delta_{S', S''} \sqrt{2J' + 1} \sqrt{2J'' + 1} \sqrt{2N' + 1} \\ & \quad \sqrt{2N'' + 1} \begin{pmatrix} J' & 1 & J'' \\ -M'_J & p & M''_J \end{pmatrix} \begin{pmatrix} N' & 1 & N'' \\ -\Lambda' & q & \Lambda'' \end{pmatrix} \begin{Bmatrix} N' & J' & S' \\ J'' & N'' & 1 \end{Bmatrix}. \quad (3.37) \end{aligned}$$

Substituting this back in (3.30)

$$\begin{aligned} & \langle n', \Lambda'; v'; N', \Lambda', S', J', M'_J | T_p^1[\boldsymbol{\mu}^{(s)}] | n'', \Lambda''; v''; N'', \Lambda'', S'', J'', M''_J \rangle \\ &= \sum_{q=-1}^{+1} (-1)^{(S' + J' + J'' - M'_J - \Lambda' + 1)} \delta_{S', S''} \sqrt{2J' + 1} \sqrt{2J'' + 1} \sqrt{2N' + 1} \sqrt{2N'' + 1} \\ & \quad \begin{pmatrix} J' & 1 & J'' \\ -M'_J & p & M''_J \end{pmatrix} \begin{pmatrix} N' & 1 & N'' \\ -\Lambda' & q & \Lambda'' \end{pmatrix} \begin{Bmatrix} N' & J' & S' \\ J'' & N'' & 1 \end{Bmatrix} \langle n', \Lambda'; v' | T_q^1[\boldsymbol{\mu}^{(m)}] | n'', \Lambda''; v'' \rangle. \quad (3.38) \end{aligned}$$

As from section (3.2.1), for the case of  $B^2\Sigma_u^+ \leftrightarrow X^2\Sigma_g^+$  Hund's case (b) to Hund's case (b) transitions,  $\Lambda' = \Lambda'' = 0$ . From the second Wigner-3j symbol above for non-zero values we get  $q = 0$  (3.21b). Thus,

$$\begin{aligned} & \langle n', \Lambda'; v'; N', \Lambda', S', J', M'_J | T_p^1[\boldsymbol{\mu}^{(s)}] | n'', \Lambda''; v''; N'', \Lambda'', S'', J'', M''_J \rangle \\ &= (-1)^{(S' + J' + J'' - M'_J + 1)} \delta_{S', S''} \sqrt{2J' + 1} \sqrt{2J'' + 1} \sqrt{2N' + 1} \sqrt{2N'' + 1} \\ & \quad \begin{pmatrix} J' & 1 & J'' \\ -M'_J & p & M''_J \end{pmatrix} \begin{pmatrix} N' & 1 & N'' \\ 0 & 0 & 0 \end{pmatrix} \begin{Bmatrix} N' & J' & S' \\ J'' & N'' & 1 \end{Bmatrix} \langle n', \Lambda'; v' | T_0^1[\boldsymbol{\mu}^{(m)}] | n'', \Lambda''; v'' \rangle. \quad (3.39) \end{aligned}$$

As in the previous section, such transitions are called *parallel* transitions.

Additional selection rules for the given transitions can be identified from properties of Wigner-3j symbols in (3.38). From (3.21c), we get the relations,  $\Delta N = 0, \pm 1$  and  $\Delta J = 0, \pm 1$ . The second Wigner-3j symbol then forbids  $\Delta N = 0$  transitions (3.21d). Thus only  $\Delta N = \pm 1$  transitions are possible. As in the previous section, this selection rule ensures that only  $+ \leftrightarrow -$  parity transitions are allowed as is expected for dipole-allowed transitions. In terms of the parity labels  $e$  and  $f$ , the selection rules can be recast as  $e \leftrightarrow e$  and  $f \leftrightarrow f$  for  $P$  ( $\Delta J = -1$ ) and  $R$  branches ( $\Delta J = +1$ ), while  $e \leftrightarrow f$  for the  $Q$  branch ( $\Delta J = 0$ ) of the rotational spectrum. Additionally, from discussions on nuclear-spin statistics presented earlier, we can note that there is no change in the overall nuclear-spin ( $ortho\text{-}N_2^+$  does not change to  $para\text{-}N_2^+$ ). The electronic spin is also conserved (given by the Dirac-delta products in (3.39)). For incident light polarized along the direction  $p$ , the selection rule for  $M_J$  can be identified as  $\Delta M_J = M'_J - M''_J = p$  from (3.21b).

Fig. (3.2) shows possible transitions from the  $X^2\Sigma_g^+$  electronic ground state to the  $B^2\Sigma_u^+$  second excited state of  $N_2^+$ , starting at the two lowest rotational levels ( $N = 0, J = 1/2$  and  $N = 2, J = 3/2$ ). All selection rules discussed above hold.

Since the square of the transition-dipole matrix element is often encountered in equations describing light-matter interactions, from (3.39),

$$\begin{aligned}
& |\langle n', \Lambda'; v'; N', \Lambda', S', J', M'_J | T_p^1[\boldsymbol{\mu}^{(s)}] | n'', \Lambda''; v''; N'', \Lambda'', S'', J'', M''_J \rangle|^2 \\
&= \delta_{S'S''}^2 (2J' + 1)(2J'' + 1)(2N' + 1)(2N'' + 1) \left( \begin{array}{ccc} J' & 1 & J'' \\ -M'_J & p & M''_J \end{array} \right)^2 \\
& \left( \begin{array}{ccc} N' & 1 & N'' \\ 0 & 0 & 0 \end{array} \right)^2 \left\{ \begin{array}{ccc} N' & J' & S' \\ J'' & N'' & 1 \end{array} \right\}^2 |\langle n', \Lambda'; v' | T_0^1[\boldsymbol{\mu}^{(m)}] | n'', \Lambda''; v'' \rangle|^2. \quad (3.40)
\end{aligned}$$

Substituting

$$|\langle n', \Lambda'; v' | T_0^1[\boldsymbol{\mu}^{(m)}] | n'', \Lambda''; v'' \rangle|^2 = \frac{3\varepsilon_0 \hbar c^3}{2\omega_0^3} A_{\text{vibronic}}, \quad (3.41)$$

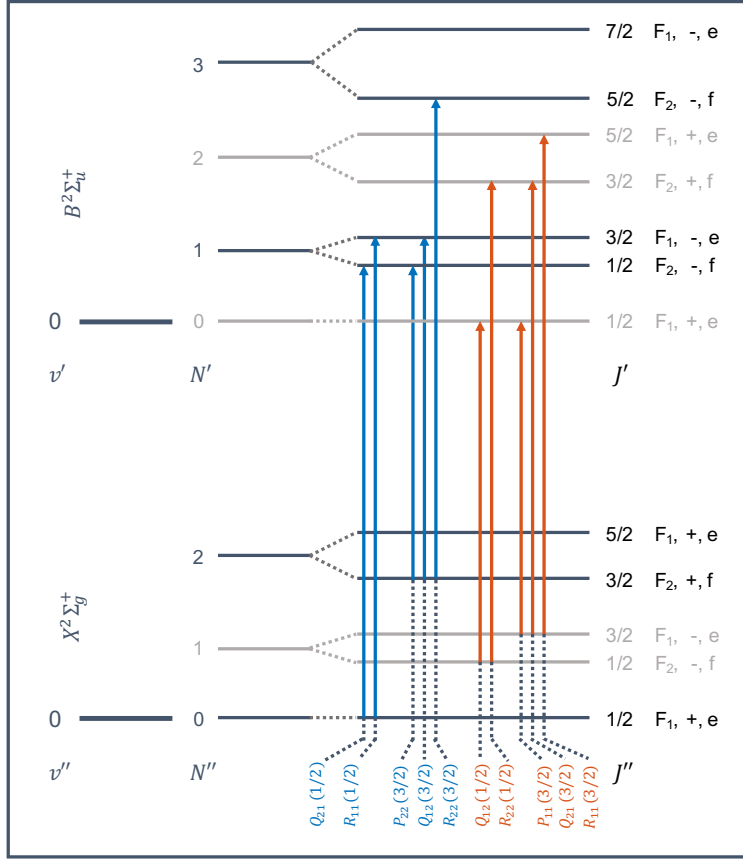


**Figure 3.2** Transition between the  $X^2\Sigma_g^+$  and  $B^2\Sigma_u^+$  electronic states of  $N_2^+$ . Transitions (blue) from the lowest ( $N'' = 0, J'' = 1/2$ ) and the first excited ( $N'' = 2, J'' = 3/2$ ) rotational levels for *ortho*- $N_2^+$  (black) are shown. Also depicted are transitions (orange) from the ground states ( $N'' = 1, J'' = 1/2, 3/2$ ) for *para*- $N_2^+$  (grey).

as before [118] and re-arranging terms,

$$\begin{aligned}
 & |\langle n', \Lambda'; v'; N', \Lambda', S', J', M_J' | T_p^1[\boldsymbol{\mu}^{(s)}] | n'', \Lambda''; v''; N'', \Lambda'', S'', J'', M_J'' \rangle|^2 \\
 &= \frac{3\varepsilon_0 hc^3}{2\omega_0^3} S A_{\text{vibronic}} \left[ \sqrt{2J'' + 1} \begin{pmatrix} J' & 1 & J'' \\ -M_J' & p & M_J'' \end{pmatrix} \right]^2, \quad (3.42)
 \end{aligned}$$

where

$$S = \delta_{S'S''}^2 (2J'' + 1)(2N' + 1)(2N'' + 1) \begin{pmatrix} N' & 1 & N'' \\ 0 & 0 & 0 \end{pmatrix}^2 \begin{Bmatrix} N' & J' & S' \\ J'' & N'' & 1 \end{Bmatrix}, \quad (3.43)$$

is the Hönl-London for Hund's case (b) to Hund's case (b) transition including spin-orbit

(fine-structure) coupling. As in the previous section, the square of the transition-dipole matrix element has been expressed in terms of a constant, the Hönl-London factor, the vibronic Einstein- $A$  coefficient and a polarization-dependent term.

### 3.2.3 Hund's case (b) to Hund's case (a) transitions including fine-structure coupling

Building on the previous two sections, transitions between Hund's cases (b) states and Hund's case (a) states can be examined. As an example of such transitions, the transition-dipole matrix elements for rovibronic transitions between the  $A^2\Pi_u \leftrightarrow X^2\Sigma_g^+$  states of the  $N_2^+$  molecular ion are presented here.

The basis states representing the Hund's coupling cases (a) and (b) have been described in section (2.1.2). For states described by Hund's coupling case (b), the basis state  $|n, \Lambda; v, N, \Lambda, S, J, M_J\rangle$  is used here while for Hund's case (a) state, the basis  $|n, \Lambda; v; \Omega, J, M_J; S, \Sigma\rangle$  is used here. As stated in section (2.1.2), it is always possible to express the quantum numbers of one coupling scheme as a summation of quantum numbers of other schemes via Clebsch-Gordon coefficients, for example, the Hund's case (b) quantum numbers can be expressed in terms of the Hund's case (a) basis as<sup>1</sup> [119],

$$|n, \Lambda; v; N, \Lambda, S, J, M_J\rangle = \sum_{\Sigma, \Omega} (-1)^{(N-S+\Omega)} \sqrt{2N+1} \begin{pmatrix} J & S & N \\ \Omega & -\Sigma & -\Lambda \end{pmatrix} |n, \Lambda; v; \Omega, J, M_J; S, \Sigma\rangle. \quad (3.44)$$

---

<sup>1</sup>Although some texts like [61, 63] define the transformation of Hund's case (b) states in terms of Hund's case (a) states as,

$$|n, \Lambda; v; N, \Lambda, S, J, M_J\rangle = \sum_{\Sigma} (-1)^{(J-S+\Lambda)} \sqrt{2N+1} \begin{pmatrix} J & S & N \\ \Omega & -\Sigma & -\Lambda \end{pmatrix} |n, \Lambda; v; \Omega, J, M_J; S, \Sigma\rangle.$$

This definition is inconsistent with respect to the parity definition in (2.14). Both definitions only defer in the sign of the expression on the right-hand side of equation (3.44).

The dipole-matrix element can be calculated as,

$$\langle n', \Lambda'; v'; \Omega', J', M'_J; S', \Sigma' | \boldsymbol{\mu}^{(s)} | n'', \Lambda''; v''; N'', \Lambda'', S'', J'', M''_J \rangle. \quad (3.45)$$

The  $p^{\text{th}}$  component of the transition-dipole matrix element in terms of spherical tensors can be expressed as (3.9),

$$\langle n', \Lambda'; v'; \Omega', J', M'_J; S', \Sigma' | T_p^1[\boldsymbol{\mu}^{(s)}] | n'', \Lambda''; v''; N'', \Lambda'', S'', J'', M''_J \rangle. \quad (3.46)$$

Further, using (3.11), and expressing the space-fixed dipole-moment operator in the molecule-fixed coordinate system,

$$\begin{aligned} & \langle n', \Lambda'; v'; \Omega', J', M'_J; S', \Sigma' | T_p^1[\boldsymbol{\mu}^{(s)}] | n'', \Lambda''; v''; N'', \Lambda'', S'', J'', M''_J \rangle \\ &= \sum_{q=-1}^{+1} \langle n', \Lambda'; v'; \Omega', J', M'_J; S', \Sigma' | [\mathcal{D}_{pq}^{(1)}(\phi, \theta, \chi)]^* T_q^1[\boldsymbol{\mu}^{(m)}] | n'', \Lambda''; v''; N'', \Lambda'', S'', J'', M''_J \rangle \\ &= \sum_{q=-1}^{+1} \langle n', \Lambda'; v' | T_q^1[\boldsymbol{\mu}^{(m)}] | n'', \Lambda''; v'' \rangle \langle \Omega', J', M'_J; S', \Sigma' | [\mathcal{D}_{pq}^{(1)}(\phi, \theta, \chi)]^* | N'', \Lambda'', S'', J'', M''_J \rangle. \end{aligned} \quad (3.47)$$

The last term in the equation above can be simplified further by expressing the Hund's case (b) state in terms of the Hund's case (a) states. From (3.44),

$$\begin{aligned} & \langle \Omega', J', M'_J; S', \Sigma' | [\mathcal{D}_{pq}^{(1)}(\phi, \theta, \chi)]^* | N'', \Lambda'', S'', J'', M''_J \rangle \\ &= \sum_{\Sigma'', \Omega''} (-1)^{(N'' - S'' + \Omega'')} \sqrt{2N'' + 1} \begin{pmatrix} J'' & S'' & N'' \\ \Omega'' & -\Sigma'' & -\Lambda'' \end{pmatrix} \\ & \quad \langle \Omega', J', M'_J; S', \Sigma' | [\mathcal{D}_{pq}^{(1)}(\phi, \theta, \chi)]^* | \Omega'', J'', M''_J; S'', \Sigma'' \rangle \\ &= \sum_{\Sigma'', \Omega''} (-1)^{(N'' - S'' + \Omega'')} \delta_{S', S''} \delta_{\Sigma', \Sigma''} \sqrt{2N'' + 1} \begin{pmatrix} J'' & S'' & N'' \\ \Omega'' & -\Sigma'' & -\Lambda'' \end{pmatrix} \\ & \quad \langle \Omega', J', M'_J | [\mathcal{D}_{pq}^{(1)}(\phi, \theta, \chi)]^* | \Omega'', J'', M''_J \rangle, \end{aligned} \quad (3.48)$$

where for the last equality we have used the fact that the Wigner-D matrix does not operate on the spin quantum number [61].

The matrix element of the Wigner-D matrices appearing in the equation above have been evaluated in (3.16). Thus,

$$\begin{aligned} & \langle \Omega', J', M'_J | [\mathcal{D}_{pq}^{(1)}(\phi, \theta, \chi)]^* | \Omega'', J'', M''_J \rangle \\ &= (-1)^{(M'_J - \Omega')} \sqrt{2J' + 1} \sqrt{2J'' + 1} \begin{pmatrix} J' & 1 & J'' \\ -M'_J & p & M''_J \end{pmatrix} \begin{pmatrix} J' & 1 & J'' \\ -\Omega' & q & \Omega'' \end{pmatrix}. \end{aligned} \quad (3.49)$$

Thus, equation (3.48) can be expressed as,

$$\begin{aligned} & \langle \Omega', J', M'_J; S', \Sigma' | [\mathcal{D}_{pq}^{(1)}(\phi, \theta, \chi)]^* | N'', \Lambda'', S'', J'', M''_J \rangle \\ &= \sum_{\Sigma'', \Omega''} (-1)^{(N'' - S'' + \Omega'' + M'_J - \Omega')} \delta_{S', S''} \delta_{\Sigma', \Sigma''} \sqrt{2N'' + 1} \sqrt{2J' + 1} \sqrt{2J'' + 1} \\ & \quad \begin{pmatrix} J'' & S'' & N'' \\ \Omega'' & -\Sigma'' & -\Lambda'' \end{pmatrix} \begin{pmatrix} J' & 1 & J'' \\ -M'_J & p & M''_J \end{pmatrix} \begin{pmatrix} J' & 1 & J'' \\ -\Omega' & q & \Omega'' \end{pmatrix}. \end{aligned} \quad (3.50)$$

Substituting this in (3.47), the  $p^{th}$  component of the transition-dipole matrix element can be expressed as,

$$\begin{aligned} & \langle n', \Lambda'; v'; \Omega', J', M'_J; S', \Sigma' | T_p^1[\boldsymbol{\mu}^{(s)}] | n'', \Lambda''; v''; N'', \Lambda'', S'', J'', M''_J \rangle \\ &= \sum_{\Sigma'', \Omega'', q} (-1)^{(N'' - S'' + \Omega'' + M'_J - \Omega')} \delta_{S', S''} \delta_{\Sigma', \Sigma''} \sqrt{2N'' + 1} \sqrt{2J' + 1} \sqrt{2J'' + 1} \\ & \quad \begin{pmatrix} J'' & S'' & N'' \\ \Omega'' & -\Sigma'' & -\Lambda'' \end{pmatrix} \begin{pmatrix} J' & 1 & J'' \\ -M'_J & p & M''_J \end{pmatrix} \begin{pmatrix} J' & 1 & J'' \\ -\Omega' & q & \Omega'' \end{pmatrix} \langle T_q^1 \rangle, \end{aligned} \quad (3.51)$$

where,

$$\langle T_q^1 \rangle = \langle n', \Lambda'; v' | T_q^1[\boldsymbol{\mu}^{(m)}] | n'', \Lambda''; v'' \rangle. \quad (3.52)$$

Since dipole-allowed transitions occur between states of well defined parity, a better understanding can be achieved by expressing the  $A^2\Pi_u$  state as a proper parity-defined state as

done in (2.15) when calculating the value of the transition dipole-matrix elements. Thus,

$$|n', \Lambda'; v'; \Omega', J', M'_J; S', \Sigma'; \pm\rangle = \frac{1}{\sqrt{2}} \left\{ |n', \Lambda'; v'; \Omega', J', M'_J; S', \Sigma'\rangle \right. \\ \left. \pm (-1)^{(J'-S')} |n', -\Lambda'; v'; -\Omega', J', M'_J; S', -\Sigma'\rangle \right\}. \quad (3.53)$$

The  $p^{\text{th}}$  component of the transition-dipole matrix element between proper parity-defined states can be expressed as,

$$\frac{1}{\sqrt{2}} \left[ \langle n', \Lambda'; v'; \Omega', J', M'_J; S', \Sigma' | \pm (-1)^{(J'-S')} \right. \\ \left. \langle n', -\Lambda'; v'; -\Omega', J', M'_J; S', -\Sigma' | \right] T_p^1[\boldsymbol{\mu}^{(s)}] |n'', \Lambda''; v''; N'', \Lambda'', S'', J'', M''_J\rangle \\ = \frac{\delta_{S', S''}}{\sqrt{2}} \sum_{\Sigma'', \Omega'', q} \left[ (-1)^{(N''-S''+\Omega''+M'_J-\Omega')} \delta_{\Sigma' \Sigma''} \sqrt{2N''+1} \sqrt{2J''+1} \begin{pmatrix} J'' & S'' & N'' \\ \Omega'' & -\Sigma'' & -\Lambda'' \end{pmatrix} \right. \\ \left. \begin{pmatrix} J' & 1 & J'' \\ -\Omega' & q & \Omega'' \end{pmatrix} \langle T_q^1 \rangle \pm (-1)^{(N''-S''+\Omega''+M'_J+\Omega'+J'-S')} \delta_{-\Sigma' \Sigma''} \sqrt{2N''+1} \sqrt{2J''+1} \right. \\ \left. \begin{pmatrix} J'' & S'' & N'' \\ \Omega'' & -\Sigma'' & -\Lambda'' \end{pmatrix} \begin{pmatrix} J' & 1 & J'' \\ \Omega' & q & \Omega'' \end{pmatrix} \langle T_q^1 \rangle \right] \sqrt{2J'+1} \begin{pmatrix} J' & 1 & J'' \\ -M'_J & p & M''_J \end{pmatrix}. \quad (3.54)$$

For the  $X^2\Sigma_g^+$  state of  $N_2^+$ ,  $\Lambda'' = 0$ . The Wigner-3j symbols then restrict  $\Omega'' = \Sigma''$ . The above equation simplifies to,

$$\frac{1}{\sqrt{2}} \left[ \langle n', \Lambda'; v'; \Omega', J', M'_J; S', \Sigma' | \pm (-1)^{(J'-S')} \right. \\ \left. \langle n', -\Lambda'; v'; -\Omega', J', M'_J; S', -\Sigma' | \right] T_p^1[\boldsymbol{\mu}^{(s)}] |n'', \Lambda''; v''; N'', \Lambda'', S'', J'', M''_J\rangle \\ = \frac{\delta_{S', S''}}{\sqrt{2}} (-1)^{(N''-S''+M'_J)} \sqrt{2N''+1} \sqrt{2J''+1} \sum_{\Sigma'', q} (-1)^{(\Sigma'')} \begin{pmatrix} J'' & S'' & N'' \\ \Sigma'' & -\Sigma'' & 0 \end{pmatrix} \\ \left[ (-1)^{(-\Omega')} \delta_{\Sigma' \Sigma''} \begin{pmatrix} J' & 1 & J'' \\ -\Omega' & q & \Sigma'' \end{pmatrix} \pm (-1)^{(\Omega'+J'-S')} \delta_{-\Sigma' \Sigma''} \begin{pmatrix} J' & 1 & J'' \\ \Omega' & q & \Sigma'' \end{pmatrix} \right] \\ \langle T_q^1 \rangle \sqrt{2J'+1} \begin{pmatrix} J' & 1 & J'' \\ -M'_J & p & M''_J \end{pmatrix}. \quad (3.55)$$

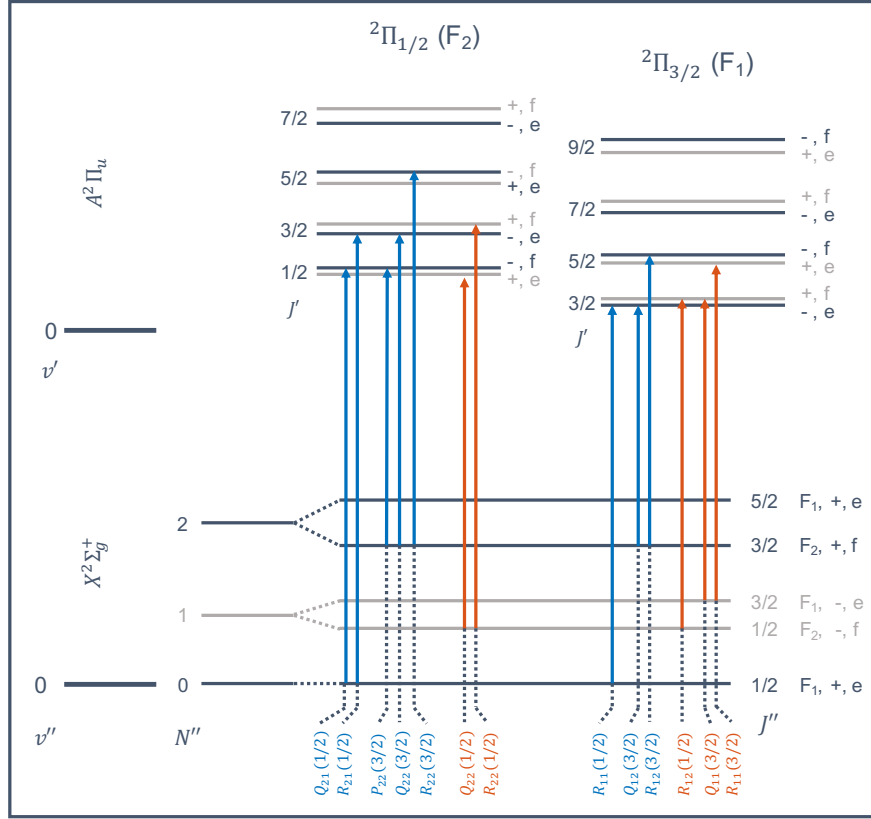


**Figure 3.3** Transition between the  $X^2\Sigma_g^+$  and  $A^2\Pi_u$  electronic states of  $N_2^+$ . Transitions (blue) from the ground ( $N'' = 0, J'' = 1/2$ ) and the first excited ( $N'' = 2, J'' = 3/2$ ) rotational levels for *ortho*- $N_2^+$  (black) are shown. Also depicted are the transitions (orange) from the ground ( $N'' = 1, J'' = 1/2, 3/2$ ) states for *para*- $N_2^+$  (grey).

The selection rules can be identified by the Wigner-3j symbols. From the Wigner-3j symbols inside the square brackets,  $\Delta J = 0, \pm 1$  (3.21c). For the  $A^2\Pi_u$  state of  $N_2^+$   $|\Omega'| = 1/2, 3/2$ .  $|\Omega''| = 1/2$  for the  $X^2\Sigma_g^+$  state of  $N_2^+$ . Thus the Wigner-3j symbol inside the square brackets give the selection rules for  $q$  as  $q = \pm 1$ . Such transitions are labelled as *perpendicular* transitions in literature [61, 67]. Additionally, although not directly apparent, it can be numerically verified that for  $N'' = \text{even}$  states (which have + parity), only the negative parity  $A^2\Pi_u$  states (states corresponding to - sign in the square brackets) contribute to the transition-dipole matrix element. The converse is true for  $N'' = \text{odd}$  states.

Fig. 3.3, shows possible transitions from the  $X^2\Sigma_g^+$  electronic ground state to the  $A^2\Pi_u$  first excited state of  $N_2^+$ , starting at the two lowest rotational levels ( $N = 0, J = 1/2$  and

$N = 2, J = 3/2$ ).

Since the square of the transition-dipole matrix element is often encountered while examining light-matter, it is useful to look at the square of (3.55),

$$\begin{aligned} \left| \langle \tilde{T}_p^1 \rangle \right|^2 &= \frac{\delta_{S', S''}{}^2}{2} (2N'' + 1)(2J'' + 1) \left( \sum_{\Sigma'', q} (-1)^{(\Sigma'')} \begin{pmatrix} J'' & S'' & N'' \\ \Sigma'' & -\Sigma'' & 0 \end{pmatrix} \right. \\ &\quad \left. \left[ (-1)^{(-\Omega')} \delta_{\Sigma' \Sigma''} \begin{pmatrix} J' & 1 & J'' \\ -\Omega' & q & \Sigma'' \end{pmatrix} \pm (-1)^{(\Omega' + J' - S')} \delta_{-\Sigma' \Sigma''} \begin{pmatrix} J' & 1 & J'' \\ \Omega' & q & \Sigma'' \end{pmatrix} \right] \right)^2 \\ &= \langle T_q^1 \rangle^2 \left| \sqrt{2J' + 1} \begin{pmatrix} J' & 1 & J'' \\ -M'_J & p & M''_J \end{pmatrix} \right|^2, \end{aligned} \quad (3.56)$$

where,

$$\begin{aligned} \langle \tilde{T}_p^1 \rangle &= \frac{1}{\sqrt{2}} \left[ \langle n', \Lambda'; v'; \Omega', J', M'_J; S', \Sigma' | \pm (-1)^{(J' - S')} \right. \\ &\quad \left. \langle n', -\Lambda'; v'; -\Omega', J', M'_J; S', -\Sigma' | \right] T_p^1[\boldsymbol{\mu}^{(s)}] | n'', \Lambda''; v''; N'', \Lambda'', S'', J'', M''_J \rangle, \end{aligned} \quad (3.57)$$

and [118],

$$\langle T_q^1 \rangle = \sqrt{\frac{3\varepsilon_0 \hbar c^3}{2\omega_0^3}} A_{\text{vibronic}}. \quad (3.58)$$

Substituting  $\langle T_q^1 \rangle^2$  from (3.58),

$$\left| \langle \tilde{T}_p^1 \rangle \right|^2 = \frac{3\varepsilon_0 \hbar c^3}{2\omega_0^3} S A_{\text{vibronic}} \left| \sqrt{2J' + 1} \begin{pmatrix} J' & 1 & J'' \\ -M'_J & p & M''_J \end{pmatrix} \right|^2, \quad (3.59)$$

where,

$$\begin{aligned} S &= \frac{\delta_{S', S''}{}^2}{2} (2N'' + 1)(2J'' + 1) \left( \sum_{\Sigma'', q} (-1)^{(\Sigma'')} \begin{pmatrix} J'' & S'' & N'' \\ \Sigma'' & -\Sigma'' & 0 \end{pmatrix} \right. \\ &\quad \left. \left[ (-1)^{(-\Omega')} \delta_{\Sigma' \Sigma''} \begin{pmatrix} J' & 1 & J'' \\ -\Omega' & q & \Sigma'' \end{pmatrix} \pm (-1)^{(\Omega' + J' - S')} \delta_{-\Sigma' \Sigma''} \begin{pmatrix} J' & 1 & J'' \\ \Omega' & q & \Sigma'' \end{pmatrix} \right] \right)^2, \end{aligned} \quad (3.60)$$

is the Hönl-London factor for Hund's case (b) to Hund's case (a),  $A^2\Pi_u \leftrightarrow X^2\Sigma_g^+$  rotational transitions taking into consideration the spin-orbit (fine-structure) coupling. Thus the square of the transition-dipole matrix element (3.59) is cast in the familiar form - a product of a numeric factor, the Hönl-London factor, the vibronic Einstein- $A$  coefficient and a polarization dependent term. A comparison between Hönl-London factors for a few transitions in  $N_2^+$ , calculated based on the above formulae with literature values is given in table 3.1.

### 3.2.4 Hund's case (b) to Hund's case (a) transitions including fine-structure and hyperfine-structure coupling

Building on the sections above, the hyperfine coupling can be included in order to examine its effects on transitions. Considering the hyperfine coupling, the Hund's case ( $a_\beta$ ) basis state can be written as  $|n, \Lambda; v; S, \Sigma; \Omega, J, I, F, M_F\rangle$  following (2.1.2). The Hund's case ( $b_\beta$ ) basis state can be written as  $|n, \Lambda; v; N, \Lambda, S, J, I, F, M_F\rangle$ .

Both basis states can be expanded in the uncoupled basis using Clebsch-Gordon coefficients [61, 62]. The Hund's case ( $a_\beta$ ) basis may be expanded as,

$$\begin{aligned} & |n, \Lambda; v; S, \Sigma; \Omega, J, I, F, M_F\rangle \\ &= \sum_{M_J, M_I} (-1)^{(J-I+M_F)} \sqrt{2F+1} \begin{pmatrix} J & I & F \\ M_J & M_I & -M_F \end{pmatrix} |n, \Lambda; v; S, \Sigma; \Omega, J, M_J\rangle |I, M_I\rangle. \end{aligned} \quad (3.61)$$

The Hund's case ( $b_\beta$ ) basis may be expanded as,

$$\begin{aligned} & |n, \Lambda; v; N, \Lambda, S, J, I, F, M_F\rangle \\ &= \sum_{M_I, M_J} (-1)^{(J-I+M_F)} \sqrt{2F+1} \begin{pmatrix} J & I & F \\ M_J & M_I & -M_F \end{pmatrix} |n, \Lambda; v; N, \Lambda, S, J, M_J\rangle |I, M_I\rangle. \end{aligned} \quad (3.62)$$

The dipole-matrix element can be calculated by evaluating

$$\langle n', \Lambda'; v'; S', \Sigma'; \Omega', J', I', F', M'_F | \boldsymbol{\mu}^{(s)} | n'', \Lambda''; v''; N'', \Lambda'', S'', J'', I'', F'', M''_F \rangle. \quad (3.63)$$

Using (3.61) and (3.62), the  $p^{th}$  component of the dipole-matrix element in terms of spherical tensors can be written as (3.9),

$$\begin{aligned}
& \langle n', \Lambda'; v'; S', \Sigma'; \Omega', J', I', F', M'_F | T_p^1[\boldsymbol{\mu}^{(s)}] | n'', \Lambda''; v''; N'', \Lambda'', S'', J'', I'', F'', M''_F \rangle \\
&= \sum_{M'_I, M'_J} \sum_{M''_I, M''_J} (-1)^{(J'-I'+M'_F+J''-I''+M''_F)} \sqrt{2F'+1} \sqrt{2F''+1} \\
&\quad \begin{pmatrix} J' & I' & F' \\ M'_J & M'_I & -M'_F \end{pmatrix} \begin{pmatrix} J'' & I'' & F'' \\ M''_J & M''_I & -M''_F \end{pmatrix} \langle I', M'_I | I'', M''_I \rangle \\
&\quad \langle n', \Lambda'; v'; S', \Sigma'; \Omega', J', M'_J | T_p^1[\boldsymbol{\mu}^{(s)}] | n'', \Lambda''; v''; N'', \Lambda'', S'', J'', M''_J \rangle, \quad (3.64)
\end{aligned}$$

where the transition-dipole matrix elements acts only on the rovibronic parts. The nuclear-spin part can be separately evaluated as,

$$\langle I', M'_I | I'', M''_I \rangle = \delta_{I'I''} \delta_{M'_I M''_I}. \quad (3.65)$$

Equation (3.64) thus simplifies as,

$$\begin{aligned}
& \langle n', \Lambda'; v'; S', \Sigma'; \Omega', J', I', F', M'_F | T_p^1[\boldsymbol{\mu}^{(s)}] | n'', \Lambda''; v''; N'', \Lambda'', S'', J'', I'', F'', M''_F \rangle \\
&= \sum_{M'_I, M'_J, M''_I, M''_J} \delta_{I'I''} \delta_{M'_I M''_I} (-1)^{(J'-2I'+M'_F+J''+M''_F)} \sqrt{2F'+1} \sqrt{2F''+1} \begin{pmatrix} J' & I' & F' \\ M'_J & M'_I & -M'_F \end{pmatrix} \\
&\quad \begin{pmatrix} J'' & I'' & F'' \\ M''_J & M''_I & -M''_F \end{pmatrix} \langle n', \Lambda'; v'; S', \Sigma'; \Omega', J', M'_J | T_p^1[\boldsymbol{\mu}^{(s)}] | n'', \Lambda''; v''; N'', \Lambda'', S'', J'', M''_J \rangle. \quad (3.66)
\end{aligned}$$

The expectation value of the  $p^{th}$  component of the transition-dipole matrix element in be-

tween the rovibronic states above has been evaluated in the previous section. From (3.51),

$$\begin{aligned}
& \langle n', \Lambda'; v'; \Omega', J', M'_J; S', \Sigma' | T_p^1[\boldsymbol{\mu}^{(s)}] | n'', \Lambda''; v''; N'', \Lambda'', S'', J'', M''_J \rangle \\
&= \sum_{\Sigma'', \Omega'', q} (-1)^{(N'' - S'' + \Omega'' + M'_J - \Omega')} \delta_{S', S''} \delta_{\Sigma' \Sigma''} \sqrt{2N'' + 1} \sqrt{2J' + 1} \sqrt{2J'' + 1} \\
& \quad \begin{pmatrix} J'' & S'' & N'' \\ \Omega'' & -\Sigma'' & -\Lambda'' \end{pmatrix} \begin{pmatrix} J' & 1 & J'' \\ -M'_J & p & M''_J \end{pmatrix} \begin{pmatrix} J' & 1 & J'' \\ -\Omega' & q & \Omega'' \end{pmatrix} \langle T_q^1 \rangle. \quad (3.67)
\end{aligned}$$

Substituting in (3.66),

$$\begin{aligned}
& \langle n', \Lambda'; v'; S', \Sigma'; \Omega', J', I', F', M'_F | T_p^1[\boldsymbol{\mu}^{(s)}] | n'', \Lambda''; v''; N'', \Lambda'', S'', J'', I'', F'', M''_F \rangle \\
&= \sum_{M'_I, M'_J, M''_J} \sum_{\Sigma'', \Omega'', q} \delta_{I' I''} \delta_{M'_I M''_I} (-1)^{(J' - 2I' + M'_F + J'' + M''_F)} (-1)^{(N'' - S'' + \Omega'' + M'_J - \Omega')} \delta_{S', S''} \delta_{\Sigma' \Sigma''} \\
& \quad \sqrt{2F' + 1} \sqrt{2F'' + 1} \sqrt{2N'' + 1} \sqrt{2J' + 1} \sqrt{2J'' + 1} \begin{pmatrix} J' & I' & F' \\ M'_J & M'_I & -M''_F \end{pmatrix} \\
& \quad \begin{pmatrix} J'' & I' & F'' \\ M''_J & M'_I & -M''_F \end{pmatrix} \begin{pmatrix} J'' & S'' & N'' \\ \Omega'' & -\Sigma'' & -\Lambda'' \end{pmatrix} \begin{pmatrix} J' & 1 & J'' \\ -\Omega' & q & \Omega'' \end{pmatrix} \begin{pmatrix} J' & 1 & J'' \\ -M'_J & p & M''_J \end{pmatrix} \langle T_q^1 \rangle, \quad (3.68)
\end{aligned}$$

where,

$$\langle T_q^1 \rangle = \langle n', \Lambda'; v' | T_q^1[\boldsymbol{\mu}^{(m)}] | n'', \Lambda''; v'' \rangle. \quad (3.69)$$

From relations of Wigner-6j symbols [62],

$$\begin{aligned}
\left\{ \begin{matrix} j_1 & j_2 & j_3 \\ j_4 & j_5 & j_6 \end{matrix} \right\} \begin{pmatrix} j_5 & j_1 & j_6 \\ -m_5 & m_1 & m_6 \end{pmatrix} &= \sum_{m_2, m_3, m_4} (-1)^{(j_1 + j_2 - j_3 + j_4 + j_5 + j_6 - m_1 - m_4)} \begin{pmatrix} j_1 & j_2 & j_3 \\ m_1 & m_2 & -m_3 \end{pmatrix} \\
& \quad \begin{pmatrix} j_4 & j_5 & j_3 \\ m_4 & -m_5 & m_3 \end{pmatrix} \begin{pmatrix} j_2 & j_4 & j_6 \\ m_2 & m_4 & -m_6 \end{pmatrix}, \quad (3.70a)
\end{aligned}$$

invariance under permutation of any two columns of the Wigner-6j symbol

$$\left\{ \begin{matrix} j_1 & j_2 & j_3 \\ j_4 & j_5 & j_6 \end{matrix} \right\} = \left\{ \begin{matrix} j_2 & j_1 & j_3 \\ j_5 & j_4 & j_6 \end{matrix} \right\} = \dots, \quad (3.70b)$$

and invariance under exchange of upper and lower arguments of any two columns,

$$\begin{Bmatrix} j_1 & j_2 & j_3 \\ j_4 & j_5 & j_6 \end{Bmatrix} = \begin{Bmatrix} j_4 & j_5 & j_3 \\ j_1 & j_2 & j_6 \end{Bmatrix} = \dots, \quad (3.70c)$$

we can get the relation,

$$\begin{Bmatrix} J' & F' & I' \\ F'' & J'' & 1 \end{Bmatrix} \begin{pmatrix} F' & 1 & F'' \\ -M'_F & p & M''_F \end{pmatrix} = \sum_{M'_I, M'_J, M''_J} (-1)^{(F''+J''+I'+J'+F'+1-M''_F-M'_J)} \\ \begin{pmatrix} J' & 1 & J'' \\ -M'_J & p & M''_J \end{pmatrix} \begin{pmatrix} J' & I' & F' \\ M'_J & M'_I & -M'_F \end{pmatrix} \begin{pmatrix} J'' & I' & F'' \\ M''_J & M'_I & -M''_F \end{pmatrix}. \quad (3.71)$$

Equation (3.68) can thus be simplified as,

$$\begin{aligned} & \langle n', \Lambda'; v'; S', \Sigma'; \Omega', J', I', F', M'_F | T_p^1[\boldsymbol{\mu}^{(s)}] | n'', \Lambda''; v''; N'', \Lambda'', S'', J'', I'', F'', M''_F \rangle \\ &= \sum_{\Sigma'', \Omega'', q} \delta_{I'I''} (-1)^{(M'_F-F''-I'-F'-1)} (-1)^{(N''-S''+\Omega''-\Omega')} \\ & \quad \delta_{S', S''} \delta_{\Sigma', \Sigma''} \sqrt{2F'+1} \sqrt{2F''+1} \sqrt{2N''+1} \sqrt{2J'+1} \sqrt{2J''+1} \\ & \quad \begin{pmatrix} J'' & S'' & N'' \\ \Omega'' & -\Sigma'' & -\Lambda'' \end{pmatrix} \begin{pmatrix} J' & 1 & J'' \\ -\Omega' & q & \Omega'' \end{pmatrix} \begin{Bmatrix} J' & F' & I' \\ F'' & J'' & 1 \end{Bmatrix} \begin{pmatrix} F' & 1 & F'' \\ -M'_F & p & M''_F \end{pmatrix} \langle T_q^1 \rangle. \quad (3.72) \end{aligned}$$

As dipole-allowed transitions occur between states of well defined parity, the Hund's case (a) state must be expressed as a proper parity-defined combination as in (3.53),

$$\begin{aligned} |n', \Lambda'; v'; S', \Sigma'; \Omega', J', I', F', M'_F; \pm\rangle &= \frac{1}{\sqrt{2}} \left\{ |n', \Lambda'; v'; S', \Sigma'; \Omega', J', I', F', M'_F\rangle \right. \\ & \quad \left. \pm (-1)^{(J'-S')} |n', -\Lambda'; v'; S', -\Sigma'; -\Omega', J', I', F', M'_F\rangle \right\}. \quad (3.73) \end{aligned}$$

The  $p^{\text{th}}$  component of the transition-dipole matrix element then is,

$$\begin{aligned}
& \frac{1}{\sqrt{2}} \left\{ |n', \Lambda'; v'; S', \Sigma'; \Omega', J', I', F', M'_F\rangle \pm (-1)^{(J'-S')} \right. \\
& \left. |n', -\Lambda'; v'; S', -\Sigma'; -\Omega', J', I', F', M'_F\rangle \right\} T_p^1[\boldsymbol{\mu}^{(s)}] |n'', \Lambda''; v''; N'', \Lambda'', S'', J'', I'', F'', M''_F\rangle \\
& = \frac{\delta_{I'I''} \delta_{S',S''}}{\sqrt{2}} (-1)^{(M'_F-F''-I'-F'-1)} \sqrt{2F''+1} \sqrt{2N''+1} \sqrt{2J'+1} \sqrt{2J''+1} \\
& \sum_{\Sigma'', \Omega'', q} \left[ (-1)^{(N''-S''+\Omega''-\Omega')} \delta_{\Sigma'\Sigma''} \begin{pmatrix} J'' & S'' & N'' \\ \Omega'' & -\Sigma'' & -\Lambda'' \end{pmatrix} \begin{pmatrix} J' & 1 & J'' \\ -\Omega' & q & \Omega'' \end{pmatrix} \langle T_q^1 \rangle \right. \\
& \left. \pm (-1)^{(N''-S''+\Omega''+\Omega'+J'-S')} \delta_{-\Sigma'\Sigma''} \begin{pmatrix} J'' & S'' & N'' \\ \Omega'' & -\Sigma'' & -\Lambda'' \end{pmatrix} \begin{pmatrix} J' & 1 & J'' \\ \Omega' & q & \Omega'' \end{pmatrix} \langle T_q^1 \rangle \right] \\
& \left\{ \begin{matrix} J' & F' & I' \\ F'' & J'' & 1 \end{matrix} \right\} \sqrt{2F'+1} \begin{pmatrix} F' & 1 & F'' \\ -M'_F & p & M''_F \end{pmatrix}. \quad (3.74)
\end{aligned}$$

For the  $X^2\Sigma_g^+$  state of  $N_2^+$ ,  $\Lambda'' = 0$ . The Wigner-3j symbols then restrict  $\Omega'' = \Sigma''$ . The above equation (3.74) thus simplifies as,

$$\begin{aligned}
& \frac{1}{\sqrt{2}} \left\{ |n', \Lambda'; v'; S', \Sigma'; \Omega', J', I', F', M'_F\rangle \pm (-1)^{(J'-S')} \right. \\
& \left. |n', -\Lambda'; v'; S', -\Sigma'; -\Omega', J', I', F', M'_F\rangle \right\} T_p^1[\boldsymbol{\mu}^{(s)}] |n'', \Lambda''; v''; N'', \Lambda'', S'', J'', I'', F'', M''_F\rangle \\
& = \frac{\delta_{I'I''} \delta_{S',S''}}{\sqrt{2}} (-1)^{(M'_F-F''-I'-F'-1)} (-1)^{(N''-S'')} \sqrt{2F''+1} \sqrt{2N''+1} \\
& \sqrt{2J'+1} \sqrt{2J''+1} \sum_{\Sigma'', q} (-1)^{(\Sigma'')} \begin{pmatrix} J'' & S'' & N'' \\ \Sigma'' & -\Sigma'' & 0 \end{pmatrix} \left[ (-1)^{(-\Omega')} \delta_{\Sigma'\Sigma''} \begin{pmatrix} J' & 1 & J'' \\ -\Omega' & q & \Sigma'' \end{pmatrix} \right. \\
& \left. \pm (-1)^{(\Omega'+J'-S')} \delta_{-\Sigma'\Sigma''} \begin{pmatrix} J' & 1 & J'' \\ \Omega' & q & \Sigma'' \end{pmatrix} \right] \langle T_q^1 \rangle \left\{ \begin{matrix} J' & F' & I' \\ F'' & J'' & 1 \end{matrix} \right\} \sqrt{2F'+1} \begin{pmatrix} F' & 1 & F'' \\ -M'_F & p & M''_F \end{pmatrix}. \quad (3.75)
\end{aligned}$$

The selection rules can be identified by the Wigner-3j symbols. Similar to the previous section,  $\Delta J = 0, \pm 1$  and  $q = \pm 1$ . Such transitions are known as *perpendicular* transitions.

The nuclear spin, projection of the nuclear-spin on the space-fixed axis and the electronic spin are conserved (given by the Dirac-delta functions). The polarization of the incident radiation defines  $p$  and gives the selection rule  $M'_F - M''_F = \Delta M_F = p$ . The last Wigner-3j symbol gives the additional selection rule  $F' - F'' = \Delta F = 0, \pm 1$ . Numerically, it can also be checked that for  $N'' = \text{even}$  states (which have + parity), only negative parity  $A^2\Pi_u$  states (corresponding to  $-$  sign in the square brackets) contribute to the transition-dipole matrix element. The converse is true for  $N'' = \text{odd}$  states.

As in the previous sections, the square of the transition-dipole matrix element can be calculated as,

$$\begin{aligned} |\langle \tilde{T}_p^1 \rangle|^2 &= \frac{\delta_{I'I''}{}^2 \delta_{S',S''}{}^2}{2} (2F'' + 1)(2N'' + 1)(2J' + 1)(2J'' + 1) \\ &\quad \left( \sum_{\Sigma'', q} (-1)^{(\Sigma'')} \begin{pmatrix} J'' & S'' & N'' \\ \Sigma'' & -\Sigma'' & 0 \end{pmatrix} \left[ (-1)^{(-\Omega')} \delta_{\Sigma'\Sigma''} \begin{pmatrix} J' & 1 & J'' \\ -\Omega' & q & \Sigma'' \end{pmatrix} \right. \right. \\ &\quad \left. \left. \pm (-1)^{(\Omega'+J'-S')} \delta_{-\Sigma'\Sigma''} \begin{pmatrix} J' & 1 & J'' \\ \Omega' & q & \Sigma'' \end{pmatrix} \right] \begin{pmatrix} J' & F' & I' \\ F'' & J'' & 1 \end{pmatrix} \right)^2 \\ &\quad \langle T_q^1 \rangle^2 \left| \sqrt{2F'+1} \begin{pmatrix} F' & 1 & F'' \\ -M'_F & p & M''_F \end{pmatrix} \right|^2, \quad (3.76) \end{aligned}$$

where,

$$\begin{aligned} \langle \tilde{T}_p^1 \rangle &= \frac{1}{\sqrt{2}} \left[ \langle n', \Lambda'; v'; \Omega', J', M'_J; S', \Sigma' | \pm (-1)^{(J'-S')} \right. \\ &\quad \left. \langle n', -\Lambda'; v'; -\Omega', J', M'_J; S', -\Sigma' | T_p^1[\boldsymbol{\mu}^{(s)}] | n'', \Lambda''; v''; N'', \Lambda'', S'', J'', M''_J \rangle \right]. \quad (3.77) \end{aligned}$$

Substituting  $\langle T_q^1 \rangle^2$  from (3.58),

$$|\langle \tilde{T}_p^1 \rangle|^2 = \frac{3\varepsilon_0 h c^3}{2\omega_0^3} S A_{\text{vibronic}} \left| \sqrt{2F'+1} \begin{pmatrix} F' & 1 & F'' \\ -M'_F & p & M''_F \end{pmatrix} \right|^2, \quad (3.78)$$

where,

$$S = \frac{\delta_{I'I''}{}^2 \delta_{S',S''}{}^2}{2} (2F'' + 1)(2N'' + 1)(2J' + 1)(2J'' + 1) \left\{ \begin{matrix} J' & F' & I' \\ F'' & J'' & 1 \end{matrix} \right\}^2$$

$$\left( \sum_{\Sigma'', q} (-1)^{(\Sigma'')} \begin{pmatrix} J'' & S'' & N'' \\ \Sigma'' & -\Sigma'' & 0 \end{pmatrix} \left[ (-1)^{(-\Omega')} \delta_{\Sigma' \Sigma''} \begin{pmatrix} J' & 1 & J'' \\ -\Omega' & q & \Sigma'' \end{pmatrix} \right. \right.$$

$$\left. \left. \pm (-1)^{(\Omega' + J' - S')} \delta_{-\Sigma' \Sigma''} \begin{pmatrix} J' & 1 & J'' \\ \Omega' & q & \Sigma'' \end{pmatrix} \right] \right)^2, \quad (3.79)$$

is the Hönl-London factor for Hund's case (b) to Hund's case (a),  $A^2\Pi_u \leftrightarrow X^2\Sigma_g^+$  rotational transitions taking into consideration the spin-orbit (fine-structure) and the hyperfine coupling. A comparison between Hönl-London factors for a few transitions in  $N_2^+$ , calculated based on the above formulae with literature values for the  $N_2^+$   $I = 0$  molecule is given in table 3.1. Thus the square of the transition-dipole matrix element (3.78) is cast in the familiar form - a product of a numeric factor, the Hönl-London factor, the vibronic Einstein- $A$  coefficient and a polarization dependent term.

### 3.2.5 Hund's case (b) to Hund's case (a) transitions including mixing of states

As discussed in section 2.3, different terms of the Hamiltonian can lead to a mixing between states. In such cases, a given Hund's case (b) or Hund's case (a) is no longer a pure state. Thus, in addition to considering states with proper parities, the transition-dipole matrices must be evaluated between all possible mixed states. For example, for the mixed states  $|\tilde{e}\rangle$  and  $|\tilde{g}\rangle$  given by,

$$|\tilde{e}\rangle = \sum_{\Omega', \Lambda', \Sigma'} \sum_{J'=|J'-1|}^{J'=J'+1} c'_{\Omega', \tilde{\Lambda}', \tilde{\Sigma}', \tilde{J}', \Omega', \Lambda', \Sigma', J'} \frac{1}{\sqrt{2}} \left\{ |n', \Lambda'; v'; S', \Sigma'; \Omega', J', I', F', M'_F\rangle \right.$$

$$\left. \pm (-1)^{(J'-S')} |n', -\Lambda'; v'; S', -\Sigma'; -\Omega', J', I', F', M'_F\rangle \right\}, \quad (3.80)$$

Transition	Literature	Fine-structure	Hyperfine-structure	Mixed state
	value	theory	theory	theory
$R_{11}(1/2)$	0.2606	0.2500	0.2500	0.2606
$Q_{12}(3/2)$	0.1827	0.2000	0.2000	0.1827
$R_{12}(3/2)$	0.1823	0.2000	0.2000	0.1824
$Q_{21}(1/2)$	0.3333	0.3333	0.3333	0.3333
$R_{21}(1/2)$	0.0727	0.0833	0.0833	0.0727
$P_{22}(3/2)$	0.1667	0.1667	0.1667	0.1667
$Q_{22}(3/2)$	0.2839	0.2667	0.2667	0.2839
$R_{22}(3/2)$	0.1176	0.0100	0.1000	0.1176

**Table 3.1 Comparison between Hönl-London factors.** Hönl-London factors for the first few transitions between the  $X^2\Sigma_g^+(v=0) \leftrightarrow A^2\Pi_u(v=2)$  state for the  $N_2^+$   $I=0$  molecule are listed. Nuclear-spin free literature values for the different transitions were calculated according to Ref. [120]. Values in the column labelled “Fine-structure theory” were calculated according to the equation (3.43) and those in the column “Hyperfine-structure theory” were calculated according to the equation (3.79). The “Mixed state theory” is discussed in section (3.2.5) and the Hönl-London factors were evaluated according to equation (3.84).

and,

$$|\tilde{g}\rangle = \sum_{J''=|N''-S''|}^{J''=N''+S''} c''_{\tilde{J}'', J''} \left| n'', \Lambda'' = 0; v''; N'', \Lambda'' = 0, S'', \tilde{J}'', I'', F'', M_F'' \right\rangle, \quad (3.81)$$

the transition-dipole matrix can be evaluated as,

$$\begin{aligned} \langle \tilde{e} | \boldsymbol{\mu}^{(s)} | \tilde{g} \rangle &= \sum_{\Omega', \Lambda', \Sigma'} \sum_{J'=|J'-1|}^{J'=J'+1} \sum_{J''=|N''-S''|}^{J''=N''+S''} c'_{\tilde{\Omega}', \tilde{\Lambda}', \tilde{\Sigma}', \tilde{J}', \Omega', \Lambda', \Sigma', J'} c''_{\tilde{J}'', J''} \\ &\frac{1}{\sqrt{2}} \left\{ \langle n', \Lambda'; v'; S', \Sigma'; \Omega', J', I', F', M_F' | \right. \\ &\quad \left. \pm (-1)^{(J'-S')} \langle n', -\Lambda'; v'; S', -\Sigma'; -\Omega', J', I', F', M_F' | \right\} \\ &\boldsymbol{\mu}^{(s)} \left| n'', \Lambda'' = 0; v''; N'', \Lambda'' = 0, S'', \tilde{J}'', I'', F'', M_F'' \right\rangle. \end{aligned} \quad (3.82)$$

Here, the tilde indicates the quantum numbers that are mixed.  $c'_{\tilde{\Omega}', \tilde{\Lambda}', \tilde{\Sigma}', \tilde{J}', \Omega', \Lambda', \Sigma', J'}$  and  $c''_{\tilde{J}'', J''}$  are the mixing coefficients obtained by diagonalizing the Hamiltonians of the states given in sections (2.3.1) and (2.3.2). The transition-dipole matrix element in the above equation

can be evaluated according to the equation (3.75). As before, the square of the transition-dipole matrix element can be separated into a numerical factor, the Hönl-London factor, the vibronic Einstein- $A$  coefficient and a polarization dependent term, i.e.,

$$\left| \langle \tilde{e} | \boldsymbol{\mu}^{(s)} | \tilde{g} \rangle \right|^2 = \frac{3\varepsilon_0 h c^3}{2\omega_0^3} S A_{\text{vibronic}} \left| \sqrt{2J'+1} \begin{pmatrix} J' & 1 & J'' \\ -M'_J & p & M''_J \end{pmatrix} \right|^2, \quad (3.83)$$

where,

$$S = \left\{ \sum_{J'=|J'-1|}^{J'=J'+1} \sum_{J''=|N''-S''|}^{J''=N''+S''} c'_{\tilde{\Omega}', \tilde{N}', \tilde{\Sigma}', \tilde{J}', \Omega', \Lambda', \Sigma', J'} c''_{\tilde{J}'', J''} \frac{\delta_{S', S''}}{\sqrt{2}} \sqrt{(2N''+1)} \sqrt{(2J''+1)} \left( \sum_{\Sigma'', q} (-1)^{(\Sigma'')} \begin{pmatrix} J'' & S'' & N'' \\ \Sigma'' & -\Sigma'' & 0 \end{pmatrix} \left[ (-1)^{(-\Omega')} \delta_{\Sigma' \Sigma''} \begin{pmatrix} J' & 1 & J'' \\ -\Omega' & q & \Sigma'' \end{pmatrix} \pm (-1)^{(\Omega'+J'-S')} \delta_{-\Sigma' \Sigma''} \begin{pmatrix} J' & 1 & J'' \\ \Omega' & q & \Sigma'' \end{pmatrix} \right] \right\}^2, \quad (3.84)$$

is the Hönl-London factor for Hund's case (b) to Hund's case (a),  $A^2\Pi_u \leftrightarrow X^2\Sigma_g^+$  rotational transitions taking into consideration the spin-orbit (fine-structure), the hyperfine-structure couplings and the effect of state mixing due to different terms of the Hamiltonians. Table 3.1 lists the spin-free Hönl-London factors from literature for the mixed  $I = 0$   $\text{N}_2^+$  molecule [120], and the calculated values following the theories developed here.

### 3.3 ac-Stark effect in $\text{N}_2^+$

Having discussed transitions between mixed Hund's case (b) and Hund's case (a) states in the previous section, dispersive interactions (the ac-Stark shift and the photon scattering rate) of the  $\text{N}_2^+$  molecule with non-resonant light can now be examined in detail. As stated earlier, such interactions are employed for the non-destructive state detection of  $\text{N}_2^+$  (see section 5.4).

The ac-Stark shift in a transition  $|\tilde{e}\rangle \leftrightarrow |\tilde{g}\rangle$  ( $\Delta E_{|\tilde{e}\rangle,|\tilde{g}\rangle}$ ) at a transition frequency  $\omega_0$ , due to a laser operating at a frequency  $\omega$  with a laser power  $P$ , beam-waist  $\omega_z$  and laser-polarization  $p$  in the space-fixed coordinates can be obtained from equations (3.2), (3.4), (3.78) as,

$$\Delta E_{|\tilde{e}\rangle,|\tilde{g}\rangle} = -\frac{3\pi\varepsilon_0 c^2}{2\omega_0^3} \left( \frac{1}{\omega_0 - \omega} + \frac{1}{\omega_0 + \omega} \right) S A_{\text{vibronic}} I(\mathbf{r}) (2F' + 1) \begin{pmatrix} F' & 1 & F'' \\ -M'_F & p & M''_F \end{pmatrix}^2, \quad (3.85)$$

where  $\varepsilon_0$  is the vacuum permittivity,  $c$  is the speed of light,  $I(\mathbf{r})$  is the intensity of the off-resonant laser given by,  $I(\mathbf{r}) = 2P / \pi\omega_z^2$  and  $S$  is the Hönl-London factor for the transition calculated in (3.84).  $A_{\text{vibronic}}$  is the Einstein- $A$  coefficient of the  $A^2\Pi_u(v' = 2) \leftrightarrow X^2\Sigma_g^+(v'' = 0)$  vibronic transition. The states  $|\tilde{e}\rangle$  and  $|\tilde{g}\rangle$  are the mixed rotational states in the  $A^2\Pi_u(v' = 2)$  and  $X^2\Sigma_g^+(v'' = 0)$  vibronic manifolds of  $\text{N}_2^+$  with a well-defined parity (equations 3.80 and 3.81).

The ac-Stark shift experienced by the  $\text{N}_2^+$  molecule in the  $|\tilde{g}\rangle$  state ( $\Delta E$ ) can then be given by the sum over all possible transitions from the  $|\tilde{g}\rangle$  state, i.e.,

$$\Delta E = \sum_{|\tilde{e}\rangle} \Delta E_{|\tilde{e}\rangle,|\tilde{g}\rangle}. \quad (3.86)$$

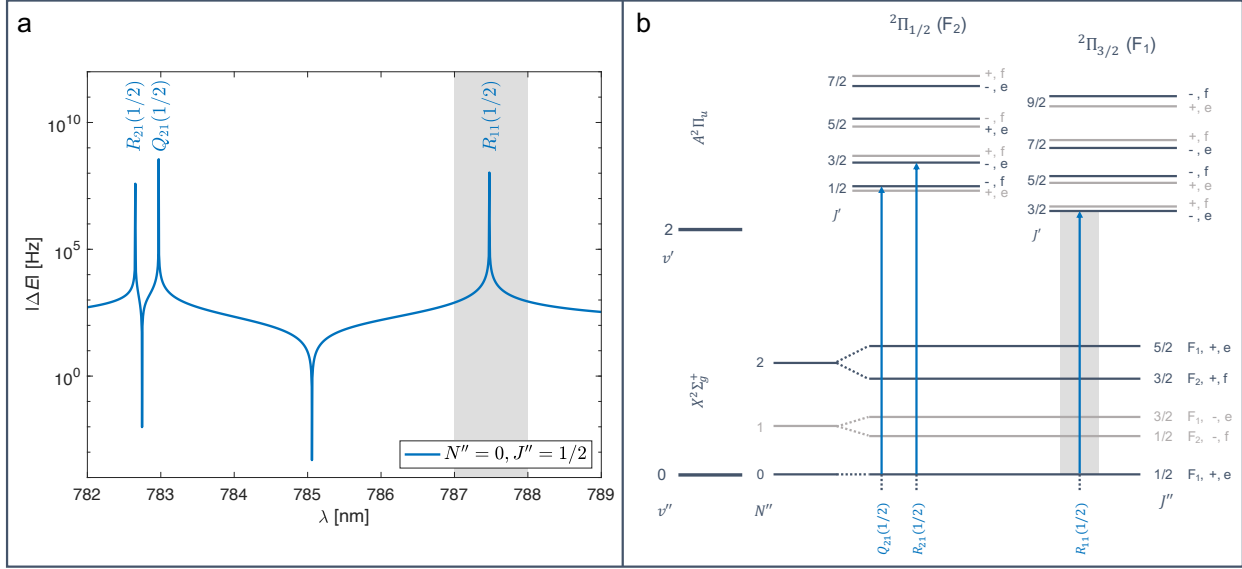
In order to calculate the total ac-Stark shift experienced by  $\text{N}_2^+$ , the contribution due to the ac-Stark shift experienced by the core electrons must also be taken into account,

$$\Delta E_{\text{Total}} = \Delta E + \Delta E_{\text{core}}. \quad (3.87)$$

The core polarizability for  $\text{N}_2^+$ ,  $\alpha^{\text{N}_2^+, \text{core}}$ , was estimated to be  $\approx 7.23$  a.u. ( $= 7.23 \times 1.648 \times 10^{-41}$  Fm<sup>2</sup>). [53], which corresponds to a negative ac-Stark shift of a few hundred Hz given by [56, 121],

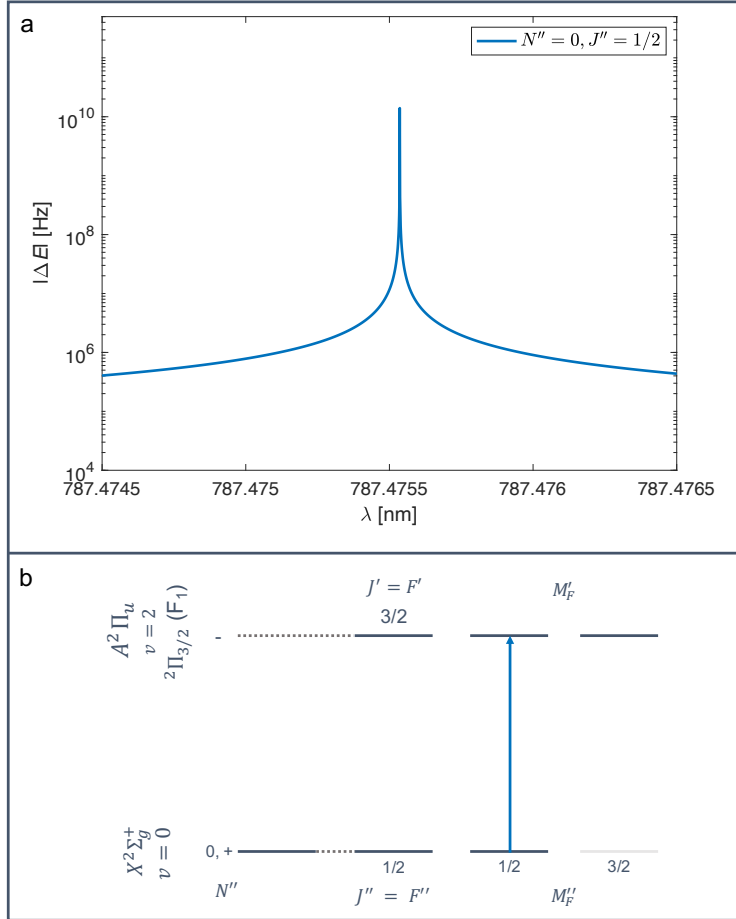
$$\Delta E_{\text{core}} = -\frac{3I}{2\varepsilon_0 hc} \alpha^{\text{N}_2^+, \text{core}}.$$

Fig. 3.4a shows the magnitude of the ac-Stark shift experienced by the  $I = 0$   $\text{N}_2^+$  ion in the ground rotational, vibrational and electronic state due to a laser between 782 nm and



**Figure 3.4** ac-Stark shift experienced by a  $\text{N}_2^+$  ion in the ground state.

789 nm. For the calculations here, the summation in equation (3.86) was carried over all possible excited states of the  $v' = 2$  vibrational manifold of the  $A^2\Pi_u$  electronic state. It was assumed that the laser was polarized such that  $p = 0$  (corresponding to the quantization axis in the experiment), had a power of 4 mW with a beam waist of 25  $\mu\text{m}$ . Additionally, the core contributions were ignored here (inclusion of which would result in a constant vertical offset). Three peaks, corresponding to the three possible  $R_{21}(1/2)$ ,  $Q_{21}(1/2)$  and  $R_{11}(1/2)$  transitions from the ground state of  $\text{N}_2^+$  can be observed. Fig. 3.4b depict the three transitions from the ground state of  $\text{N}_2^+$ . The parity-selection rules and the selection rules set by the transition-dipole matrix forbid other transitions. Intuitively, since the ac-Stark shift varies inversely with the detuning (see equation (3.85)), the magnitude of the ac-Stark shift increases as the off-resonant light approaches a transition. In the regions between the  $R_{21}(1/2) - Q_{21}(1/2)$  and  $Q_{21}(1/2) - R_{11}(1/2)$  transitions in fig. 3.4a, two dips in the magnitude of the ac-Stark shift can be observed. This is because the ac-Stark shift changes sign as the off-resonant radiation is tuned across a transition. Thus for a  $\text{N}_2^+$  in the ground state and a laser at a wavelength  $\lambda \approx 785$  nm, the ac-Stark shift experienced by the molecule due to the  $Q_{21}(1/2)$  transition is positive while the ac-Stark shift due to the  $R_{11}(1/2)$  transition is negative. The



**Figure 3.5** The  $R_{11}(1/2)$  transition in  $\text{N}_2^+$   $I = 0$ . The Zeeman level in grey does not exist.

resultant magnitude of the ac-Stark shift is small and appears as a dip in fig. 3.4a.

Of the three possible transitions, the  $R_{11}(1/2)$  transition was of importance in this thesis for the determination of the state of the  $\text{N}_2^+$  using quantum-logic spectroscopy. Fig. 3.5a shows the magnitude of the ac-Stark shift for the  $R_{11}(1/2)$  transition. The relevant energy levels for the  $I = 0$  molecule is shown in Fig. 3.5b. In the absence of nuclear spin,  $J = F$  and for the case of the laser polarization  $p = 0$  being considered here, only  $\Delta M_F = 0$  transition is possible restricted by the Wigner-3j symbols in the transition-dipole matrix element. Since the Zeeman interaction has not been included here, the hyperfine-Zeeman states are degenerate.

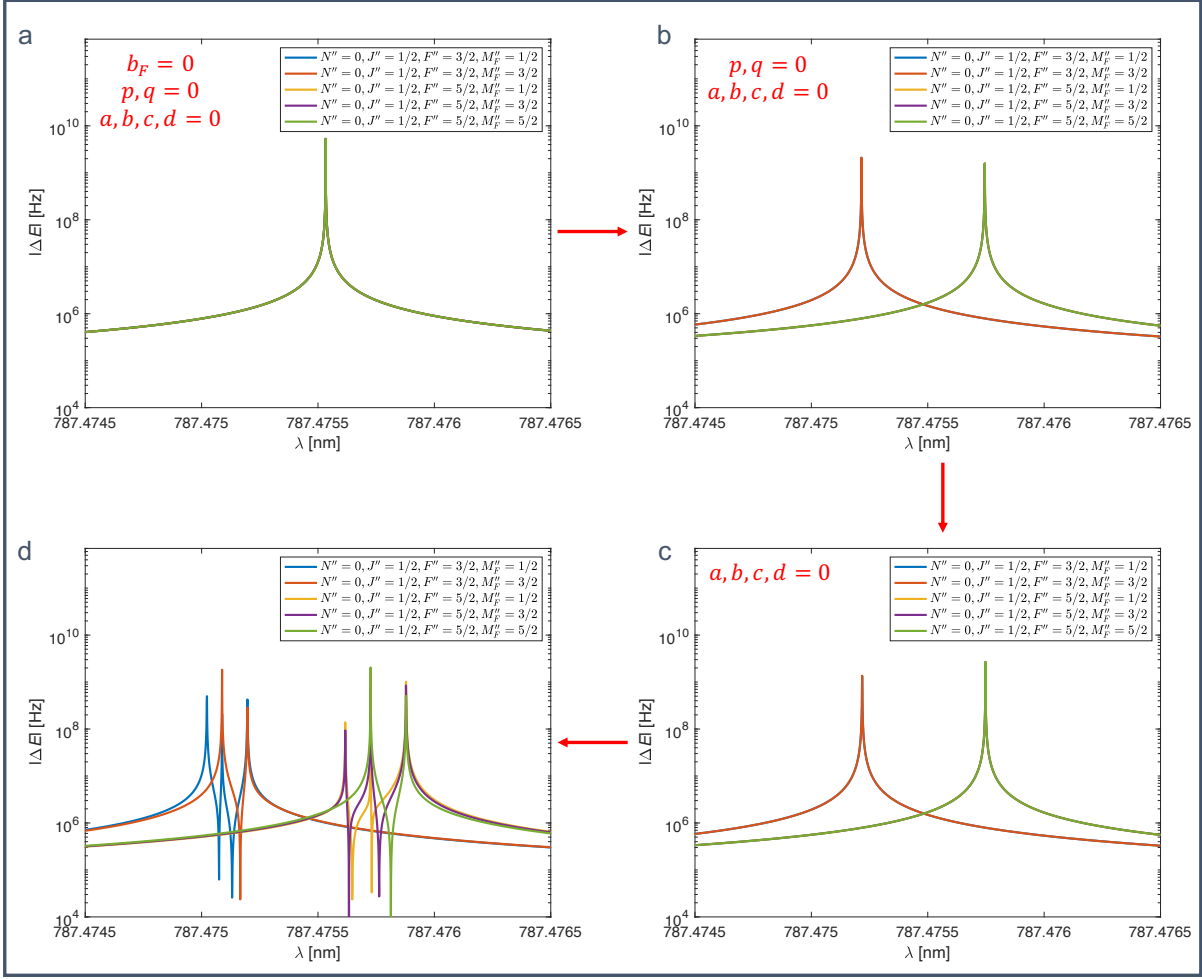
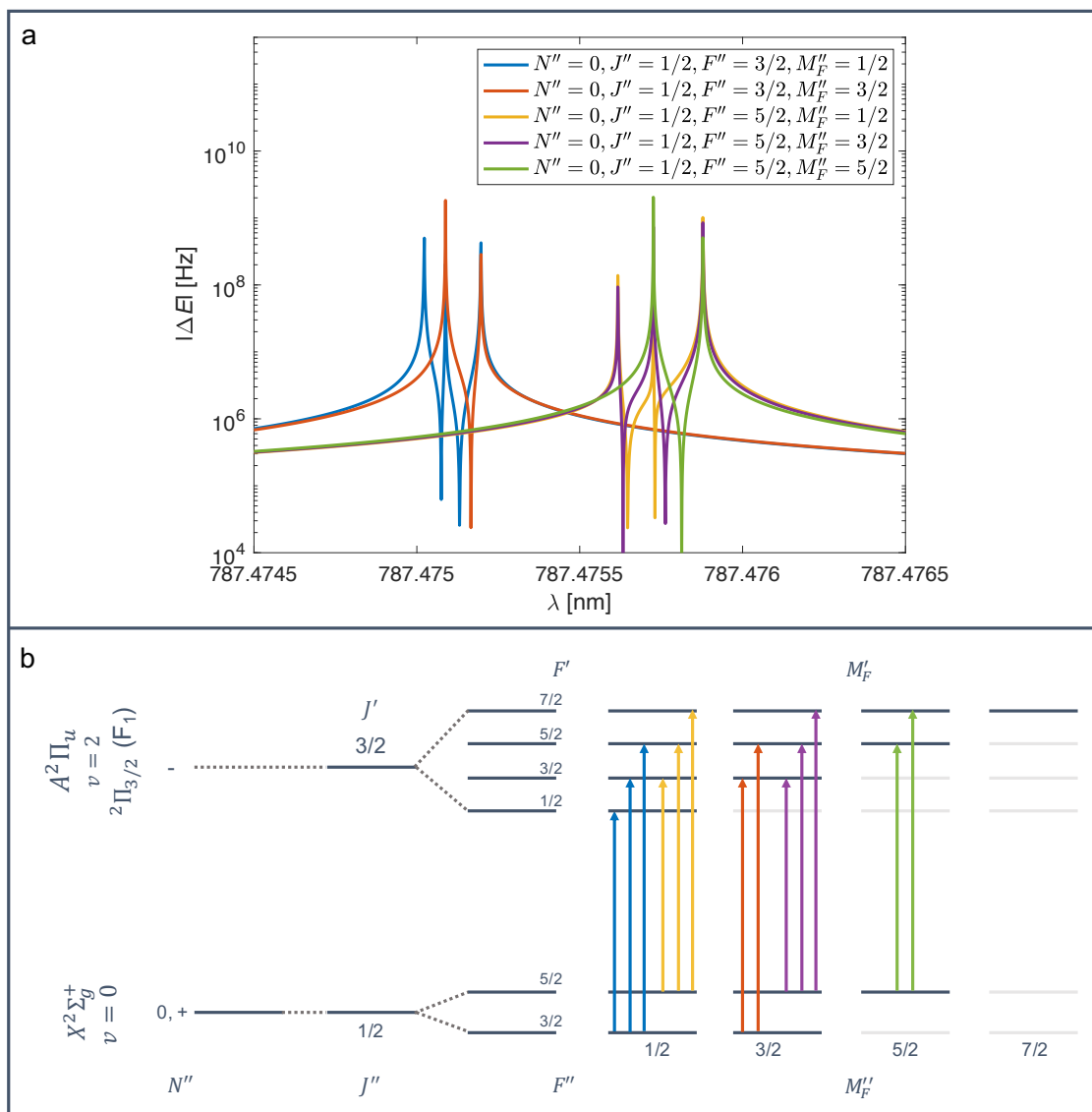


Figure 3.6 Hyperfine structure effects in the  $R_{11}(1/2)$  transition in  $N_2^+$ .

### 3.3.1 Effects due to the hyperfine structure

Hyperfine-structure effects are subtle and are expected to be negligible far away from a transition. In order to observe the influence of the hyperfine structure on a transition and develop an intuitive picture of the consequence of the various terms of the Hamiltonians of the  $A^2\Pi_u$  and  $X^2\Sigma_g^+$  states discussed in sections (2.3.1) and (2.3.1), the region in the vicinity of the  $R_{11}(1/2)$  transition is explored in fig. 3.6 for the  $I = 2$  spin isomer.

In fig. 3.6a, the hyperfine couplings of the  $X^2\Sigma_g^+$  state (characterized by  $b_F$ ) and the  $A^2\Pi_u$  state (characterized by  $a, b, c$  and  $d$ ) and the  $\Lambda$ -doubling of the  $A^2\Pi_u$  rotational states



**Figure 3.7** The  $R_{11}(1/2)$  transition in  $I = 2 \text{ N}_2^+$ . The Zeeman levels in grey do not exist.

(characterized by  $p$  and  $q$ ) were fictitiously turned off. Under these conditions, the  $\text{N}_2^+$   $I = 2$  molecule behaved exactly like the  $I = 0$  molecule. All hyperfine levels of the  $X^2\Sigma_g^+$  and  $A^2\Pi_u$  states were degenerate. In fig. 3.6b, the hyperfine coupling of the  $X^2\Sigma_g^+$  state was switched on. This led to a splitting of the  $R_{11}(1/2)$  transition into two manifolds. This was because transitions could now originate from the non-degenerate  $N'' = 0, J'' = 1/2, F'' = 3/2$  and  $N'' = 0, J'' = 1/2, F'' = 5/2$  states of the  $X^2\Sigma_g^+$  electronic state of  $\text{N}_2^+$ . In fig. 3.6c, the

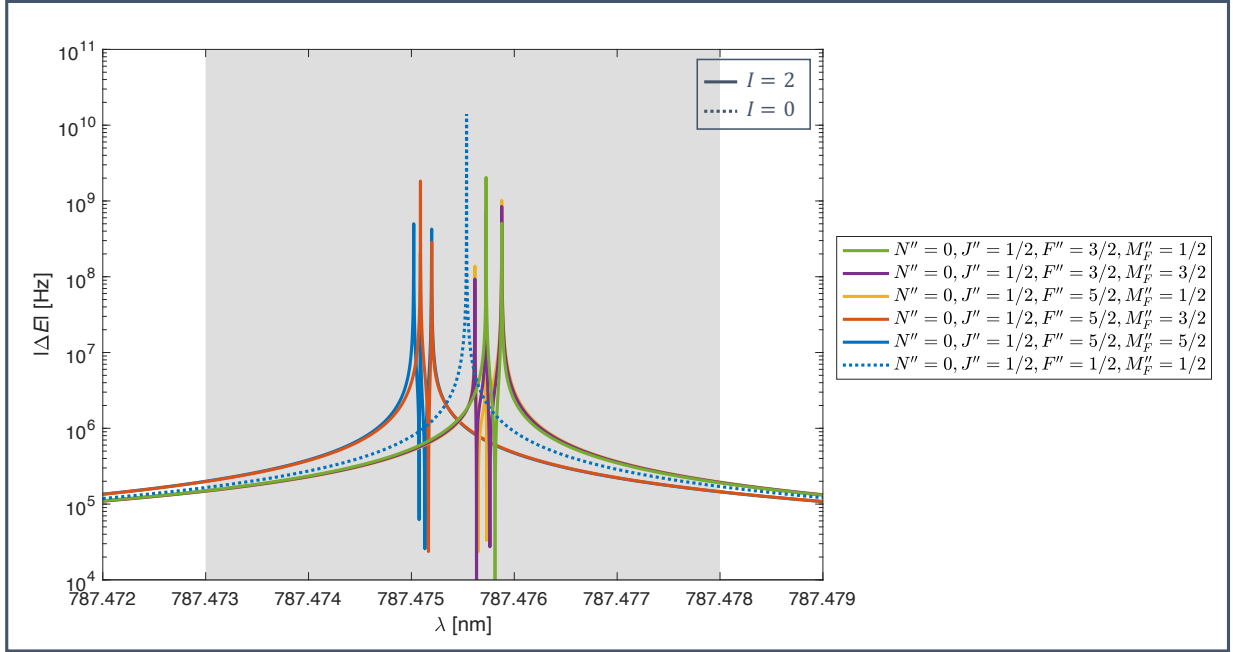


**Figure 3.8** Comparison of the  $R_{11}(1/2)$  transition in  $N_2^+$  between the  $I = 0$  (dotted line) and  $I = 2$  (solid lines) molecules. The grey shaded area shows a region spanning  $\sim 0.005$  nm ( $\sim 2.5$  GHz) around the transition frequency of the  $I = 0$  molecule where hyperfine structure affects the ac-Stark shift by an amount  $>10\%$ .

$\Lambda$ -doubling of the  $A^2\Pi_u$  states were switched on. This causes a small shift in the energies of the  $A^2\Pi_u$  states (not visible in the figures). In addition,  $\Lambda$ -doubling also caused a mixing between rotational states of the  $A^2\Pi_u$  manifold. Due to the mixing, the Hönl-London factor and consequently the transition-dipole matrix element and  $\Delta E$  changed slightly. This can be observed as a small change in the peak intensities between the fig. 3.6b and fig. 3.6c. In fig. 3.6d, all couplings were switched on. This resulted in further splitting of the  $R_{11}(1/2)$  transition because the degeneracy of the hyperfine states of the  $A^2\Pi_u$  manifold was lifted. The transitions between the hyperfine energy levels for the  $I = 2$  molecule leading to the various peaks in 3.6d are detailed in fig. 3.7. As before, the laser polarization was set such that  $p = 0$  in equation (3.85). Thus only  $\Delta M_F = 0$  transitions were allowed. Since the Zeeman effect due to external magnetic field was not considered here, all Zeeman states of a hyperfine state were degenerate. Inclusion of the Zeeman Hamiltonian would lead to a further splitting of the peaks.

From fig. 3.7, it can be noted that the hyperfine effects become crucial in the vicinity of the transition only. This is clearly depicted by fig. 3.8 which shows a comparison of the  $R_{11}(1/2)$  transition in  $N_2^+$  between the  $I = 0$  (dotted line) and  $I = 2$  (solid lines) molecules. For the case of the  $R_{11}(1/2)$  transition, significant difference ( $>10\%$ ) in the ac-Stark shift can be observed in a region spanning  $\sim 0.005$  nm (or  $\sim 2.5$  GHz) around the line-center at  $\sim 787.4755$  nm (grey shaded area in fig. 3.8). For lasers detuned further from the line-center, the hyperfine effects become negligible (for state-detection applications).

### 3.3.2 Off-resonant photon-scattering rates

The photon-scattering rate due to the off-resonant laser beam can be estimated from equations (3.5), (3.4) and (3.79). For a  $|\tilde{e}\rangle \leftrightarrow |\tilde{g}\rangle$  transition, the scattering rate ( $\Gamma_{\text{sc-}|\tilde{e}\rangle,|\tilde{g}\rangle}$ ) is given as,

$$\Gamma_{\text{sc-}|\tilde{e}\rangle,|\tilde{g}\rangle} = \frac{3\pi^2 c^2}{h\omega_0^3} \left(\frac{\omega}{\omega_0}\right)^3 \left(\frac{1}{\omega_0 - \omega} + \frac{1}{\omega_0 + \omega}\right)^2 S^2 A_{\text{vibronic}}^2 I(\mathbf{r}) (2F' + 1)^2 \begin{pmatrix} F' & 1 & F'' \\ -M'_F & p & M''_F \end{pmatrix}^4. \quad (3.88)$$

As was the case with the ac-Stark shift, the scattering rate due to the off-resonant laser beam for a molecule in the state  $|\tilde{g}\rangle$  is given by the sum over all possible transitions from the state  $|\tilde{g}\rangle$ , i.e.,

$$\Gamma_{\text{sc}} = \sum_{|\tilde{e}\rangle} \Gamma_{\text{sc-}|\tilde{e}\rangle,|\tilde{g}\rangle}. \quad (3.89)$$

Fig. 3.9a. shows the calculated scattering rate (dotted line - right y-axis) compared to the ac-Stark shift (solid line - left y-axis) for a  $N_2^+$  ion in the ground state. As is expected, the scattering rate increases sharply near the line-centers for the transition. Fig. 3.9b. shows the case for the  $R_{11}(1/2)$  transition. For a laser sufficiently detuned from the line-center (black-dashed line at 787.51 nm) by  $\sim 20$  GHz, the scattering rate was small compared to the ac-Stark shift. For this laser configuration, the state of the  $N_2^+$  ion could be non-destructively read out with good a signal-to-noise ratio (SNR) before the  $N_2^+$  scattered a

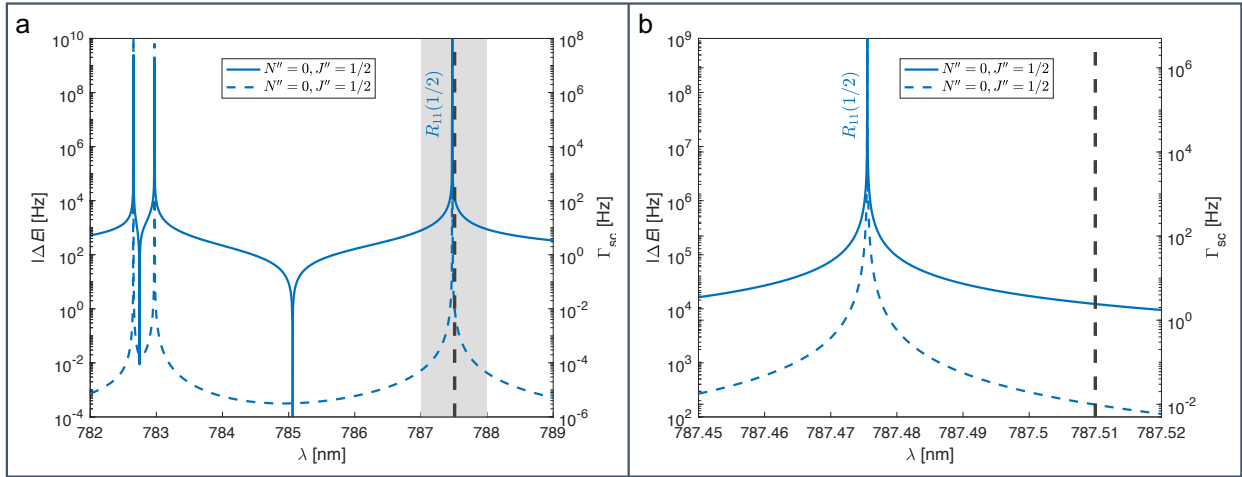


**Figure 3.9 Comparison between ac-Stark shift and photon scattering for a ground state  $N_2^+$  ion due to an off-resonant laser.**

photon in our setup. In fact, the state of  $N_2^+$  could be determined with a good SNR even as close as  $\sim 5$  GHz from the transition (corresponding to a laser at  $\sim 787.48$  nm).

In summary, this chapter discussed the theory behind transition-dipole matrix elements, ac-Stark shift and photon scattering due to off-resonant lasers in homonuclear diatomic molecules with a focus on the  $N_2^+$  ion. The effect of state mixing due to the hyperfine Hamiltonian have also been examined. Hyperfine effects in mixed Hund's case (b) to Hund's case (a) transitions have been investigated and transition parameters like the Hönl-London have been derived. Although many (but not all) parts of the molecular theory discussed in this chapter is available in the literature [61, 63, 64, 101, 102], a unified and consistent treatment is presented here.

# Chapter Four

## Spectrally Pure, SI-referenced lasers for high-precision spectroscopy

Recent years have witnessed dramatic progress in the development of optical frequency standards for high-resolution and high-precision metrology and spectroscopy [44, 122–124], frequency comparisons [41, 125–127], tests of fundamental physics [128, 129], geodesy [130, 131], very-long-baseline interferometry [38], geology and seismology [132] and optical communication. The advent of optical frequency combs (OFCs) has revolutionized direct-frequency and frequency-ratio measurements and allows for unprecedented control over the phase and frequency of coherent optical sources by providing convenient ways for accurate frequency evaluations in the radio frequency (RF) domain. Ultrastable, accurate and SI-referenced lasers can now be generated at remote locations [133–135] and disseminated over thousands of kilometers of fiber-links [136–138] eliminating the need for long, cumbersome and failure-prone frequency-divider chains and frequency-reference cells which provide limited stability.

This chapter discusses the characterization, stabilization and delivery of stable lasers for precision spectroscopy of  $\text{Ca}^+$  atomic and  $\text{N}_2^+$  molecular ions trapped in a RF ion trap. Fig. 4.1 shows the relevant energy levels for the atomic and molecular ion. In the case of the  $\text{Ca}^+$  ion, we probed the electric-quadrupole  $4\text{S}_{1/2} \leftrightarrow 3\text{D}_{5/2}$  transition at a wavelength of 729 nm. For the  $\text{N}_2^+$  ion, the electric-quadrupole  $(v'' = 0, N'' = 0) \leftrightarrow (v' = 1, N' = 2)$  transition

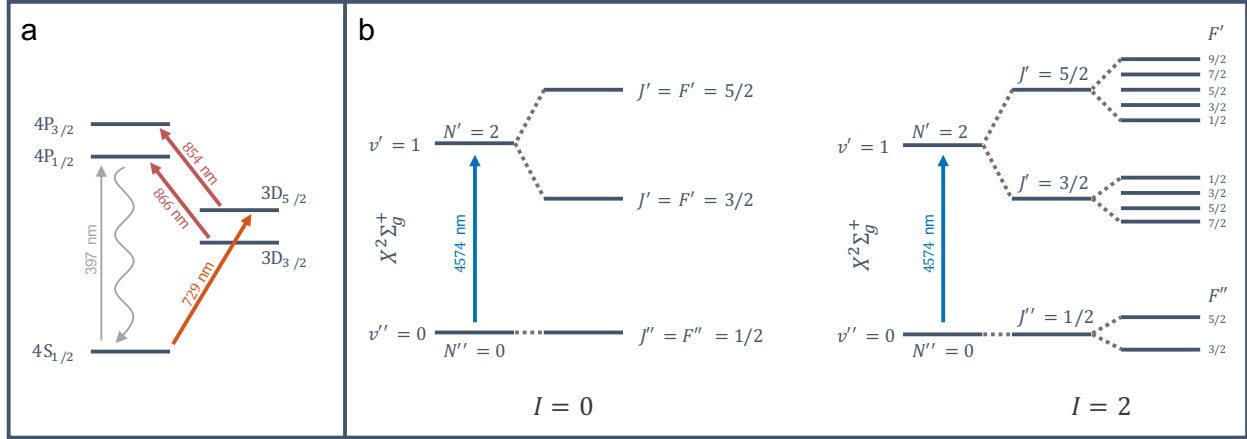


**Figure 4.1 Relevant energy levels of the  $\text{Ca}^+$  and  $\text{N}_2^+$  ions for precision spectroscopy.** (a) For the  $\text{Ca}^+$  ion, the quadruple  $4\text{S}_{1/2} \leftrightarrow 3\text{D}_{5/2}$  transition at 729 nm was probed. The lasers at 866 nm and 854 nm were used to re-pump the population from the long lived  $3\text{D}_{3/2}$  and  $3\text{D}_{5/2}$  states while the fast dipole  $4\text{S}_{1/2} \leftrightarrow 4\text{P}_{1/2}$  transition at 397 nm was used for detecting the internal state of the  $\text{Ca}^+$  ion [140]. (b) In the case of the  $\text{N}_2^+$  ion, two nuclear-spin isomers ( $I = 0, 2$ ) can exist [53, 75]. The relevant rotation-vibration transitions in the electronic ground  $X^2\Sigma_g^+$  state at 4574 nm are shown.  $v'(v'')$ ,  $N'(N'')$ ,  $J'(J'')$ ,  $F'(F'')$  represent the vibrational, rotational, fine-structure and hyperfine-structure quantum numbers of the ground(excited) state. For clarity, the Zeeman states are not shown here.

in the electronic-ground  $X^2\Sigma_g^+$  state, at a transition wavelength of 4574 nm was chosen to be investigated in the future. Due to the narrow natural linewidths of 136 mHz [139] and sub- $\mu\text{Hz}$  [75] of the transitions in  $\text{Ca}^+$  and  $\text{N}_2^+$  ions respectively, spectrally pure laser sources were developed for coherent interrogation and high-resolution spectroscopy. The lasers were additionally referenced to the Swiss coordinated universal time [135], UTC(CH) which is based on the International Atomic Time (TAI). The TAI is a stable and accurate international timescale derived from over 300 atomic clocks and many primary frequency standards located at several timing and metrology institutes around the world. The referencing of the lasers to the UTC thus allows for absolute frequency measurements.

In order to drive the transition in  $\text{Ca}^+$ , a continuous-wave (CW) external-cavity diode laser was chosen at 729 nm<sup>1</sup>. The laser featured a free-running linewidth of a few-hundred kHz. For the  $\text{N}_2^+$  ion, several CW room-temperature (RT) distributed-feedback (DFB)

<sup>1</sup>TA-Pro - Toptica Photonics AG

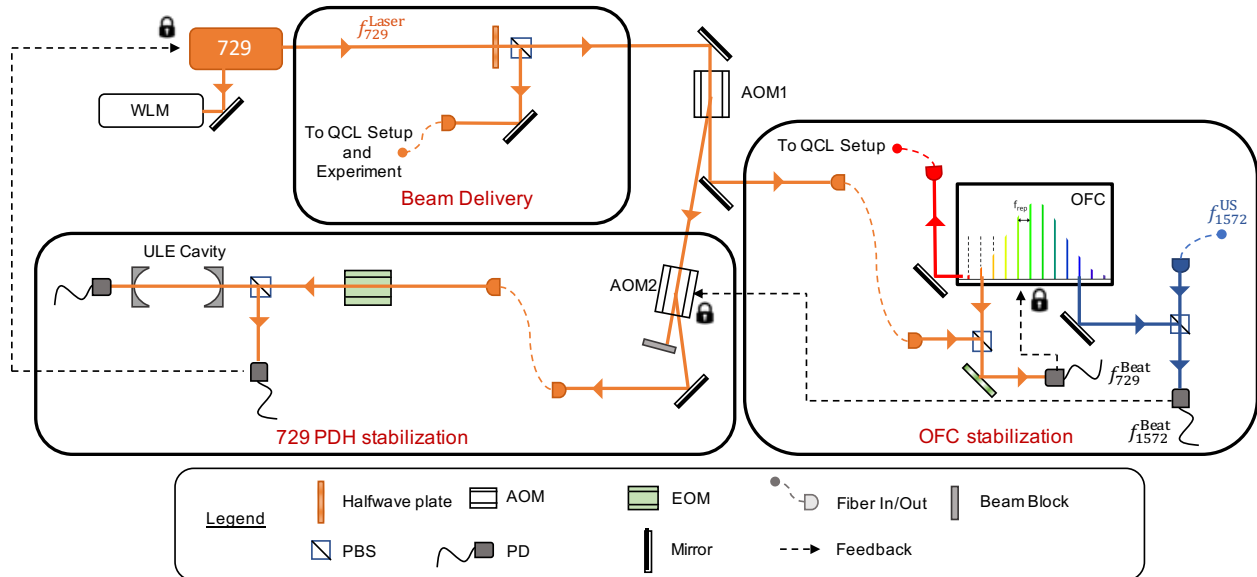


**Figure 4.2 Stabilization setup for the 729 nm and the OFC laser systems.** The 729 nm laser (orange) and the OFC are locked to the ULE cavity for short-term stabilization. The long-term stabilization is performed by comparing the OFC to an ultrastable 1572 nm laser (blue) generated at the Swiss Federal Metrological Institute (METAS) (located in Bern,  $\sim 105$  km from our laboratory). 629 nm light from the OFC (red) is used for stabilization of the QCL discussed in section 4.2.

quantum-cascade lasers (QCLs) and one external-cavity (EC) QCL operating at  $\sim 4574$  nm were studied as a part of this thesis and a suitable laser was chosen. Ideally, such QCLs are expected to have free-running linewidths of the order of a few-hundred kHz to few MHz. The DFB-QCLs are expected to have mode-hop-free operation over their entire operational range. Exceptions to ideal behaviour were observed in many cases rendering many QCLs unsuitable for precision spectroscopy applications. In order to lock the QCL and reference both lasers to the UTC(CH), a commercial OFC<sup>2</sup> operating at a repetition rate of  $\sim 250$  MHz was chosen.

## 4.1 The 729 nm and the OFC laser systems

The scheme for the stabilization of the 729 nm and the OFC laser systems is illustrated in Fig. 4.2. The setup can be functionally divided into two major parts: the stabilization of the 729 nm laser (labelled “729 PDH stabilization”) and the stabilization of the OFC (labelled “OFC stabilization”). The “Beam Delivery” setup was used for the delivery of the 729 nm laser for experiments on the  $\text{Ca}^+$  ion and the stabilization of the QCL (labelled “Beam Delivery”).

### 4.1.1 The PDH stabilization setup

The Pound-Drever-Hall (PDH) stabilization technique [28, 141] relies on fast modulation of a laser in order to measure the magnitude and error in the laser frequency. Phase modulated light from the laser, consisting of a carrier frequency and two equally spaced sidebands is directed into a cavity. An error signal corresponding to the laser frequency noise can be extracted by a suitable demodulation of the interference signal between the reflected power from the cavity and the incoming light. A PID controller is then used to scale the measured error signal in order to generate a feedback [142] which can be used to lock the laser on top of a cavity resonance profile. This allows for high-precision short-term stabilization of the laser.

A description of our implementation of the PDH lock for the 729 nm laser can be found in [56]. The 729 nm laser was locked to a  $L = 100$  mm long high-finesse ultra-low-expansion (ULE) optical cavity<sup>3</sup> with a cavity finesse of  $\mathcal{F} = 270000$  and a cavity linewidth of 8 kHz. The cavity was enclosed in an isolation box, maintained at a vacuum below  $3 \times 10^{-6}$  mbar, and temperature stabilized at its zero-crossing temperature of  $T_0 = 26.83$  °C in order to minimize acoustic noises and thermal drifts.

---

<sup>2</sup>FC1500-250-ULN - Menlo Systems

<sup>3</sup>ATF-6020-4 - Stable Laser Systems

For the stabilization, a small portion ( $< 10$  mW) of the total emitted power ( $\sim 400$  mW) from the laser, at a frequency  $f_{729}^{\text{Laser}} \approx 411.04$  THz, was coupled into an Acousto-Optic Modulator AOM (labelled “AOM1”) operating at  $\sim 1.1$  GHz. The first-order output of the “AOM1” at a frequency  $f_{729}^{\text{Laser}} + f_{\text{AOM1}}$  was directed into another AOM (labelled “AOM2”) which operated at lower frequencies centered around 100 MHz. The first-order output, at a frequency  $f_{729}^{\text{Laser}} + f_{\text{AOM1}} + f_{\text{AOM2}}$ , was then coupled to a single mode fiber for laser-spatial-mode cleaning. The output of the fiber was aligned to the optical cavity via an EOM<sup>4</sup> which generated the required sidebands at  $f_{\text{EOM}} \approx 20$  MHz for PDH locking. The reflected power from the cavity was recorded on a fast photodiode and demodulated by a commercially-available PDH-electronics unit<sup>5</sup>. A commercial PID module<sup>6</sup> was used to generate a feedback signal which was in turn used to lock the laser via current and piezo modulations of the laser.

Since the cavity featured a free spectral range (FSR) of  $\sim 1.5$  GHz (defined by the cavity length), the “AOM1” was used to bridge the frequency gap between the laser-emission frequency and the cavity-transmission modes. Cavities are prone to poorly-predictable non-linear shrinkage in the resonator length on the order of  $dL/L = 10^{-17}/\text{s}$  to  $10^{-16}/\text{s}$  due to aging of the ULE glass [143,144]. The drifts in the cavity lengths lead to frequency drifts of the cavity-transmission mode (to which the laser is locked) which in-turn leads to a drift in the laser frequency ( $f$ ) given by,

$$df/f = dL/L. \tag{4.1}$$

In our setup, the drifts of the cavity were detected by comparison of the locked 729 nm laser to a ultrastable reference laser (4.1.2). A drift of 230 Hz/hour (or  $\sim 64$  mHz/s) [56] was measured corresponding to changes in cavity length  $dL/L \approx 1.5 \times 10^{-17}/\text{s}$ . The drifts were corrected by applying a suitable correction frequency to the “AOM2”.

---

<sup>4</sup>Thorlabs EO-PM-NR-C1

<sup>5</sup>PDD 110 - Toptica Photonics AG

<sup>6</sup>FALC 110 - Toptica Photonics AG

### 4.1.2 The OFC stabilization setup

Locking of lasers to optical cavities can result in impressive short-term laser stability. However, as mentioned in the previous section, optical cavities drift leading to drifts in the locked-laser frequency. Additionally, optical cavities do not serve as absolute frequency reference, i.e. the exact frequency of a laser cannot be determined by a lock to an optical cavity. In order to mitigate both these problems, we referenced our cavity-stabilized 729 nm laser to our OFC with a central emission wavelength of  $\sim 1560$  nm.

The spectrum of an OFC consists of equally spaced comb lines. The  $p^{\text{th}}$  comb line for an OFC can be given by,

$$f_{\text{COMB}} = p \cdot f_{\text{REP}} \pm f_{\text{CEO}}, \quad (4.2)$$

where  $f_{\text{CEO}}$  is the carrier-envelope offset (CEO) frequency and  $f_{\text{REP}}$  is the repetition rate (REP) frequency of the OFC. The sign in the above equation depends on the phase of the CEO. In the case the  $f_{\text{COMB}}$  increases on increasing the  $f_{\text{CEO}}$ , a positive sign is used. Conversely, if  $f_{\text{COMB}}$  decreases on increasing the  $f_{\text{CEO}}$ , a negative sign is used. OFCs thus feature two independent degrees of freedom<sup>7</sup>. Under free-running conditions, the comb lines are broad featuring linewidths of a few hundred Hz to few tens of kHz and stabilization of the  $f_{\text{CEO}}$  and  $f_{\text{REP}}$  results in a stable OFC.

In our setup, the  $f_{\text{CEO}}$  was stabilized by  $f - 2f$  interferometry and locked a GPS disciplined Rb oscillator (Rb-GPSDO)<sup>8</sup>. The 10 MHz Rb-GPSDO had a stability of  $\sim 2 \times 10^{-11}$  on 1 s and  $\sim 1 \times 10^{-12}$  on 100 s timescales.

In order to narrow the comb lines and improve the short term stability of the OFC, the repetition rate of the OFC was locked to the cavity-stabilized 729 nm laser. A small portion of the OFC emission at 1560 nm was amplified, frequency shifted to  $\sim 1460$  nm and frequency doubled to generate comb line at 729 nm<sup>9</sup>. The  $n^{\text{th}}$  comb line centered around

---

<sup>7</sup>Some OFCs do not have carrier-envelope offsets

<sup>8</sup>FS725 - Stanford Research Systems

<sup>9</sup>M-VIS package - Menlo Systems

729 nm could then be given by,

$$f_{729}^{\text{OFC}} = n \cdot f_{\text{REP}} \pm 2f_{\text{CEO}}, \quad (4.3)$$

where the factor 2 in the above equation appears due to the frequency doubling of the OFC for generating 729 nm output. For the lock of the REP, a beat note was generated between the OFC and the cavity-stabilized 729 nm laser in a fully-fiber-coupled beat-detection unit<sup>10</sup>. The beat note, at a RF frequency of  $f_{729}^{\text{Beat}}$ , was compared to the Rb-GPSDO and a filtered feedback signal was generated to lock the OFC-REP by a commercial electronics-lockbox unit<sup>11</sup>.

With a tight-lock of a comb to the cavity-stabilized 729 nm laser, the short-term and long-term spectral characteristics of the 729 nm laser were copied onto the comb lines. Thus, the comb lines were narrowed in their FWHM linewidths but drifted with the drifts of the cavity. The frequency of the cavity-stabilized 729 nm laser could be determined from the beat note and was given by,

$$f_{729}^{\text{Laser}} \pm \delta = n \cdot f_{\text{REP}} \pm 2f_{\text{CEO}} \pm f_{729}^{\text{Beat}}, \quad (4.4)$$

where  $\delta$  was the drift in the cavity-transmission frequency or in the  $f_{729}^{\text{Laser}}$  frequency. Rearranging the above equation, the OFC REP could be expressed as,

$$f_{\text{REP}} = \frac{f_{729}^{\text{Laser}} \mp 2f_{\text{CEO}} \mp f_{729}^{\text{Beat}}}{n} \pm \frac{\delta}{n}. \quad (4.5)$$

Thus, cavity drifts of  $\delta$  caused a drift in the comb REP by  $\delta/n$ .

The drifts of the REP could be mitigated by a comparison to a second ultrastable (US) reference laser with a good long-term stability. Such a reference laser is generated and distributed by the Swiss Federal Metrological Institute (METAS) in the telecommunication L-band at a frequency  $f_{1572}^{\text{US}} \approx 1572.06$  nm [138] via phase-stabilized optical fiber networks.

---

<sup>10</sup>729.3 nm BDU-FF - Menlo Systems

<sup>11</sup>SYNCRO - Menlo Systems

The optical fiber network currently connects institutes in Bern, Basel and Zurich in Switzerland with over 456 km fiber network in a ring topology and features a round-trip link stability of  $4.7 \times 10^{-16}$  at 1 s and  $3.8 \times 10^{-19}$  at 2000 s integration time. The round trip stability is a measure of the stability of the fiber link itself and does not quantify the instability of the reference laser. The reference laser is itself compared to the TAI via an active hydrogen maser, which contributes to the Swiss Coordinated Universal Time - UTC(CH), for determining its precise frequency [138].

The frequency of the reference laser with respect to our OFC could be determined by a beat note,  $f_{1572}^{\text{Beat}}$ , between the OFC and the reference laser as,

$$f_{1572}^{\text{US}} = m \cdot f_{\text{REP}} \pm f_{\text{CEO}} \pm f_{1572}^{\text{Beat}}. \quad (4.6)$$

Comparing equation 4.5, the frequency of the reference laser could be determined from the 729 nm laser frequency as,

$$f_{1572}^{\text{US}} = m \cdot \frac{f_{729}^{\text{Laser}} \mp 2f_{\text{CEO}} \mp f_{729}^{\text{Beat}}}{n} \pm f_{\text{CEO}} \pm f_{1572}^{\text{Beat}} \pm \frac{m}{n}\delta. \quad (4.7)$$

Re-arranging, the beat frequency between the OFC and the reference laser could be expressed as,

$$\pm f_{1572}^{\text{Beat}} = f_{1572}^{\text{US}} - \frac{m}{n}[f_{729} \pm (n/m - 2)f_{\text{CEO}} \mp f_{729}^{\text{Beat}}] \mp \frac{m}{n}\delta. \quad (4.8)$$

Thus, a cavity drift of  $\delta$  caused a drift of  $m/n \cdot \delta$  in the beat note frequency between the OFC and the reference laser. This slow drift could be detected by counting the beat frequency on a RF-counter<sup>12</sup> and a filtered feedback could be applied to the ‘‘AOM2’’ (in figure 4.2) that compensated for the drifts.

With the slow feedback loop closed ( $\delta \approx 0$ ) and with the precise knowledge of the reference laser frequency  $f_{1572}^{\text{US}}$ , the comb line numbers  $m$  and  $n$ , the comb offset  $f_{\text{CEO}}$ , the beat notes frequencies  $f_{729}^{\text{Beat}}$  and  $f_{1572}^{\text{Beat}}$  and their relative signs, the frequency of the cavity-stabilized 729

---

<sup>12</sup>FXM50 - Menlo Systems

nm spectroscopy laser could be absolutely determined as,

$$f_{729}^{\text{Laser}} = \frac{n}{m} \cdot [f_{1572}^{\text{US}} \mp f_{\text{CEO}} \mp f_{1572}^{\text{Beat}}] \pm 2f_{\text{CEO}} \pm f_{729}^{\text{Beat}}. \quad (4.9)$$

The comb line numbers were determined by measuring the frequencies of the lasers on a calibrated wavelength meter<sup>13</sup>. The remaining parameters lie in the typical RF domain between a few MHz and hundred MHz and could be measured using locally available counters and/or RF-spectrum analyzers<sup>14</sup> referenced to the Rb-GPSDO. The limiting factor in the long-term frequency stabilization was then the instability of the reference laser generated at METAS itself.

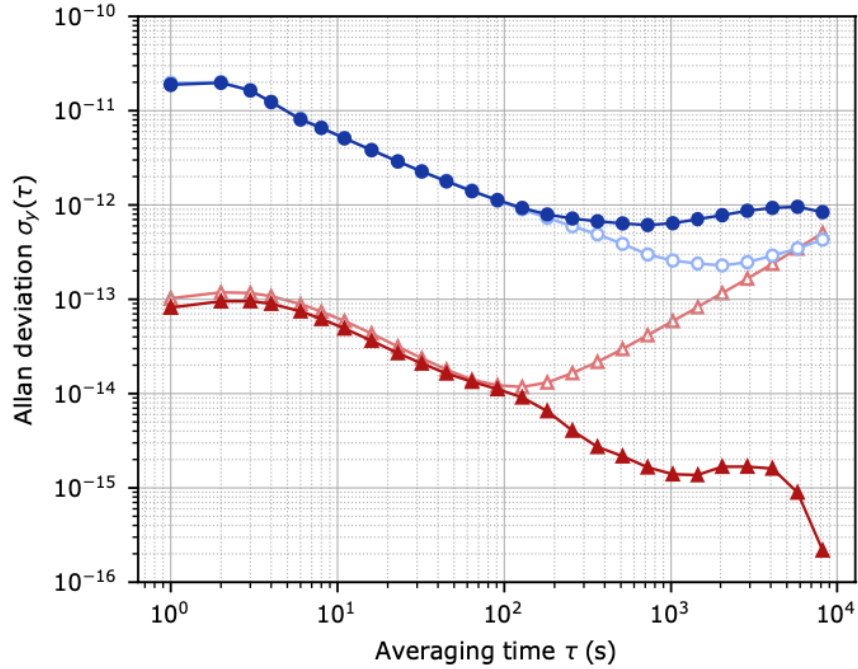
In addition to the method presented above, the frequency of the 729 nm laser could also be determined directly by a direct measurement of the REP (as can be seen from equation [4.4]). The REP could be measured on a frequency counter which was referenced to the locally available Rb-GPSDO. Since the Rb-GPSDO, operating at 10 MHz, had a stability of  $2 \times 10^{-11}$  in 1 s and  $1 \times 10^{-12}$  in 100 s, the  $f_{\text{REP}}$  at  $\sim 250$  MHz could be determined to  $500 \times 10^{-5}$  Hz in 1 s and  $25 \times 10^{-5}$  Hz in 100 s. Since the comb line number  $n$  was a large number of the order of  $10^6$ , the  $f_{729}^{\text{Laser}}$  could not be determined to better than 5 kHz in 1 s or 250 Hz in 100 s. This highlights the need and the importance of good SI referenced optical reference (which may be generated in remote frequency-metrology institutes) in improving the SI traceability and frequency stability of precision-spectroscopy lasers in other laboratories.

Fig. 4.3 depict four measurements of the Allan deviation of the 729 nm laser frequency. The blue traces show two measurements when the comb was locked to the cavity-stabilized 729 nm laser but the reference laser was not used to determine the 729 nm laser frequency. The 729 nm frequency was determined from the OFC REP measured by a counter referenced to the Rb-GPSDO. As expected, the measured stability was dominated by the Rb-GPSDO and an instability of  $2 \times 10^{-11}$  in 1 s and  $1 \times 10^{-12}$  in 100 s was recorded. For the light blue trace, the slow drifts of the ULE cavity were not compensated. For a cavity with drifts of

---

<sup>13</sup>WSU-30 - High Finesse

<sup>14</sup>HMS-X - Rhode and Schwarz



**Figure 4.3 Allan deviations of the 729 nm laser.** In blue, the 729 nm frequency was determined after a determination of the OFC-REP. In red, the 729 nm frequency was determined from the frequency of the ultrastable 1572 nm laser. For the dark-red and dark-blue measurements, the slow lock for the compensation of the drifts of the optical cavity was switched on while for the light-red and light-blue measurements the cavity drifts were not compensated.

$\sim 200$  Hz/hour, a frequency instability  $\Delta f_{729}$  of  $(200/3600) * 2000 \approx 111$  Hz was expected in 2000 s which corresponded to an instability  $\Delta f_{729}/f_{729}$  of  $\sim 2.7 \times 10^{-13}$  at  $f_{729} \approx 411$  THz. This can be observed on the figure.

In the thick blue trace, the slow feedback to “AOM2” for drift compensation was switched on which compensated for the cavity drifts. However, an improved stability was not observed due to the instability in the determination of the REP determined by the Rb-GPSDO. The difference in the light and thick blue traces were due to measurement-to-measurement effects such as changes in locking parameters due to changes in optical powers, jitter in Rb-GPSDO frequency due to GPS update, etc.

The red traces depict the stability of the 729 nm frequency determination by the reference laser signal from METAS. A stability of  $\sim 1 \times 10^{-13}$  was recorded in 1 s which was the stability

of the reference laser. In the hollow-light red trace, although the reference laser was used to determine the frequency of the 729 nm laser, but the slow feedback loop to “AOM2” for drift compensation was not closed. The drifts of the ULE cavity then became significant around 100 s of averaging time. As before, for a cavity with a drifts of  $\sim 200$  Hz/hour, a frequency instability  $\Delta f_{729}$  of  $(200/3600) * 100 \approx 5.5$  Hz was expected in 100 s which corresponds to an instability  $\Delta f_{729}/f_{729}$  of  $\sim 1.3 \times 10^{-14}$  at  $f_{729} \approx 411$  THz. The cavity drifted linearly and an increased instability was recorded for averaging times  $> 100$  s. In the solid-red trace, the slow feedback compensating the cavity drifts was switched on. The stability in  $f_{729}$  was then the stability of the reference laser.

### 4.1.3 Beam Delivery setup

In order to deliver 729 nm light to the experiment for spectroscopy on  $\text{Ca}^+$  and for the stabilization of the QCL, a major portion of the output light from the laser was split off by a combination of a half-wave plate and a polarizing beam splitter cube. The light was coupled into a 10 m uncompensated optical fiber and delivered from the 729 nm optical table to the experimental table. At the experimental table, a portion of the power was further split to the QCL stabilization setup (see Fig. [4.4]). The remaining power was made available for the experiments on the  $\text{Ca}^+$  ion.

## 4.2 The 4574 nm laser system

High-resolution spectroscopy in the mid-infrared (MIR) is becoming an important tool for the investigation of fine details of molecular structure and dynamics. In the past, gas lasers have frequently been employed for molecular spectroscopy. However the unavailability of such lasers over the entire MIR region and the inability to tune such lasers often restrict their applicability. Gas-laser-sideband generation [145] and difference-frequency generation (DFG) in the visible and NIR [146] often allow for tunable sources which can be used for

spectroscopy. Lead salt diodes, color-center lasers and optical parametric oscillators (OPOs) can also serve as tunable sources for MIR spectroscopy. However these generally suffer from low power and/or single-mode emission issues in the MIR making them challenging to work with.

The availability of QCLs spanning wavelengths from near-infrared (NIR) wavelengths to above 25  $\mu\text{m}$ , have made them versatile laser sources in the infrared (IR) spectral regions leading to applications in many fields such as defense, free-space optical communication, physiological and clinical studies, atmospheric-gas detection and trace-gas sensing. QCLs can now offer CW operation with both high power (upto many hundreds of milliwatts) and relatively wide frequency tuning (upto few wavenumbers) making them a popular choice for MIR spectroscopy. Manufacturers can often develop QCLs in a distributed feedback (DFB) configuration (leading to mode-hop-free single-frequency operation over the whole lasing range) or external cavity (EC) configuration (which often have higher power outputs). QCLs can be available as buried-heterostructure (BH) or ridge-waveguide (RWG) devices. They may operate at room temperature (RT) or under cryogenic conditions [147]. The free-running linewidths of these lasers can vary from several hundreds to several thousands of kilohertz on timescales of 0.1 – 1 s [148–152].

Here we report the characterization of several 4574 nm BH-RT QCLs. All QCLs studied here had a DFB design except one which was in an EC configuration. It was shown in past studies that BH-RT QCLs often feature lower free-running linewidths when compared to RWG QCLs operating under cryogenic conditions [147, 150]. Absence of commercially available MIR optical cavities makes the frequency stabilization challenging. Many of the QCLs studied here were stabilized by a lock to our stabilized OFC. Since the OFC has emission in the visible and NIR regions, a sum-frequency generation (SFG) process was used to upconvert the QCLs to the visible domain for stabilization. It was also possible to determine the absolute frequency of the QCL.

The stabilization techniques employed here can be compared to the approaches adopted

by Hansen et al. [153] and Argence et al. [154]. For the stabilization, Hansen et al. [153] employed two optical cavities and an extra laser for upconverting their QCL to the NIR. The implementation presented here relied upon using a single laser and a single optical cavity leading to a simpler approach, lower costs, fewer phase-locked loops and lesser experimental overheads. The stabilization technique employed by Argence et al. [154] closely resemble the technique presented here. A difference, however, arises in the manner the SFG was implemented. Unlike the SFG implementation here where the MIR radiation was mixed with amplified output from our cavity stabilized laser, Argence et al. [154] combined the radiation from their MIR source with an amplified and stabilized OFC. Additionally, both Hansen et al. [153] and Argence et al. [154] employed low-powered QCLs with output powers of  $\sim 40$  mW, while many of the QCLs investigated here were featured many hundreds of watts of power. Other QCL stabilization techniques that have been implemented in the past are - direct frequency stabilization of QCLs to high-finesse cavities [155,156] and micro-cavities [157,158] and injection locking of stabilized difference-frequency-generated (DFG) radiation [159]. However, besides the higher costs involved, such techniques often do not allow for direct absolute frequency measurements.

Fig. 4.4 shows our setup for delivering a narrowed and stabilized QCL for interrogation of  $N_2^+$ . The setup can be functionally divided into three independent parts - the characterization setup, the stabilization setup and the beam-delivery setup (from right to left). Each part of the setup was important for proper locking of the QCL and delivering a high intensity, S.I. referenced and narrow-linewidth laser for interrogation of weak transitions in  $N_2^+$ .

### 4.2.1 The Characterization Setup

The spectral purity of a laser can be characterized by measuring the full width at half maximum (FWHM) of the optical lineshape. For lasers with emissions in the visible or the NIR, the optical lineshape is often directly measured by techniques like self-homodyning,

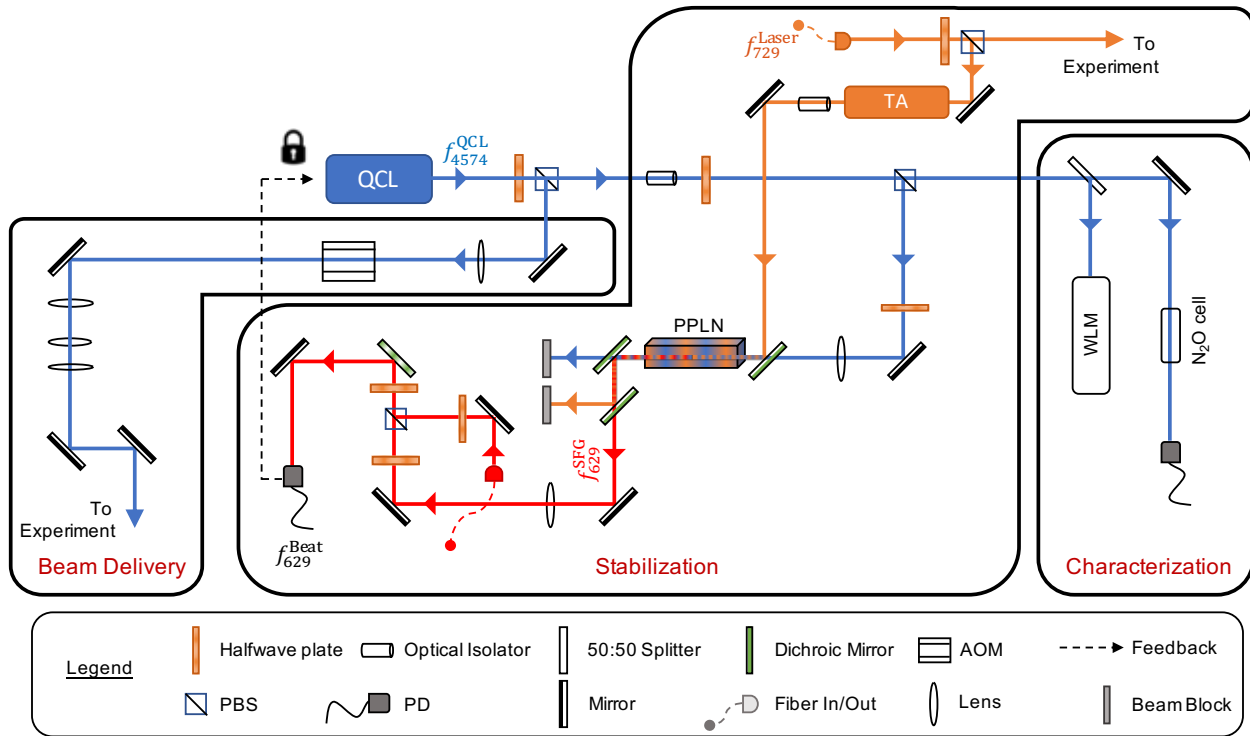


**Figure 4.4 Stabilization setup for the 4574 nm QCL.** The 4574 nm laser (blue) was characterized by using a N<sub>2</sub>O gas-cell which served as a frequency discriminator. For locking, the QCL was upconverted by SFG with the 729 nm laser (orange) in a PPLN. The generated 629 nm light (red) was used to phase lock the QCL to the OFC.

which employs a long-delay-line interferometry setup, or heterodyne beat-note measurement between the laser and a spectrally pure reference laser. Absence of commercially available low loss optical fibers in the MIR and spectrally pure MIR reference lasers pose a challenge for use of these methods directly for measuring the QCL linewidth in our case. Additionally, direct linewidth measurements do not give the complete knowledge about the distribution of laser noise at different frequencies. Such information, besides predicting whether or not a laser can be tightly locked, is often extremely helpful in identifying sources of noises which can be very useful in optimizing the laser lock.

Here, the laser-frequency-noise power-spectral density (FNPSD) was measured by using an optical-frequency discriminator which converted laser-frequency noise into intensity fluctuations which were then recorded on a suitable photodiode [147, 160]. An optical-frequency

discriminator features frequency-dependent transmission or reflection in a narrow frequency range. Due to absence of commercially available Fabry-Perot cavities, which are a popular choice of frequency discriminators in the visible and NIR frequencies, we employ molecular transitions in a gas filled absorption cell. Depending on the frequency, gas-cells filled with  $\text{N}_2\text{O}$ ,  $\text{CO}_2$ ,  $\text{CO}$  or methanol are some popular choices for MIR frequency discriminators [148–152, 161, 162].

In order to record the laser FNPSD, a small portion of the QCL power was split between a MIR-Wavelength meter (WLM)<sup>15</sup> and a  $\text{N}_2\text{O}$  gas cell in our case. Light passing through the gas cell was collected on a low-noise photodiode<sup>16</sup>. The following measurements were carried out:

1. **Measurement of the laser tuning coefficient:** The tuning coefficient of a laser characterizes the frequency change of the laser per mA change of the driving current. It was used as a scaling parameter for FNPSD measurements. Additionally, it was a measure of the sensitivity of the QCL to the current noise fluctuations of the current driver used to drive the QCL and helped in determining a suitable current driver for low-noise operation. The tuning coefficient was measured by changing the laser driving current in small incremental steps, and recording the transmitted intensity on a photodiode after the gas cell. Several  $\text{N}_2\text{O}$  molecular-absorption lines were recorded as a function of the laser current (fig. 4.5a., b. and c.). Additionally, the approximate frequency of the absorption lines were recorded by the WLM. The recorded data was then be compared to a standard molecular absorption database (The HITRAN molecular spectroscopic database [163]) (fig. 4.5d.). The slope of a fit between the expected absorption frequency and the laser current then gave the tuning coefficient of the QCL (fig. 4.5e.). For the QCL shown in fig. 4.5, a tuning coefficient of 421.1 MHz/mA was measured. Since the WLM can drift, comparison to the HITRAN database resulted in

---

<sup>15</sup>Bristol Instruments Model 621

<sup>16</sup>VIGO System PVI-4TE-5-1×1

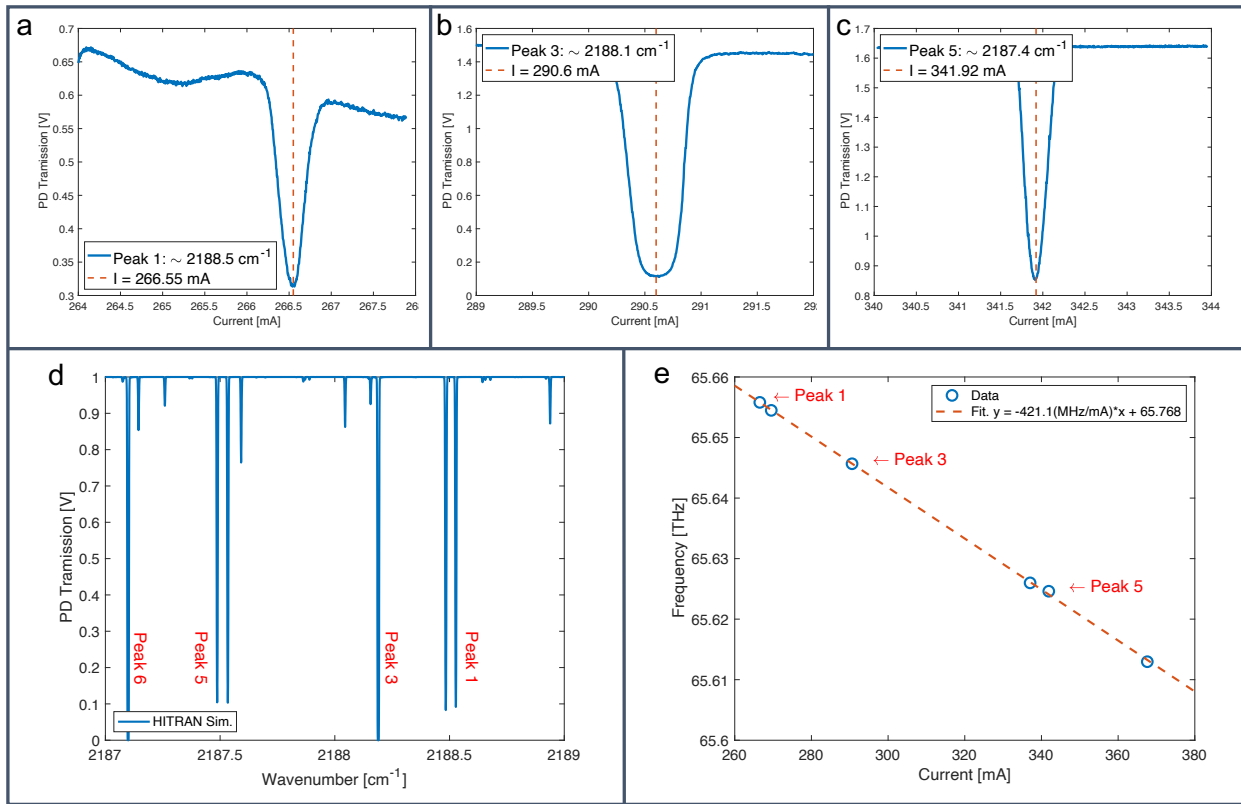


**Figure 4.5 Measurements for determining the QCL tuning coefficient.**

Many  $N_2O$  absorption lines were recorded as a function of the QCL driving current (for the packaged CM7-CIA120 laser in table (4.1)). Three of these lines labelled “Peak 1”, “Peak 3” and “Peak 5” are shown explicitly in (a), (b), and (c). “Peak 6” was used as the frequency discriminator for recording the laser FNPSD in fig. (4.6). (d) Expected positions of the recorded peaks from the HITRAN molecular spectroscopic database. (e) A linear fit (orange-dashed line) between the current and the expected peak positions was used for determining the QCL tuning coefficient.

a more precise determination of the tuning coefficient.

2. **Measurement of the discriminator slope:** In order to record the FNPSD, the QCL was tuned to the side of the absorption line in a linear region where frequency noise was linearly converted into intensity fluctuations. The slope of the linear absorption region, also known as the discriminator slope was recorded by a fit to the measured absorption feature on the photodiode (fig. 4.6a.). Here a discriminator slope of 5.3 V/mA was measured. This was used as another scaling parameter in order to determine

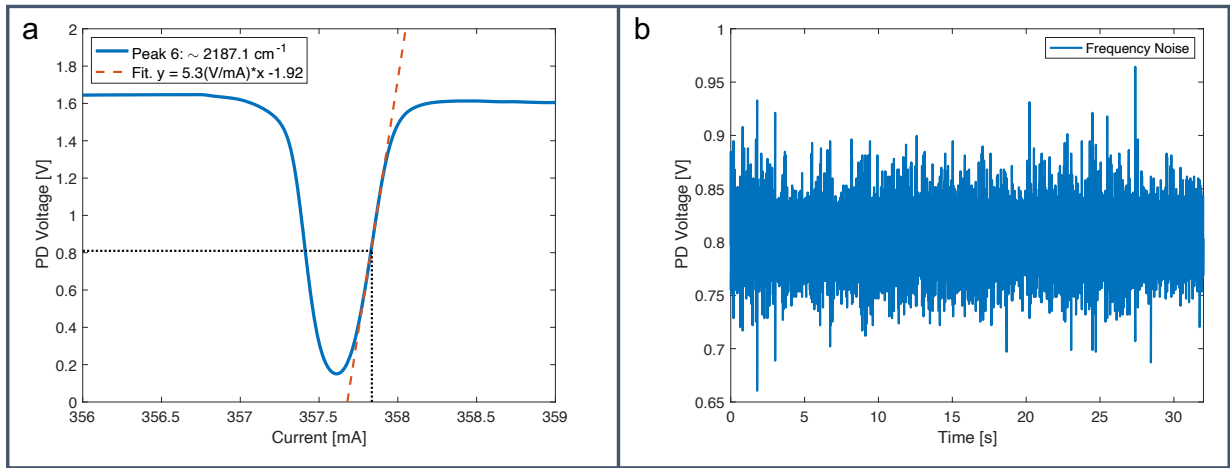


**Figure 4.6 Measurements of the discriminator slope and laser frequency noise for FNPSD determination.** (a) The discriminator slope was measured by a linear fit (orange-dashed line) of the recorded gas-absorption profile in the linear region (for the packaged CM7-CIA120 laser in table (4.1)). The QCL was tuned such that the frequency noise was linearly converted into intensity fluctuations (black-dotted lines). (b) Photodiode signal of the QCL frequency noise recorded on an oscilloscope.

the FNPSD and was a measure of the photodiode voltage as a function of the laser current.

3. **Measurement of the laser frequency noise:** The frequency noise of the laser was recorded as intensity noise (in Volts) by the photodiode when the laser was tuned to the linear region of the absorption line. The photodiode signal could be directly recorded on a suitable spectrum analyzer. Here, due to absence of spectrum analyzers with low  $1/f$  noise in the low frequency (DC - few MHz) region, the photodiode signal was recorded on an oscilloscope (fig. 4.6b.).
4. **Fourier transform and scaling of the recorded data:** A discrete Fourier transform (DFT) [164, 165] of the data recorded on the scope was performed. The noise of the laser was then obtained in units of  $V^2/\text{Hz}$  which is a measure of the Voltage noise

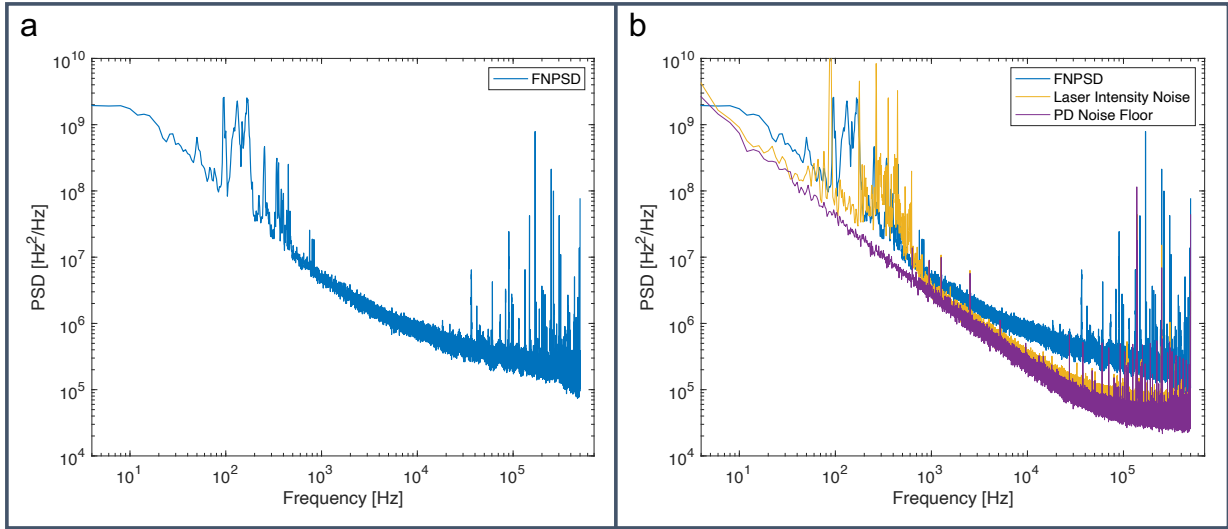


**Figure 4.7 Measured noises of the QCL.** (a) FNPSD of the QCL (blue) in units of  $\text{Hz}^2/\text{Hz}$  obtained after a scaled DFT of the data in 4.6b. The measurement was limited by the oscilloscope memory to an cut-off frequency of 500 kHz. (b) Intensity noise and measurement noise floor along with the QCL FNPSD.

power spectral density (VNPSD). In addition to the laser noise, it was function of the response of the measurement setup and repeated measurements of the same laser in different setups would give different measurements. In order to make meaningful comparisons, the VNPSD was converted into FNPSD by scaling the obtained results with the discriminator slope (which resulted in the current noise power spectral density) and then the tuning coefficient which gave the laser FNPSD in units of  $\text{Hz}^2/\text{Hz}$ . The FNPSD is intrinsic property of the laser under test and independent of the measurement setup. Fig. 4.7a. shows the measured FNPSD for one of the QCL (the packaged CM7-CIA120 laser in table (4.1)) studied here.

For the FNPSD measurements, it was ensured that the chosen discriminator slope was sufficiently high such that the recorded data was not dominated by the intrinsic intensity fluctuation of the laser itself. A direct measurement of the laser intensity noise was also performed by tuning the laser out of the absorption line and measuring the FNPSD in a region close to the absorption line where the gas cell has complete transmission (eg. at

$I = 356.5$  mA in fig. 4.6a.). Additionally, the noise floor of the measurement setup was recorded in order to ensure that the measured laser FNPSD was not dominated by the noise of the measurement setup (photodiode + spectrum analyzer/oscilloscope). For the measurement of the noise floor, the laser input to the gas cell was blocked and an FNPSD of the background photodiode signal was measured. Fig. 4.7b. shows these measurements along with the laser FNPSD. A few things could be noted here. The noise peaks around 100 Hz had a dominant contribution from the laser intensity noise. Spurious noise peaks in the  $> 10^4$  Hz region appear due to noise of the measurement setup itself. These were attributed to other noisy electronics in the lab around the QCL characterization setup (e.g. Turbomolecular pump drivers). Additionally, the frequency and intensity noise could have a significant contribution from the noise floor of the measurement setup. This problem could be mitigated by a lower-noise photodiode (which was the dominant source of noise for the noise floor measurements here). Nonetheless, the measured frequency and intensity noises were treated as upper limit here which was sufficient to gauge the performance of the laser.

The optical spectrum,  $S_E(\nu)$ , of the laser under test can be calculated from the measured FNPSD,  $S_{\delta\nu}(f)$  as [166–168],

$$S_E(\nu) = 2 \int_{-\infty}^{\infty} e^{-i2\pi\nu\tau} \left[ E_0^2 e^{i2\pi\nu_0\tau} \exp\left( -2 \int_0^{\infty} S_{\delta\nu}(f) \frac{\sin^2(\pi f\tau)}{f^2} df \right) \right]. \quad (4.10)$$

Due to the involved numerical integration and ease of introducing numerical artifacts [169], here a simple approximation was employed to calculate the linewidth of the QCL after obtaining the FNPSD. The concept of the  $\beta$ -separation line [160,170] was used which divides the FNPSD spectra into two halves (fig. 4.8). The  $\beta$ - separation line, as a function of the measurement frequency  $f$ , is defined as,

$$S_{\delta\nu}(f) = \frac{8\ln(2)}{\pi^2} f. \quad (4.11)$$

For the laser under test, the components of noise with  $S_{\delta\nu}(f) > (8\ln(2)/\pi^2)f$ , also known as the slow-modulation area (purple shaded area in fig. 4.8), contribute to linewidth of the

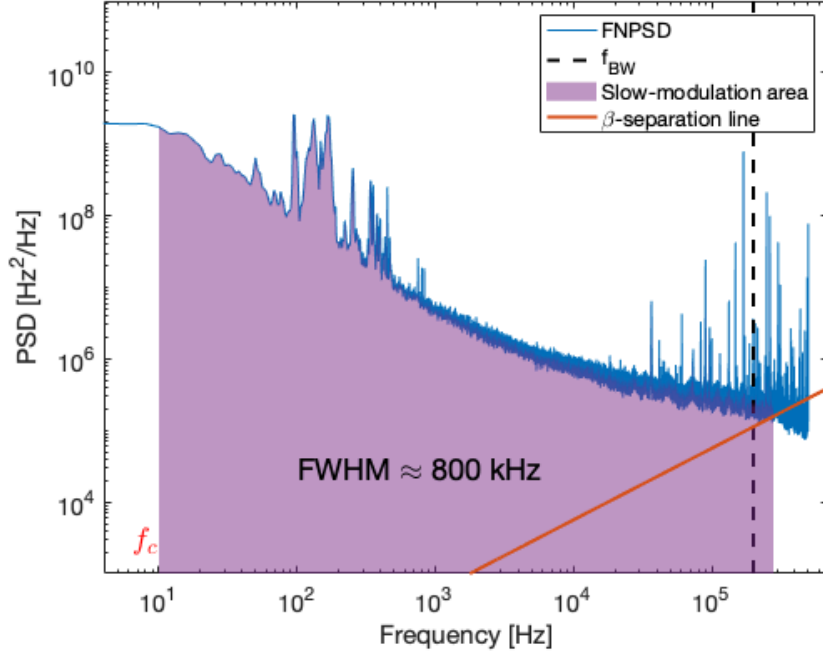


**Figure 4.8 QCL linewidth and modulation bandwidth measurements.** The linewidth of the QCL is given by the area of the slow-modulation area (purple-shaded area) defined by the  $\beta$ -separation line (orange line). The linewidth was measured for an observation time of 100 ms corresponding to a cut-off frequency of  $f_c = 10$  Hz. The measured modulation bandwidth is shown by the black-dashed line.

laser. The regions of FNPSD with  $S_{\delta v}(f) < (8\ln(2)/\pi^2)f$  only contribute to the wings of the lineshape of a free-running laser and do not affect the linewidth. The FWHM linewidth can then be approximately determined from the surface area  $A$  of the slow-modulation area as [160, 170],

$$\text{FWHM} = \sqrt{8\ln(2)A}. \quad (4.12)$$

The surface area is the total geometrical area under the FNPSD obtained between a lower cutoff frequency  $f_c$  and all frequencies  $f > f_c$  for which the laser's  $S_{\delta v}(f)$  exceeds the  $\beta$ -separation line. The frequency  $f_c$  defines the observation time  $\tau_0$  in which the linewidth was measured. Typically, the frequency  $f_c$  is chosen to be 1 Hz or 10 Hz corresponding to an observation time of 1 s or 100 ms respectively. Here, an observation time of 100 ms corresponding to  $f_c = 10$  Hz was chosen. The measured linewidth was  $\sim 800$  kHz which can

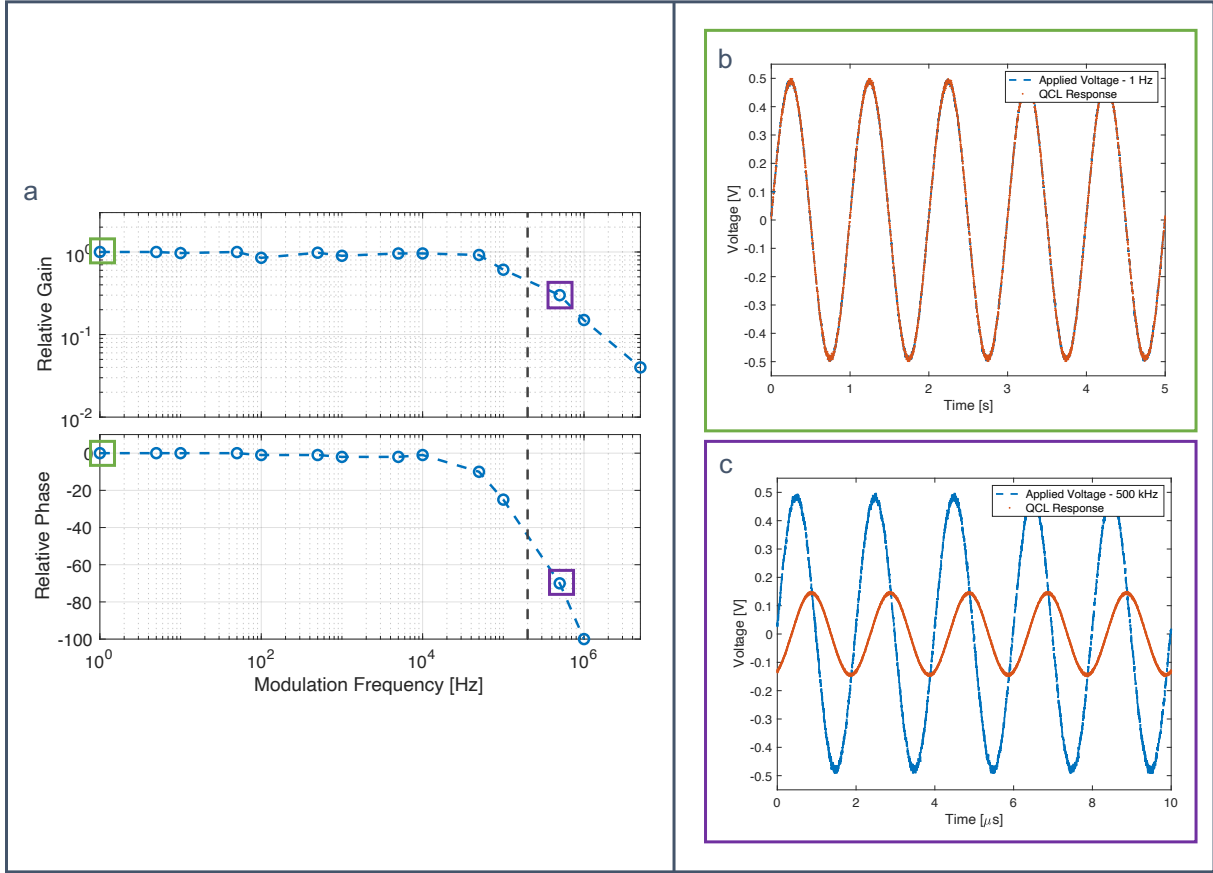


**Figure 4.9 QCL modulation bandwidth measurements.** a) Bode-frequency and Bode-phase plots showing the modulation response of the packaged CM7-CIA120 QCL. The measured response was first scaled by the discriminator slope (see fig. (4.6a)) and then compared to the amplitude of the applied modulation voltage to obtain the relative gain. The relative phase was calculated by observing the lag in time of the QCL response with respect to the applied modulation. The dashed-black line depicts the measured modulation bandwidth. b), c) Two measurements of the response of the QCL under a modulation of 1 Hz and 500 kHz. The QCL followed the modulation perfectly at 1 Hz, but lagged considerably in the phase and amplitude response when modulated at 500 kHz.

be observed in fig. 4.8.

An additional measurement can be carried out on the same frequency-discriminator setup in order to measure the modulation bandwidth of the laser [147] (shown in fig. (4.9)). This is important as the knowledge of the modulation index along with the laser FNPSD and the  $\beta$ -separation line allows for predicting whether or not the laser can be tightly locked

and narrowed irrespective of the exact locking method. For this, the QCL was once again tuned to the side of the absorption line where the intensity was a linear function of the laser frequency. The QCL was then modulated by modulating the current supplied to the laser. In order to modulate the current, here, a small-amplitude low-frequency sine wave was applied on the voltage modulation port of the current driver. The amplitude of the modulation was kept small enough ( $\sim 0.1$  mA corresponding to a voltage modulation of  $0.5 V_{pp}$ ) such that the QCL remained in the linear region of the frequency discriminator. The photodiode response was recorded as the QCL was modulated. At sufficiently low frequencies (for example at 1 Hz or 10 Hz), it can be assumed that the laser follows the modulation perfectly and any lag in the photodiode phase or attenuation of the photodiode amplitude response in comparison to the scaled modulation can be attributed to technical factors like optical path length, cable lengths, electronic delays and attenuation, etc.. Fig. (4.9b) shows an applied modulation voltage of amplitude  $0.5 V_{pp}$  and a frequency of 1 Hz (blue). The laser followed the modulation perfectly as can be seen from the measured photodiode response (orange). The measurement at the initial low frequency served as a calibration of the measurement system. The same measurement was then carried out with increasing modulation frequencies. Fig. (4.9c) shows an applied modulation voltage of amplitude  $0.5 V_{pp}$  and a frequency of 500 kHz (blue). The laser could not follow the modulation (orange). Thus, beyond some frequency, the QCL response started lagging in phase and amplitude. The frequency,  $f_{BW}$ , at which the QCL response is 3dB smaller in amplitude than the first measurement is the modulation bandwidth of the laser. Plotting the frequency and phase response of the laser with respect to the input modulation on a Bode-frequency and Bode-phase plot (fig. (4.9a)) gives complete information of the modulation response of the laser. For the QCL under test here (the packaged CM7-CIA120 laser in table (4.1)), a modulation bandwidth of  $\sim 200$  kHz (dashed-black line in fig. (4.9a)) can be observed from the bode plots which is typical for DFB-QCLs.

Comparing the  $f_{BW}$  and the extent of the slow-modulation area, three distinct situations

may arise for any laser under test.:

- The modulation bandwidth  $f_{\text{BW}}$  is higher in frequency than the entire slow-modulation area of the laser. This would imply that the laser linewidth (which is the FNPSD in the slow-modulation area) can be narrowed by suitable feedback signal to the laser. It would thus be possible to correct for the laser frequency noise which contributes to the laser linewidth and a tight lock is achievable.
- The modulation bandwidth  $f_{\text{BW}}$  lies in the slow-modulation area. Since the laser cannot be modulated properly above the  $f_{\text{BW}}$ , contribution to the laser linewidth from frequency noise in the spectral region  $f > f_{\text{BW}}$  cannot be effectively corrected. This would imply that a laser cannot be tightly locked.
- The modulation bandwidth  $f_{\text{BW}}$  lies at the edge of (or slightly inside) the slow-modulation area. This is a borderline case. By use of suitable differentiator parameters in the feedback loop which attempts to lock the laser, it could be possible to achieve a tight lock. This was the case for the QCL studied here as can be seen in fig. [4.8]. This particular QCL could be tightly locked to the stabilized OFC.

#### 4.2.1.1 Different QCLs investigated in this work

In order to drive weak ro-vibrational transitions in  $\text{N}_2^+$ , a high-powered ( $> 100$  mW) QCL with low intrinsic noise that could be locked to our OFC was required. Since QCL manufacturers often do not characterize the spectral purity of free-running lasers, many QCL chips from several manufacturers were investigated here. Table 4.1 shows different laser chips characterized as a part of this thesis.

It can be noted that QCLs investigated here varied widely in their free-running characteristics and different QCLs (even from the same manufacturer) varied in linewidth from  $< 1$  MHz to  $> 5$  MHz. The output powers varied from  $< 60$  mW to  $> 400$  mW for the

QCL Chip Number	Manufacturer	Driver	FWHM	Comments
#sbcw8358 DN	Alpes Lasers	Homemade Driver	1 – 2 MHz	160 mW power. Laser malfunction after ~ 10 hours of continuous operation.
#sbcw5339 DN	Alpes Lasers	Homemade Driver	> 3 MHz	60 mW low output power, poor beam quality.
21045-MHF	Daylight Solutions	Daylight Driver	< 3 MHz	250 mW output power. EC design. Laser exhibited discrete mode jumps and could not be modulated.
#sbcw10534 DN	Alpes Lasers	QCL1000LAB	> 5 MHz	80 mW output power. Intrinsically noisy laser.
#sbcw10649 DN	Alpes Lasers	QubeCL	~ 7 MHz	100 mW output power. Intrinsically noisy laser.
CM7-CIA120	Adtech Photonics	QubeCL	1.6 MHz	~ 400 mW output power. Laser in homemade housing.
CM7-CIA124	Adtech Photonics	QubeCL	1.7 MHz	~ 400 mW output power. Laser in homemade housing.
CM7-CIA120	Adtech Photonics	QubeCL	800 kHz	~ 400 mW output power. Laser in HHL packaging

**Table 4.1 Different QCLs investigated in this thesis.** Several QCLs were studied here and linewidth  $< 1$  MHz to  $> 7$  MHz were measured. Many QCLs could not be locked due to the large linewidths. The CM7-CIA120 and CM7-CIA124 chips had favourable properties and were chosen for precision spectroscopy of  $N_2^+$ .

chips studies here. It was evident that not all the QCLs investigated here could be locked rendering them unsuitable for  $N_2^+$  spectroscopy.

Fig. 4.10 shows a comparison of three different QCL chips: the #sbcw10649 DN (purple),

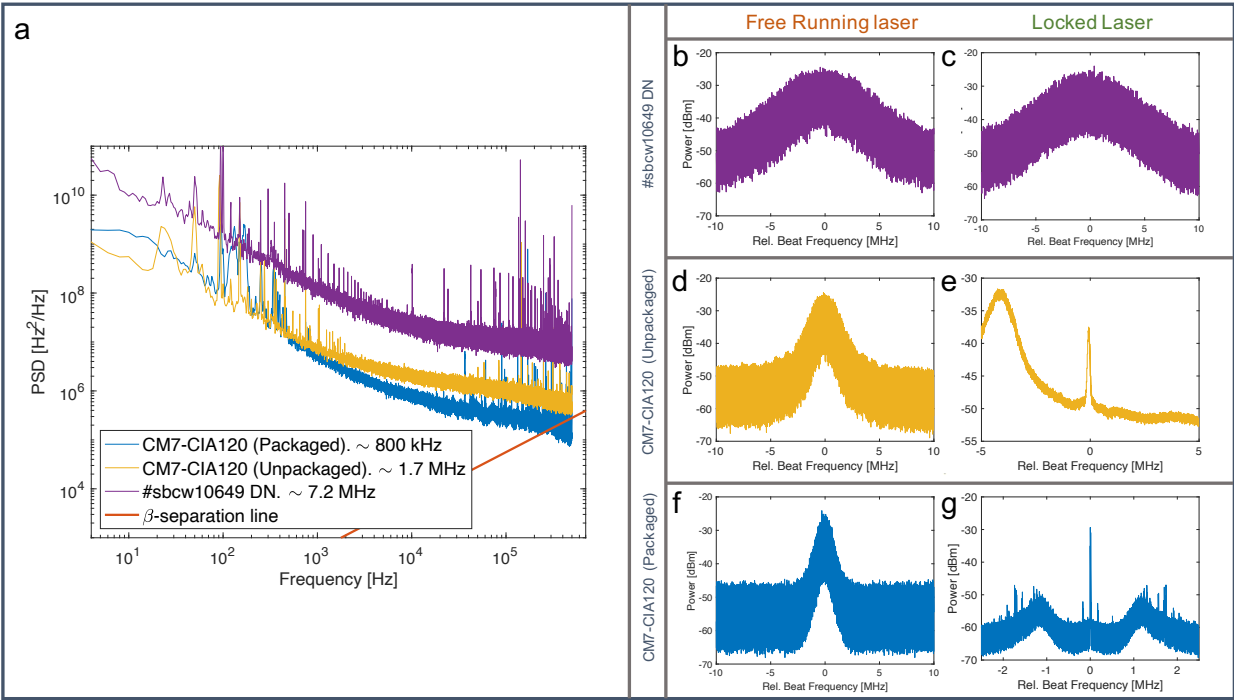


**Figure 4.10 Comparisons of linewidths and locking performance of different QCLs.** (a) FNPSD of three different QCLs showing linewidths of  $\sim 7.2$  MHz (purple),  $\sim 1.7$  MHz (yellow) and 800 kHz (blue). (b)-(e) Free-running and locked beat notes of the lasers with the OFC.

the CM7-CIA120 in a homemade housing (labelled "Unpackaged") and the CM7-CIA120 in a High-Heat-Load (HHL) package (labelled "Packaged"). The panel on the left is a measurement of the FNPSDs for the lasers. All lasers had a modulation bandwidth of 200 – 300 kHz. Locking of all three lasers was attempted via the locking scheme discussed in section 4.2.2. The beat note of the free-running and the locked lasers (right panel) with the OFC is also shown for comparison. All lasers were operated under similar conditions and by the same current driver in order to eliminate effects due to laser-driver noise.

The #sbcw10649 DN (purple) featured a high frequency noise leading to a large linewidth of at least  $\sim 7.2$  kHz (see fig. 4.10a.). Since the FNPSD did not meet the  $\beta$ -separation line in the measured frequency range and higher frequency measurements were restricted by the memory availability of the available oscilloscope, the linewidth was estimated based on a

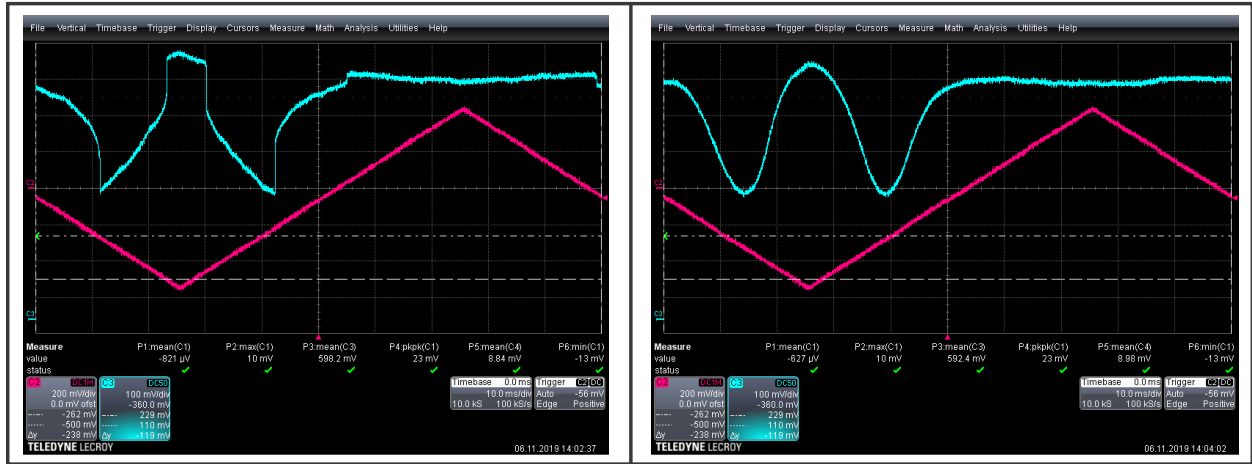


**Figure 4.11** Effects of optical feedback into the QCL. The  $N_2O$  absorption lines were heavy distorted (left) due to unwanted optical feedback into the laser. A  $-30$  dB optical isolator was used to prevent feedback resulting in stable QCL operation(right).

simple linear fit to the high frequency tail of the laser frequency noise. The estimated free-running linewidth was verified by the beat note measurement of the free-running QCL with our OFC (Fig. 4.10b.). Given that the  $f_{BW} \ll f_{\beta}$ , the laser could not be tightly locked. This was seen by the absence of a coherent locking peak in the locked beat note spectra (Fig. 4.10c.). This QCL could only follow the OFC without any significant linewidth reduction under locked conditions.

The Unpackaged CM7-CIA120 (yellow) featured a smaller linewidth of  $\sim 1.7$  MHz (Fig. 4.10a.). This was treated as a borderline locking case where  $f_{BW} \lesssim f_{\beta}$ . The free-running beat note spectra was significantly narrower (Fig. 4.10d.). The laser could “almost” be locked tightly to the OFC. A coherent peak of  $\sim 15$  dB could be observed at the locking point (Fig. 4.10e.). However, an increased noise was observed close to the locking point. The laser lock, although tight, was unstable and required frequent re-locking. This behavior was attributed to uncontrolled optical feedback into the laser.

The Packaged CM7-CIA120 (blue) featured an even smaller linewidth of  $\sim 800$  kHz (Fig. 4.10a.). Here,  $f_{BW}$  was comparable to  $f_{\beta}$ . The laser was a borderline locking case as well. The reduction of the free-running linewidth was most likely due to better shielding of the

laser chip from electronic noise in the HHL package (Fig. 4.10f.). Additionally, a  $-30$  dB optical isolator<sup>17</sup> was used to limit unwanted optical feedback from the stabilization setup into the lase. Fig. 4.11. shows the distortion in a molecular absorption spectrum due to optical feedback into the laser<sup>18</sup>. Under these conditions, this QCL could be tightly locked to the OFC (Fig. 4.10g). A Signal-to-Noise ratio (SNR) of  $\sim 30$  dB was measured on the coherent peak of the locked spectra. The small noise peaks appearing in the locked spectra were attributed to noisy electronics present in the vicinity of the laser. Servo bumps appear at  $> 1$  MHz indicating the achievable bandwidth of the feedback loop.

#### 4.2.1.2 Effect of current noise of QCL drivers

QCLs are sensitive devices with large current tuning coefficients of the order of  $400 - 900$  MHz/mA. The current noise of the QCL driving electronics directly impacts its free-running spectral properties. A detailed study on the effect of the current noise on the QCL spectral characteristics has been done in the past [147, 152]. It has been shown that when a noisier current is used to supply the QCL, the additional current noise induces fluctuations of the laser chip temperature, and therefore of the optical frequency. The white current noise is scaled by the dynamic response (tuning coefficient) of the QCL at low frequencies and results in an increased FNPSD [147, 152]. Depending on the exact tuning coefficient, current noise densities above  $1$  nA/Hz<sup>1/2</sup> of the driving electronics can lead to several MHz of free-running linewidths. Thus, low-noise current drivers are essential for sub-MHz operations. QCLs also typically operate at voltages on the order to  $10$  V to  $> 15$  V rendering many of the commercially-available low-noise semiconductor-laser drivers unsuitable since they typically have a maximum compliance voltage of  $< 8$  V. Thus, in order to choose a suitable current

---

<sup>17</sup>Thorlabs I4500W4

<sup>18</sup>Note: In order to avoid optical feedback during frequency noise measurements of other lasers, the path to the stabilization setup was blocked. Additionally, it was verified that blocking the path and installing an optical isolator had the same effect in the case of CM7-CIA120

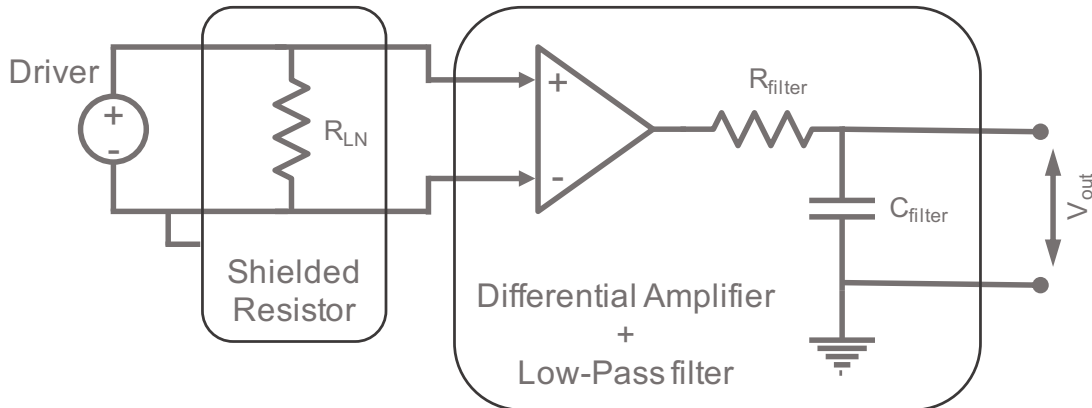


**Figure 4.12 Schematic of setup for current noise measurements.** The current noise of the driver was converted into voltage noise by a shielded precision resistor. The voltage noise was amplified by a differential amplifier and recorded on a scope. A scaled DFT was performed to extract the current noise.

drive for low noise operation, two commercially-available current drivers and one homemade current driver were investigated here.

For the characterization of the current noise of the drivers, the measurement setup shown in 4.12 was used. The current noise of the driver was converted into voltage noise by a precision metal film resistor<sup>19</sup>. The resistor had a low tolerance in the resistivity which allowed for accurate scaling of the measured voltage to current. The resistor was shielded in a metal box grounded to the driver in order to limit spurious noise pickup from the environment. Since the voltage noise was small, the voltage across the resistor was amplified by a factor of  $\times 10^4$  using a low-noise and low-drift differential amplifier<sup>20</sup>. The amplified voltage was low-pass filtered in order to remove high-frequency noise and recorded on an oscilloscope. The data was Fourier transformed [164, 165] in order to obtain the voltage noise which is then scaled by the resistor's value and the amplification factor in order to obtain the current noise of the driver.

Fig. 4.13a. shows the current noise of three drivers investigated as a part of this thesis. The noise floor of the measurement setup was measured when the resistor was shorted. Of

<sup>19</sup>CAR7 10 $\Omega$  resistor with a 25 ppm/K thermal coefficient of resistance and  $\pm 0.1\%$  tolerance

<sup>20</sup>SP 1'004 Differential Amplifier - Department of Physics, University of Basel

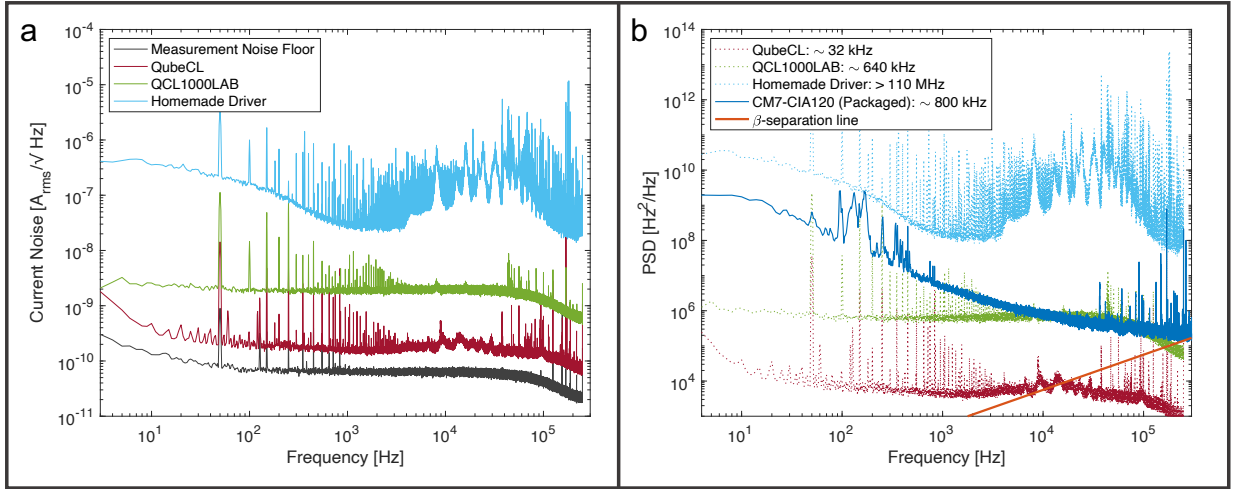


**Figure 4.13 Comparisons of current noise of different drivers.** (a) Measured current noise of three different QCL drivers investigated in this thesis. (b) Contributions to the free-running QCL linewidths due to the current noise of the drivers (dotted traces) assuming a tuning coefficient of 421.1 MHz/mA. Low-noise performance (solid blue trace) could only be achieved when operating with the QubeCL driver (red dotted trace).

the three drivers, the QubeCL driver showed the best noise performance of  $\sim 2$  nA/Hz $^{1/2}$ . This driver was used to drive the lasers for stabilization and locking.

Fig. 4.13b shows the contribution of the driver current noise to the frequency noise of the CM7-CIA120 laser. For this the current noise is scaled by the tuning coefficient of the laser. The low frequency noise of the laser (solid blue trace) could only be recorded when using the QubeCL driver. The contribution to the linewidth of the free-running chip due to the current noise of the QubeCL driver is  $\sim 32$  kHz (dotted red trace). The QCL1000LAB and the homemade drivers would have contributed  $\sim 640$  kHz (dotted green trace) and  $> 110$  MHz (dotted light-blue trace) in linewidth respectively and low-noise free-running performance would not have been achieved. The results of the current noise measurements for different drivers are summarized in Table 4.2.

Driver	Manufacturer	Current Noise	Linewidth Contribution
Homemade	–	$\sim 100 \text{ nA/Hz}^{1/2}$	$> 110 \text{ MHz}$
QCL1000LAB	Wavelength Electronics	$3 \text{ nA/Hz}^{1/2}$	$\sim 640 \text{ kHz}$
QubeCL	ppqSense	$400 \text{ pA/Hz}^{1/2}$	$\sim 32 \text{ kHz}$

**Table 4.2 Summary of current noise measurements for three different QCL drivers.**

## 4.2.2 Stabilization Setup

This section deals with the locking of our Mid-IR QCL to the OFC which was itself stabilized to the cavity-stabilized 729 nm laser and referenced to the ultrastable 1572 nm laser (see section (4.1.2)). Locking of the QCL results in a narrow linewidth laser which can be used to drive long-lived dipole-forbidden transitions in  $\text{N}_2^+$ . Additionally, since the OFC was referenced to TAI, the frequency of the QCL could be determined absolutely and accurately.

The QCL stabilization setup is shown in Fig. 4.4. Since the QCL had emission in the MIR while the OFC had emission only upto the NIR, the frequency of the QCL was upconverted. This was achieved by a second-order non-linear sum-frequency-generation (SFG) process in a periodically-poled Lithium-Niobate (PPLN) crystal. In order to achieve a decent conversion efficiency, a custom PPLN was simulated [171] and fabricated<sup>21</sup> to fit our requirements. A single grating with a period of  $15.9 \mu\text{m}$  was chosen for SFG operation within a temperature range of  $40 - 50 \text{ }^\circ\text{C}$ . This temperature range was far below the maximum operational temperatures for PPLNs ( $> 200 \text{ }^\circ\text{C}$ ) and demanded slight heating of the crystal above room temperature which allowed for good temperature stability while avoiding issues like water condensation which is often encountered while cooling. Dimensions of  $l = 35 \text{ mm}$ ,  $b = 2 \text{ mm}$  and a fabrication limited  $h = 1 \text{ mm}$  were chosen. This ensured that the QCL radiation was not clipped at the edges of the crystal during its focusing due to the short Rayleigh length.

<sup>21</sup>HC Photonics Corporation

For the SFG, 150 – 200 mW of the QCL power at  $f_{4574}^{\text{QCL}} \approx 4574.12$  nm and  $\sim 500$  mW of the stabilized 729 nm laser at  $f_{729}^{\text{Laser}} \approx 729.34$  (generated by seeding a tapered amplifier<sup>22</sup> (TA) with 25 mW of 729 nm light) were combined on a dichroic mirror and focused into the PPLN. This lead to the generation of  $\sim 150$   $\mu$ W of visible light at  $f_{629}^{\text{SFG}} \approx 629.04$  nm.

The generated light was separated from the QCL and the 729 nm laser by dichroic mirrors and was then used for generating a beat note with the OFC. For the beat note, 2 mW of comb light at 629 nm was super-imposed with  $f_{629}^{\text{SFG}}$  on a polarizing beam splitter. The beams interfered and were spectrally filtered on a diffraction grating<sup>23</sup> following which the beat note was recorded on an avalanche photodetector<sup>24</sup>. The diffraction grating separated out the different comb modes which might otherwise result in an increased background noise on the photodetector. The generated beat note was filtered<sup>25</sup> and amplified<sup>26</sup>. A small portion of the amplified RF power was coupled out<sup>27</sup> for monitoring of the beat note on a spectrum analyzer. The remaining RF beat note power was mixed with a sinusoidal RF signal referenced to the Rb-GPSDO for phase detection. The error signal was filtered and used to lock the QCL via fast and slow current modulation. The processing of the beat note to lock the QCL to the OFC was done by a commercially-available electronics module<sup>28</sup>.

Fig.4.14 shows the beat note of the free-running and locked CM7-CIA120 Packaged QCL with the stabilized OFC. For easier comparison with the drifting unlocked laser, the beat note was expressed on a relative frequency scale centered at 0 MHz. Since the ultrastable 729 nm laser and the OFC had much lower linewidth (due to their locks to the high-finesse optical cavity) than the free-running QCL, the FWHM linewidth of the beat note of  $\sim 800$  kHz in the unlocked case could be attributed to the noise of the free-running QCL and

---

<sup>22</sup>TEC-400-0730-0500, Sacher Lasertechnik GmbH

<sup>23</sup>GH25-24V Thorlabs GmbH

<sup>24</sup>APD210 - Menlo Systems

<sup>25</sup>ZX75LP-105-S+ - Mini Circuits

<sup>26</sup>ZX60-100VH+ - Mini Circuits

<sup>27</sup>ZX30-9-4-S+ - Mini Circuits

<sup>28</sup>mFALC 110 - Toptica Photonics

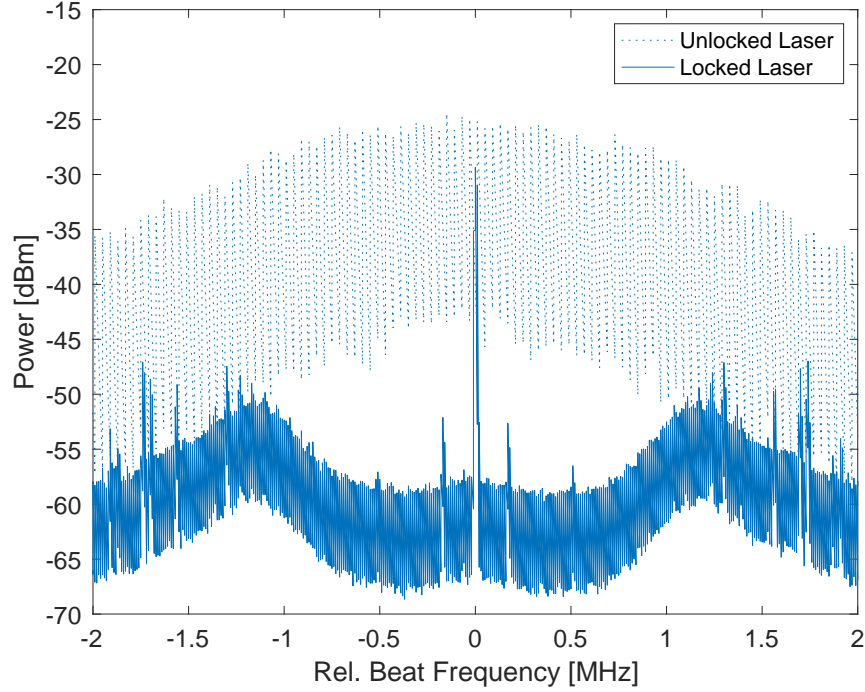


**Figure 4.14 Beat note of the QCL with the OFC.** The beat note of the unlocked QCL (blue-dotted measurement). A FWHM (width  $-3$  dB below the maximum) of  $\sim 800$  kHz was observed as expected. The laser was then locked to the OFC. The linewidth of the in-loop beat note (solid blue measurement) was limited by the resolution bandwidth of the spectrum analyzer. For convenience, both beat notes were expressed on a relative frequency scale centered at 0 MHz.

agreed with the FNPSD measurements. The in-loop locked linewidth was determined to be  $< 100$  Hz by observing the FWHM of the locked beat note. The measurement was limited by the resolution bandwidth of the spectrum analyzer employed.

#### 4.2.2.1 Determination of the QCL frequency

Similar to the determination of the absolute frequency of the 729 nm laser, the frequency of the QCL could be accurately determined by the lock between the laser and the OFC. The frequency of the generated 629 nm radiation after the SFG process could be expressed as,

$$f_{629}^{\text{SFG}} = f_{4574}^{\text{QCL}} + f_{729}^{\text{Laser}}. \quad (4.13)$$

For a lock at a beat frequency of  $f_{4574}^{\text{Beat}}$ ,

$$f_{629}^{\text{SFG}} = q \cdot f_{\text{REP}} \pm 2f_{\text{CEO}} \pm f_{4574}^{\text{Beat}}, \quad (4.14)$$

where  $q$  is the comb mode number of the comb line which interferes with the QCL. The factor 2 in the  $f_{\text{CEO}}$  was due to the comb light at 629 nm being generated from the OFC after a second harmonic generation process.

From 4.6, the comb repetition rate could be expressed in relation to the ultrastable 1572 nm reference laser as,

$$f_{\text{REP}} = \frac{f_{1572}^{\text{US}} \mp f_{\text{CEO}} \mp f_{1572}^{\text{Beat}}}{m}, \quad (4.15)$$

and thus,

$$f_{629}^{\text{SFG}} = \frac{q}{m} \cdot [f_{1572}^{\text{US}} \mp f_{\text{CEO}} \mp f_{1572}^{\text{Beat}}] \pm 2f_{\text{CEO}} \pm f_{4574}^{\text{Beat}}. \quad (4.16)$$

From 4.9 and 4.16, the frequency of the QCL could be expressed as,

$$\begin{aligned} f_{4574}^{\text{QCL}} &= f_{629}^{\text{SFG}} - f_{729}^{\text{Laser}} \\ &= \frac{(q-n)}{m} [f_{1572}^{\text{US}} \mp f_{\text{CEO}} \mp f_{1572}^{\text{Beat}}] \pm [f_{4574}^{\text{Beat}} - f_{729}^{\text{Beat}}]. \end{aligned} \quad (4.17)$$

### 4.2.3 Beam Delivery Setup

Two major problems occurred when aligning the QCL to the center of the ion trap which was used to trap  $\text{Ca}^+$  and  $\text{N}_2^+$  ions. Firstly, the MIR emission of the QCL was invisible to the human eye and outside the bandwidth of operation of commonly available laboratory instruments (e.g. beam profilers, CCD cameras, etc). This made the characterization of the beam quality and subsequently beam shaping and alignment challenging. Secondly, in order to achieve fast Rabi frequencies on the  $\text{N}_2^+$  ion, it was desirable for the QCL to be strongly focused on the ions. However, due to the mechanical construction of our ion trap and the relatively short Rayleigh range of the MIR radiation at 4574 nm, a limit of 50  $\mu\text{m}$  was imposed on the achievable QCL beam waist (radius) determined by Gaussian-beam propagation. For a QCL power of 100 mW, this would then correspond to a Rabi frequency

$\Omega$  of few tens of kHz on the  $S(0)$  ro-vibrational transition in  $N_2^+$  [53]. In order to align the QCL on the ion (spatial and focal alignment), a new measurement technique was adopted here.

#### 4.2.3.1 Characterization of the laser beam profile

For the characterization of the beam shape of the QCL, several knife-edge measurements of the laser beam at various positions along the laser beam path were performed. For these, a blackened blade with a sharp edge was mounted on a micrometer translation stage. A power meter<sup>29</sup> was used to measure the transmitted power after the blade. A fit to the measured power as a function of the blade position then gave the beam waist of the laser at that spot. For the fit, the function,

$$P = P_0 + \frac{P_{\max}}{2} \left[ 1 - \operatorname{erf}\left(\frac{\sqrt{2}(x - x_0)}{w_0}\right) \right] \quad (4.18)$$

was used. Here,  $P_0$  was the background power measured by the power meter,  $P_{\max}$  was the maximum power,  $x_0$  was the position of the knife edge for half the maximum power,  $w_0$  was the beam waist (radius) and erf was the standard error function defined as,

$$\operatorname{erf}(x) = \frac{2}{\sqrt{\pi}} \int_0^x e^{-t^2} dt.$$

Fig. 4.16a. shows a schematic of the laser beam characterization setup. The measured beam waist at two different lasing currents for the packaged CM7-CIA120 QCL is shown in Fig. 4.16b. It could be observed that the beam size was the same irrespective of the current. This was verified for different currents in the entire operational range of the laser. In order to obtain the complete picture, the beam waist was measured along both the horizontal and the vertical axes perpendicular to the laser beam propagation for a few positions. Both measurements agreed with each other within the measurement error indicating a near Gaussian beam characteristics. For later measurements, the beam shape was measured only along the horizontal axis for simplicity.

---

<sup>29</sup>S470C - Thorlabs GmbH

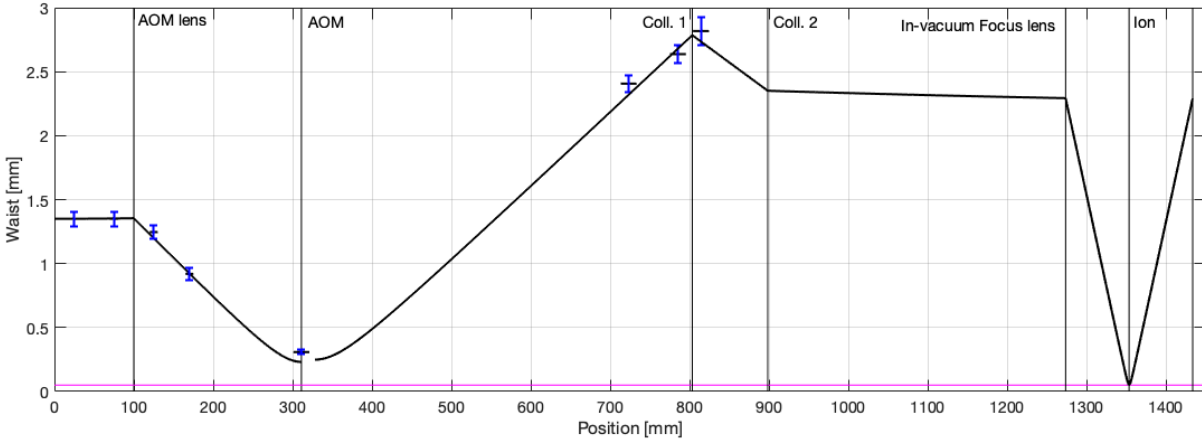


**Figure 4.15 QCL-Ion Alignment.** The beam path of the QCL was simulated following Gaussian beam propagation after measurements of the beam waist. A focus of  $\sim 50 \mu\text{m}$  was expected at the ion position. Note a small discontinuity after the AOM was due to a small change in the beam waist of the light passing through the AOM.

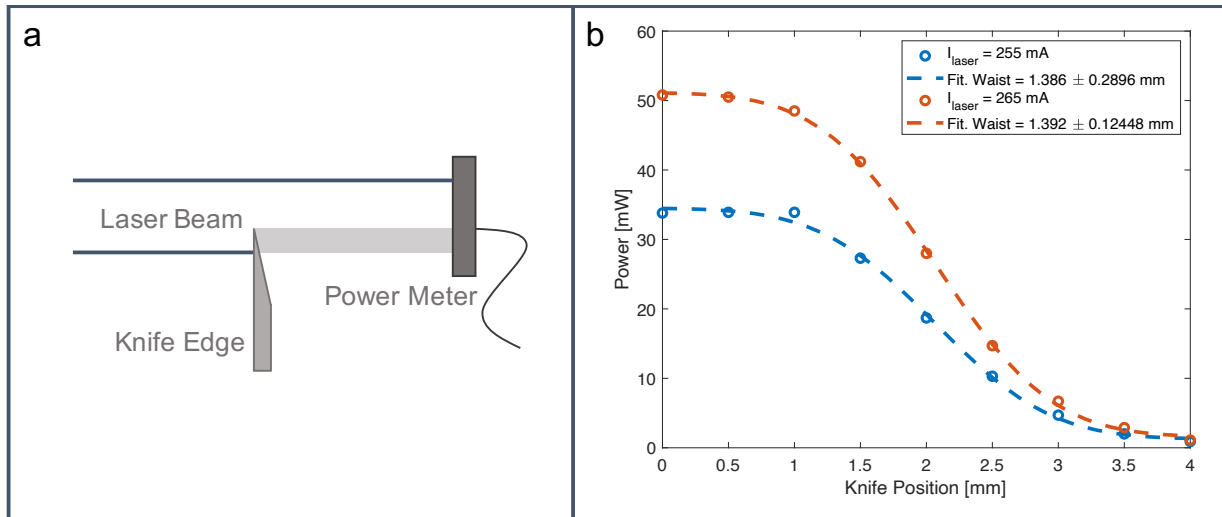


**Figure 4.16 QCL Beam Characterization.** (a) Schematic of the characterization setup used to measure the QCL beam waist. (b) Measured QCL waist at a position along the optical-beam path for two lasing currents (blue and orange points). A fit (with the fitting function given by equation 4.18) was used to determine the beam waist (blue and orange dashed lines).

the “In-vacuum Focus lens” at a distance of  $\sim 75 \text{ mm}$ .

After the alignment of the QCL following the simulation, a beam waist of  $\sim 180 \mu\text{m}$  was measured at the position of the ion (see section (4.2.3.2)) leading to a  $\sim 13$  times weaker

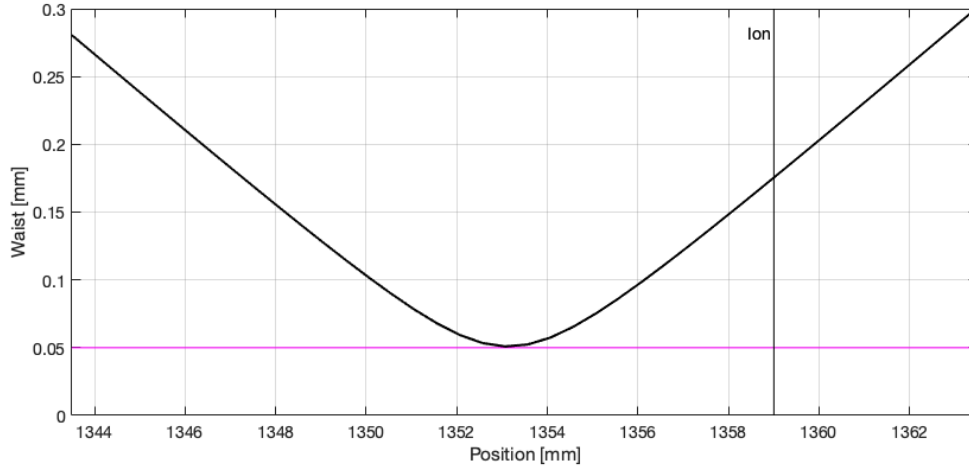


**Figure 4.17 Simulated alignment of the QCL on the ion.** Due to the small Rayleigh length, the QCL diverged quickly after focusing before the ion position. The beam waist at the ion position was thus larger than expected.

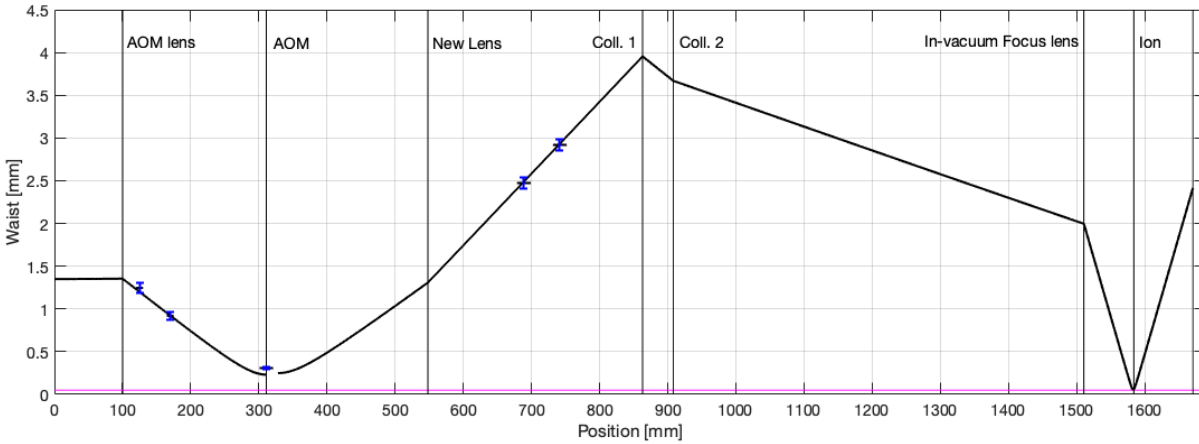


**Figure 4.18 QCL-Ion Alignment.** Due to the focal length shift of the fixed in-vacuum focusing lens, the beam size of the QCL was modified to focus on the ion.

intensity than expected (since intensity scales as  $1/w^2$ ). The reason for this was a finite focal length shift of the “In-vacuum Focus lens” of 5 mm at the wavelength  $\lambda = 4574$  nm. Given the short Rayleigh range of  $z_R = \pi w_0^2/\lambda = 1.72$  mm for a beam waist  $w_0 = 50$   $\mu\text{m}$ , the laser diverged quickly after focusing 5 mm before the actual position of the ion. The simulated result is shown in Fig. 4.17. Since the “In-vacuum Focus lens” was fixed in position, the only other possibility to correct for the focal length shift was by tailoring the beam waist to

be converging at the position of the lens. For this a “New Lens”<sup>33</sup> was added to the beam path to first diverge the beam and the “Coll. 1”<sup>34</sup> and “Coll. 2”<sup>35</sup> lenses converged the beam to the in-vacuum lens. The resultant situation is shown in Fig. 4.6. A beam waist of 57  $\mu\text{m}$  at the position of the ion was achieved.

#### 4.2.3.2 QCL intensity measurements at the ion position

It is known that the interaction of matter with off-resonant radiation causes a shift in the energy levels of the matter due to the ac-Stark effect. In order to align the QCL on the ion and measure the beam waist ( $w_0$ ) of the focused QCL at the ion position, the ac-Stark shift experienced by the  $4S_{1/2}(m = -1/2) \leftrightarrow 3D_{5/2}(m = -5/2)$  Zeeman quadrupole transition of a single trapped  $\text{Ca}^+$  due to the far detuned 4574 nm radiation was recorded. The beam waist of the QCL could be determined by comparison of the measured energy shift with the expected theoretical calculations for a given QCL power.

Fig. 4.19a. shows the reduced energy level diagram of  $\text{Ca}^+$  relevant for this measurement. The  $\text{Ca}^+$  ion was cooled to the ground state of motion in the ion trap and prepared in the ( $m = -1/2$ ) Zeeman component of the ground  $4S_{1/2}$  state [56]. The unperturbed transition frequency,  $f$ , to the excited ( $m = -5/2$ ) Zeeman level of the  $3D_{5/2}$  state was then measured by scanning the 729 nm laser across the transition. For this measurement, the QCL was switched off and the ion experienced no ac-Stark shift. The blue trace in fig. 4.19b. shows this measurement on a relative frequency axis. For convenience and ease of comparison, the frequency of the unperturbed transition was shifted to 0 kHz here. In a second measurement, (shown in orange in 4.19a), the QCL was switched on and the ion was irradiated with focused light from the QCL. This caused a shift in the energy levels and a shifted transition frequency was measured. The orange trace in fig. 4.19b shows the shifted transition-frequency measurement with the QCL focused and aligned on the ion. In this

---

<sup>33</sup>LC5893-E - Thorlabs GmbH

<sup>34</sup>LA5255-E - Thorlabs GmbH

<sup>35</sup>LF5394-E - Thorlabs GmbH

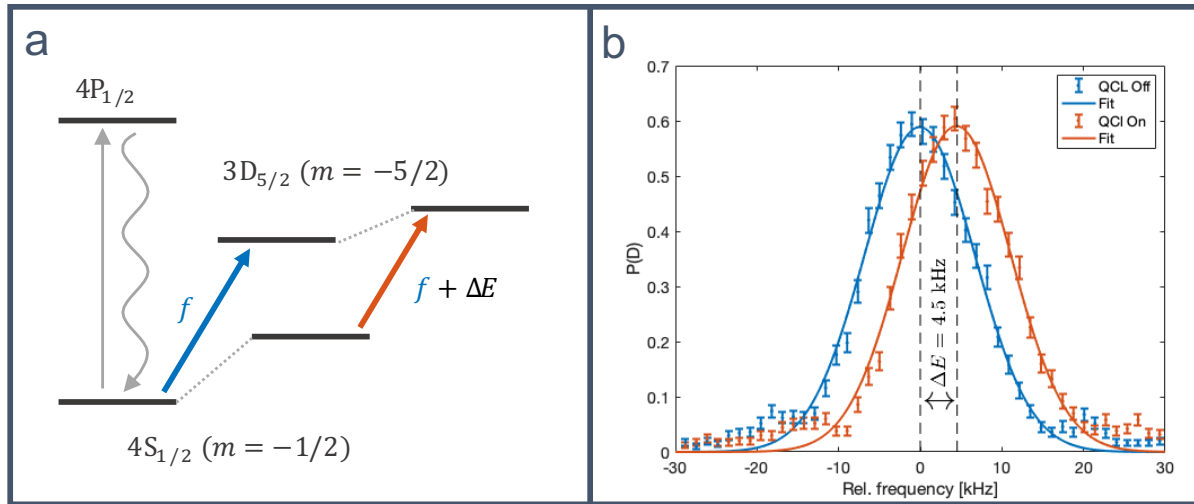


**Figure 4.19 Ac-Stark shift measurements.** (a) Relevant energy levels of the  $\text{Ca}^+$  ion involved in the measurement. (b) Measurement of the  $4S_{1/2}(m = -1/2) \leftrightarrow 3D_{5/2}(m = -5/2)$  transition with the QCL switched off (blue points) and switched on (orange points). The measured lines were fitted with a Gaussian fitting function (blue and orange lines) of the form  $A \cdot e^{-(x-x_0)^2/2s^2}$ , where  $x_0$  was the line center and  $s$  was the standard deviation of the measurements and corresponded to the measurement FWHM. The energy shift,  $\Delta E$ , could be extracted from the fits.

example, a shift of  $\Delta E = 4.5 \text{ kHz}$  was measured which corresponded to a QCL beam-waist of  $58 \mu\text{m}$  for a laser power  $P \approx 78 \text{ mW}$  on the ion. The laser power was estimated based on the power coupled into the vacuum chamber and the transmission of the optical elements (optical viewports and in-vacuum lenses) before the ion. The theoretical calculations of the ac-shift of the individual levels and the shift in the total transition frequency is discussed in Appendix A.

Although the beam waist can be determined by this method a few challenges may arise specially when the energy shifts are small. For example:

- Since the FWHM linewidth of the quadrupole transition in our case was large (a few kHz), very long averaging times were needed in order to measure small shifts. The large linewidth in our case was due to fast magnetic-field noise and/or the noise introduced by the uncompensated fiber delivering the 729 nm light to the experimental table for the measurements.

- In the case where the measured lines may drift due to slow drifts of the magnetic field or the interrogation laser, small shifts may not be detected.

The ac-shift  $\Delta E$  scales as,

$$\Delta E \propto P,$$

$$\Delta E \propto 1/w_0^2,$$

where  $P$  is the power of the laser irradiating the ion and  $w_0$  is the beam waist of the focused laser. Thus, small shifts were often encountered when the QCL was not aligned correctly on the ion (leading to small  $P$ ) or if the light from the QCL was not focused on the ion correctly (leading to large  $w_0$ ). This was often the case during the initial phases of aligning the QCL on the ion making it difficult to measure the ac-shift with a good signal-to-noise ratio.

In our experiments, shifts  $< 1$  kHz were not measurable. A Ramsey measurement was thus adopted in order to measure small shifts. Fig. 4.20 shows the measurement technique. The Bloch sphere representation allows for easier visualization of the technique. The same quadrupole transition from the ground  $|g\rangle = 4S_{1/2}(m = -1/2)$  state to the excited  $|e\rangle = 3D_{5/2}(m = -5/2)$  state was employed. Two separate measurements (shown in panels a and b of fig. 4.20) were carried out in order to detect small ac-shifts.

In a first measurement (panel a of fig. 4.20), the QCL was always switched off and the energy levels of the  $\text{Ca}^+$  ion were unperturbed. The ion was prepared in the ground state ( $|g\rangle$ ). A first 729 nm  $\pi/2$ -pulse with a phase<sup>36</sup>  $\phi = 0^\circ$  excited the ion to the equatorial plane on the Bloch sphere. Following this, the 729 nm excitation laser was switched off and the ion was allowed to evolve freely in the equatorial plane for a certain amount of “wait time” defined by the total dark time  $t_D$  of the Ramsey sequence and the number of spin-echo  $\pi$  pulses ( $N$ ) to be used in the experiment. The example shows the case of  $N = 1$

---

<sup>36</sup>The phase of the laser is defined with respect to the first  $\pi/2$ -pulse. Without loss of generality, the phase of the first  $\pi/2$ -pulse can be chosen to be  $\phi = 0^\circ$ . The phase of the remaining pulses can be changed by changing the phase of the RF drive applied to an AOM in the optical path.

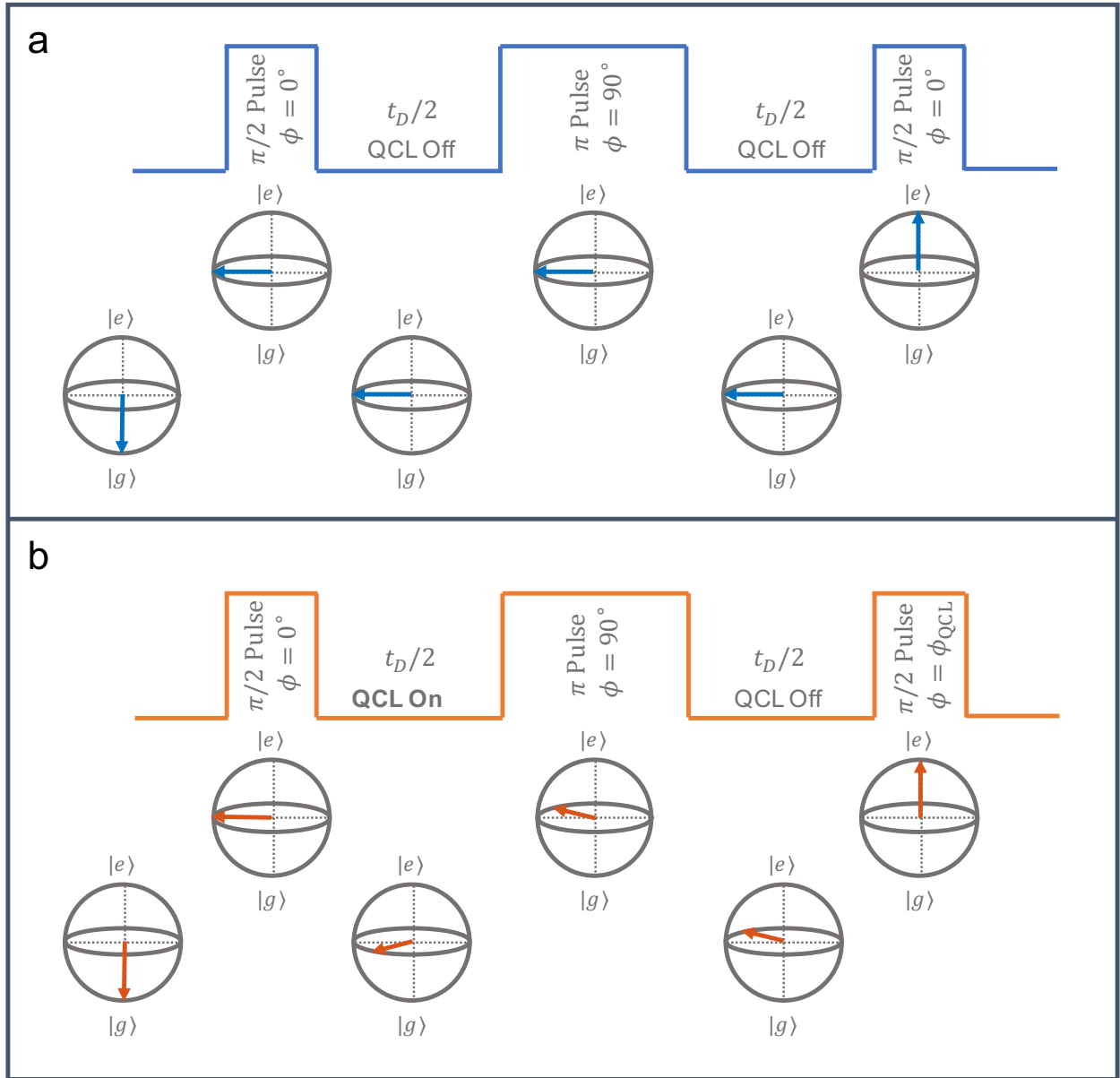


**Figure 4.20 Bloch sphere representation of the Ramsey ac-Stark shift measurement technique.** Two measurements - one with the QCL switched off (blue) and one with the QCL switched on in the odd wait time (orange) were carried out on the  $4S_{1/2}(m = -1/2) \leftrightarrow 3D_{5/2}(m = -5/2)$  transition in  $\text{Ca}^+$ . In the case when the QCL was switched on, an additional phase,  $\phi_{QCL}$ , was accumulated during the wait time due to the ac-Stark shift in the energy levels of the  $\text{Ca}^+$  ion. The power and the beam waist could be estimated from the measured phase shift.

spin-echo pulse. The wait time in the equatorial plane is given as  $t_D/(N + 1) = t_D/2$  here. During the wait time, the ion could accumulate random uncontrolled phase due to

noises like the magnetic field noise. In order to correct for the accumulated random phase, a spin-echo 729 nm  $\pi$ -pulse at a relative phase  $\phi = 90^\circ$  was implemented. The echo pulses suppressed dephasing of the ion during the wait time and thus increased the ion-coherence times significantly which allowed for even longer wait/dark times. The ion was then allowed to evolve freely after the echo pulse for the same wait time during which the accumulated random phase was corrected. Following this, a second 729 nm  $\pi/2$ -pulse excited the ion to the excited state ( $|e\rangle$ ). Ideally, since any random phase collected during the first wait time was corrected in the second wait time, a relative phase of  $\phi = 0^\circ$  for the second  $\pi/2$ -pulse was needed in order to excite the ion to the excited state with maximum probability.

In a second measurement, the ion was prepared in the  $|g\rangle$  ground state and a 729 nm  $\pi/2$  pulse was used to excite the ion to the equatorial plane as before. During the first wait time, the ion accumulated random uncontrolled phase. Additionally, the QCL was also switched on during this wait time which resulted in the ion accumulating an additional phase,  $\phi_{\text{QCL}}$ , due to a shift in the  $|g\rangle$  and  $|e\rangle$  energy levels. The additional phase accumulated (in radians) during the wait time of  $t_{\text{D}}/2$  is given as,

$$\phi_{\text{QCL}} = 2\pi \cdot \Delta E \cdot \left(\frac{t_{\text{D}}}{2}\right). \quad (4.20)$$

The rest of the experiment continued as before. A spin-echo  $\pi$  pulse at a relative phase  $\phi = 0^\circ$  was implemented. During the second wait time, the QCL was switched off. This ensured that random phase collected by the ion due to noise was corrected while the phase accumulated due to the QCL in the first wait time was not nullified. Due to the additional phase accumulated, a relative phase of  $\phi = \phi_{\text{QCL}}$  was needed for the second  $\pi/2$  pulse in this measurement to excite the ion to the excited state with maximum probability.

Thus, in order to measure the acquired phase  $\phi_{\text{QCL}}$ , the relative phase  $\phi$  of the second  $\pi/2$  pulse was scanned and the probability to excite the ion to the excited  $|e\rangle$  state ( $P(\text{D})$ ) was recorded with and without the QCL during the first wait time. An example of such a measurement is shown in Fig. 4.21. Here, a total dark time  $t_{\text{D}} = 300 \mu\text{s}$  with  $N = 1$

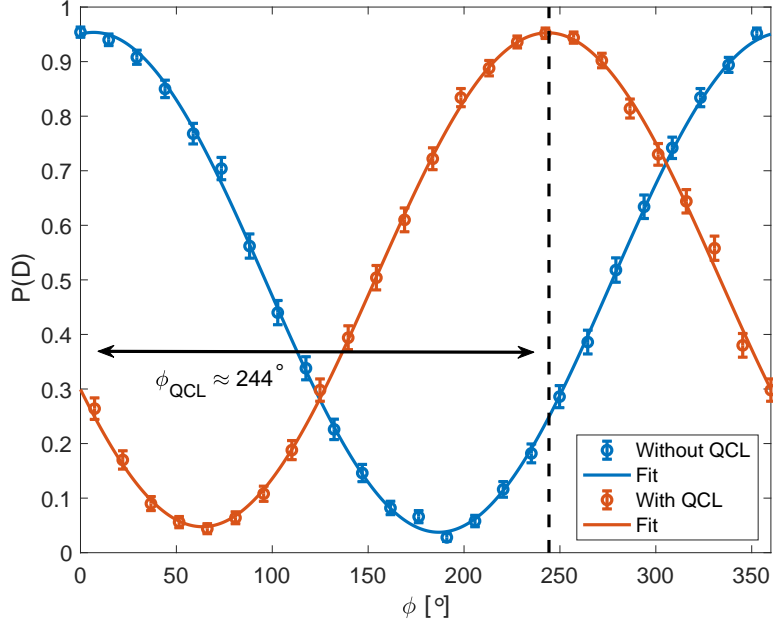


**Figure 4.21 Ramsey ac-Stark shift measurement.** Measurement of the phase shift of the second  $\pi/2$  pulse ( $\phi$ ) due to the ac-Stark shift of the QCL. When the QCL was completely switched off (blue), a phase  $\phi = 0^\circ$  was needed to excite the ion with maximum probability. With the QCL switch on during the odd wait time (orange), an additional phase  $\phi_{\text{QCL}} \approx 244^\circ$  was accumulated causing a shift in the scan. A fitting function of the form  $A \cdot \cos(x + \phi) + C$  was used to fit the measurements and extract the phase shift.

spin-echo pulses was used which corresponded to a wait time of  $150 \mu\text{s}$  during which the QCL irradiated the ion causing a phase gain of  $\phi_{\text{QCL}} = 244^\circ = 4.2586 \text{ rad}$ . The ac-Stark shift could then be calculated from equation (4.20) as,

$$\Delta E = \frac{2}{t_D} \cdot \frac{\phi_{\text{QCL}}}{2\pi} = \frac{2}{300 \times 10^{-6}} \cdot \frac{4.2586}{2\pi} = 4.51 \text{ kHz},$$

and the beam-waist of the QCL on the ion could be extracted by comparison to theoretical calculations for the QCL power of  $\sim 78 \text{ mW}$ .

In the Ramsey measurement, the phase shift due to the QCL was accumulated during the dark times. Thus, for small ac-Stark shifts, large phase shifts could be accumulated by longer wait times. This provided a large improvement in the achievable signal-to-noise ratios when compared to Rabi measurements. In our experiments, ac-Stark shifts as small

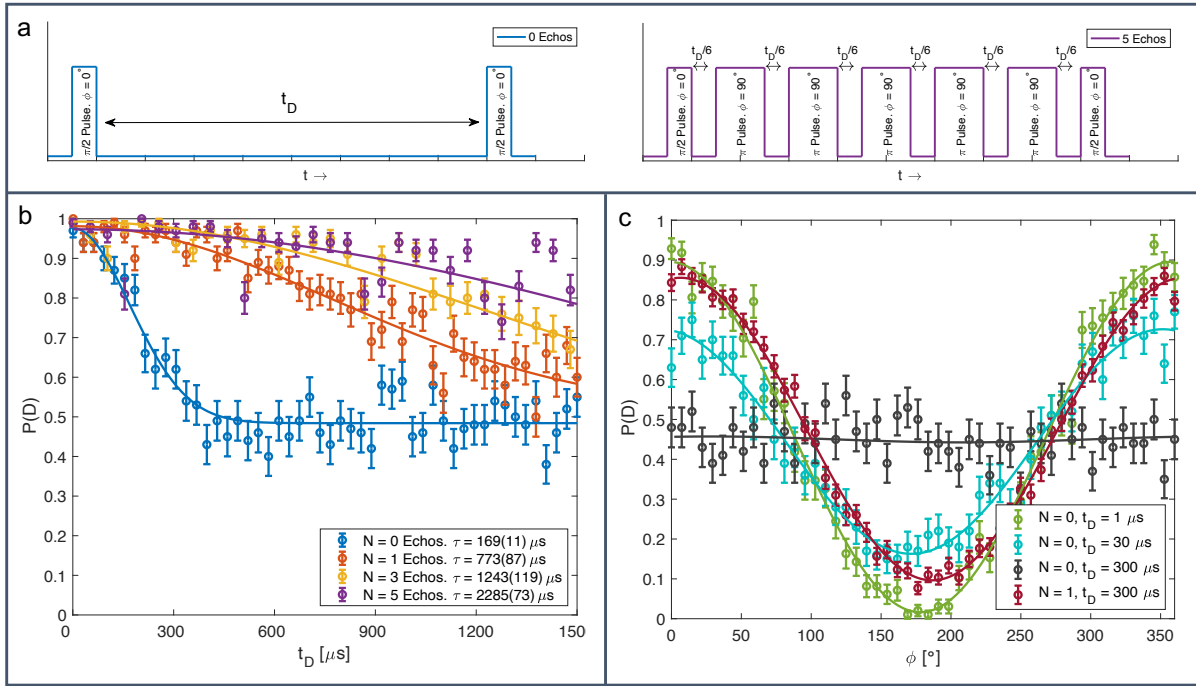


**Figure 4.22 Measurements of the  $\text{Ca}^+$  ion coherence.** (a) Two examples of the relevant experimental pulse sequence for characterizing the coherence of a single  $\text{Ca}^+$  ion. (b) Loss in ion coherence as a function of the total dark time. The ion lost its coherence rather quickly when no ( $N = 0$ ) echo pulses were employed (blue). Adding spin-echo pulses (orange, yellow and purple) helped in reducing the decoherence. A Gaussian fitting function of the form  $A \cdot e^{(-t_D^2/(2\tau^2))} + C$  was used to extract the coherence time. (c) Four measurements showing the loss in contrast during the scan of the phase of the second  $\pi/2$  pulse as a function of spin echos. When no ( $N = 0$ ) spin echos were employed and the dark time was small ( $t_D = 1 \mu\text{s}$  - green), the fringe could be measured with a good contrast. As the dark time was increased ( $t_D = 30 \mu\text{s}$  - light blue trace), a loss in contrast could be observed. At  $t_D = 300 \mu\text{s}$  (black trace), the fringe contrast was completely lost and it would not have been possible to perform a good fit to extract the phase of the laser pulse. Addition of a single ( $N = 1$ ) spin echo was sufficient to restore the contrast of the fringe at  $t_D = 300 \mu\text{s}$ .

as 50 Hz could be detected with good signal-to-noise ratios by the Ramsey measurement compared to 1 kHz by the Rabi measurements. An increase in sensitivity of a factor of 20 was thus observed. The ion could lose its coherence for longer wait times leading to a loss in the fringe contrast when the phase of the second  $\pi/2$  pulse is scanned. However, the loss of coherence can be compensated by the use of more spin-echo pulses. Fig. 4.22 shows the loss in coherence of the  $\text{Ca}^+$  ion in our case as a function of the total dark time  $t_D$ . When

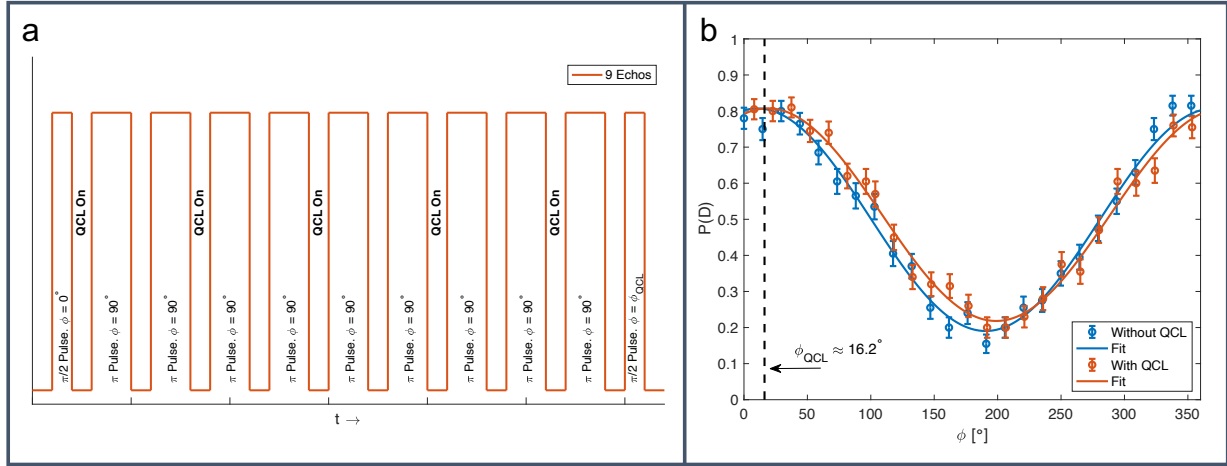


**Figure 4.23 Measurement of small ac-Stark shifts.** (a) An example of the relevant pulse sequence with  $N = 9$  echo pulses for measuring small ac-Stark shifts on the  $\text{Ca}^+$  ion. The QCL was switched on during the odd wait times only. (b) Measurement of 100 Hz of ac-Stark shift due to the QCL. A total dark time of 900  $\mu\text{s}$  with  $N = 9$  echos was employed. Good fringe contrast was observed for the phase scans.

no ( $N = 0$ ) spin-echo pulses are employed (left panel on fig. 4.22a.), the ion quickly loses coherence around  $t_D = 169 \mu\text{s}$  (blue trace in fig. 4.22b.). The coherence time increased with the number of echos. The effect of spin-echos on the ion-coherence times can be seen in fig. 4.22b. The ion maintained coherence for longer dark times as the number of spin-echo pulses increased from  $N = 0$  to  $N = 5$ . It could be noted that only odd numbers of spin-echo pulses were employed since even number of echo pulses did not help in ion-noise suppression. As stated earlier, the wait time between pulses can be given as  $t_D/(N + 1)$ . Fig. 4.22c. shows the loss contrast when the phase of the second  $\pi/2$  pulse is scanned as a function of the total dark time. It can be observed that there was a loss in contrast due to decoherence as the dark time increased from  $t_D = 1$  to  $t_D = 300 \mu\text{s}$ . Implementation of a single spin-echo pulse was sufficient to restore the contrast of the scan at  $t_D = 300 \mu\text{s}$ .

Fig. 4.23 shows a measurement of an ac-Stark shift  $\Delta E$  of  $\sim 100$  Hz experienced by the ion due to a misaligned QCL. For the measurement, a total dark time of 900  $\mu\text{s}$  with 9 echo pulses was used. The pulse sequence is shown in Fig. 4.23a. Note that the QCL was switched

on only at odd wait times in order to accumulate phase. Switching on the QCL at even wait times would result in cancellation of the accumulated phase of the previous wait time. As expected, a total phase shift of,  $\phi_{\text{QCL}} = (2\pi \cdot 100 \cdot (900 \times 10^{-6}/2)) = 0.2827 \text{ rad} = 16.2^\circ$  was measured (fig. 4.23b).

In addition to the increased measurement sensitivity, the Ramsey measurements require less averaging. The requirements on the ground-state cooling of the ion were also relaxed and decent fringe contrasts could be measured with imperfectly cooled ions. Thus, the measurements could be carried out at much faster rates. In order to mitigate any effects of magnetic field drifts during measurements, the measurements with and without QCL were interleaved.

In order to simplify alignment of the QCL on the ion, an automated alignment procedure was developed. For this a piezoelectric-mirror mount<sup>37</sup> was installed. This allowed for the scanning of the QCL on the ion along the horizontal and vertical directions by scanning the voltages (labelled “ $V_H$ ” and “ $V_V$ ” in fig. (4.24)) applied on the respective axis. An automated scanning routine was used to measure the ac-Stark shift due to different alignments of QCL on the ion. Finally, the laser was aligned at position of the maximum measured shift. Fig. 4.24 depicts such an automatic alignment procedure. The beam profile of the focused QCL on the ion was almost Gaussian as can be seen in the 3d-surface plot (fig. 4.24a) and the contour map (fig. 4.24b). Fig. 4.24c and d are one-dimensional scans and the dashed-black lines show the voltages required for the piezoelectric mirror in the horizontal and vertical directions for optimal alignment.

In conclusion, this chapter dealt with the characterization and short and long term stabilization of the 729 nm laser, OFC and the 4574 nm QCL. Details of the characterization techniques adopted in our case were presented specially for the long-term stability of the 729 nm laser and the OFC. Additionally challenges with the MIR laser were presented. A suitable QCL chip was identified and frequency-locked. Stabilization of these lasers was

---

<sup>37</sup>POLARIS-K1S2P, KPZ101 - Thorlabs GmbH

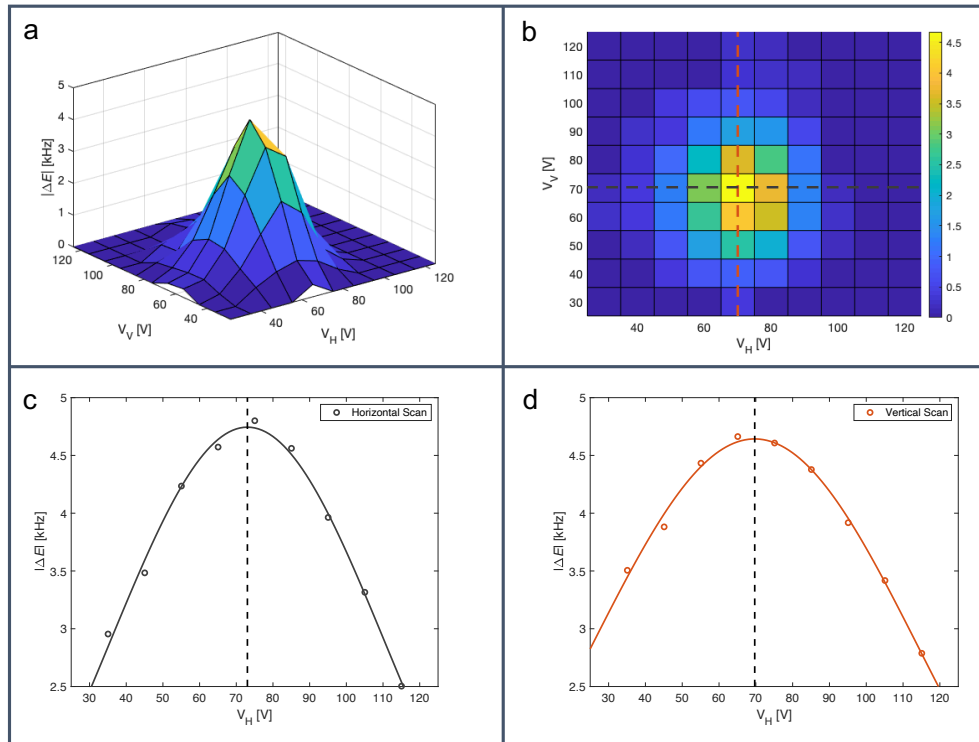


**Figure 4.24 Automated alignment of the QCL on the ion.** (a) 3d surface plot showing measurements of the ac-Stark shift due to different horizontal and vertical alignment of the QCL on the ion. The QCL was scanned by scanning the voltage applied on the horizontal ( $V_H$ ) and vertical ( $V_V$ ) axis of a piezoelectric mirror. The Gaussian shape of the focused beam can be observed. (b) Contour plot corresponding to the measurements in (a). (c), (d) 1d scans showing the measured ac-Stark shift caused by the QCL as it is scanned in the horizontal and the vertical directions on the ion. Best alignment was at a horizontal position of  $\sim 75$  V and a vertical position of  $\sim 70$  V of the piezoelectric mirror.

important for spectroscopic measurements on the  $\text{Ca}^+$  and  $\text{N}_2^+$  ions.

# Chapter Five

## Quantum control of a single trapped

### $\text{N}_2^+$ ion

The past two decades have witnessed tremendous progress in the quantum control of molecules and molecular ions. Cold, trapped molecules have been created by various methods, e.g., by binding ultracold atoms via Feshbach resonances [172] and photoassociation [173, 174], deceleration of molecular-beams [175], direct laser cooling [176, 177] and sympathetic cooling [178, 179]. The trapping of cold molecules has enabled experiments with long interaction times thus facilitating precision studies with molecules [49, 86, 92, 93, 95, 180].

Unlike many atomic systems, the complex energy level structure and the absence of optical cycling transitions in most molecular systems constitute a major challenge in the direct state preparation, laser cooling, state detection and coherent manipulation of molecules. Molecular ions trapped in radiofrequency ion traps which are sympathetically cooled by simultaneously trapped atomic ions [178, 179] have proven a promising route for overcoming these obstacles. Recently, their rotational cooling and state preparation has been achieved [181–184], precision measurements of quantum electrodynamics and fundamental constants have been performed [51, 180], the first studies of dipole-forbidden spectroscopic transitions in the mid-infrared spectral domain have been reported [185] and state- and energy-controlled collisions with cold atoms have been realized [60, 186]. However, in order to reach the same

exquisite level of control on the quantum level for molecules which can be achieved with trapped atoms [187], new methodological developments are required.

Here, we present and discuss a quantum-logic approach [116, 188, 189] for the manipulation of molecular ions. For applications such as precision spectroscopy [53, 55, 56, 185, 188] and upcoming quantum technologies [72, 190–194], it is advantageous, and indeed in many cases necessary, to suppress ensemble averaging and work with small samples or even single particles. In our experiments, a single  $^{28}\text{N}_2^+$  ion was co-trapped with a single  $^{40}\text{Ca}^+$  ion. The  $\text{Ca}^+$  ion was used to cool the  $\text{N}_2^+$  ion and manipulate and detect its internal and external energy quantum states [56, 114, 115, 195]. The aim was the precise control and spectroscopy of  $\text{N}_2^+$  [53, 56, 196] while preserving its internal state and chemical identity. The duty cycles and measurement statistics in our experiments were enhanced by several orders of magnitude compared to previous state-readout schemes [179, 185, 197] due to the non-destructive nature of our techniques. The present method lays the foundations for new approaches to molecular precision spectroscopy on the single-molecule level and for implementation of molecular qubits. Seamless interplay between several experimental techniques is required for achieving complete quantum-state control over a single trapped molecule including:

- Internal-state preparation of the molecule.
- Cooling of the external motion of the molecule.
- Non-destructive detection of the internal state of the molecule.
- Coherent manipulation of an isolated sub-space of the molecular quantum states.

Our implementations of the state preparation, cooling and state detection for  $\text{N}_2^+$  are presented in the sections below. Although the  $\text{N}_2^+$  ion has been chosen as a prototypical example here, many of the techniques are directly adaptable to different diatomic and polyatomic molecules.

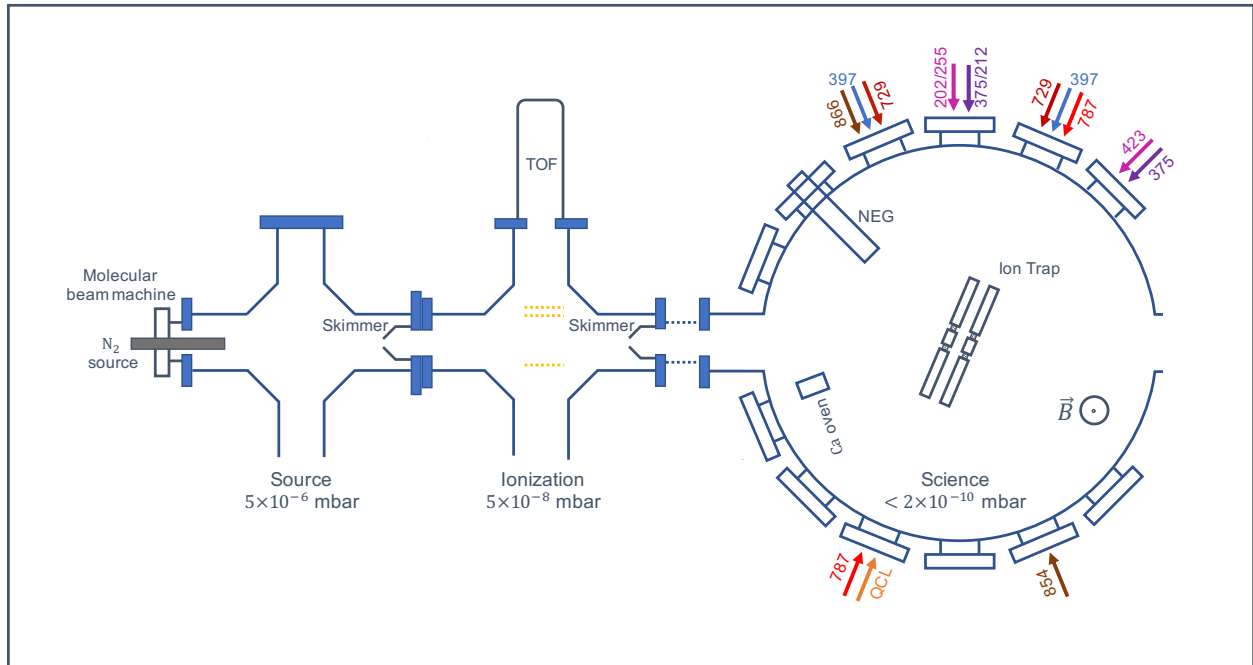


**Figure 5.1 Schematic of the experimental setup.** The “source” chamber, under high-vacuum conditions, contained a molecular-beam source which was used to create packets of rovibrationally cold  $N_2$  molecules. The “ionization” chamber hosted a time-of-flight mass spectrometer (labelled “TOF”) for the characterization of the molecular beam. It also served as a differential pumping stage for achieving ultra-high vacuum conditions in the “science” chamber which consisted of the ion-trap apparatus. Coloured arrows represent different laser beams entering the science chamber. All lasers and the molecular beam were aligned to the center of the ion trap. Pulsed dye laser beams at 375 (212) and 202 (255) nm were used to ionize single  $N_2^+$  molecules from the molecular beam while two continuous-wave diode laser beams at 423 nm and 375 nm were employed to ionize Ca atoms from an atomic beam generated by the Ca oven in the science chamber. ECDLs at 397, 866, 729 and 854 nm were used for Doppler and ground-state cooling of the two-ion crystal via the  $Ca^+$  ion. Another ECDL at 787 nm created a running one-dimensional optical lattice used for the non-destructive state detection of  $N_2^+$ . A narrow QCL at 4574 nm will allow the coherent manipulation of the  $N_2^+$  ion in the infrared domain in the near future.

## 5.1 The Experimental setup

Fig. 5.1 shows our experimental apparatus for interrogation and manipulation of  $Ca^+$  and  $N_2^+$  ions. The setup was a combination of a molecular-beam machine and an ion-trap [56] experiment capable of performing quantum logic. It was composed of three vacuum stages

with decreasing pressures from high ( $\sim 5 \times 10^6$  mbar) to ultra-high ( $< 2 \times 10^{10}$  mbar) vacuum conditions during operation. The first “source” chamber consisted of a pulsed gas valve which was used to create a molecular beam of internally cold molecules. The second “ionization” chamber, separated by a skimmer from the first, contained a time-of-flight mass spectrometer which could be used to characterize the molecular beam. It also served as a differential pumping stage facilitating ultra-high vacuum conditions in the third “science” chamber. The science chamber was isolated from the second chamber by another skimmer and consisted of the ion trap. Ten different lasers were aligned to the center of the ion trap for the ionization of Ca and N<sub>2</sub> and cooling, detection and manipulation of Ca<sup>+</sup> and N<sub>2</sub><sup>+</sup>. The gas valve and the skimmers were also aligned such that the molecular beam passed through the center of the ion trap.

The ion trap was a linear segmented radiofrequency (rf) quadrupole trap. In addition, to the main electrodes used for generating rf harmonic potentials and dc endcap potentials for trapping ions, the ion-trap consisted of four additional electrodes for applying auxiliary fields to the trapping region. These additional electrodes were used for compensating the micromotion experienced by the ion, for coherent motional excitation of motional modes and for driving transitions in Ca<sup>+</sup> (and N<sub>2</sub><sup>+</sup> in the future) lying in the rf domain (eg. Zeeman transitions in the ground electronic state of Ca<sup>+</sup>). Further details about the design of the ion-trap can be found in ref. [56].

Positively charged ions could be trapped with trapping frequencies ranging from 290 kHz ( $m = 200$  amu) to 1280 kHz ( $m = 10$  amu) along the longitudinal trap axis. The linear segmented design was tailored for precision spectroscopy of linear ion crystals. It enabled a harmonic trapping potential with an rf-free trapping region along the longitudinal trap axis. The trap was optimized for simultaneously trapping of a Ca<sup>+</sup> – N<sub>2</sub><sup>+</sup> two-ion chain.

Ca<sup>+</sup> ions were loaded into the trap from a skimmed atomic beam of neutral Ca atoms emitted by an oven contained in the science chamber. For its ionization, a [1+1'] resonant ionization scheme was employed using an external-cavity diode laser (ECDL) at 423 nm and

a free-running diode laser (DL) at 375 nm. Multiple  $\text{Ca}^+$  ions could be loaded in a short time depending on the oven temperature and the lasers' intensities and detunings. An external electron-multiplying charge-coupled-device (EMCCD) camera aligned to the center of the ion trap and an external single-photon counter with a high-numerical-aperture objective mounted in vacuum close to the ion trap (not shown in fig. 5.1 for clarity) were used to collect photons at 397 nm scattered by the  $\text{Ca}^+$  ion for imaging and state identification of the ion.

## 5.2 Preparation of $\text{N}_2^+$ in the rovibronic ground state

$\text{N}_2^+$  is a homonuclear diatomic molecule with no permanent electric-dipole moment rendering the often employed black-body-radiation-assisted probabilistic state-preparation technique [116, 189] for molecular ions inefficient. Thus, an alternative state-preparation scheme, in which the  $\text{N}_2^+$  ion was produced in the required ground state during the photoionization of neutral  $\text{N}_2$ , was employed here.

For the state-selective production of  $\text{N}_2^+$ , a supersonic molecular beam of short and dense, rotationally and vibrationally cold packets of  $\text{N}_2$  was generated by using a pulsed gas valve in a first step. Resonance-enhanced multi-photon ionization (REMPI) was then employed to ionize one  $\text{N}_2$  molecule from the molecular beam as it passed through the center of the ion trap. Since mm-scale ion traps, such as the one used in our experiments, support large trapping volumes and trapping depths, a molecular ion generated in the center of the trap will remain confined with almost unit probability. Thus, a single ionization-laser pulse was synchronized with one molecular packet from the molecular beam in the center of the ion trap.

For the REMPI, a [2+1'] colour scheme was employed with ns-pulsed laser beams at 202 and 375 nm [183]. This led to the creation of  $\text{N}_2^+$  in the rovibronic ground  $|X^2\Sigma_g^+, v = 0, N = 0, J = 1/2\rangle$  state. Here,  $X^2\Sigma_g^+$  is the electronic ground state of  $\text{N}_2^+$ ,  $v$  denotes the

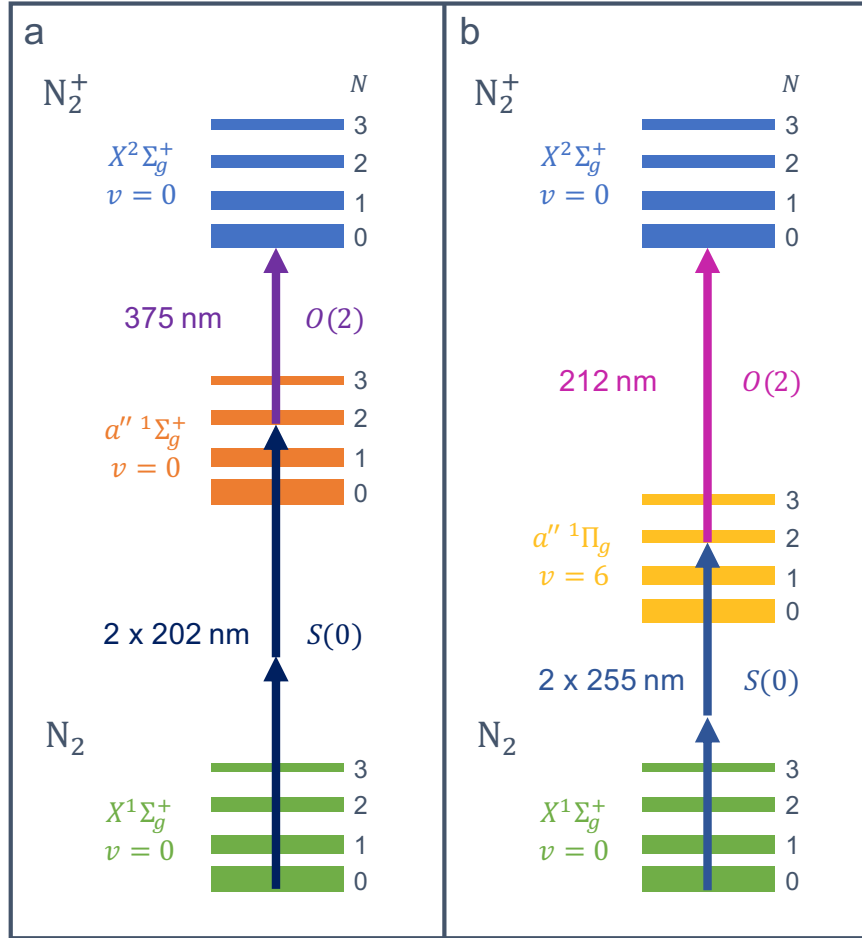


**Figure 5.2 REMPI schemes for the ionization of  $N_2$ .** Two possible [2+1'] REMPI schemes for the production of  $N_2^+$  in the rovibronic ground state from the cold molecular beam. For a(b), two photons at 202(255) nm couple the ground  $|X^1\Sigma_g^+, v=0, N=0\rangle$  level of  $N_2$  to the intermediate  $|a''^1\Sigma_g^+, v=0, N=2\rangle$  ( $|a''^1\Pi_g, v=6, N=2\rangle$ ) state. An additional photon at 375(212) nm ionized the molecule to ground  $|X^2\Sigma_g^+, v=0, N=0, J=1/2\rangle$  state of  $N_2^+$ .

vibrational,  $N$  the rotational and  $J$  the total-angular-momentum quantum numbers of the molecule excluding nuclear spin. The ground state of the ionized  $N_2^+$  is henceforth referred to as  $|\downarrow\rangle_{N_2}$  in the rest of this chapter.

The ionization scheme is shown in fig. 5.2a. Both laser intensities were tuned to achieve less than one ionization event on average per trail in order to minimize the probability of creating two or more  $N_2^+$  ions. Although the presented REMPI scheme allowed for the

initialization of  $\text{N}_2^+$  in a specific vibrational, rotational and fine-structure state, the hyperfine and Zeeman structure (quantum numbers  $F$  and  $m_F$ ) were not resolved with the current laser system. Since the state-detection scheme presented in this thesis (see sec. 5.4) was only dependent on the fine structure component of the rovibrational state, the exact hyperfine and Zeeman occupancies were inconsequential. However, for future experiments like precision spectroscopy and coherent manipulation, a fully resolved state preparation is indispensable. Although hyperfine-selective REMPI schemes can be devised using narrow-bandwidth lasers [198, 199], here a projective state preparation scheme would be adopted [53] for coherent experiments with  $\text{N}_2^+$ . This is further discussed in sec. 5.6.

A particular challenge with the REMPI scheme was the [2+1] background signal since the energy of the excitation two-photon laser at 202 nm was much higher than the ionization single-photon laser at 375 nm. The background ionization often resulted in the  $\text{N}_2^+$  being produced in incorrect rovibrational state. In the absence of additional pumping schemes, the experiment had to be restarted for attempting to load  $\text{N}_2^+$  in the correct state. This led to poor experimental-duty cycles. The REMPI scheme was thus reconfigured to employ different [2+1'] ionization colours (shown in fig. 5.2b) [200]. For this, laser beams at 255 nm and 212 nm were used. A strong suppression in the [2+1] background ionization signal was observed, as expected, in a separate test experimental setup.

### 5.3 Cooling of external motion of the $\text{N}_2^+$ ion

The goal of cooling was to reduce the kinetic energy of the ions, after they were loaded into the trap, ideally to a point at which the ions were in the ground state of the trapping potential with a very high probability [201]. The neutral Ca atoms from the hot oven had kinetic energies  $\gtrsim 600$  K depending on the oven temperature. The kinetic energy of the the molecular beam after its supersonic expansion from the pulsed valve was  $\sim 1300$  K (corresponding to a beam velocity of  $\sim 780$  m/s). Upon ionization in the trapping region,

the  $\text{Ca}^+$  and the rovibrationally cold  $\text{N}_2^+$  ions had excess kinetic energy which was to be rapidly removed before state-manipulation experiments. The lifetime of the  $\text{N}_2^+$  ion in our experiments was often the limiting factor. Under our vacuum conditions, the  $\text{N}_2^+$  was lost due to chemical reactions with background  $\text{H}_2$  and  $\text{H}_2\text{O}$  on a time scale of  $\sim 5$  minutes. Thus cooling, and subsequently spectroscopy and state detection were to be performed on a time scale of a few minutes before the experiment had to be reinitialized. In order to efficiently cool the two-ion chain, a two-stage cooling process was employed.

### 5.3.1 Sympathetic Doppler cooling of $\text{Ca}^+$ and $\text{N}_2^+$ ions

In a first stage, to cool the ions from high starting temperatures, Doppler laser cooling was employed. It involves fast scattering of photons on closed-cycling dipole-allowed transitions which many atomic systems readily feature. The cooling laser is red-detuned from the transition such that photons are preferably absorbed when the atom move towards the light source, thus leading to a loss in momentum of the atom. After many thousands of photon-scattering events, the atom can be cooled from the initial temperatures of many hundreds of K to a few mK. Since the upper state lifetimes of the transitions employed in Doppler cooling is considerably shorter than one period of oscillation of the commonly used ions in most traps, the first cooling stage occurs in what is known as the “unresolved-sideband” regime [201].

In our experiments, Doppler cooling was accomplished by scattering photons on the  $4\text{S}_{1/2} \leftrightarrow 4\text{P}_{1/2} \leftrightarrow 3\text{D}_{3/2}$  cycling transition in  $\text{Ca}^+$  addressed by lasers at 397 nm and 866 nm (see fig. 5.3). Due to the absence of closed cycling transitions, the molecular  $\text{N}_2^+$  ion could not be directly Doppler cooled. An alternative “sympathetic” cooling technique was thus applied in which  $\text{N}_2^+$  was cooled by the laser-cooled  $\text{Ca}^+$  ion. Due to long-range Coulomb interactions between the  $\text{N}_2^+$  and  $\text{Ca}^+$ , energy was constantly exchanged between the hot  $\text{N}_2^+$  ion and the continuously laser-cooled  $\text{Ca}^+$  ion. This lead to heat dissipation from the system

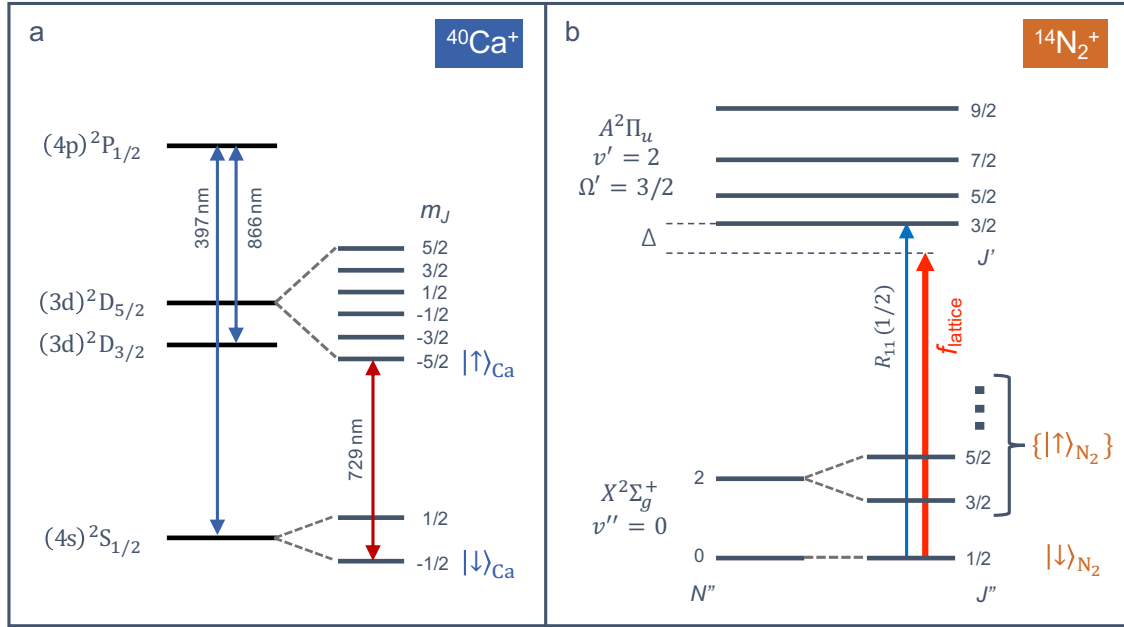


**Figure 5.3 Relevant energy levels of the  $\text{Ca}^+$  and  $\text{N}_2^+$  ions [114].** (a) The  $(4s)^2S_{1/2} \leftrightarrow (4p)^2P_{1/2} \leftrightarrow (3d)^2D_{3/2}$  closed cycling transitions, addressed by lasers at 397 nm and 866 nm (blue arrows), were used for the Doppler cooling of the  $\text{Ca}^+ - \text{N}_2^+$  two-ion string. They were also used for the detection of the  $|\downarrow\rangle_{\text{Ca}} = |S_{1/2}, m = -1/2\rangle$  and  $|\uparrow\rangle_{\text{Ca}} = |D_{5/2}, m = -5/2\rangle$  states. These states were coherently coupled by a narrow-linewidth laser beam at 729 nm (red arrow). (b) For the state-detection of  $\text{N}_2^+$ , the lattice laser frequency at  $\sim 787$  nm (red arrow) was detuned by  $\Delta$  from the  $R_{11}(1/2)$  transition (blue arrow). The ground state of the  $\text{N}_2^+$  (referred to as  $|\downarrow\rangle_{\text{N}_2}$ ) was strongly coupled to the lattice while all other states (collectively referred to as  $\{|\uparrow\rangle_{\text{N}_2}\}$ ) were far detuned and did not couple.

via the  $\text{Ca}^+$  ion until both species thermalized close to the Doppler limit. Depending on the exact trapping conditions, a mean motional state occupation,  $\langle n \rangle$ , between 10 and 20 was achievable in a Doppler cooling time of 3 - 5 ms [56].

Since the  $\text{N}_2^+$  ion could not be directly laser cooled, often very long cooling times were observed when cooling the  $\text{N}_2^+$  with a single  $\text{Ca}^+$  ion. Typically after the ionization from the fast molecular beam, many tens of minutes were required for the cooling of  $\text{N}_2^+$  which was much longer than the  $\text{N}_2^+$  chemical lifetime. Thus, a faster cooling technique was developed (fig. 5.4). Since the sympathetic cooling rate is proportional to the number of the cooling ions [202],  $\sim 30$  laser cooled  $\text{Ca}^+$  ions were trapped to begin with. After its ionization, a single  $\text{N}_2^+$  ion could be cooled on a timescale of a few seconds with the  $\text{Ca}^+$  Coulomb crystal.

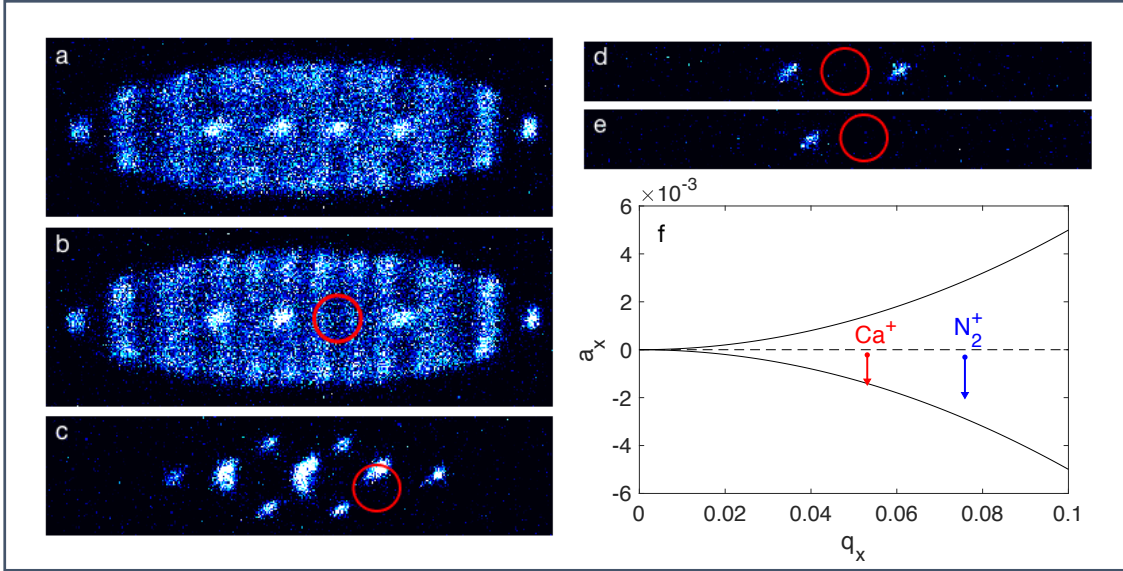


**Figure 5.4 Sympathetic Doppler cooling of  $N_2^+$  [115].** (a) In order to quickly cool the ionized  $N_2^+$  ion, a small Coulomb crystal of  $\sim 30$   $Ca^+$  ions was loaded. (b) The  $N_2^+$  was Doppler cooled on a timescale of a few seconds and appeared as a “hole” (red circle) in the Coulomb crystal. (c), (d) The number of  $Ca^+$  ions were reduced until a two-ion  $Ca^+-N_2^+$  chain was obtained (e). (f) The reduction in the  $Ca^+$  ion was accomplished by evaporating the  $Ca^+$  ions in a probabilistic manner by tuning the trapping potential to the edge of the stability region for  $Ca^+$ . Since  $N_2^+$  is lighter, it remained unaffected during the reduction of  $Ca^+$  from the trap.

In a successive step, the number of trapped  $Ca^+$  ions were reduced until a  $Ca^+-N_2^+$  two-ion chain was obtained. For the reduction of the  $Ca^+$  ions, the trapping potential was lowered to the edge of the stability diagram for the heavier  $Ca^+$  ion by reducing the rf power applied to the trap. At this configuration,  $Ca^+$  ions were probabilistically lost from the trap due to their semi-stable trajectories. Under well-controlled conditions, the reduction of  $Ca^+$  ions could be carried out on a timescale of tens of seconds. Although the exact characterization of the ion-loss mechanism remains to be performed, a preliminary study can be found in [56].

### 5.3.2 Sympathetic sideband cooling of the $Ca^+-N_2^+$ two-ion string

In order to reach the ground state of motion of the two-ion crystal, a second stage of cooling in the “resolved-sideband” regime is necessary [201]. Three different methods have

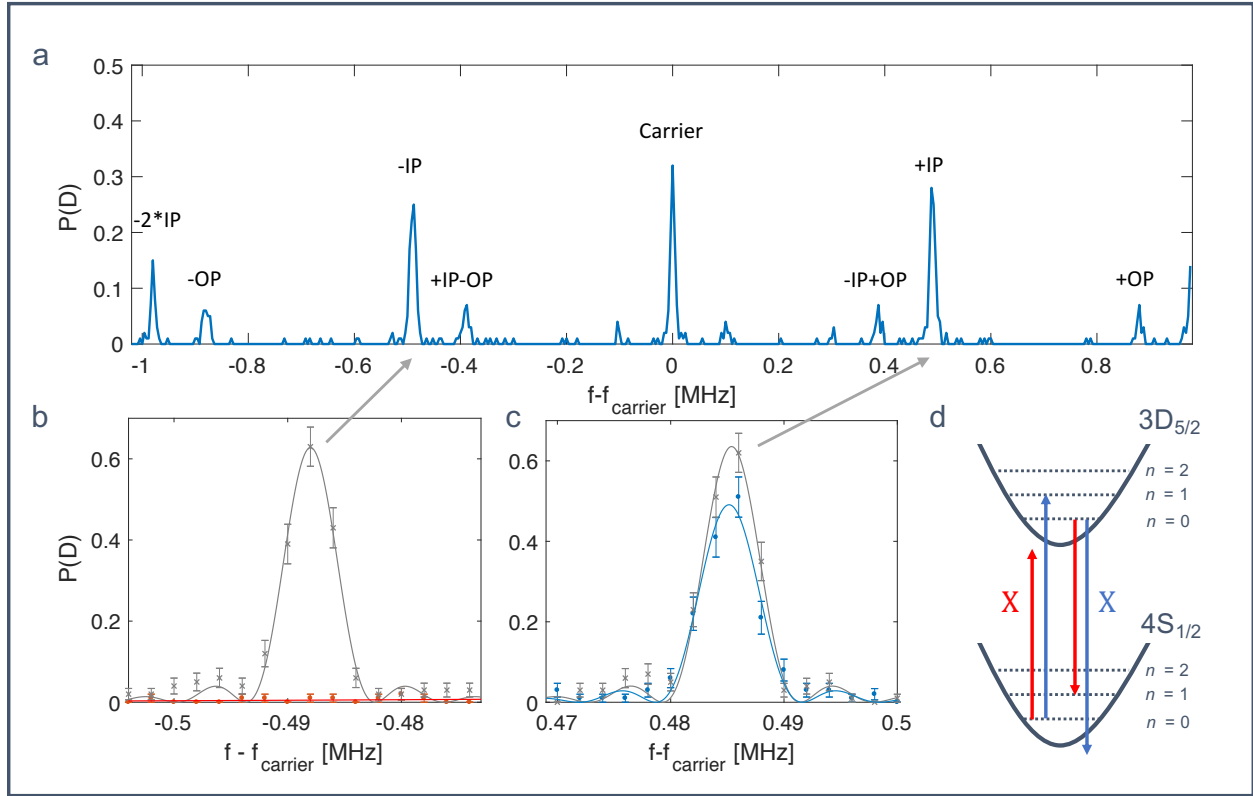


**Figure 5.5 Sympathetic sideband cooling of a  $\text{Ca}^+ - \text{N}_2^+$  two-ion string [115].** (a) Resolved sideband spectra of the narrow  $4\text{S}_{1/2}(m = -1/2) \rightarrow 3\text{D}_{5/2}(m = -5/2)$  quadrupole transition in  $\text{Ca}^+$  for the two-ion string. (b), (c) Red and blue IP sidebands of the two-ion string before (grey lines) and after (red and blue lines) after cooling of the motion of the two-ion crystal to the ground state of the trapping potential from the  $4\text{S}_{1/2}(m = -1/2)$  state of  $\text{Ca}^+$ . (d) In the ground state, no red-sideband transitions were possible from the  $4\text{S}_{1/2}(m = -1/2)$  state of  $\text{Ca}^+$ . In the case when the  $\text{Ca}^+$  was excited to the  $3\text{D}_{5/2}(m = -5/2)$  state, no blue sidebands were possible. The absence of blue sidebands from the  $3\text{D}_{5/2}(m = -5/2)$  state was exploited for the state-detection of  $\text{N}_2^+$  (see sec. 5.4).

often been employed, namely, sideband cooling on a dipole-forbidden quadrupole transition, cooling by stimulated Raman transitions, and cooling utilizing electromagnetically induced transparency (EIT) [203,204].

For our experiments, we sympathetically sideband cooled the motion of the  $\text{Ca}^+ - \text{N}_2^+$  ion string on the narrow  $4\text{S}_{1/2}(m = -1/2) \rightarrow 3\text{D}_{5/2}(m = -5/2)$  quadrupole transition in  $\text{Ca}^+$ . For this, a cavity-stabilized narrow-linewidth laser at 729 nm (sec. 4.1 discusses the laser stabilization in detail) was employed. A resolved-sideband spectrum of the quadrupole

transition in  $\text{Ca}^+$  after Doppler cooling is shown in fig. 5.5. For a two-ion crystal, two distinct modes of oscillations are present along the axial trapping axis, namely, the in-phase (IP) mode (also known as the center-of-mass (COM) mode for ions of the same mass) and the out-of-phase (OP) mode (also known as the stretch mode (STR) mode). For the experiments presented here, it was sufficient to cool the IP mode of the  $\text{Ca}^+ - \text{N}_2^+$  string. This was accomplished by a series of second- and first-red-sideband pulses which changed the motional quantum number by  $\Delta n = -2$  and  $\Delta n = -1$ , respectively [56]. The OP and radial modes were maintained at the Doppler-cooling temperature.

After the ground state cooling which required between 5 and 9 ms of time depending on the experimental conditions, the motional occupancy could be estimated by sideband thermometry (fig. 5.5b and c). For this, measurements of the first blue and the residual first red sideband strengths were made and a mean motional-state occupation  $\langle n \rangle \approx 0.05$  was determined for IP mode of the  $\text{Ca}^+ - \text{N}_2^+$  string [56]. A ground state occupation probability of  $\sim 97 \pm 2\%$  could be estimated from repeated experiments<sup>1</sup> [56].

## 5.4 Quantum-nondemolition state detection of $\text{N}_2^+$

Typically, the internal states of atomic ions used in ion-trap experiments can be detected by laser-induced fluorescence (LIF) on electric-dipole-allowed cycling transitions [201]. Usually, the same transitions employed for Doppler cooling can be used for state detection. On such a transition, a single atomic ion can scatter several millions of photons per second and a sufficient fraction may be detected on devices like an electron-multiplying charge-coupled device (EMCCD) cameras or on photomultiplier tubes (PMTs). In the case of the  $\text{Ca}^+$

---

<sup>1</sup>Another complementary method, namely, Rabi sideband thermometry, could also be used to determine the ground state population. For this, it was sufficient to measure Rabi oscillations on the first-blue sideband after ground-state cooling. Determination of the motional state using Rabi sideband thermometry was employed for the  $\text{N}_2^+$  state-detection experiments and is presented in sec. 5.4.

ion in our experiments, the internal state was detected on the  $4S_{1/2} \leftrightarrow 4P_{1/2} \leftrightarrow 3D_{3/2}$  transition. For this, the 397 nm and 866 nm lasers were switched on for a detection time ranging between 0.5 and 1 ms. In the  $4S_{1/2}$  state, the  $\text{Ca}^+$  ion could absorb and emit 397 nm photons. The state thus appeared “bright” and a strong fluorescence signal could be recorded on the CCD camera and the PMT. In other states, like the long-lived  $D_{5/2}$  state employed for example in ground-state cooling, the  $\text{Ca}^+$  did not scatter any photon. The state appeared “dark”. Any photons recorded either on the CCD or the PMT in the dark state was due to noise from electronics or background photons from the environment and the lasers. A suitable thresholding of the photon counts accumulated during the detection time was used to discriminate between the bright and dark states of the  $\text{Ca}^+$  ion.

Due to the large number of possible decay channels from excited states in most molecules, implementation of direct non-destructive molecular-state-readout schemes has been challenging. In the past, detection schemes which destroyed either the state of the molecular ion or its chemical identity have been employed [48, 185]. These schemes often require replenishing of the ions in the trap after every measurement thus limiting the duty cycle and the achievable accuracies with molecular ions. The past decade has seen rapid progress in development of novel techniques for non-destructive molecular-state detection [96, 114–116, 189, 195, 205]. These techniques often rely on quantum logic protocols. Such protocols have now been proposed and successfully demonstrated for precision spectroscopy of atomic [35, 188, 206, 207], molecular ions [96, 189, 208], for frequency comparisons of high-accuracy optical clocks [209], for implementing qubit-gate operations on trapped neutral [210–212] and ionic species [213, 214] and for investigating chemical reactions between ultracold atoms and ions [215]. Recently, Chou et al. [189] demonstrated the coherent manipulation of a single trapped  $\text{CaH}^+$  ion based on quantum-logic techniques. Transitions in the molecule were excited in a way such that a change in the state of the molecule was accompanied by an excitation of the shared motion with a co-trapped  $\text{Ca}^+$  ion. By detecting the excited motion, high resolution spectra of the molecule was recorded and coherent

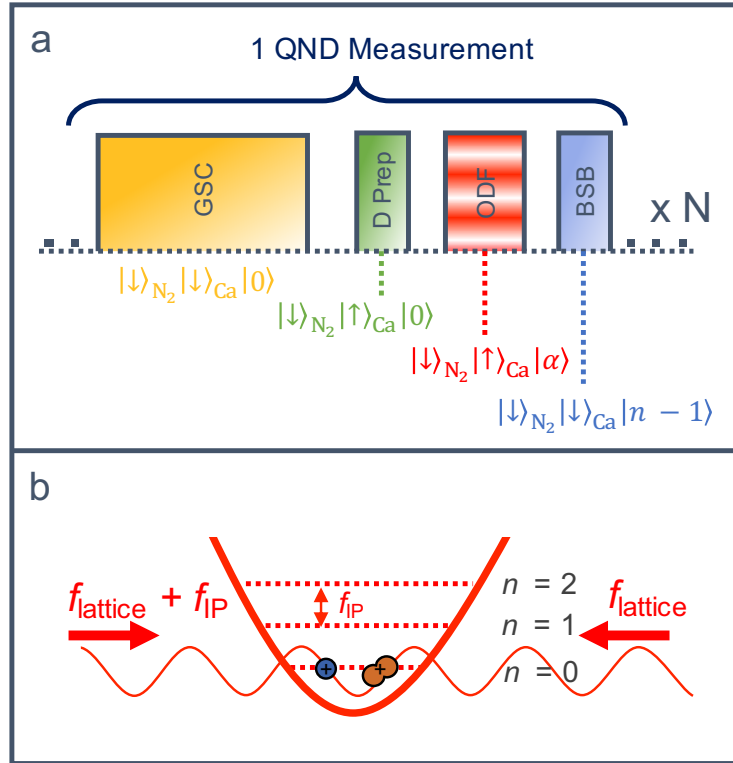


**Figure 5.6 Schematic for the state detection of  $N_2^+$ .** (a) Experimental sequence for a QND state determination. The ions were first cooled to the ground state of motion (labelled as ‘‘GSC’’). The  $Ca^+$  was then pumped to the  $|\uparrow\rangle_{Ca}$  state (‘‘D Prep’’). An ‘‘ODF’’ pulse was used to excite coherent motion of the two-ion chain. The excited motion was dependent on the state of  $N_2^+$  and was determined by Rabi-sideband thermometry (‘‘BSB’’) on the  $Ca^+$  ion. The measurement was repeated several ( $N$ ) times for a high-fidelity state determination. The relevant state of the two-ions after each step is also shown. (b) Schematic of the two-ion crystal in the ground state of the trapping potential after ‘‘GSC’’. For the state detection, two counter-propagating laser beams,  $f_{lattice}$ , were used to create a one-dimensional optical lattice. One of the beams was detuned by the IP frequency of motion ( $f_{IP}$ ) in order to create a running lattice which could excite coherent motion of the IP mode of the  $Ca^+-N_2^+$  string.

phenomena such as Rabi flopping and Ramsey fringes were observed. In a successive experiment, by extending the methods employed, Lin et al. [96] demonstrated entanglement between the rotational states of the  $CaH^+$  ion and the internal states of the  $Ca^+$  ion.

Here, a quantum-logic based quantum-non-demolition (QND) [216–218] detection of the ground spin-rovibrational state of the  $N_2^+$  ion via the  $Ca^+$  ion is presented. For our implementation of the quantum logic protocol, we employed a molecular-state-dependent optical-

dipole force (ODF) [72,114,195]. ODFs have proven to be an efficient tools for manipulation of particles at micron length scales. These have been utilized in experiments on ultracold atomic [105] and molecular physics [219], atomic optics [220] and optical tweezers [221,222]. Within the framework of quantum-logic operations, ODFs have also been proposed and employed in order to demonstrate two-qubit gate operations [223,224] and for nondestructive molecular-state identification [225]. Recently, Wolf et al. [116] experimentally demonstrated the nondestructive state detection of a single trapped  $\text{MgH}^+$  molecular ion. For this, a motional qubit was implement on the shared motion between the  $\text{MgH}^+$  ion and a co-trapped  $\text{Mg}^+$  ion. The rovibrational state of the molecular ion was mapped onto the motional qubit via ODFs which was then readout using the atomic ion. Our implementation here allows a simpler approach for molecular state detection by coherently exciting motion, which also readily enables the extraction of accurate values for spectroscopic quantities such as transition strengths.

The experimental sequence to detect the spin-rovibrational state of the  $\text{N}_2^+$  ion is illustrated in fig. 5.6a. The state-detection sequence begins once the IP motional mode of the  $\text{Ca}^+-\text{N}_2^+$  crystal is cooled to the ground state of the trap, henceforth represented as  $|0\rangle$ , by resolved-sideband cooling (“GSC” in fig. 5.6a) on the  $\text{Ca}^+$  ion [115]. At the end of the cooling cycle, the  $\text{Ca}^+$  ion is optically pumped into its  $|S_{1/2}, m = -1/2\rangle$  state, henceforth referred to as  $|\downarrow\rangle_{\text{Ca}}$  (also shown in fig. 5.3a). Pumping to the  $|\downarrow\rangle_{\text{Ca}}$  state is accomplished by the narrow 729 nm laser which drives the quadrupole  $4S_{1/2} \leftrightarrow 3D_{5/2}$  transition. Specifically, in our experiment, the 729 nm laser propagated perpendicular to the direction of the magnetic field with its polarization,  $\vec{p}$ , perpendicular to both the magnetic field and the direction of propagation ( $\vec{p} \perp \vec{k}$ ,  $\vec{k} \perp \vec{B}$ ,  $\vec{p} \perp \vec{B}$  –  $\sigma$ -polarized light). Under these conditions, the electric-quadrupole 729 nm transitions were restricted to  $\Delta m = \pm 2$  transitions due to the selection rules. Thus in order to pump the  $\text{Ca}^+$  to the  $|\downarrow\rangle_{\text{Ca}}$  Zeeman state, the  $|S_{1/2}, m = +1/2\rangle \rightarrow |D_{5/2}, m = -3/2\rangle$  quadrupole transition was driven. Another  $\sigma$ -polarized 854 nm laser was then used to re-pump the population from the  $|D_{5/2}, m = -3/2\rangle$

state to the  $|P_{3/2}, m = -1/2\rangle$  on the dipole allowed  $D_{5/2} \leftrightarrow P_{3/2}$  transition. Spontaneous decay from the  $|P_{3/2}, m = -1/2\rangle$  state to the  $|\downarrow\rangle_{\text{Ca}}$  and  $|S_{1/2}, m = +1/2\rangle$  states then populated the  $|\downarrow\rangle_{\text{Ca}}$  state. The pumping sequence was repeated several times in order to ensure that almost all population was transferred to the required  $|\downarrow\rangle_{\text{Ca}}$  state. The complete state of the two ion crystal, assuming an ideal loading of  $\text{N}_2^+$  ion in the ground state, and after their cooling and the initialization of  $\text{Ca}^+$  in the  $|\downarrow\rangle_{\text{Ca}}$  state, could be given by,

$$|\psi\rangle_{\text{init}} = |\downarrow\rangle_{\text{N}_2} |\downarrow\rangle_{\text{Ca}} |0\rangle. \quad (5.1)$$

The  $\text{Ca}^+$  ion was then shelved in the metastable  $|D_{5/2}, m = -5/2\rangle$  state, henceforth referred to as  $|\uparrow\rangle_{\text{Ca}}$ , using a  $\pi$ -pulse on the narrow  $|\uparrow\rangle_{\text{Ca}} \leftarrow |\downarrow\rangle_{\text{Ca}}$  transition. Preparing the  $\text{Ca}^+$  ion in the  $|\uparrow\rangle_{\text{Ca}}$  state suppressed background signal during the state detection and thus enabled an efficient determination of the rovibrational state of  $\text{N}_2^+$  [115] (see sec. 5.4.1). Typically only  $\sim 97\%$  of the  $\text{Ca}^+$  population could be shelved to the  $|\uparrow\rangle_{\text{Ca}}$  state. The remaining 3% population in the  $|\downarrow\rangle_{\text{Ca}}$  state, due to imperfect ground-state cooling and pulse parameters, introduced background noise in the state-detection measurement. In order to reduce this background, a D-purification detection pulse was applied in which the  $\text{Ca}^+$  detection lasers were switched on for  $\sim 500 \mu\text{s}$ . In a particular experiment, if the  $\text{Ca}^+$  ion remained in the  $|\downarrow\rangle_{\text{Ca}}$  state, a large number of scattered photons were recorded on the PMT and the experiment was excluded from analysis. For experiments in which the  $\text{Ca}^+$  ion was successfully prepared in the  $|\uparrow\rangle_{\text{Ca}}$  state, negligible photons (due to background scattering from the lasers) were recorded on the PMT. Thus, such a pulse [189] allowed for post-selecting experiments in which the  $\text{Ca}^+$  ion could be confirmed to be in the  $|\uparrow\rangle_{\text{Ca}}$  state. The sequence after GSC for preparing  $\text{Ca}^+$  in the  $D_{5/2}$  state is referred to as “D Prep” in fig. 5.6a. The state of the two ions after the purification pulse could be given by,

$$|\psi\rangle_{\text{state-prep}} = |\downarrow\rangle_{\text{N}_2} |\uparrow\rangle_{\text{Ca}} |0\rangle. \quad (5.2)$$

The detection sequence was continued by applying a state-dependent ODF (“ODF” in fig. 5.6a). Depending on the rovibrational state of the molecular ion the previously-cooled exter-

nal motion of the two ion crystal was excited [226]. In the case that the molecular ion was in the  $|\downarrow\rangle_{N_2}$  state, a coherent motion of amplitude  $|\alpha\rangle$  was excited such that the probability to populate a motional Fock state,  $|n\rangle$ , could be given by [201],

$$P(n|\alpha) = |\langle n|\alpha\rangle|^2 = e^{-|\alpha|^2} |\alpha|^{2n}/n!. \quad (5.3)$$

The state of the two ions could thus be given as,

$$|\psi\rangle_{|\downarrow\rangle_{N_2}} = |\downarrow\rangle_{N_2} |\uparrow\rangle_{Ca} |\alpha\rangle. \quad (5.4)$$

However, if the molecular ion was in any other rotational or vibrational states, henceforth referred to as  $\{|\uparrow\rangle_{N_2}\}$ , a motional state  $\{|\beta\rangle\}$  was excited where  $\{|\beta\rangle\} \ll |\alpha\rangle$ . Here, the curly brackets serve to emphasize that  $\{|\uparrow\rangle_{N_2}\}$  referred to many possible states, all of which resulted in vanishingly small amplitudes of the coherent motion,  $\{|\beta\rangle\} \ll 1$ . In the  $\{|\uparrow\rangle_{N_2}\}$  state, the state of the ions after the ODF pulse could be given as,

$$|\psi\rangle_{\{|\uparrow\rangle_{N_2}\}} = \{|\uparrow\rangle_{N_2}\} |\uparrow\rangle_{Ca} \{|\beta\rangle\}. \quad (5.5)$$

The ODF itself was implemented via a state-dependent ac-Stark shift. The theory behind the ac-Stark shift in  $N_2^+$  is discussed in detail in sec. 3.3. The ac-Stark shift was generated by two counter-propagating laser beams with frequencies  $f_{\text{lattice}}$ , aligned with the crystal axis which formed a one-dimensional optical lattice [227] (fig. 5.6b). The lattice beams were linearly polarized along the direction of the magnetic field in our experiments ( $\vec{p} \perp \vec{k}$ ,  $\vec{k} \perp \vec{V}$ ,  $\vec{p} \parallel \vec{B}$  –  $\pi$ -polarized light,  $\Delta m = 0$  transitions). By further detuning one of the beams by the frequency of the IP motional mode of the two-ion crystal,  $f_{IP} \approx 620$  kHz, a running lattice was generated causing a modulation of the amplitude of the ac-Stark shift which resonantly excited coherent motion of the ion crystal depending on the rotational and vibrational state of the  $N_2^+$  ion.

Fig. 5.7 shows the calculated ac-Stark shift of a single lattice beam as a function of its frequency for  $N_2^+$  in the  $|\downarrow\rangle_{N_2}$  state (blue) and the maximum ac-Stark shift experienced by

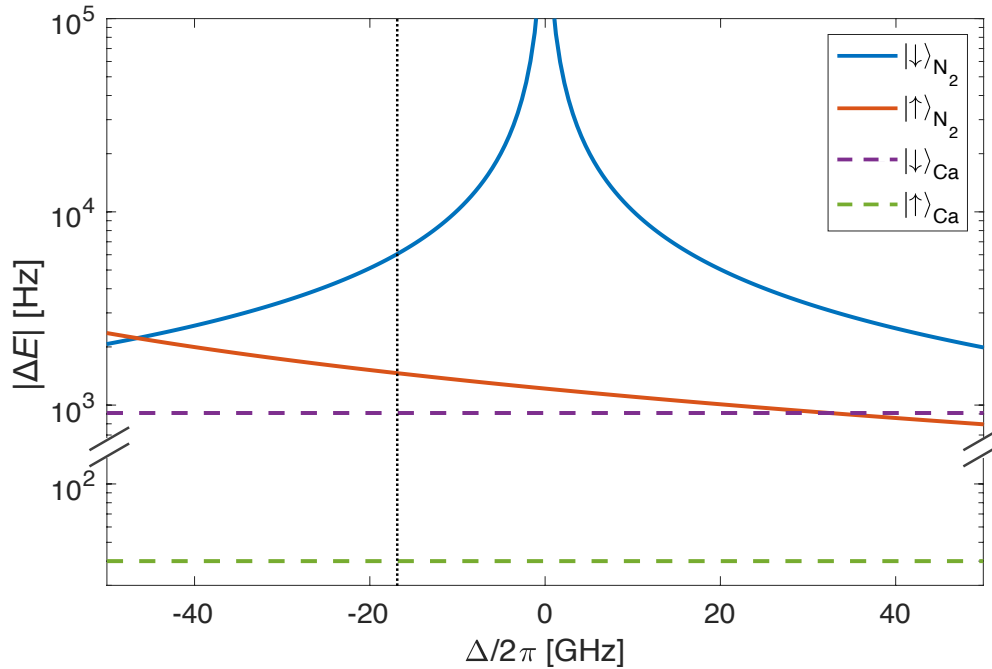


**Figure 5.7 Ac-Stark shift generated on  $N_2^+$  by the one-dimensional optical lattice [114].** Calculated magnitude of the ac-Stark shift,  $|\Delta E|$ , experienced by  $N_2^+$ , as a function of the laser-frequency detuning,  $\Delta$ , from the  $A^2\Pi_u(v' = 2) \leftarrow X^2\Sigma_g^+(v'' = 0)$ ,  $R_{11}(1/2)$ , spin-rovibronic transition [228] at  $\sim 787.47$  nm [76] for a single lattice beam of intensity  $2 \times 10^6$  W/m $^2$ . The ac-Stark shift experienced by  $N_2^+$  when in the  $|\downarrow\rangle_{N_2}$  state is given by the blue trace. The red trace is the maximum ac-Stark shift experienced by the  $N_2^+$  in the  $\{|\uparrow\rangle_{N_2}\}$  state. The  $Ca^+$  in the  $|\uparrow\rangle_{Ca}$  ( $|\downarrow\rangle_{Ca}$ ) state experiences an ac-Stark shift of 40 Hz (910 Hz) indicated by the dashed green (purple) line. The black dotted line indicates the frequency detuning,  $\Delta/2\pi \approx -17$  GHz, of the optical lattice used to generate the optical dipole force which was employed for collecting the data shown in fig. (5.8).

the  $N_2^+$  ion when not in the  $|\downarrow\rangle_{N_2}$  state (red) arising from the  $|X^2\Sigma_g^+, v = 0, N = 2, J = 3/2\rangle$  state. The strength of the ac-Stark shift depends on the detuning of the lattice laser beam from spectroscopic transitions in the molecule. The peak in the ac-Stark shift of the blue trace corresponds to an on-resonance condition of the  $A^2\Pi_u(v' = 2) \leftarrow X^2\Sigma_g^+(v'' = 0)$ ,  $R_{11}(1/2)$  spin-rovibronic transition [228] originating from the  $|\downarrow\rangle_{N_2}$  state (see fig. 5.3b). The lattice laser was set close to the resonance (black dashed line) due to which the  $N_2^+$  ion experienced a much stronger ac-Stark shift leading to a large coherent motional excitation  $|\alpha\rangle$  when in the  $|\downarrow\rangle_{N_2}$  state. In the case when the  $N_2^+$  was not in the  $|\downarrow\rangle_{N_2}$  state, a much

weaker coherent motion,  $\{|\beta\rangle\}$ , was excited. This ensured the state selectivity of the present scheme with respect to  $|\downarrow\rangle_{N_2}$  state of  $N_2^+$ .

The state-dependent coherent motional excitation [115, 229] mapped the problem of distinguishing between the different internal states  $|\downarrow\rangle_{N_2}$  and  $\{|\uparrow\rangle_{N_2}\}$  of the molecule to distinguishing between different excited motional states  $|\alpha\rangle$  and  $\{|\beta\rangle\}$  of the two-ion crystal. The latter was achieved by Rabi sideband thermometry [226] on the  $Ca^+$  ion which shared the motional state with the  $N_2^+$  ion. A blue-sideband (BSB) pulse using the laser at 729 nm was used to drive population between  $|\uparrow\rangle_{Ca}|n\rangle \rightarrow |\downarrow\rangle_{Ca}|n-1\rangle$  states. It was followed by state-selective fluorescence on the  $S_{1/2} \leftrightarrow P_{1/2} \leftrightarrow D_{3/2}$  transition of the  $Ca^+$  which projected the  $Ca^+$  to the  $|\uparrow\rangle_{Ca}$  “dark” or the  $|\downarrow\rangle_{Ca}$  “bright” state, thereby measuring the success of the BSB pulse (“BSB” in fig. 5.6a). The probability to project to the “bright” state after the BSB pulse was given by [201],

$$P(|\downarrow\rangle_{Ca}) = \sum_n P(n) \sin^2 \left( \frac{\Omega_n \cdot t_{729}}{2} \right), \quad (5.6)$$

where  $t_{729}$  was the BSB pulse time,  $\Omega_n = \eta\sqrt{n}\Omega_0$  was the BSB Rabi-frequency,  $\eta \approx 0.1$  was the Lamb-Dicke parameter and  $\Omega_0 \approx (2\pi)90$  kHz was the bare Rabi frequency. The motional Fock state population distributions were given by  $P(n|\alpha)$  or  $P(n|\{\beta\})$  depending on the state of  $N_2^+$ .

The evaluation of the above equation resulted in the BSB probabilities  $P(|\downarrow\rangle_{Ca}|\alpha)$  and  $P(|\downarrow\rangle_{Ca}|\{\beta\})$  for the  $|\downarrow\rangle_{N_2}$  and the  $\{|\uparrow\rangle_{N_2}\}$  states of  $N_2^+$  respectively. Since, in general,

$$0 < P(|\downarrow\rangle_{Ca}|\{\beta\}) < P(|\downarrow\rangle_{Ca}|\alpha) < 1,$$

the outcome of a single BSB pulse was insufficient to determine the motional state and hence the  $N_2^+$  internal state in a single shot. However, due to the fact that the internal state of  $N_2^+$  was not changed during the measurement, the detection sequence, i.e., cooling of the two-ion string to the motional ground state, preparing  $Ca^+$  in the  $|\uparrow\rangle_{Ca}$  state, exciting motion by the ODF and measuring the result by a BSB pulse, could be repeated until sufficient statistics

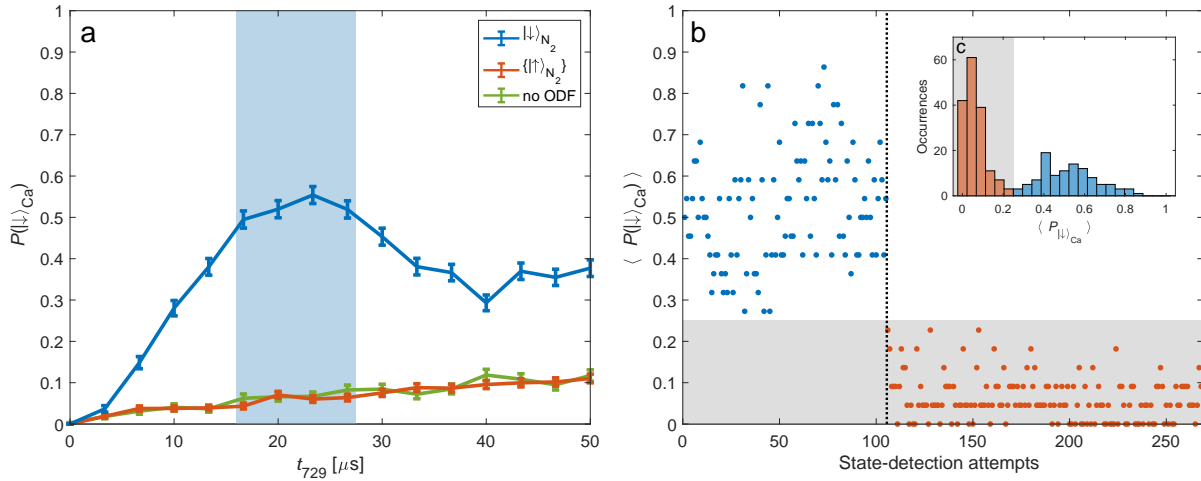


**Figure 5.8 Quantum non-demolition state detection of  $N_2^+$  [114].** a) Blue-sideband (BSB) Rabi-oscillation signal for  $N_2^+$  in the  $|\downarrow\rangle_{N_2}$  state (blue) and in one of the  $\{|\uparrow\rangle_{N_2}\}$  states (red). Error bars correspond to  $1\sigma$  binomial errors. Green is a background measurement of the Rabi oscillation signal without ODF beams. The light blue area indicates the region of BSB pulse lengths for which maximum state-detection contrast is achieved. b) Time trace of state-detection attempts. A single state-detection data point is composed of an average of 22 consecutive BSB-measurement results for pulse lengths indicated by the light-blue area in (a). A threshold of  $P(|\downarrow\rangle_{Ca})=0.25$  was used to distinguish between  $N_2^+$  in the  $|\downarrow\rangle_{N_2}$  or  $\{|\uparrow\rangle_{N_2}\}$  states (grey area). The blue (red) dots indicate assignment of  $|\downarrow\rangle_{N_2}$  ( $\{|\uparrow\rangle_{N_2}\}$ ) states by the detection scheme. The dashed black line shows the onset of a quantum jump out of the  $|\downarrow\rangle_{N_2}$  state to one of the  $\{|\uparrow\rangle_{N_2}\}$  states. c) Histogram of state-detection attempts. The grey area separates between  $|\downarrow\rangle_{N_2}$  (blue) and  $\{|\uparrow\rangle_{N_2}\}$  (red) state-detection assignments.

was gathered to distinguish between different molecular states. The experiment therefore represented a quantum-non demolition (QND) measurement [216–218].

An experimental demonstration of the presented QND scheme for molecular-state detection is shown in fig. 5.8. Here, the ODF beams were turned on for 500  $\mu s$  with a single lattice-beam intensity of  $\sim 2 \times 10^6$  W/m<sup>2</sup>. The lattice lasers were detuned by  $\Delta/2\pi \approx -17$  GHz from the  $R_{11}(1/2)$  transition ( $f_{\text{lattice}} \approx 787.510500$  nm) (black dashed line in fig. 5.7). The BSB pulse time,  $t_{729}$ , was scanned in order to observe Rabi oscillations, shown in fig. 5.8a. When the  $N_2^+$  ion was in the  $|\downarrow\rangle_{N_2}$  state, a strong Rabi oscillation was observed (blue), in contrast to when the  $N_2^+$  was in one of the  $\{|\uparrow\rangle_{N_2}\}$  states where almost no oscillation was observed (red). The residual signal of the  $\{|\uparrow\rangle_{N_2}\}$  states is attributed to imperfect ground-state

cooling of the two-ion crystal rather than motional excitation by the lattice beams as can be seen from a comparison to the background signal (green) obtained when the ODF beams were completely turned off. For the parameters used in the experiment shown in fig. 5.8a, the maximum contrast between the  $|\downarrow\rangle_{N_2}$  and the  $\{|\uparrow\rangle_{N_2}\}$  signals was reached at  $t_{729} \approx 20 \mu\text{s}$ . For this BSB pulse time, it can be noted from fig. 5.8a,

$$P(|\downarrow\rangle_{Ca}|\alpha) = 0.52, \quad (5.7)$$

and,

$$P(|\downarrow\rangle_{Ca}|\beta) = 0.06. \quad (5.8)$$

Given the above probabilities, an average of 22 QND measurements was sufficient to distinguish between the  $|\downarrow\rangle_{N_2}$  and the  $\{|\uparrow\rangle_{N_2}\}$  states of the  $N_2^+$  ion with a confidence level above 99.5% (see sec. 5.4.2 for a detailed discussion on fidelity calculations).

A QND determination of the  $N_2^+$  state is shown in fig. 5.8b. One state-detection attempt (a single blue or orange dot) was the BSB success probability,  $P(|\downarrow\rangle_{Ca})$ , determined from the average of the results of 22 BSB pulses with pulse times in the range of 16.7–26.7  $\mu\text{s}$  (light blue area in fig. 5.8a). A threshold of  $P(|\downarrow\rangle_{Ca})=0.25$  (grey shaded area) was set to determine if the molecule was in the  $|\downarrow\rangle_{N_2}$  (“bright molecule” - blue dots) or  $\{|\uparrow\rangle_{N_2}\}$  (“dark molecule” - orange dots) states. The molecular state was repeatably determined to be “bright” 105 times with zero false detections. Afterwards, the molecular state was repeatedly determined to be “dark” 163 times with zero false detections. Bayesian inference states that for  $k$  measurements, the fidelity  $\mathcal{F}$  of the measurement can be given as,

$$\mathcal{F} = \frac{k + 1}{k + 2}. \quad (5.9)$$

Thus, for 105 “bright” and 163 “dark” detections, experimental fidelities of 99.1(9)% and 99.4(6)% were measured. The sudden change in the state of the molecule from “bright” to “dark” during the experiment was due to a quantum jump that was most likely caused by a

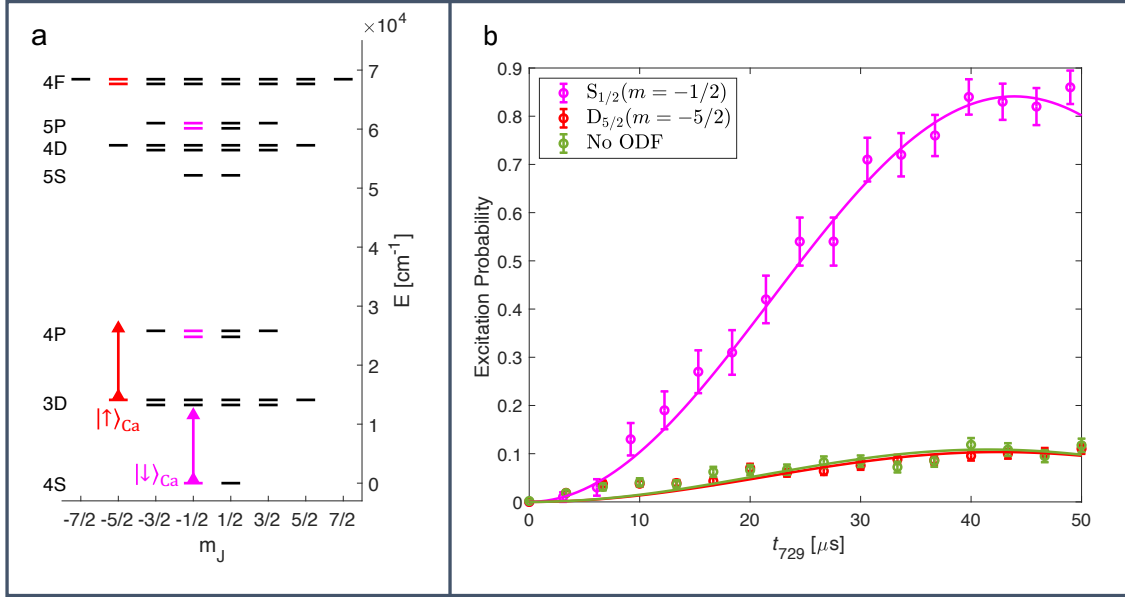


**Figure 5.9 Motional excitation due to  $\text{Ca}^+$  [115].** Due to the relatively close lying P states,  $\text{Ca}^+$  ion in the  $|\downarrow\rangle_{\text{Ca}}$  state experiences a large motional excitation (shown in magenta in a. and b.). In the  $|\uparrow\rangle_{\text{Ca}}$  state, the closest F state which can be coupled by the lattice is much farther detuned leading to a negligible motional excitation (shown in red in a. and b.).

state-changing collision with a background-gas molecule in our vacuum system at a pressure of  $1 \times 10^{-10}$  mbar.

The inset of fig. 5.8b shows a histogram of the QND determination. It can be noted that below the threshold  $P(|\downarrow_{\text{Ca}}\rangle) < 0.25$  (grey region), the state of the  $\text{N}_2^+$  was  $\{|\uparrow\rangle_{\text{N}_2}\}$  while above the threshold, the state was determined to be  $|\downarrow\rangle_{\text{N}_2}$ . An analogy can be drawn here between the QND molecular state detection and LIF atomic state detection where the recorded photons from atomic ions can be represented on similar histograms with a threshold for discriminating the atomic state. The QND measurement serves as the molecular counterpart for state detections.

#### 5.4.1 Suppression of motional excitation due to the $\text{Ca}^+$ ion

In the  $|\downarrow\rangle_{\text{Ca}}$  state, the  $\text{Ca}^+$  ion experienced a significant ac-Stark shift of 910 Hz due to the lattice laser (purple-dashed line in fig. 5.7). This was because the  $\pi$ -polarized lattice

laser, following the selection rule  $\Delta m = 0$ , coupled the  $|\downarrow\rangle_{\text{Ca}}$  state with the relatively close lying  $P_{1/2}$  and  $P_{3/2}$  states in  $\text{Ca}^+$  (shown by the magenta arrow in fig. 5.9a). Fig. 5.9b shows measurements of the excited motion of a single ground-state-cooled  $\text{Ca}^+$  ion for a lattice-laser duration of 1.5 ms and a single lattice-beam intensity of  $\sim 2 \times 10^6 \text{ W/m}^2$ . In the  $|\downarrow\rangle_{\text{Ca}}$  state, significant motion was excited and a strong Rabi sideband oscillation could be observed (shown in magenta in fig. 5.9b). This would lead to a loss in the SNR for the  $N_2^+$  state identification.

In order to prevent motional excitation due to ac-Stark shift experienced by the  $\text{Ca}^+$  ion in the  $|\downarrow\rangle_{\text{Ca}}$  state, the D Prep step was used to prepare the  $\text{Ca}^+$  in the  $|\uparrow\rangle_{\text{Ca}}$  state prior to the  $N_2^+$  state detection. In the  $|\uparrow\rangle_{\text{Ca}}$  state, the closest available state that lattice laser could couple ( $4F_{7/2}(m = -5/2)$ ) was much farther detuned (shown by the red arrow in fig. 5.9a). Thus, the ac-Stark shift experienced by the  $\text{Ca}^+$  due to the lattice laser was only 40 Hz (green-dashed line in fig. 5.7). In the  $|\uparrow\rangle_{\text{Ca}}$  state, almost no motion was excited (shown in red in fig. 5.9b) and the residual Rabi sideband signal was comparable to the case when the two-ion chain was cooled to the ground state and no ODF was implemented (shown in green in fig. 5.9b). Thus, any measured motional excitation could be attributed to the ac-Stark shift experienced by the  $N_2^+$  ion. The calculation of the ac-Stark shifts experienced by  $\text{Ca}^+$  is discussed in appendix A<sup>2</sup>.

### 5.4.2 Estimation of the state-detection fidelities

The problem of discriminating between the BSB success probabilities for the coherent states  $|\alpha\rangle$  and  $\{|\beta\rangle\}$  can be considered equivalent to the problem of distinguishing between two weighted coins, coin- $\alpha$  and coin- $\beta$ , with biased probabilities to get a heads,  $h$  (success in BSB measurements in the state-detection experiment). For the biased coin- $\beta$ , the probability to

---

<sup>2</sup>Although the calculations in the appendix A were done for a QCL, the ac-Stark shifts due to the lattice laser can be calculated in exactly the same manner by using the appropriate laser parameters for the lattice laser.

get a heads on a single coin toss,  $p_\beta = p(h|\beta)$ , was much less than the probability to get a heads on a single coin toss of the coin- $\alpha$ ,  $p_\alpha = p(h|\alpha)$ .  $p_\beta$  was non-zero but small and  $p_\alpha$  was less than unity, i.e.,

$$0 < p_\beta < p_\alpha < 1. \quad (5.10)$$

Because of this, a single coin toss was not sufficient to determine the coin with absolute certainty. Nonetheless, since the act of flipping a coin did not destroy the coin in any way, a given unknown coin could be repeatedly flipped in order to gather sufficient statistics to identify the coin with some certainty. Given  $p_\beta$ , the likelihood ( $L$ ) that  $N$  repeated coin flips would result in  $k$  heads can be given by,

$$L(p_\beta|k, N) = \frac{N!}{k!(N-k)!} p_\beta^k (1-p_\beta)^{N-k}. \quad (5.11)$$

Similarly for the coin- $\alpha$  with  $p_\alpha$ ,

$$L(p_\alpha|k, N) = \frac{N!}{k!(N-k)!} p_\alpha^k (1-p_\alpha)^{N-k}. \quad (5.12)$$

In order to distinguish between the coins in  $N$  measurements, a threshold  $k_t$  can be defined. In the case  $k \leq k_t$  heads occur in  $N$  coin flips, the coin can be guessed to be coin- $\beta$  while if  $k > k_t$  heads occur, the coin can be guessed to be coin- $\alpha$ . We define the threshold as the number of attempts where the likelihoods for both coins are the same, i.e.,

$$L(p_\beta|k_t, N) = L(p_\alpha|k_t, N). \quad (5.13)$$

From the equations (5.11) and (5.12),  $k_t$  can be found as,

$$k_t = \left[ \frac{N}{\frac{\log[p_\alpha/p_\beta]}{\log[(1-p_\beta)/(1-p_\alpha)]} + 1} \right]. \quad (5.14)$$

Based on the threshold, the errors in the coin-identification ( $\varepsilon_\alpha$  and  $\varepsilon_\beta$ ) can be estimated. Any residual likelihood  $L(p_\beta|k_t, N)$  for  $k > k_t$  and  $L(p_\alpha|k_t, N)$  for  $k < k_t$  would contribute

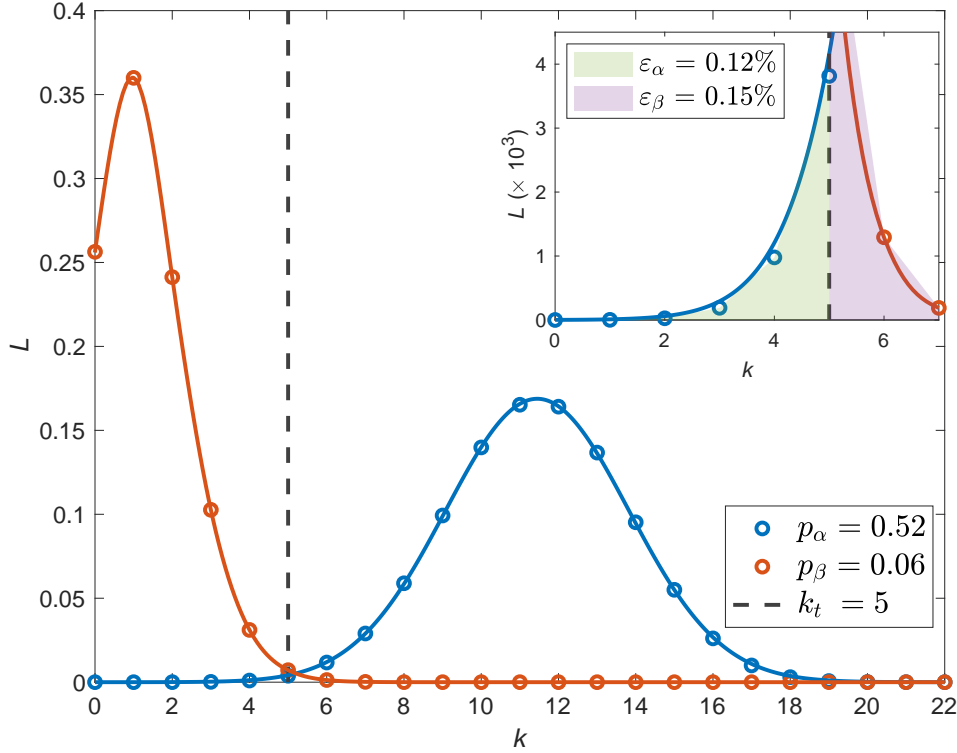


**Figure 5.10** Likelihood estimates ( $L$ ) of getting  $k$  successes (heads) in  $N = 22$  coin tosses for two weighted coins  $\alpha$  (blue) and  $\beta$  (orange). The probability to get heads for coin- $\alpha$  was  $p_\alpha = 0.52$  while that for coin- $\beta$  was  $p_\beta = 0.06$ . The probabilities were chosen similar to the experimentally measured probabilities during the QND state detection of the  $N_2^+$  ion (equation 5.7 and equation 5.8). For 22 repetitions, a threshold of  $k_t = 5$  heads (black dashed line) was determined and a maximal error rate of  $\varepsilon = 0.15\%$  was estimated (equation 5.15 and 5.16) in the coin identification. The error was due to residual non-zero likelihoods for incorrect coin identification (green and pink coloured areas in the inset).

to these errors indicating a finite chance of incorrect identification. Thus,

$$\varepsilon_\alpha = \sum_0^{k_t} L(p_\alpha|k_t, N), \quad (5.15)$$

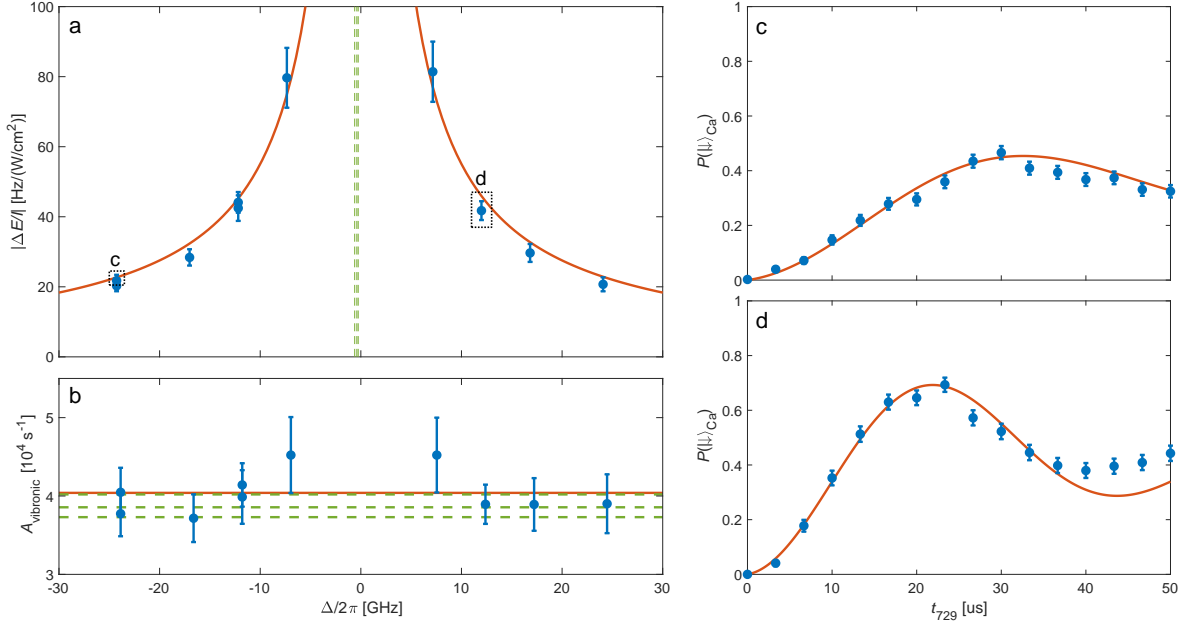
$$\varepsilon_\beta = \sum_{k_t+1}^N L(p_\beta|k_t, N). \quad (5.16)$$

Fig. 5.10 shows the estimated likelihood for the coin toss experiment with coin- $\alpha$  having a probability  $p_\alpha = 0.52$  (like  $P(|\downarrow\rangle_{C_a}|\alpha)$  in the experiments) for heads and coin- $\beta$  having  $p_\beta = 0.06$  (like  $P(|\downarrow\rangle_{C_a}|\beta)$  in the experiments).  $N = 22$  (number of repetitions for a single

QND measurement in the experiments) repeated coin flips were carried out. The likelihood of getting heads for coin- $\alpha$  (blue) is much greater than that of coin- $\beta$  (orange). A threshold of  $k_t = 5$  was determined. Thus, if  $> 5$  heads were measured in the 22 coin flips, the coin was identified to be coin- $\alpha$  and conversely for  $\leq 5$  heads measurements, the coin was identified to be coin- $\beta$ . In other words, the probability of getting heads in 22 measurements for coin- $\alpha$  was  $\geq 6/22 = 0.27$  while for coin- $\beta$ , the probability of  $\leq 5/22 = 0.23$ . For clarity, a threshold of 0.25 can be set. Errors due to a finite chance of wrongly identifying a coin- $\alpha$  as a coin- $\beta$  and vice-versa due to small but finite likelihood below and above the threshold respectively were  $\varepsilon_\alpha = 0.12\%$  and  $\varepsilon_\beta = 0.15\%$ , as can be seen from the inset of the fig. 5.10. Thus a fidelity of 99.85% could be achieved.

## 5.5 Force spectroscopy

Since the state-detection signal (i.e. the strength of the BSB oscillation measured on  $\text{Ca}^+$ ) was proportional to the ac-Stark shift experienced by the molecule, it could be used to perform a measurement of a spectroscopic transition in the molecule. Such a spectroscopic experiment was demonstrated on the  $R_{11}(1/2)$  spin-rotational component of the  $A^2\Pi_u(v' = 2) \leftarrow X^2\Sigma_g^+(v'' = 0)$  electronic-vibrational transition in  $\text{N}_2^+$  (fig. 5.11). Rabi oscillations on the BSB transition in  $\text{Ca}^+$  resulting from the ODF acting on a molecule in the  $|\downarrow\rangle_{\text{N}_2}$  state were measured for different detunings of the lattice-laser beams from the resonance. As the resonance was approached, the ac-Stark shift increased as  $\sim 1/\Delta$  leading to a larger coherent excitation,  $|\alpha\rangle$ , of the ion crystal. The value of the ac-Stark shift was extracted from a fit to the Rabi signal (fig. 5.11c, d). The fitting function was experimentally determined by applying a well-defined force on the  $\text{Ca}^+$  ion when the  $\text{N}_2^+$  ion was in one of the  $\{|\uparrow\rangle_{\text{N}_2}\}$  states and experienced no force. The use of an experimentally determined fitting function circumvented the need for characterizing the exact motional state, which could deviate from ideal coherent motion. For the chosen ODF pulse length of 500  $\mu\text{s}$ , the Rabi signal was



**Figure 5.11 Non-destructive force spectroscopy on a single  $\text{N}_2^+$  molecule [114].** Spectroscopic measurement of the  $A^2\Pi_u(v' = 2) \leftarrow X^2\Sigma_g^+(v'' = 0)$ ,  $R_{11}(1/2)$ , transition in  $\text{N}_2^+$ . a) The blue data points represent the amplitude of the ac-Stark shift normalized by the lattice-laser intensity and experienced by the  $\text{N}_2^+$  ion as a function of the detuning from resonance as extracted from fits to BSB Rabi-oscillation signals (insets (c),(d)). Error bars ( $1\sigma$ ) correspond to the uncertainty in the beam intensity and in the extraction of the ODF strength from the BSB signals. The red line is a fit to the experimental data used to extract the line center. The green dashed lines are the values of the line centers reported in the literature [76, 230, 231]. b) The blue data points represent values for Einstein-A coefficients of the  $A^2\Pi_u(v' = 2) \rightarrow X^2\Sigma_g^+(v'' = 0)$  vibronic transition in  $\text{N}_2^+$  extracted from the measurements in (a). The red line is the mean of all measurements. Different literature values [232–234] are given by the dashed green lines.

sensitive to ac-Stark shifts in the interval from 2.5 to 13 kHz. To extend the dynamic range of our measurement, the lattice-beam powers were scaled to keep the Rabi signal within the experimental sensitivity range. Further details about the determination of the fitting function can be found in sec. 5.5.1.

Fig. 5.11a depicts such a force spectrum of this transition. The experimentally measured ac-Stark shifts were fitted with a  $\sim 1/|f - f_0|$  ac-Stark-shift profile to determine the line center,  $f_0 = 380.7011(2)$  THz, which agrees well with previous measurements [76, 230, 231] using ensembles of molecules which yielded results in the range  $f_0 = 380.7007(3)$  THz (dashed

green lines in fig. 5.11a). The precision of our measurement can be enhanced by using smaller detunings, however, at the expense of an increased probability to scatter a photon at the molecule by the lattice beams and thus losing the molecular state. As an example, for the current experimental parameters of  $\sim 10$  GHz detuning and  $\sim 10$  kHz ac-Stark shift, an average of 1'000 QND state determination cycles (22'000 BSB pulses) can be expected before the molecular state is lost due to off-resonant scattering. Decreasing the detuning to 100 MHz will reduce the number of expected QND state determinations to 10 (2'200 BSB pulses) due to the  $1/\Delta^2$  scaling of the scattering rate (compared to the ac-Stark shift scaling of  $1/\Delta$ ). Nevertheless, these measurements are possible with efficient and reliable replenishment of molecular ions in the trap. For such close detunings, our method is expected to be sensitive to the hyperfine structure of the transition (see sec. 3.3) which is not resolved here and has, to our knowledge, not been studied experimentally yet. In this experiment, the absolute accuracy of the wavemeter used to evaluate the lattice-laser frequency was estimated to be better than 50 MHz by a repetitive measurements of the  $P_{3/2} \leftarrow D_{5/2}$  spectroscopic transition in  $\text{Ca}^+$  during the experiment.

The vibronic Einstein- $A$  coefficient,  $A_{\text{vibronic}}$ , of the  $A^2\Pi_u(v' = 2) \rightarrow X^2\Sigma_g^+(v'' = 0)$  transition was extracted from the ac-Stark-shift measurements as shown in fig. 5.11b. For each ac-Stark-shift determination,  $\Delta E(\Delta)$  (fig. 5.11a), a corresponding value  $A_{\text{vib}}(\Delta)$  was calculated. The mean value of  $A_{\text{vib}} = 4.03(11) \times 10^4 \text{ s}^{-1}$  is in good agreement with previous results in the range  $A_{\text{vib}} = 3.87(14) \times 10^4 \text{ s}^{-1}$  [232–234] (fig. 5.11b dashed green lines). The two data points with the smallest detuning in fig. 5.11b seem to slightly deviate from the other points. This might be due to the unresolved hyperfine structure of the transition which becomes non-negligible at close detunings. Nevertheless, all points were included in the determination of  $A_{\text{vib}}$ .

### 5.5.1 Determination of the fitting function for Rabi sideband oscillations

In principle, the BSB signal could be calculated analytically knowing the Fock-state distribution [201] which was expected for the chosen ODF parameters [115, 227]. However, due to experimental imperfections and decoherence, the underlying Fock-state distribution could deviate from the theoretical predictions. Thus, a direct approach was adopted here in which a generalized calibration function was experimentally established to fit the measured BSB oscillation and determine the ac-Stark shift experienced by the  $N_2^+$ .

As stated earlier, to simulate the expected BSB Rabi signal due to the coherent motional excitation of  $N_2^+$ , an experiment was performed in which the  $Ca^+$  ion experienced a modulated ac-Stark shift while the  $N_2^+$  molecular state was chosen such that its interaction with the lattice beams was negligible and thus experienced no ac-Stark shift. This was accomplished by choosing experiments in which the  $N_2^+$  was ionized in the  $\{|\uparrow\rangle_{N_2}\}$  state due to an imperfect REMPI. The  $Ca^+$  ion was initialized in the  $|\downarrow\rangle_{Ca} = |S_{1/2}(m = -1/2)\rangle$  state which coupled strongly to the lattice beams due to its interaction with the  $P_{1/2}$  and  $P_{3/2}$  states as stated before. In this case, the magnitude of the ac-Stark shift experienced by the  $Ca^+$  could be directly measured on the narrow electric-quadrupole  $|\downarrow\rangle_{Ca} \leftarrow |\uparrow\rangle_{Ca}$  transition. The magnitude of the ac-Stark shift experienced by the  $Ca^+$  ion could be tuned by changing the lattice-laser powers. The same lattice-beam duration of  $500 \mu s$  was then used to excite coherent motion in the ion crystal at different laser powers. Since in this experiment, as opposed to the state-determination experiments on the  $N_2^+$ , the  $Ca^+$  was prepared in the  $|\downarrow\rangle_{Ca}$  state, a red-sideband (RSB) pulse (instead of a BSB pulse) was applied to measure Rabi oscillations. Several Rabi oscillations were measured for several ac-Stark shifts experienced by  $Ca^+$ . Coloured data points in fig. 5.12a show the RSB Rabi oscillations due to coherent excitation of the  $Ca^+-N_2^+$  two-ion string, measured on the  $Ca^+$  ion, due to 10 different ac-Stark shifts experienced by the  $Ca^+$ . In order to find a generalized fitting function

(coloured solid lines in fig. 5.12a), a theoretical model for Rabi sideband oscillations in a mixed-species two-ion chain was explored (see sec. 5.5.1.1 and sec. 5.5.1.2 below). Three fitting parameters were used to achieve a good agreement with the experimental data. These were the average Fock state  $\langle n \rangle$  of the coherently excited  $\text{Ca}^+ - \text{N}_2^+$  string, the detuning  $\delta$  of the 729 nm laser exciting RSB oscillations on the  $\text{Ca}^+$  and a phase decoherence time with a time constant  $T_2$ . The parameters (blue points) and the polynomial fits to the parameters (solid red line) as a function of the ac-Stark shift experienced by the  $\text{Ca}^+$  are discussed and shown in fig. 5.12b, c and d below.

### 5.5.1.1 Theory of Rabi sideband oscillations in mixed-species two-ion crystals

The coupling of the IP axial mode used in our QND protocol to the light field is affected by excitation of the other normal modes of the two ion-string. In the present case, this particularly applies to the OP axial mode which lies parallel to the in-phase mode and to the k-vector of the optical lattice. The derivation of normal modes in two-ion chains of unequal masses can be found, e.g., in [235, 236]. After establishing the normal modes of the system, standard techniques for deriving the ion-light coupling can be used [237]. Here, for the purpose of completeness, we reproduce these derivations for the specific case of a molecular ion of mass  $m(\text{N}_2^+)$  and an atomic ion of mass  $M(\text{Ca}^+)$ . A more detailed description can be found in [56, 227].

In the regime where the radial confinement is much stronger than the axial confinement, the system can be treated as a one dimensional system with a Lagrangian for small displacements from equilibrium given by [235],

$$\mathcal{L} = \frac{1}{2}(m\dot{q}_1^2 + M\dot{q}_2^2) - \frac{1}{2} \sum_{i,j=1}^2 q_i q_j V_{ij}. \quad (5.17)$$

Here,  $q_1(q_2)$  is a small axial displacement from the equilibrium point of the ion of mass  $m(M)$  and  $V$  is the potential energy expanded around the equilibrium positions of the ions in Taylor series up to second order thus neglecting anharmonic terms. The potential energy

components are  $V_{11} = V_{22} = 2u_0$  and  $V_{12} = V_{21} = u_0$  where  $u_0$  is the spring constant of the axial-trapping confinement. For our experiments,  $u_0 = 1.04 \times 10^{-12}$  J/m<sup>2</sup> (estimated from equation 5.21 below).

To derive the normal modes  $\beta$  of the system, we perform a scaling transformation,  $q_1 = \sqrt{\mu}q'_1$  and  $q_2 = q'_2$  where  $\mu = M/m$  is the ratio of the mass of the ions followed by a rotation,

$$\begin{pmatrix} \beta_+ \\ \beta_- \end{pmatrix} = \begin{pmatrix} \cos \theta & \sin \theta \\ -\sin \theta & \cos \theta \end{pmatrix} \begin{pmatrix} q'_1 \\ q'_2 \end{pmatrix}, \quad (5.18)$$

where,

$$\sin \theta = \sqrt{\frac{\mu/2}{1 - \mu + \mu^2 - (1 - \mu)\sqrt{1 - \mu + \mu^2}}}. \quad (5.19)$$

These transformations yield a Lagrangian of two uncoupled harmonic oscillators,

$$\mathcal{L} = \frac{1}{2} M \left( \dot{\beta}_+^2 + \dot{\beta}_-^2 \right) - \frac{1}{2} M \left( \Omega_+^2 \beta_+^2 + \Omega_-^2 \beta_-^2 \right). \quad (5.20)$$

Here,  $\beta_{\pm}$  are the scaled and rotated (about an angle  $\theta = 35.14^\circ$  in our system) coordinates of the normal modes of harmonic oscillators of mass  $M$  and frequency,

$$\Omega_{\pm}^2 = \frac{u_0}{M} \left( 1 + \mu \pm \sqrt{1 + \mu^2 - \mu} \right). \quad (5.21)$$

For our experiment,  $\Omega_+ \approx 2\pi \times 1210$  kHz is the frequency of the OP mode of motion and  $\Omega_- \approx 2\pi \times 678$  kHz is the frequency of the IP mode of motion.

The Hamiltonian for describing the Rabi-oscillation signal is given by,

$$\hat{H} = \hat{H}^{(m)} + \hat{H}^{(e)} + \hat{H}^{(i)}. \quad (5.22)$$

Here,

$$\hat{H}^{(m)} = \hbar\Omega_+ \left( \hat{a}_+^\dagger \hat{a}_+ + 1/2 \right) + \hbar\Omega_- \left( \hat{a}_-^\dagger \hat{a}_- + 1/2 \right), \quad (5.23)$$

is the Hamiltonian of the ion motion in the normal modes of the system with  $\hat{a}_{\pm}^\dagger$  ( $\hat{a}_{\pm}$ ) the raising (lowering) operators which obey the following relation to the quantized normal-modes

position operators,  $\hat{\beta}_{\pm} = \beta_{\pm}^0 (\hat{a}_{\pm}^{\dagger} + \hat{a}_{\pm})$  with  $\beta_{\pm}^0 = \sqrt{\hbar/2M\Omega_{\pm}}$ . The electronic part of the Hamiltonian

$$\hat{H}^{(e)} = \hbar\omega_0\hat{\sigma}_z/2, \quad (5.24)$$

describes the splitting of the  $|\downarrow\rangle_{\text{Ca}}$  and the  $|\uparrow\rangle_{\text{Ca}}$  levels by the transition frequency,  $\omega_0$ , where  $\hat{\sigma}_z$  is the Pauli  $z$ -matrix. The last term of the Hamiltonian describes the interaction with light,

$$\hat{H}^{(i)} = \frac{\hbar}{2}\Omega_0(\hat{\sigma}_+ + \hat{\sigma}_-)(e^{i(k\hat{x}_2 - \omega t + \phi)} + e^{-i(k\hat{x}_2 - \omega t + \phi)}). \quad (5.25)$$

The Rabi frequency  $\Omega_0$  characterizes the coupling strength. In our system, we measured the bare Rabi frequency to be  $\Omega_0 \approx (2\pi) \times 90$  kHz.

The laser wavenumber, frequency and phase are given by  $k$ ,  $\omega$  and  $\phi$ . The internal states are coupled through the raising and lowering Pauli operators,  $\hat{\sigma}_{\pm}$ , and the motional states are coupled through the position operator of the ion of mass  $M$  ( $\text{Ca}^+$ ),  $\hat{x}_2$ . Note that this operator is given in real space while the normal modes are in the scaled and rotated space. The transformation is given by,

$$\hat{x}_2 \propto \hat{q}_2 = \sin(\theta)\hat{\beta}_+ + \cos(\theta)\hat{\beta}_-, \quad (5.26)$$

neglecting the ion's equilibrium position in the transformation which gives a constant phase factor.

In the interaction picture and after performing the rotating-wave approximation, the interaction Hamiltonian can be stated as,

$$\hat{H}^{(i)} = \frac{\hbar}{2}\Omega_0\hat{\sigma}_+e^{i\left(\eta_+(\hat{a}_+^{\dagger}e^{i\Omega_+t} + \hat{a}_+e^{-i\Omega_+t}) + \eta_-(\hat{a}_-^{\dagger}e^{i\Omega_-t} + \hat{a}_-e^{-i\Omega_-t}) - \Delta t + \phi\right)} + H.c. \quad (5.27)$$

Here,  $\eta_+ = k\beta_+^0 \sin(\alpha)$  and  $\eta_- = k\beta_-^0 \cos(\alpha)$  are the Lamb-Dicke parameters of for the OP and the IP modes, respectively. In our system,  $\eta_+ = 0.051$  and  $\eta_- = 0.096$ . The laser-frequency detuning from the carrier resonance,  $\Delta = \omega - \omega_0$ , is set in the experiment to  $\Delta = \pm\Omega_-$  for blue- and red-sideband spectroscopy of the IP motional mode. The OP

“spectator” mode is off resonance and is affecting the transition through a Debye-Waller factor [237].

The effect of the motional modes on the Rabi frequency is given by,

$$\Omega_{n_+, n_- \pm 1} = \Omega_0 |\langle n_+, n_- \pm 1 | e^{i\eta_+(\hat{a}_+^\dagger + \hat{a}_+) + i\eta_-(\hat{a}_-^\dagger + \hat{a}_-)} | n_+, n_- \rangle | \quad (5.28)$$

$$= \Omega_0 e^{-\eta_+^2/2} L_{n_+}^0(\eta_+^2) e^{-\eta_-^2/2} n_{->}^{-1/2} \eta_- L_{n_-<}^1(\eta_-^2). \quad (5.29)$$

Here,  $\Omega_{n_+, n_- \pm 1}$  is the Rabi frequency for a sideband transition on the IP mode in which the IP mode of motion changes its motional state by one quanta. The OP mode does not change its motional state in this transition. For a red sideband,  $n_{->} = n_- + 1$  and  $n_{-<} = n_-$ .  $L_n^\alpha(x)$  is a generalized Laguerre polynomial. The motional state of the IP mode has a dramatic effect on the Rabi frequency since  $\Omega_{n_+, n_- \pm 1} \propto \eta_- \sqrt{n_-}$  to first order in the IP Lamb-Dicke parameter. This is why Rabi sideband oscillations are sensitive to the amplitude of motion excited by the lattice. The motional state of the OP mode has a much less dramatic effect since  $\Omega_{n_+, n_- \pm 1} \propto (1 - \eta_+^2(n_+ + 1/2))$  to first order in the OP Lamb-Dicke parameter.

The general solution for the Rabi oscillation signal is given by [237],

$$y(t_{729}) = \sum_{n_+, n_-} P_{\{n_+, n_-\}} \frac{\Omega_{n_+, n_- \pm 1}^2}{\Omega_{n_+, n_- \pm 1}^2 + \delta^2} \sin^2 \left( \sqrt{\Omega_{n_+, n_- \pm 1}^2 + \delta^2} t_{729}/2 \right). \quad (5.30)$$

Here,  $P_{\{n_+, n_-\}}$  is the joint probability to be in the motional state  $|n_+, n_-\rangle$ . We further assume that  $P_{\{n_+, n_-\}} = P_T(n_+|T_D) \times P(n_-|\alpha)$ , i.e., that the probabilities of the different modes are independent and follow a specific distribution. Here,  $P(n_-|\alpha) = e^{-|\alpha|^2} |\alpha|^{2n_-} / n_-!$  is a coherent state distribution of the IP mode with amplitude of motion  $\alpha$ , and  $P_T(n_+|T_D) = \bar{n}_+^{n_+} / (1 + \bar{n}_+)^{n_++1}$  is a thermal distribution of the OP mode with  $\bar{n} = (e^{\hbar\Omega_+/k_B T_+} - 1)^{-1} \approx k_B T_+ / \hbar\Omega_+$ . For the thermal distribution,  $k_B$  is the Boltzmann constant and  $T_+ = 0.8 \pm 0.1$  mK is the temperature of the OP mode extracted from carrier Rabi spectroscopy. This temperature corresponds to  $\bar{n} \approx 13.8$  quanta which results in a mean reduction of the Rabi frequency by 4.5% compared to when the OP mode is completely cooled to its ground state. The detuning in the above equation,  $\delta_\pm = \Delta \mp \Omega_-$ , is given with respect to the frequency of the sideband transition.

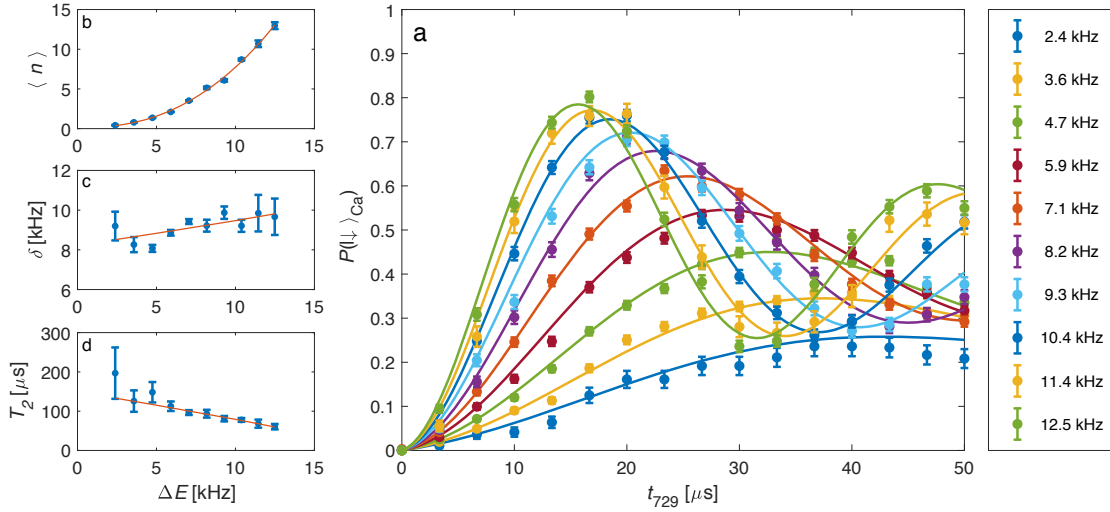


**Figure 5.12 Ac-Stark shift calibration [114].** a) Red-sideband oscillations due to a pre-determined modulated ac-Stark shift amplitude applied on  $\text{Ca}^+$  when  $\text{N}_2^+$  experiences no ac-Stark shift. Lines are fits to the function defined in equations 5.30 and 5.31. The ac-Stark shift experienced by the molecule is given in the legend. b-d) Polynomial fits (red lines) of the parameters (blue points) extracted from fits to the RSB oscillations in (a). Error bars represent 68% confidence intervals.

### 5.5.1.2 Extracting molecular ac-Stark shifts from blue-sideband Rabi flops

We fitted the RSB flops to the general solution of RSB Rabi oscillations (equation 5.30) with the addition of phase decoherence characterized by a time constant  $T_2$  [237],

$$P(|\downarrow\rangle_{\text{Ca}}) = y(t_{729})e^{-t_{729}/T_2} + (1 - e^{-t_{729}/T_2})/2. \quad (5.31)$$

Although, the three fitting parameters  $\langle n \rangle = \alpha^2$ ,  $\delta$ ,  $T_2$  have physical meanings, they were treated as phenomenological quantities here used to model the Rabi flops with a minimum number of fit parameters. Since the measurements were performed in the same apparatus and conditions as the experimental data was taken, the measured RSB signals represent faithfully the expected molecular signal. Further, a fitting function  $P(|\downarrow\rangle_{\text{Ca}}|\Delta E, t_{729})$  with a single fit parameter, the ac-Stark shift ( $\Delta E$ ), was constructed to fit the BSB oscillation data recorded when the force acted on the  $\text{N}_2^+$ . For that, the three fit parameters  $\langle n \rangle(\Delta E)$ ,  $\delta(\Delta E)$  and  $T_2(\Delta E)$  were further fit to second and first order polynomial functions as shown

in fig. 5.12b, c and d.

The values of the ac-Stark shifts extracted from the fitting function,  $P(|\downarrow\rangle_{\text{Ca}}|\Delta E, t_{729})$ , corresponds to the ac-Stark shift applied on the  $\text{Ca}^+$  ion. However, from the scaling transformation applied to the Lagrangian of the system (discussions of equation (5.20)) it is clear that the energy of the system after applying the same force on the  $\text{N}_2^+$  is scaled by a factor due to the mass difference of the ions. To avoid this factor, the  $\text{Ca}^+$  calibration experiments should have been performed with a laser wavelength scaled by  $\sqrt{\mu}$ . In our case, this corresponds to a wavelength of 940 nm instead of 787 nm. We confirmed this prediction with a numerical simulation. Instead of using a different laser for the calibration experiment, we used a classical simulation (see the appendix of [115] for details) to extract the correction factor for the ac-Stark shift. This correction factor increases the ac-Stark shift and the resulting vibronic-Einstein-A coefficient by  $\sim 17\%$ . The treatment is vindicated by the good agreement of our experimental results on  $\text{N}_2^+$  with the literature values (see fig. 5.11).

## 5.6 Coherent manipulation of the $\text{N}_2^+$ ion

Non-destructive detection of the internal rovibrational state of  $\text{N}_2^+$  facilitates coherent-control experiments on the molecular ion. Several transitions, ranging from the rf to the IR frequency domain, from the ground  $|\downarrow\rangle_{\text{N}_2}$  state of the  $\text{N}_2^+$  ion were theoretically identified [53,56] which can enable the use of  $\text{N}_2^+$  as a molecular qubit and in precision spectroscopy experiments [53–56]. Many of these transitions are expected to feature first- and second-order magnetic-field-noise insensitivity and coherence times of up to tens of minutes in a room temperature environments are predicted. Clock transitions, in the mid-IR frequency region, which are free from electric-quadrupole shifts and are measurable to relative uncertainties of  $10^{-17}$  were also determined.

In a first step, we plan to investigate the weak electric-quadrupole,  $S(0)$ ,  $|X^2\Sigma_g^+, v'' = 0, N'' = 0\rangle \leftrightarrow |X^2\Sigma_g^+, v' = 1, N' = 2\rangle$  transition at  $\sim 65.2$  THz (shown in fig. 5.13b). These

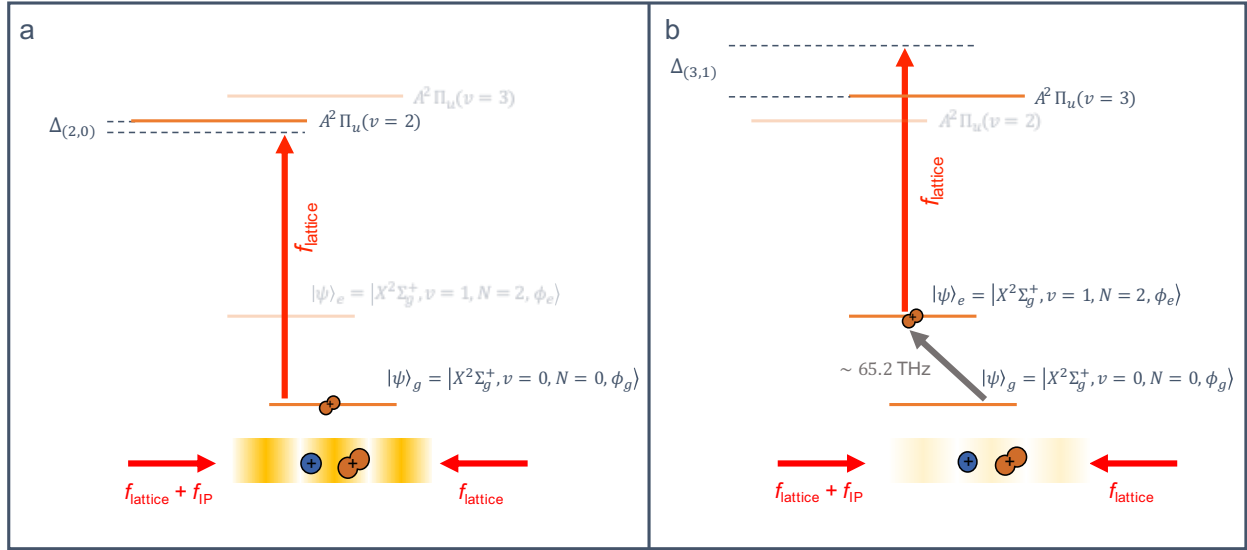


**Figure 5.13 Simplified energy-level scheme of  $N_2^+$  to illustrate the effect of vibrational excitation on the ODF.** (a) In the vibronic ground  $|\psi\rangle_g$  state, the ODF experienced by the  $Ca^+-N_2^+$  was strong due to the relatively closer detuned optical lattice ( $f_{\text{lattice}}$ ). The frequency detuning of the lattice from the closest available transition is given as  $\Delta_{(2,0)}$  (where the subscripts indicate the upper and the lower vibrational levels coupled by the lattice). (b) After an excitation of the  $N_2^+$  ion to the  $|\psi\rangle_e$  state by the mid-IR laser, the closest available transition coupled by the optical lattice is much farther detuned ( $\Delta_{(3,1)} \gg \Delta_{(2,0)}$ ). Thus the expected ODF is much weaker in this case. Levels greyed out in (a) and (b) do not contribute during the state detection of  $N_2^+$ .

transitions are of interest due to their unique properties for precision measurements like spectroscopic tests of a possible temporal variations of the ratio of the proton-to-electron mass [54,55]. For this, a narrow-linewidth, spectrally-pure, mid-IR QCL has been setup (see sec. 4.2 for the details of the stabilization setup). This would facilitate the coherent coupling of rovibrational states in the molecule.

The coherent coupling between the rovibrational states could also be used to project the molecule into a specific spin-rotation, hyperfine and Zeeman level. For instance, after the non-hyperfine and non-Zeeman resolved REMPI preparation of the  $N_2^+$  in the ground state, the state of the  $N_2^+$  ion can be given by,

$$|\psi\rangle_g = |\downarrow\rangle_{N_2} = |X^2\Sigma_g^+, v=0, N=0, \phi_g\rangle, \quad (5.32)$$

where,  $|\phi\rangle_g = |J = 1/2, F, m_F\rangle$ , represents the fine quantum number and the many possible hyperfine and the Zeeman quantum numbers. A coherent pulse on the mid-IR transition could be used to create a superposition between the ground and the excited states (fig. 5.13b),

$$|\psi\rangle_{\text{QCL}} = a |\psi\rangle_g + b |\psi\rangle_e, \quad (5.33)$$

where,

$$|\psi\rangle_e = |X^2\Sigma_g^+, v = 1, N = 2, \phi_e\rangle, \quad (5.34)$$

and,  $|\phi\rangle_e = |J = 3/2, F, m_F\rangle$  or  $|\phi\rangle_e = |J = 5/2, F, m_F\rangle$  depending on the fine structure transition addressed by the QCL. An ODF pulse to detect the molecular state could then be applied which would project the molecule either in the ground state or the excited state with the probabilities  $|a|^2$  and  $|b|^2$  respectively. In case the ion was projected to the  $|\psi\rangle_g$  state, a strong motion would be excited due to the relatively closer detuned optical-lattice (labelled as  $\Delta_{(2,0)}$  in fig. 5.13a). In the case when the molecule was projected in the  $|\psi\rangle_e$  state, almost no coherent excitation is expected due to the farther detuned optical lattice (labelled as  $\Delta_{(3,1)}$  in fig. 5.13b). In either case, the projection prepares the molecule in a specific hyperfine and Zeeman state. The motion of the ions can then be re-cooled and the excitation and state-detection can be repeated in order to measure the excitation probability,  $|b|^2$ , as a function of the QCL frequency. Thus, the spectra of the IR transition can be obtained. In order to excite a different transition from another hyperfine or Zeeman state, additional Raman, rf and microwave couplings can be implemented in order to mix different states in  $|\psi\rangle_g$  manifold [53, 56, 115].

## 5.7 Implications and summary

This chapter discussed new developments for the quantum control of molecules. A single  $\text{N}_2^+$  ion is trapped with one  $\text{Ca}^+$  ion for precision measurements on the  $\text{N}_2^+$  ion. REMPI

techniques for the internal-state preparation of the  $N_2^+$  ion, unresolved and resolved sympathetic cooling techniques for the motion of the two-ion crystal and the non-destructive and non-demolition state-detection of the  $N_2^+$  ion have been presented. Fidelities  $>99\%$  were demonstrated for the state-detection scheme. Due to the non-invasive nature of the state-detection scheme (i.e., no transitions were excited in the  $N_2^+$  during the detection), the fidelity was not limited by the state lifetime and off-resonant photon scattering as is often the case in atomic ions [187, 238]. Longer measurements with better statistics can be used to further improve the measurement fidelity at the expense of a slower data acquisition rate. Also, as an application of the detection scheme, a new approach for measuring a spectroscopic line positions and transition strengths in molecules using “force” spectroscopy has been presented.

The presented QND scheme is universally applicable to both polar and apolar molecular ions [195]. It represents a highly sensitive method to repeatedly and non-destructively read out the quantum state of a molecule [114] and thus introduces a molecular counterpart to the state-dependent fluorescence on closed-cycling transitions which forms the basis of sensitive readout schemes in atomic systems [187, 238]. It enables state-selected and coherent experiments with single trapped molecules with duty cycles several orders of magnitude higher than previous destructive state-detection schemes [181, 185]. It thus lays the foundations for vast improvements in the sensitivity and, therefore, precision of spectroscopic experiments on molecular ions, as discussed in ref. [53, 56, 115]. The possibility for efficient, non-destructive state readout also lays the foundation for the application of molecular ions in quantum-information and coherent-control experiments as are currently being performed with great success using atomic ions [187]. In this context, the potentially very long lifetimes and coherence times of molecular states may offer new possibilities for, e.g., realising quantum memories. As another application, the present scheme also enables studies of cold collisions and chemical reactions between ions and neutrals with state control on the single-molecule level and, therefore, offers prospects for the exploration of molecular collisions and chemical

reaction mechanisms in unprecedented detail. Finally, our approach can also be employed not only to *detect*, but also to *prepare* the quantum state of a single molecule through a projective measurement down to the Zeeman level [115] opposed to previous schemes [181, 183] which could prepare only the rovibronic level of the molecule. The present scheme thus also represents a key element in the methodological toolbox of the upcoming field of molecular quantum technologies and the realization of molecular qubits encoded in the rovibrational spectrum.

# Chapter Six

## Conclusion and outlook

This thesis discusses the quantum control of single molecules. The  $\text{N}_2^+$  ion has been chosen as a prototypical example for the studies presented in this thesis, although many theoretical and experimental concepts presented here are either directly applicable to different diatomic and polyatomic molecules or require slight adaptations. Being apolar, the  $\text{N}_2^+$  ion serves as a good candidate for tests of fundamental physics, precision studies and for developing new frequency standards and molecular qubits [53–56].

To begin with theory behind light-molecule interaction is developed with a focus on off-resonant dipole-allowed interactions between the  $\text{N}_2^+$  ion and far-detuned laser light. Effects due to the hyperfine structure and rotational-state mixing of the molecule have also been explored. Although many parts of the theory presented in the thesis can be found scattered across various spectroscopic texts [61,63,64,101,102], a complete and consistent discussion is often lacking. Thus, here, a rigorous treatment of hyperfine effects electric-dipole transition transitions between states described by different Hund’s coupling cases has been presented and transition parameters like the transition-dipole matrix elements and Hönl-London factors have been calculated from first principles.

The theory behind resonant dipole-forbidden transitions in  $\text{N}_2^+$  can be found in [53, 56, 75, 196]. While experiments in the past [75, 185] demonstrated incoherent techniques for spectroscopic studies of  $\text{N}_2^+$ , this thesis aims at setting the stage for coherent manipulation

of the molecular ion. In addition to a gain of many orders of magnitude in the duty cycle of experiments, coherent techniques would allow for accurate and precise measurements of rovibrational transitions of the molecule. This thesis discusses the stabilization of a mid-IR laser source which would be employed for such interrogations. We reference the laser to a Cs fountain clock [135] and a hydrogen maser in a remote location for the absolute determination of the laser frequency. Additionally, a novel alignment technique for the mid-IR laser, based on off-resonant atom-light interaction, is also presented.

A key advancement discussed here is the non-destructive and the non-demolition state-detection of molecular ions. A number of advanced experimental techniques for manipulating the internal and external states of molecules are presented. These include threshold-ionization techniques for preparing the molecular ion in the required internal state and quantum-logic techniques for the cooling of the external motion and the internal state detection of the  $N_2^+$  ion. Demonstration of state-detection fidelities exceeding 99% are presented. As an application to the state detection technique, a novel “force” spectroscopic measurement of dipole-allowed rovibronic transition in  $N_2^+$  is also presented. Line-center and transition parameter were calculated.

In the near future, direct excitation of mid-IR electric quadrupole rovibrational transitions in electronic ground state of  $N_2^+$  could be performed. Such measurements might be exploited for precision measurements and studies of possible variations in universal constants like the proton-to-electron mass ratio. In addition, these would facilitate state and energy controlled investigations of chemical reactions on the single molecule level. They would also allow for development of new frequency standards and molecular qubits.

## Appendices

# Appendix A

## Ac-Stark effect in $\text{Ca}^+$ atomic ions

### A.1 Valence contributions

Here we list the parameters needed to calculate the energy shifts of the quadrupole  $4\text{S}_{1/2}(m = -1/2) \leftrightarrow 3\text{D}_{5/2}(m = -5/2)$  transition in  $\text{Ca}^+$  ion due to the ac-Stark effect. The total shift in the transition frequency can be given by the difference of the total ac-shift experienced by the  $3\text{D}_{5/2}(m = -5/2)$  state and the total ac-shift of the  $4\text{S}_{1/2}(m = -1/2)$  state due to their interactions with all other possible states following the usual dipole selection rules of  $\Delta l = \pm 1$  and  $\Delta m = 0, \pm 1$ .

Table A.1 lists the unperturbed transition frequencies ( $\lambda_0$ ) [239], Einstein-A coefficients ( $A$ ) [121, 239] and upper-state lifetimes ( $\tau$ ) [121] of all possible dipole-allowed transitions from the  $4\text{S}_{1/2}$  and the  $3\text{D}_{5/2}$  energy levels in  $\text{Ca}^+$  ion. The individual ac-Stark shifts ( $\Delta E_i$ ) due to the interaction of the  $4\text{S}_{1/2}(m = -1/2)$  and  $3\text{D}_{5/2}(m = -5/2)$  Zeeman sublevels with all other possible Zeeman sublevels of other states are calculated as [240],

$$\Delta E_i = -\frac{3\pi c^2 \cdot I \cdot A}{\omega_0^2 \cdot (\omega_0^2 - \omega_l^2)} \sum_k \sum_q \left| \sqrt{2J_k + 1} \begin{pmatrix} J_k & 1 & J_i \\ -m_k & q & m_i \end{pmatrix} p \right|^2. \quad (\text{A.1})$$

The table A.1 shows the calculated ac-Stark shifts due to a QCL operating at a wavelength of  $\lambda_l = 4574$  nm, with an optical power  $P \approx 78$  mW and focused to a beam waist of  $w_0 \approx 58$   $\mu\text{m}$  (not to be confused with  $\omega_0$ ). The laser intensity ( $I$ ) could be given as,  $I = 2P/\pi w_0^2 = 14.76$  W/m<sup>2</sup>.  $\omega_0$  and  $\omega_l$  are the unperturbed-transition frequency and the laser frequency respectively. The double row symbols in the parenthesis are the Wigner-3j

symbols. The terms  $J_i$  and  $J_k$  represent the lower and upper fine-structure states respectively (for example for the  $3D_{5/2} \rightarrow 4P_{3/2}$  interactions,  $J_i = 5/2$  and  $J_k = 3/2$ ). The terms  $m_i$  and  $m_k$  represent the lower and the upper Zeeman components.  $q = (-1, 0, 1)$  define the three components of a spherical vector.  $p$  is the polarization factor which accounts for the laser polarization with respect for the quantization axis defined as [241],

$$p = c_i^{(q)} \epsilon_i,$$

where the vector  $c_i^{(q)}$  are the usual normalized spherical basis vector given by,

$$\begin{aligned} \mathbf{c}^{(1)} &= -\frac{1}{\sqrt{2}}(1, -i, 0) \\ \mathbf{c}^{(0)} &= (0, 0, 1) \\ \mathbf{c}^{(-1)} &= \frac{1}{\sqrt{2}}(1, i, 0) \end{aligned}$$

Here, we assumed the QCL to be polarized linearly parallel to the quantization axis (defined by the magnetic field in the experiment) and propagating perpendicular to the quantization axis ( $\epsilon_i = (0, 0, 1)$  for a magnetic field  $\mathbf{B} = (0, 0, B)$ ). The total ac-shift for the  $4S_{1/2}(m = -1/2) \leftrightarrow 3D_{5/2}(m = -5/2)$  transition can then be given by,

$$\Delta E = \Delta E_{3D_{5/2}(m=-5/2)} - \Delta E_{4S_{1/2}(m=-1/2)}$$

where  $\Delta E_{3D_{5/2}(m=-5/2)}$  and  $\Delta E_{4S_{1/2}(m=-1/2)}$  are the total ac-shifts experienced by the  $3D_{5/2}(m = -5/2)$  and  $4S_{1/2}(m = -1/2)$  states respectively. A total ac-shift of 4.79 kHz is then expected.

Lower state	Upper state	$\lambda_0$ [nm]	A [ $\times 10^6$ rad/sec]	$\tau$ [ $\times 10^9$ s $^{-1}$ ]	$\Delta E_i$ [Hz]
$4S_{1/2}$	$4P_{1/2}$	396.9591	136.0 [121]	1/6.88	$-1.700 \times 10^3$
$4S_{1/2}$	$4P_{3/2}$	393.4777	139.7 [121]	1/6.69	$-3.371 \times 10^3$
$4S_{1/2}$	$5P_{1/2}$	165.1991	1.02 [121]	1/35.4	-0.3800
$4S_{1/2}$	$5P_{3/2}$	164.9858	1.02 [121]	1/34.8	-0.7562

$3D_{5/2}$	$4P_{3/2}$	854.4438	8.876 [121]	1/6.69	0
$3D_{5/2}$	$4F_{7/2}$	184.0061	216.5 [121]	1/3.54	$-1.0646 \times 10^2$
$3D_{5/2}$	$5F_{7/2}$	155.4642	136.9 [121]	1/3.54	-34.2872
$3D_{5/2}$	$6F_{7/2}$	143.3749	86.0 [121]	1/3.54	-15.5784
$3D_{5/2}$	$7F_{7/2}$	136.9559	56.1 [121]	1/3.54	-8.4602
$3D_{5/2}$	$8F_{7/2}$	133.0912	49.1 [239]	1/3.54	-6.6031
$3D_{5/2}$	$9F_{7/2}$	130.5668	35.2 [239]	1/3.54	-4.3846
$3D_{5/2}$	$10F_{7/2}$	128.8210	25.8 [239]	1/3.54	-3.0452
$3D_{5/2}$	$nF_{7/2}$	120	695*	1/3.54	-61.7609
$3D_{5/2}$	$4F_{5/2}$	184.0061	14.5 [121]	1/3.55	-17.8256
$3D_{5/2}$	$5F_{5/2}$	155.4642	11.3 [239]	1/3.55	-7.0753
$3D_{5/2}$	$6F_{5/2}$	143.3749	7.2 [239]	1/3.55	-3.2606
$3D_{5/2}$	$7F_{5/2}$	136.9559	4.73 [239]	1/3.55	-1.7833
$3D_{5/2}$	$8F_{5/2}$	133.0912	3.28 [239]	1/3.55	-1.1028
$3D_{5/2}$	$9F_{5/2}$	130.5668	2.34 [239]	1/3.55	-0.7287
$3D_{5/2}$	$10F_{5/2}$	128.8210	1.72 [239]	1/3.55	-0.5075
$3D_{5/2}$	$nF_{5/2}$	120	48.6*	1/3.55	-10.7971
$3D_{5/2}$	$5P_{3/2}$	213.2178	1.8 [239]	1/34.8	0
$3D_{5/2}$	$6P_{3/2}$	164.4443	1.3 [239]	1/90	0

**Table A.1 Different parameters for  $\text{Ca}^+$  ion.** The calculated ac-Stark shifts  $\Delta E_i$  are for the  $m = -1/2$  and  $m = -5/2$  Zeeman states of the  $4S_{1/2}$  and  $3D_{5/2}$  states respectively. The Einstein-A coefficients were taken either from [239] or derived from the oscillator strengths in Table VI. of [121] or calculated from the scalar polarizability contributions in Table IX. of [121]. Numbers in square brackets indicate the reference for the Einstein-A coefficients. The fictitious levels  $nF_{7/2}$  and  $nF_{5/2}$  were added in order to account for the ac-shift due to the interaction with states lying above the  $10F_{7/2}$  and  $10F_{5/2}$  states. They were assigned the remaining scalar polarizability of Table IX. in [121] at a transition frequency of 120 nm.

## A.2 Core contributions

It is assumed that the contribution to the ac-shift experienced by the electronic energy levels due to the atomic core are equal. Hence the core-contribution cancels out and does not play a role in the determination of the ac-shift between two energy levels. However, in order to determine the absolute ac-shift experienced by a single level, the non-negligible core contribution must be accounted for. The contribution to the ac-shift can be calculated from the core polarizability ( $\alpha^{\text{Ca}^+, \text{core}}$ ) given in Table VIII of [121],  $\alpha^{\text{Ca}^+, \text{core}} = 3.26$  a.u.  $= 3.26 \times 1.648 \times 10^{-41}$  F.m<sup>2</sup>. The ac-shift due to the QCL can be given as [121],

$$\Delta E_{\text{core}} = -\frac{3I}{2\varepsilon_0 hc} \alpha^{\text{Ca}^+, \text{core}} = -6.7635 \times 10^2 \text{ Hz},$$

where  $I$  is the laser intensity,  $c$  is the speed of light,  $h$  is the Planck's constant and  $\varepsilon_0$  is the permittivity of free space.

# References

- [1] J. Fermor. Timing the sun in Egypt and Mesopotamia. *Vistas Astron.*, 41(1):157–167, 1997.
- [2] J. Jespersen and J. Fitz-Randolph. *From sundials to atomic clocks: understanding time and frequency*. Courier Corporation, 1999.
- [3] P. Machamer and B. Hepburn. Galileo and the Pendulum: Latching on to Time. *Sci. Edu.*, 13(4):333–347, 2004.
- [4] C. Huygens. *Horologium oscillatorium*, 1980.
- [5] C. Huygens. *Horologium Oscillatorium* [Latin with English translation by Ian Bruce], 2007.
- [6] F. Sorge, M. Cammalleri, and G. Genchi. On the birth and growth of pendulum clocks in the early modern era. In *Essays on the history of mechanical engineering*, pages 273–290. Springer, 2016.
- [7] J. Ellicott. An account of the influence which two Pendulum Clocks were observed to have upon each other, 1760.
- [8] W. Ellis. On sympathetic influence between clocks. *Mon. Notices Royal Astron. Soc.*, 33(8):480–484, 1873.

- [9] M. A. Lombardi. The evolution of time measurement, Part 2: quartz clocks [Recalibration]. *IEEE Instrum. Meas. Mag.*, 14(5):41–48, 2011.
- [10] C. Piguet. The first quartz electronic watch. In *International Workshop on Power and Timing Modeling, Optimization and Simulation*, pages 1–15. Springer, 2002.
- [11] I. I. Rabi, J. R. Zacharias, S. Millman, and P. Kusch. A new method of measuring nuclear magnetic moment. *Phys. Rev.*, 53(4):318, 1938.
- [12] N. F. Ramsey. History of early atomic clocks. *Metrologia*, 42(3):S1, 2005.
- [13] H. Lyons. *The Atomic Clock: An Atomic Standard of Frequency and Time*, 1949.
- [14] M. A. Lombardi, T. P. Heavner, and S. R. Jefferts. NIST primary frequency standards and the realization of the SI second. *NCSL Int. Meas.*, 2(4):74–89, 2007.
- [15] R. E. Beehler. A historical review of atomic frequency standards. *Proc. IEEE*, 55(6):792–805, 1967.
- [16] J. Terrien. News from the international bureau of weights and measures. *Metrologia*, 4(1):41, 1968.
- [17] Comptes Rendus de la 13<sup>e</sup> CGPM (1967), 1969, 103.
- [18] J. Hecht. Beam: the race to make the laser. *Opt. Photon. News*, 16(7):24–29, 2005.
- [19] A. D. White. Recollections of the first continuous visible laser. *Opt. Photon. News*, 22(10):34–39, 2011.
- [20] C. H. Townes. EIGHT. The first laser. In *A Century of Nature*, pages 107–112. University of Chicago Press, 2010.
- [21] J. D. Knox and Y. H. Pao. Laser wavelength and frequency standards based on He-Ne lasers and  $I_2^{129}$  vapor. In *1970 International Electron Devices Meeting*, pages 90–90. IEEE, 1970.

- [22] W. J. Tomlinson and R. L. Fork. Frequency stabilization of a gas laser. *Appl. Opt.*, 8(1):121–129, 1969.
- [23] R. C. Miller. Optical second harmonic generation in piezoelectric crystals. *Appl. Phys. Lett.*, 5(1):17–19, 1964.
- [24] C. K. N. Patel. Optical Harmonic Generation in the Infrared Using a CO<sub>2</sub> Laser. *Phys. Rev. Lett.*, 16(14):613, 1966.
- [25] P. Rabinowitz and S. F. Jacobs. Theoretical and Experimental Investigation of Optical Heterodyning. Technical report, Control data corp. Melville N.Y. trg. div., 1963.
- [26] J. J. Jimenez. Microwave to visible frequency synthesis. *Radio Sci.*, 14(4):541–560, 1979.
- [27] G. M. R. Winkler, R. G. Hall, and D. B. Percival. The US Naval Observatory clock time reference and the performance of a sample of atomic clocks. *Metrologia*, 6(4):126, 1970.
- [28] R. W. P. Drever, J. L. Hall, F. V. Kowalski, J. Hough, G. M. Ford, A. J. Munley, and H. Ward. Laser phase and frequency stabilization using an optical resonator. *Appl. Phys. B*, 31(2):97–105, 1983.
- [29] J. Ye and S. T. Cundiff. *Femtosecond optical frequency comb: principle, operation and applications*. Springer Science & Business Media, 2005.
- [30] S. A. Diddams. The evolving optical frequency comb. *J Opt Soc Am B*, 27(11):B51–B62, 2010.
- [31] T. W. Hänsch. Nobel lecture: passion for precision. *Rev. Mod. Phys.*, 78(4):1297, 2006.
- [32] J. L. Hall. Nobel Lecture: Defining and measuring optical frequencies. *Rev. Mod. Phys.*, 78(4):1279, 2006.

- [33] Proceedings of the 26<sup>th</sup> CGPM (2018), 2019, 472.
- [34] N. Huntemann, C. Sanner, B. Lipphardt, Chr. Tamm, and E. Peik. Single-ion atomic clock with  $3 \times 10^{-18}$  systematic uncertainty. *Phys. Rev. Lett.*, 116:063001, 2016.
- [35] S. M. Brewer, J. S. Chen, A. M. Hankin, E. R. Clements, C. W. Chou, D. J. Wineland, D. B. Hume, and D. R. Leibbrandt.  $^{27}\text{Al}^+$  quantum-logic clock with a systematic uncertainty below  $10^{-18}$ . *Phys. Rev. Lett.*, 123(3):033201, 2019.
- [36] P. Delva et al. Test of special relativity using a fiber network of optical clocks. *Phys. Rev. Lett.*, 118(22):221102, 2017.
- [37] R. Lange, N. Huntemann, J. M. Rahm, C. Sanner, H. Shao, B. Lipphardt, C. Tamm, S. Weyers, and E. Peik. Improved limits for violations of local position invariance from atomic clock comparisons. *Phys. Rev. Lett.*, 126(1):011102, 2021.
- [38] C. Clivati et al. A VLBI experiment using a remote atomic clock via a coherent fibre link. *Sci. Rep.*, 7(1):1–8, 2017.
- [39] P. W. Graham, J. M. Hogan, M. A. Kasevich, and S. Rajendran. New method for gravitational wave detection with atomic sensors. *Phys. Rev. Lett.*, 110(17):171102, 2013.
- [40] S. Kolkowitz, I. Pikovski, N. Langellier, M. D. Lukin, R. Walsworth, and J. Ye. Gravitational wave detection with optical lattice atomic clocks. *Phys. Rev. D*, 94(12):124043, 2016.
- [41] F. Riehle. Optical clock networks. *Nat. Photonics*, 11(1):25–31, 2017.
- [42] B. Jaduszliwer and J. Camparo. Past, present and future of atomic clocks for GNSS. *GPS Solut.*, 25(1):1–13, 2021.

- [43] T. Schuldt et al. Optical clock technologies for global navigation satellite systems. *GPS Solut.*, 25(3):1–11, 2021.
- [44] W. F. McGrew et al. Atomic clock performance enabling geodesy below the centimetre level. *Nature*, 564(7734):87–90, 2018.
- [45] C. Lisdat et al. A clock network for geodesy and fundamental science. *Nat. Commun.*, 7(1):1–7, 2016.
- [46] M. Abgrall et al. Atomic fountains and optical clocks at SYRTE: Status and perspectives. *C. R. Phys.*, 16(5):461–470, 2015.
- [47] T. L. Nicholson, S. L. Campbell, R. B. Hutson, G. E. Marti, B. J. Bloom, R. L. McNally, W. Zhang, M. D. Barrett, M. S. Safronova, G. F. Strouse, W. L. Tew, and J. Ye. Systematic evaluation of an atomic clock at  $2 \times 10^{-18}$  total uncertainty. *Nature Commun.*, 6:6896, 2015.
- [48] S. Patra, M. Germann, J.-Ph. Karr, M. Haidar, L. Hilico, V. I. Korobov, F. M. J. Cozijn, K. S. E. Eikema, W. Ubachs, and J. C. J. Koelemeij. Proton-electron mass ratio from laser spectroscopy of  $\text{HD}^+$  at the part-per-trillion level. *Science*, 369(6508):1238–1241, 2020.
- [49] S. Schiller and V. Korobov. Tests of time independence of the electron and nuclear masses with ultracold molecules. *Phys. Rev. A*, 71:032505, 2005.
- [50] L. D. Carr, D. DeMille, R. V. Krems, and J. Ye. Cold and ultracold molecules: Science, technology and applications. *New J. Phys.*, 11:055049, 2009.
- [51] J. Biesheuvel, J. P. Karr, L. Hilico, K. S. E. Eikema, W. Ubachs, and J. C. J. Koelemeij. Probing QED and fundamental constants through laser spectroscopy of vibrational transitions in  $\text{HD}^+$ . *Nat. Commun.*, 7:10385, 2016.

- [52] W. Ubachs, R. Buning, K. S. E. Eikema, and E. Reinhold. On a possible variation of the proton-to-electron mass ratio:  $\text{H}_2$  spectra in the line of sight of high-redshift quasars and in the laboratory. *J. Mol. Spectrosc.*, 241(2):155–179, 2007.
- [53] K. Najafian, Z. Meir, and S. Willitsch. From megahertz to terahertz qubits encoded in molecular ions: theoretical analysis of dipole-forbidden spectroscopic transitions in  $\text{N}_2^+$ . *Phys. Chem. Chem. Phys.*, 22(40):23083–23098, 2020.
- [54] M. Kajita.  $\text{N}_2^+$  quadrupole transitions with small Zeeman shift. *Phys. Rev. A*, 92:043423, 2015.
- [55] M. Kajita, G. Gopakumar, M. Abe, M. Hada, and M. Keller. Test of  $m_p/m_e$  changes using vibrational transitions in  $\text{N}_2^+$ . *Phys. Rev. A*, 89:032509, 2014.
- [56] K. Najafian. *Quantum manipulation of a single trapped molecular ion*. PhD thesis, University of Basel, 2021.
- [57] S. Willitsch. Chemistry with controlled ions. *Adv. Chem. Phys.*, 162:307, 2017.
- [58] F. H. J. Hall and S. Willitsch. Millikelvin reactive collisions between sympathetically cooled molecular ions and laser-cooled atoms in an ion-atom hybrid trap. *Phys. Rev. Lett.*, 109:233202, 2012.
- [59] A. D. Dörfler, E. Yurtsever, P. Villarreal, T. González-Lezana, F. A. Gianturco, and S. Willitsch. Rotational-state-changing collisions between  $\text{N}_2^+$  and Rb at low energies. *Phys. Rev. A*, 101(1):012706, 2020.
- [60] A. D. Dörfler, P. Eberle, D. Koner, M. Tomza, M. Meuwly, and S. Willitsch. Long-range versus short-range effects in cold molecular ion-neutral collisions. *Nat. Commun.*, 10:5429, 2019.
- [61] J. M. Brown and A. Carrington. *Rotational Spectroscopy of Diatomic Molecules*. Cambridge University Press, 2003.

- [62] R. N. Zare. *Angular Momentum*. John Wiley & Sons, New York, 1988.
- [63] H. Lefebvre-Brion and R. W. Field. *The Spectra and Dynamics of Diatomic Molecules: Revised and Enlarged Edition*. Elsevier, 2004.
- [64] P. F. Bernath. *Spectra of Atoms and Molecules*. Oxford University Press, Oxford, 2. edition edition, 2005.
- [65] T. M. Dunn. Nuclear Hyperfine Structure in the Electronic Spectra of Diatomic Molecules. In K. R. Narahari and C. M. Weldon, editors, *Molecular Spectroscopy: Modern Research*, page 231. Academic Press, New York, 1972.
- [66] R. A. Frosch and H. M. Foley. Magnetic hyperfine structure in diatomic molecules. *Phys. Rev.*, 88(6):1337, 1952.
- [67] J. T. Hougen. The calculation of rotational energy levels and rotational line intensities in diatomic molecules. Technical report, NATIONAL STANDARD REFERENCE DATA SYSTEM, 1970.
- [68] J. M. Brown, J. T. Hougen, K-P. Huber, J. W. C. Johns, I. Kopp, H. Lefebvre-Brion, A. J. Merer, D. A. Ramsay, J. Rostas, and R. N. Zare. The labeling of parity doublet levels in linear molecules. *J. Mol. Spectrosc.*, 55(1-3):500–503, 1975.
- [69] J. M. Brown, M. Kaise, C. M. L. Kerr, and D. J. Milton. A determination of fundamental zeeman parameters for the OH radical. *Mol. Phys.*, 36(2):553–582, 1978.
- [70] E. Klisch, S. P. Belov, R. Schieder, G. Winnewisser, and E. Herbst. Transitions between Hund’s coupling cases for the  $X_2\Pi$  state of NO. *Mol. Phys.*, 97(1-2):65–79, 1999.
- [71] E. Hirota, J. M. Brown, J. T. Hougen, T. Shida, and N. Hirota. Symbols for fine and hyperfine structure parameters (IUPAC Recommendations 1994). *Pure Appl. Chem.*, 66(3):571–576, 1994.

- [72] J. Mur-Petit, J. J. García-Ripoll, J. Pérez-Ríos, J. Campos-Martínez, M. I. Hernández, and S. Willitsch. Temperature-independent quantum logic for molecular spectroscopy. *Phys. Rev. A*, 85:022308, 2012.
- [73] T.M. Miller, R.E. Wetterskog, and J.F. Paulson. Temperature dependence of the ion-molecule reactions  $N^+ + CO$ ,  $C^+ + NO$ , and  $C^+$ ,  $CO^+$ ,  $CO_2^+ + O_2$  from 90-450 K. *J. Chem. Phys.*, 80:4922–4925, 1984.
- [74] N. Berrah Mansour, C. Kurtz, T. C. Steimle, G. L. Goodman, L. Young, T. J. Scholl, S. D. Rosner, and R. A. Holt. Laser-rf double-resonance study of  $N_2^+$ . *Phys. Rev. A*, 44:4418–4429, 1991.
- [75] M. Germann. *Dipole-Forbidden Vibrational Transitions in Molecular Ions*. PhD thesis, University of Basel, 2016.
- [76] Y. D. Wu, J. W. Ben, B. Li, L. J. Zheng, Y. Q. Chen, and X. H. Yang. Study of (2, 0) band of  $A^2\Pi_u - X^2\Sigma_g^+$  system of  $N_2^+$  by optical heterodyne detected velocity modulation spectroscopy. *Chinese J. Chem. Phys.*, 20:285, 2007.
- [77] T. J. Scholl, R. A. Holt, and S. D. Rosner. Fine and Hyperfine Structure in  $^{14}N_2^+$  : The  $B - X(0, 0)$  Band. *J. Mol. Spectrosc.*, 192:424, 1998.
- [78] W. L. Meerts, J. P. Bekooy, and A. Dymanus. Vibrational effects in the hydroxyl radical by molecular beam electric resonance spectroscopy. *Mol. Phys.*, 37(2):425–439, 1979.
- [79] W. L. Meerts. A theoretical reinvestigation of the rotational and hyperfine lambda doubling spectra of diatomic molecules with a  $^2\Pi$  state: the spectrum of NO. *Chem. Phys.*, 14(3):421–425, 1976.
- [80] W. L. Meerts. On the microwave spectrum of the  $X_2\Pi$  state of the hydroxyl radical. *Chem. Phys. Lett.*, 46(1):24–28, 1977.

- [81] D. T. Cramb, A. G. Adam, D. M. Steunenbergh, A. J. Merer, and M. C. L. Gerry. Electronic absorption spectroscopy of  $N_2^+$  using velocity modulation: Rotational structure in the (6, 1) and (13, 6) vibrational bands of the  $A - X$  system. *J. Mol. Spectrosc.*, 141(2):281–289, 1990.
- [82] T. A. Miller, T. Suzuki, and E. Hirota. High resolution, cw laser induced fluorescence study of the  $A^2\Pi_u - X^2\Sigma_g^+$  system of  $N_2^+$ . *J. Chem. Phys.*, 80(10):4671–4678, 1984.
- [83] D. W. Ferguson, K. N. Rao, P. A. Martin, and G. Guelachvili. High Resolution Infrared Fourier Transform Emission Spectra of the  $^{14}N_2^+$  Meinel System:  $A^2\Pi_u - X^2\Sigma_g^+$ . *J. Mol. Spectrosc.*, 153:599–609, 1992.
- [84] J. H. Van Vleck. *The theory of electric and magnetic susceptibilities*. Clarendon Press, 1932.
- [85] P. J. Bruna and F. Grein. The  $A^2\Pi_u$  state of  $N_2^+$ : Electric properties, fine and hyperfine coupling constants, and magnetic moments (g-factors). A theoretical study. *J. Mol. Spectrosc.*, 250(2):75–85, 2008.
- [86] S. Ospelkaus, K.-K. Ni, D. Wang, M. H. G. de Miranda, B. Neyenhuis, G. Quémener, P. S. Julienne, J. L. Bohn, D. S. Jin, and J. Ye. Quantum-state controlled chemical reactions of ultracold potassium-rubidium molecules. *Science*, 327:853, 2010.
- [87] B. Yan, S. A. Moses, B. Gadway, J. P. Covey, K. R. A. Hazzard, A. M. Rey, D. S. Jin, and J. Ye. Observation of dipolar spin-exchange interactions with lattice-confined polar molecules. *Nature*, 501:521, 2013.
- [88] M. H. G. De Miranda, A. Chotia, B. Neyenhuis, D. Wang, G. Quémener, S. Ospelkaus, J. L. Bohn, J. Ye, and D. S. Jin. Controlling the quantum stereodynamics of ultracold bimolecular reactions. *Nat. Phys.*, 7(6):502–507, 2011.

- [89] L. Ploenes, P. Straňák, H. Gao, J. Küpper, and S. Willitsch. A novel crossed-molecular-beam experiment for investigating reactions of state- and conformationally selected strong-field-seeking molecules. *arXiv preprint arXiv:2105.06427*, 2021.
- [90] C. Sanner, N. Huntemann, R. Lange, C. Tamm, and E. Peik. Autobalanced ramsey spectroscopy. *Phys. Rev. Lett.*, 120(5):053602, 2018.
- [91] H. A. Füst et al. Coherent Excitation of the Highly Forbidden Electric Octupole Transition in  $^{172}\text{Yb}^+$ . *Phys. Rev. Lett.*, 125(16):163001, 2020.
- [92] M. S. Safronova, D. Budker, D. DeMille, Derek F. Jackson Kimball, A. Derevianko, and Charles W. Clark. Search for new physics with atoms and molecules. *Rev. Mod. Phys.*, 90:025008, 2018.
- [93] David DeMille, John M Doyle, and Alexander O Sushkov. Probing the frontiers of particle physics with tabletop-scale experiments. *Science*, 357:990, 2017.
- [94] I. V. Kortunov, S. Alighanbari, M. G. Hansen, G. S. Giri, V. I. Korobov, and S. Schiller. Proton–electron mass ratio by high-resolution optical spectroscopy of ion ensembles in the resolved-carrier regime. *Nat. Phys.*, 17(5):569–573, 2021.
- [95] K. Beloy, M. G. Kozlov, A. Borschevsky, A. W. Hauser, V. V. Flambaum, and P. Schwerdtfeger. Rotational spectrum of the molecular ion  $\text{NH}^+$  as a probe for  $\alpha$  and  $m_e/m_p$  variation. *Phys. Rev. A*, 83:062514, 2011.
- [96] Y. Lin, D. R. Leibbrandt, D. Leibfried, and C. W. Chou. Quantum entanglement between an atom and a molecule. *Nature*, 581(7808):273–277, 2020.
- [97] H. Kimble. The quantum internet. *Nature*, 453:1023, 2008.
- [98] S. Wehner, D. Elkouss, and R. Hanson. Quantum internet: A vision for the road ahead. *Science*, 362:eaam9288, 2018.

- [99] S. Somaroo, C. H. Tseng, T. F. Havel, R. Laflamme, and D. G. Cory. Quantum simulations on a quantum computer. *Phys. Rev. Lett.*, 82(26):5381, 1999.
- [100] T. Jaako, R. Garcia, J. Juan, and P. Rabl. Quantum Simulation of Non-Perturbative Cavity QED with Trapped Ions. *Adv. Quantum Technol.*, 3(4):1900125, 2020.
- [101] G. M. Barrow. *Introduction to molecular spectroscopy*. McGraw-Hill, 1962.
- [102] P. R. Bunker. *Molecular Symmetry and Spectroscopy*. Academic Press, Inc., London, 1979.
- [103] A. B. Meinel. The Auroral Spectrum from 6200 TO 8900 A. *Astrophys. J.*, 113:583, 1951.
- [104] L. V. Wallace and R. W. Nicholls. The interpretation of intensity distributions in the N<sub>2</sub> second positive and N<sub>2</sub><sup>+</sup> first negative band systems. *J. Atmospheric Terrest.*, 7:101–105, 1955.
- [105] R. Grimm, M. Weidemüller, and Y. B. Ovchinnikov. Optical dipole traps for neutral atoms. In *Adv. At. Mol. Opt. Phys.*, volume 42, pages 95–170. Elsevier, 2000.
- [106] J. Ye, H. J. Kimble, and H. Katori. Quantum state engineering and precision metrology using state-insensitive light traps. *Science*, 320:1734, 2008.
- [107] P. D. Gregory, J. A. Blackmore, J. Aldegunde, J. M. Hutson, and S. L. Cornish. ac Stark effect in ultracold polar <sup>87</sup>Rb<sup>133</sup>Cs molecules. *Phys. Rev. A.*, 96(2):021402, 2017.
- [108] R. V. Krems. Cold controlled chemistry review. *Phys. Chem. Chem. Phys.*, 10:4079, 2008.
- [109] M. H. G. de Miranda, A. Chotia, B. Neyenhuis, D. Wang, G. Qéméner, S. Ospelkaus, J. L. Bohn, J. Ye, and D. S. Jin. Controlling the quantum stereodynamics of ultracold bimolecular reactions. *Nat. Phys.*, 7:502, 2011.

- [110] L. Santos, G. V. Shlyapnikov, P. Zoller, and M. Lewenstein. Bose-einstein condensation in trapped dipolar gases. *Phys. Rev. Lett.*, 85(9):1791, 2000.
- [111] M. A. Baranov, M. Dalmonte, G. Pupillo, and P. Zoller. Condensed matter theory of dipolar quantum gases. *Chem. Rev.*, 112(9):5012–5061, 2012.
- [112] D. DeMille. Quantum computation with trapped polar molecules. *Phys. Rev. Lett.*, 88:067901, 2002.
- [113] S. F. Yelin, K. Kirby, and R. Côté. Schemes for robust quantum computation with polar molecules. *Phys. Rev. A*, 74:050301, 2006.
- [114] M. Sinhal, Z. Meir, K. Najafian, G. Hegi, and S. Willitsch. Quantum-nondemolition state detection and spectroscopy of single trapped molecules. *Science*, 367(6483):1213–1218, 2020.
- [115] Z. Meir, G. Hegi, K. Najafian, M. Sinhal, and S. Willitsch. State-selective coherent motional excitation as a new approach for the manipulation, spectroscopy and state-to-state chemistry of single molecular ions. *Faraday Discuss.*, 217:561–583, 2019.
- [116] F. Wolf, Y. Wan, J. C. Heip, F. Gebert, C. Shi, and P. O. Schmidt. Non-destructive state detection for quantum logic spectroscopy of molecular ions. *Nature*, 530:457, 2016.
- [117] E. E. Whiting, A. Schadee, J. Tatum, J. T. Hougen, and R. W. Nicholls. Recommended conventions for defining transition moments and intensity factors in diatomic molecular spectra. *J. Mol. Spectrosc.*, 80(2):249–256, 1980.
- [118] R. C. Hilborn. Einstein coefficients, cross sections,  $f$  values, dipole moments, and all that. *Am. J. Phys.*, 50(11):982–986, 1982.
- [119] C. Mainos. Multiphoton rotational line strength in diatomic molecules and for states with Hunds case-(a) or case-(b) coupling. *Phys. Rev. A*, 33(6):3983, 1986.

- [120] R. J. M. Bennett. Hönl–London factors for doublet transitions in diatomic molecules. *Mon. Notices Royal Astron. Soc.*, 147(1):35–46, 1970.
- [121] M. S. Safronova and U. I. Safronova. Blackbody radiation shift, multipole polarizabilities, oscillator strengths, lifetimes, hyperfine constants, and excitation energies in  $\text{Ca}^+$ . *Phys. Rev. A*, 83(1):012503, 2011.
- [122] A. D. Ludlow et al. Optical frequency measurements at  $1 \times 10^{-18}$  uncertainty with ytterbium optical lattice clocks. In *2018 Conference on Precision Electromagnetic Measurements (CPEM 2018)*, pages 1–2. IEEE, 2018.
- [123] M. Schioppo et al. Ultrastable optical clock with two cold-atom ensembles. *Nat. Photonics*, 11(1):48–52, 2017.
- [124] H. Leopardi et al. Measurement of the  $^{27}\text{Al}^+$  and  $^{87}\text{Sr}$  absolute optical frequencies. *Metrologia*, 58(1):015017, 2021.
- [125] M. Pizzocaro et al. Intercontinental comparison of optical atomic clocks through very long baseline interferometry. *Nat. Phys.*, 17(2):223–227, 2021.
- [126] T. Akatsuka, H. Ono, K. Hayashida, K. Araki, M. Takamoto, T. Takano, and H. Katori. 30-km-long optical fiber link at 1397 nm for frequency comparison between distant strontium optical lattice clocks. *Jpn. J. Appl. Phys.*, 53(3):032801, 2014.
- [127] Boulder Atomic Clock Optical Network, K. Beloy, et al. Frequency ratio measurements with 18-digit accuracy using a network of optical clocks. *arXiv preprint arXiv:2005.14694*, 2020.
- [128] M. S. Safronova, D. Budker, D. DeMille, D. F. J. Kimball, A. Derevianko, and C. W. Clark. Search for new physics with atoms and molecules. *Rev. Mod. Phys.*, 90(2):025008, 2018.

- [129] I. V. Kortunov, S. Alighanbari, M. G. Hansen, G. S. Giri, V. I. Korobov, and S. Schiller. Ultra-high-resolution spectroscopy of trapped ion ensembles in the lamb-dicke regime: demonstration and determination of the proton-electron mass ratio. *arXiv preprint arXiv:2103.11741*, 2021.
- [130] T. Takano et al. Geopotential measurements with synchronously linked optical lattice clocks. *Nat. Photonics*, 10(10):662–666, 2016.
- [131] J. Grotti et al. Geodesy and metrology with a transportable optical clock. *Nat. Phys.*, 14(5):437–441, 2018.
- [132] G. Marra et al. Ultrastable laser interferometry for earthquake detection with terrestrial and submarine cables. *Science*, 361(6401):486–490, 2018.
- [133] J. M. Robinson, E. Oelker, W. R. Milner, W. Zhang, T. Legero, D. G. Matei, F. Riehle, U. Sterr, and J. Ye. Crystalline optical cavity at 4 k with thermal-noise-limited instability and ultralow drift. *Optica*, 6(2):240–243, 2019.
- [134] D. G. Matei et al. 1.5  $\mu\text{m}$  lasers with sub-10 mHz linewidth. *Phys. Rev. Lett.*, 118(26):263202, 2017.
- [135] A. Jallageas, L. Devenoges, M. Petersen, J. Morel, L. G. Bernier, D. Schenker, P. Thomann, and T. Südmeyer. First uncertainty evaluation of the focs-2 primary frequency standard. *Metrologia*, 55(3):366, 2018.
- [136] C. Clivati et al. Measuring absolute frequencies beyond the gps limit via long-haul optical frequency dissemination. *Opt. Express*, 24(11):11865–11875, 2016.
- [137] R. Santagata et al. High-precision methanol spectroscopy with a widely tunable si-traceable frequency-comb-based mid-infrared qcl. *Optica*, 6(4):411–423, 2019.
- [138] D. Husmann et al. Si-traceable frequency dissemination at 1572.06 nm in a stabilized fiber network with ring topology. *arXiv preprint arXiv:2104.09966*, 2021.

- [139] A. Kreuter et al. Experimental and theoretical study of the  $3d^2D$ -level lifetimes of  $^{40}\text{Ca}^+$ . *Phys. Rev. A*, 71(3):032504, 2005.
- [140] D. Leibfried, R. Blatt, C. Monroe, and D. Wineland. Quantum dynamics of single trapped ions. *Rev. Mod. Phys.*, 75(1):281, 2003.
- [141] E. D. Black. An introduction to pound-drever-hall laser frequency stabilization. *Am. J. Phys.*, 69(1):79–87, 2001.
- [142] G. Poulsen. *Sideband cooling of atomic and molecular ions*. PhD thesis, University of Aarhus, 2011.
- [143] P. Dubé, A. A. Madej, J. E. Bernard, L. Marmet, and A. D. Shiner. A narrow linewidth and frequency-stable probe laser source for the  $^{88}\text{Sr}^+$  single ion optical frequency standard. *Appl. Phys. B*, 95(1):43–54, 2009.
- [144] C. Hagemann, C. Grebing, C. Lisdat, S. Falke, T. Legero, U. Sterr, F. Riehle, M. J. Martin, and J. Ye. Ultrastable laser with average fractional frequency drift rate below  $5 \times 10^{-19}/\text{s}$ . *Opt. Lett.*, 39(17):5102–5105, 2014.
- [145] B. Meyer, S. Saupe, M. H. Wappelhorst, T. George, F. Kühnemann, M. Schneider, M. Havenith, W. Urban, and J. Legrand. CO-laser side-band spectrometer: Sub-doppler heterodyne frequency measurements around  $5 \mu\text{m}$ . *Appl. Phys. B*, 61(2):169–173, 1995.
- [146] L. Wang, Z. Cao, H. Wang, H. Zhao, W. Gao, Y. Yuan, W. Chen, W. Zhang, Y. Wang, and X. Gao. A widely tunable ( $5$ – $12.5 \mu\text{m}$ ) continuous-wave mid-infrared laser spectrometer based on difference frequency generation in  $\text{AgGaS}_2$ . *Opt. Commun.*, 284(1):358–362, 2011.
- [147] L. Tombez. *Analysis and Improvement of the Spectral Properties in Mid-Infrared Semiconductor Quantum Cascade Lasers*. PhD thesis, EPFL, 2014.

- [148] S. Borri, S. Bartalini, P. C. Pastor, I. Galli, G. Giusfredi, D. Mazzotti, M. Yamanishi, and P. De Natale. Frequency-noise dynamics of mid-infrared quantum cascade lasers. *IEEE J. Quantum Electron.*, 47(7):984–988, 2011.
- [149] S. Bartalini, S. Borri, I. Galli, G. Giusfredi, D. Mazzotti, T. Edamura, N. Akikusa, M. Yamanishi, and P. De Natale. Measuring frequency noise and intrinsic linewidth of a room-temperature DFB quantum cascade laser. *Opt. Express*, 19(19):17996–18003, 2011.
- [150] L. Tombez, S. Schilt, J. Di Francesco, P. Thomann, and D. Hofstetter. Temperature dependence of the frequency noise in a mid-IR DFB quantum cascade laser from cryogenic to room temperature. *Opt. Express*, 20(7):6851–6859, 2012.
- [151] L. Tombez, J. Di Francesco, S. Schilt, G. Di Domenico, J. Faist, P. Thomann, and D. Hofstetter. Frequency noise of free-running 4.6  $\mu\text{m}$  distributed feedback quantum cascade lasers near room temperature. *Opt. Lett.*, 36(16):3109–3111, 2011.
- [152] L. Tombez, S. Schilt, J. Di Francesco, T. Führer, B. Rein, T. Walther, G. Di Domenico, D. Hofstetter, and P. Thomann. Linewidth of a quantum-cascade laser assessed from its frequency noise spectrum and impact of the current driver. *Appl. Phys. B*, 109(3):407–414, 2012.
- [153] M. G. Hansen, E. Magoulakis, Q. F. Chen, I. Ernsting, and S. Schiller. Quantum cascade laser-based mid-IR frequency metrology system with ultra-narrow linewidth and  $1 \times 10^{-13}$ -level frequency instability. *Opt. Lett.*, 40(10):2289–2292, 2015.
- [154] B. Argence, B. Chanteau, O. Lopez, D. Nicolodi, M. Abgrall, C. Chardonnet, C. Daussy, B. Darquié, Y. Le Coq, and A. Amy-Klein. Quantum cascade laser frequency stabilization at the sub-Hz level. *Nat. Photonics*, 9:456, 2015.

- [155] E. Fasci, N. Coluccelli, M. Cassinerio, A. Gambetta, L. Hilico, L. Gianfrani, P. Laporta, A. Castrillo, and G. Galzerano. Narrow-linewidth quantum cascade laser at 8.6  $\mu\text{m}$ . *Opt. Lett.*, 39(16):4946–4949, 2014.
- [156] M. S. Taubman, T. L. Myers, B. D. Cannon, R. M. Williams, F. Capasso, C. Gmachl, D. L. Sivco, and A. Y. Cho. Frequency stabilization of quantum-cascade lasers by use of optical cavities. *Opt. Lett.*, 27(24):2164–2166, 2002.
- [157] S. Borri et al. Tunable microcavity-stabilized quantum cascade laser for mid-IR high-resolution spectroscopy and sensing. *Sensors*, 16(2):238, 2016.
- [158] M. Siciliani de Cumis et al. Microcavity-Stabilized Quantum Cascade Laser. *Laser Photonics Rev.*, 10(1):153–157, 2016.
- [159] S. Borri, I. Galli, F. Cappelli, A. Bismuto, S. Bartalini, P. Cancio, G. Giusfredi, D. Mazzotti, J. Faist, and P. De Natale. Direct link of a mid-infrared QCL to a frequency comb by optical injection. *Opt. Lett.*, 37(6):1011–1013, 2012.
- [160] S. Schilt, L. Tombez, G. Di Domenico, and D. Hofstetter. Frequency noise and linewidth of mid-infrared continuous-wave quantum cascade lasers: An overview. *The Wonders of Nanotechnology: Quantum and Optoelectronic Devices and Applications (chapter 12)*, pages 261–287, 2013.
- [161] T. L. Myers, R. M. Williams, M. S. Taubman, C. Gmachl, F. Capasso, D. L. Sivco, J. N. Baillargeon, and A. Y. Cho. Free-running frequency stability of mid-infrared quantum cascade lasers. *Opt. Lett.*, 27(3):170–172, 2002.
- [162] S. Bartalini, S. Borri, P. Cancio, A. Castrillo, I. Galli, G. Giusfredi, D. Mazzotti, L. Gianfrani, and P. De Natale. Observing the intrinsic linewidth of a quantum-cascade laser: beyond the Schawlow-Townes limit. *Phys. Rev. Lett.*, 104(8):083904, 2010.

- [163] I. E. Gordon et al. The HITRAN2016 molecular spectroscopic database. *J. Quant. Spectrosc. Radiat. Transf.*, 203:3–69, 2017.
- [164] H. Schmid. How to use the FFT and Matlabs pwelch function for signal and noise simulations and measurements. *FHNW/IME*, pages 2–13, 2012.
- [165] G. Heinzl, A. Rüdiger, and R. Schilling. Spectrum and spectral density estimation by the Discrete Fourier transform (DFT), including a comprehensive list of window functions and some new at-top windows, 2002.
- [166] L. B. Mercer.  $1/f$  frequency noise effects on self-heterodyne linewidth measurements. *J. Light. Technol.*, 9(4):485–493, 1991.
- [167] P. Gallion and G. Debarge. Quantum phase noise and field correlation in single frequency semiconductor laser systems. *IEEE J. Quantum Electron.*, 20(4):343–349, 1984.
- [168] D. S. Elliott, R. Roy, and S. J. Smith. Extracavity laser band-shape and bandwidth modification. *Phys. Rev. A*, 26(1):12, 1982.
- [169] N. Bucalovic, V. Dolgovskiy, C. Schori, P. Thomann, G. Di Domenico, and S. Schilt. Experimental validation of a simple approximation to determine the linewidth of a laser from its frequency noise spectrum. *Appl. Opt.*, 51(20):4582–4588, 2012.
- [170] G. Di Domenico, S. Schilt, and P. Thomann. Simple approach to the relation between laser frequency noise and laser line shape. *Appl. Opt.*, 49(25):4801–4807, 2010.
- [171] O. Gayer, Z. Sacks, E. Galun, and A. Arie. Temperature and wavelength dependent refractive index equations for MgO-doped congruent and stoichiometric LiNbO<sub>3</sub>. *Appl. Phys. B*, 91(2):343–348, 2008.
- [172] K.-K. Ni, S. Ospelkaus, M. H. G. de Miranda, A. Pe’er, B. Neyenhuis, J. J. Zirbel, S. Kotochigova, P. S. Julienne, D. S. Jin, and J. Ye. A High Phase-Space-Density Gas of Polar Molecules. *Science*, 322:231, 2008.

- [173] Jeremy M Sage, Sunil Sainis, Thomas Bergeman, and David DeMille. Optical production of ultracold polar molecules. *Phys. Rev. Lett.*, 94:203001, 2005.
- [174] L. R. Liu, J. D. Hood, Y. Yu, J. T. Zhang, N. R. Hutzler, T. Rosenband, and K.-K. Ni. Building one molecule from a reservoir of two atoms. *Science*, 360:900, 2018.
- [175] S. Y. T. van de Meerakker, H. L. Bethlem, N. Vanhaecke, and G. Meijer. Manipulation and control of molecular beams. *Chem. Rev.*, 112:4828, 2012.
- [176] J.F. Barry, D.J. McCarron, E.B. Norrgard, M.H. Steinecker, and D. DeMille. Magneto-optical trapping of a diatomic molecule. *Nature*, 512:286, 2014.
- [177] Loïc Anderegg, Benjamin L. Augenbraun, Yicheng Bao, Sean Burchesky, Lawrence W. Cheuk, Wolfgang Ketterle, and John M. Doyle. Laser cooling of optically trapped molecules. *Nat. Phys.*, 14:890, 2018.
- [178] K. Mølhave and M. Drewsen. Formation of translationally cold  $\text{MgH}^+$  and  $\text{MgD}^+$  molecules in an ion trap. *Phys. Rev. A*, 62:011401, 2000.
- [179] S. Willitsch. Coulomb-crystallised molecular ions in traps: methods, applications, prospects. *Int. Rev. Phys. Chem.*, 31:175, 2012.
- [180] S. Alighanbari, M. G. Hansen, V. I. Korobov, and S. Schiller. Rotational spectroscopy of cold and trapped molecular ions in the Lamb–Dicke regime. *Nat. Phys.*, 14:555, 2018.
- [181] P. F. Sta anum, K. Højbjjerre, P. S. Skyt, A. K. Hansen, and M. Drewsen. Rotational laser cooling of vibrationally and translationally cold molecular ions. *Nat. Phys.*, 6:271, 2010.
- [182] T. Schneider, B. Roth, H. Duncker, I. Ernsting, and S. Schiller. All-optical preparation of molecular ions in the rovibrational ground state. *Nat. Phys.*, 6:275, 2010.

- [183] X. Tong, A. H. Winney, and S. Willitsch. Sympathetic cooling of molecular ions in selected rotational and vibrational states produced by threshold photoionization. *Phys. Rev. Lett.*, 105:143001, 2010.
- [184] C.-Y. Lien, C. M. Seck, Y.-W. Lin, J. H. V. Nguyen, D. A. Tabor, and B. C. Odom. Broadband optical cooling of molecular rotors from room temperature to the ground state. *Nat. Commun.*, 5:4783, 2014.
- [185] M. Germann, X. Tong, and S. Willitsch. Observation of electric-dipole-forbidden infrared transitions in cold molecular ions. *Nat. Phys.*, 10:820, 2014.
- [186] T. Sikorsky, Z. Meir, R. Ben-shlomi, N. Akerman, and R. Ozeri. Spin-controlled atom-ion chemistry. *Nat. Comm.*, 9:920, 2018.
- [187] T. P. Harty, D. T. C. Allcock, C. J. Ballance, L. Guidoni, H. A. Janacek, N. M. Linke, D. N. Stacey, and D. M. Lucas. High-Fidelity Preparation; Gates; Memory; and Readout of a Trapped-Ion Quantum Bit. *Phys. Rev. Lett.*, 113:220501, 2014.
- [188] P. O. Schmidt, T. Rosenband, C. Langer, W. M. Itano, J. C. Bergquist, and D. J. Wineland. Spectroscopy Using Quantum Logic. *Science*, 309:749, 2005.
- [189] C. W. Chou, C. Kurz, D. B. Hume, P. N. Plessow, D. R. Leibbrandt, and D. Leibfried. Preparation and coherent manipulation of pure quantum states of a single molecular ion. *Nature*, 545:203, 2017.
- [190] R. Blatt and D. Wineland. Entangled states of trapped atomic ions. *Nature*, 453:1008, 2008.
- [191] H. Häffner, C. F. Roos, and R. Blatt. Quantum computing with trapped ions. *Phys. Rep.*, 469:155, 2008.

- [192] F. Schmidt-Kaler, H. Häffner, S. Gulde, M. Riebe, G. P.T. Lancaster, T. Deuschle, C. Becher, W. Hänsel, J. Eschner, C. F. Roos, and R. Blatt. How to realize a universal quantum gate with trapped ions. *App. Phys. B*, 77:789, 2003.
- [193] D. Leibfried. Quantum state preparation and control of single molecular ions. *New J. Phys.*, 14:023029, 2012.
- [194] S. Ding and D. N. Matsukevich. Quantum logic for control and manipulation of molecular ions using a frequency comb. *New J. Phys.*, 14:023028, 2012.
- [195] K. Najafian, Z. Meir, M. Sinhal, and S. Willitsch. Identification of molecular quantum states using phase-sensitive forces. *Nat. Commun.*, 11(1):1–10, 2020.
- [196] M. Germann and S. Willitsch. Line strengths for fine- and hyperfine-resolved electric-quadrupole rotation–vibration transitions in hund’s case b molecules. *Mol. Phys.*, 114:769, 2016.
- [197] S. Willitsch. Experimental Methods in Cation Spectroscopy. In M. Quack and F. Merkt, editors, *Handbook of High-Resolution Spectroscopy*, volume 3, page 1691. John Wiley & Sons, 2011.
- [198] Matthias Germann and Stefan Willitsch. Fine- and hyperfine-structure effects in molecular photoionization. I. General theory and direct photoionization. *J. Chem. Phys.*, 145:044314, 2016.
- [199] Matthias Germann and Stefan Willitsch. Fine- and hyperfine-structure effects in molecular photoionization. II. Resonance-enhanced multiphoton ionization and hyperfine-selective generation of molecular cations. *J. Chem. Phys.*, 145:044315, 2016.
- [200] A. Gardner, T. Softley, and M. Keller. Multi-photon ionisation spectroscopy for rotational state preparation of  $N_2^+$ . *Sci. Rep.*, 9:506, 2019.

- [201] D. Leibfried, R. Blatt, C. Monroe, and D. Wineland. Quantum dynamics of single trapped ions. *Rev. Mod. Phys.*, 75:281, 2003.
- [202] M. Guggemos, D. Heinrich, O. A. Herrera-Sancho, R. Blatt, and C. F. Roos. Sympathetic cooling and detection of a hot trapped ion by a cold one. *New J. Phys.*, 17:103001, 2015.
- [203] W. Neuhauser, M. Hohenstatt, P. Toschek, and H. Dehmelt. Optical sideband cooling of visible atom cloud confined in parabolic well. *Phys. Rev. Lett.*, 41:233, 1978.
- [204] D. J. Wineland and W. M. Itano. Laser cooling of atoms. *Phys. Rev. A*, 20:1521–1540, Oct 1979.
- [205] C. W. Chou, A. L. Collopy, C. Kurz, Y. Lin, M. E. Harding, P. N. Plessow, T. Fortier, S. Diddams, D. Leibfried, and D. R. Leibbrandt. Frequency-comb spectroscopy on pure quantum states of a single molecular ion. *Science*, 367(6485):1458–1461, 2020.
- [206] M. Guggemos, M. Guevara-Bertsch, D. Heinrich, O. A. Herrera-Sancho, Y. Colombe, R. Blatt, and C. Roos. Frequency measurement of the  $^1S_0, F = 5/2 \leftrightarrow ^3P_1, F = 7/2$  transition of  $^{27}\text{Al}^+$  via quantum logic spectroscopy with  $^{40}\text{Ca}^+$ . *New J. Phys.*, 21(10):103003, 2019.
- [207] P. Micke, T. Leopold, S. A. King, E. Benkler, L. J. Spieß, L. Schmoeger, M. Schwarz, J. R. C. López-Urrutia, and P. O. Schmidt. Coherent laser spectroscopy of highly charged ions using quantum logic. *Nature*, 578(7793):60–65, 2020.
- [208] P. O. Schmidt. *Quantum Logic-Enabled Spectroscopy*. Wiley Online Library, 2016.
- [209] C. Chou, D. B. Hume, J. C. J. Koelemeij, D. J. Wineland, and T. Rosenband. Frequency Comparison of Two High-Accuracy  $\text{Al}^+$  Optical Clocks. *Phys. Rev. Lett.*, 104:070802, 2010.

- [210] G. K. Brennen, C. M. Caves, P. S. Jessen, and I. H. Deutsch. Quantum logic gates in optical lattices. *Phys. Rev. Lett.*, 82(5):1060, 1999.
- [211] M. Saffman and T. G. Walker. Analysis of a quantum logic device based on dipole-dipole interactions of optically trapped Rydberg atoms. *Phys. Rev. A*, 72(2):022347, 2005.
- [212] A. Bermudez, P. Schindler, T. Monz, R. Blatt, and M. Müller. Micromotion-enabled improvement of quantum logic gates with trapped ions. *New J. Phys.*, 19(11):113038, 2017.
- [213] C. Ospelkaus, C. E. Langer, J. M. Amini, K. R. Brown, D. Leibfried, and D. J. Wineland. Trapped-ion quantum logic gates based on oscillating magnetic fields. *Phys. Rev. Lett.*, 101(9):090502, 2008.
- [214] C. Ospelkaus, U. Warring, Y. Colombe, K. R. Brown, J. M. Amini, D. Leibfried, and D. J. Wineland. Microwave quantum logic gates for trapped ions. *Nature*, 476:181, 2011.
- [215] O. Katz, M. Pinkas, N. Akerman, and R. Ozeri. Quantum-Logic Detection of Chemical Reactions. *arXiv preprint arXiv:2107.08441*, 2021.
- [216] V. B. Braginsky, Y. I. Vorontsov, and K. S. Thorne. Quantum nondemolition measurements. *Science*, 209(4456):547–557, 1980.
- [217] V. B. Braginsky and F. Y. Khalili. Quantum nondemolition measurements: the route from toys to tools. *Rev. Mod. Phys.*, 68(1):1, 1996.
- [218] D. B. Hume, T. Rosenband, and D. J. Wineland. High-fidelity adaptive qubit detection through repetitive quantum nondemolition measurements. *Phys. Rev. Lett.*, 12:120502, 2007.

- [219] H. Stapelfeldt, H. Sakai, E. Constant, and P. B. Corkum. Deflection of neutral molecules using the nonresonant dipole force. *Phys. Rev. Lett.*, 79(15):2787, 1997.
- [220] T. Weber, J. Herbig, M. Mark, H. C. Nägerl, and R. Grimm. Bose-Einstein condensation of cesium. *Science*, 299(5604):232–235, 2003.
- [221] A. Ashkin. Optical trapping and manipulation of neutral particles using lasers. *Proc. Natl. Acad. Sci.*, 94(10):4853–4860, 1997.
- [222] J. R. Moffitt, Y. R. Chemla, S. B. Smith, and C. Bustamante. Recent advances in optical tweezers. *Annu. Rev. Biochem.*, 77:205–228, 2008.
- [223] P. Staannum, M. Drewsen, and K. Mølmer. Geometric quantum gate for trapped ions based on optical dipole forces induced by Gaussian laser beams. *Phys. Rev. A*, 70(5):052327, 2004.
- [224] Dietrich Leibfried et al. Experimental demonstration of a robust, high-fidelity geometric two ion-qubit phase gate. *Nature*, 422(6930):412–415, 2003.
- [225] J. C. J. Koelemeij, B. Roth, and S. Schiller. Blackbody thermometry with cold molecular ions and application to ion-based frequency standards. *Phys. Rev. A*, 76:023413, 2007.
- [226] D. M. Meekhof, C. Monroe, B. E. King, W. M. Itano, and D. J. Wineland. Generation of nonclassical motional states of a trapped atom. *Phys. Rev. Lett.*, 76:1796, 1996.
- [227] G. Hegi. *Towards A Non-Destructive Single Molecular Ion State Readout*. PhD thesis, University of Basel, 2021.
- [228] G. Herzberg. *Molecular Spectra and Molecular Structure, Volume II, Infrared and Raman Spectra of Polyatomic Molecules*. Krieger, Malabar, 1991.

- [229] D.B. Hume, C. W. Chou, D. R. Leibbrandt, M. J. Thorpe, D. J. Wineland, and T. Rosenband. Trapped-ion state detection through coherent motion. *Phys. Rev. Lett.*, 107:243902, 2011.
- [230] I. H. Bachir, H. Bolvin, C. Demuynck, J. L. Destombes, and A. Zellagui. High-Resolution Optogalvanic Spectrum of  $N_2^+$  Using a Ti: Sapphire Laser: The (2, 0) Vibration Band of the Meinel System  $A^2\Pi_u-X^2\Sigma_g^+$ . *J. Mol. Spectrosc.*, 166:88, 1994.
- [231] K. Harada, T. Wada, and T. Tanaka. Near-Infrared Diode Laser Spectroscopy of the (2, 0) Band of the  $A^2\Pi_u-X^2\Sigma_g^+$  System of the  $N_2^+$  Ion. *J. Mol. Spectrosc.*, 163:436, 1994.
- [232] D. C. Cartwright. Transition probabilities for the Meinel band system of  $N_2^+$ . *J. Chem. Phys.*, 58:178, 1973.
- [233] S. R. Langhoff, C. W. Bauschlicher Jr., and H. Partridge. Theoretical study of the  $N_2^+$  Meinel system. *J. Chem. Phys.*, 87(8):4716–4721, 1987.
- [234] F. R. Gilmore, R. R. Laher, and P. J. Espy. Franck–Condon factors, r-centroids, electronic transition moments, and Einstein coefficients for many nitrogen and oxygen band systems. *J. Phys. Chem. Ref. Data*, 21(5):1005–1107, 1992.
- [235] G. Morigi and H. Walther. Two-species Coulomb chains for quantum information. *Eur. Phys. J. D*, 13:261, 2001.
- [236] J. P. Home. Quantum science and metrology with mixed-species ion chains. *Adv. At. Mol. Opt. Phys.*, 62:231, 2013.
- [237] D. J. Wineland, C. Monroe, W. M. Itano, D. Leibfried, B. E. King, and D. M. Meekhof. Experimental issues in coherent quantum-state manipulation of trapped atomic ions. *J. Res. Natl. Inst. Stand. Technol.*, 103(3):259, 1998.

- [238] J. E. Christensen, D. Hucul, W. C. Campbell, and E. R. Hudson. High-fidelity manipulation of a qubit enabled by a manufactured nucleus. *Npj Quantum Inf.*, 6(1):1–5, 2020.
- [239] A. Kramida, Yu. Ralchenko, J. Reader, and NIST ASD Team (2020). NIST Atomic Spectra Database (version 5.8), [Online]. Available: <http://physics.nist.gov/asd> [Mon May 17, 2021]. National Institute of Standards and Technology, Gaithersburg, MD.
- [240] X. Zhou, X. Xu, X. Chen, and J. Chen. Magic wavelengths for terahertz clock transitions. *Phys. Rev. A*, 81(1):012115, 2010.
- [241] D. F. V. James. Quantum computation and quantum information theory. *Appl. Phys. B*, 66:181–190, 1998.